Doctoral Dissertation

博士論文

Mid-Cretaceous marine osmium isotopic record

(白亜紀中期海洋オスミウム同位体記録)

A Dissertation Submitted for the Degree of Doctor of Philosophy
December 2021

令和３年１２月 博士（理学）申請

Department of Earth & Planetary Science
Graduate School of Science, The University of Tokyo
東京大学大学院理学系研究科地球惑星科学専攻

Hironao Matsumoto

松本 廣直

Abstract

Mid-Cretaceous (~120 to 90 Ma) experienced several dramatic environmental perturbations (e.g., oceanic anoxic events: OAEs, biotic crises, and extremely high temperatures). Although they are considered linked to the massive submarine volcanism forming large igneous provinces (LIPs), reliable evidence supporting their linkages has been limited so far. Marine Os isotope ratio ($^{187}Os/^{188}Os$) reflects the balance between the unradiogenic Os input from the mantle and extraterrestrial materials, and radiogenic Os input through continental weathering. Therefore, paleo-marine Os isotopic information recorded in the sedimentary sequence has the potential as a tracer of the mantle-derived LIPs volcanic activity. In this dissertation, I reconstructed a continuous high-resolution paleo-marine osmium isotopic record ($^{187}Os/^{188}Os$) throughout the mid-Cretaceous and tried to constrain the exact timing of massive volcanic events and explored their relationship to the mid-Cretaceous environmental perturbations.

In Chapter I, I reviewed the previous studies on the temperature, pCO_2, and hydrothermal activity during the mid-Cretaceous and verify the conventional mid-Cretaceous image of "*the greenhouse world supported by high pCO_2 released from the intensive hydrothermal activity associated oceanic crustal production*". Subsequently, I summarized the major environmental perturbations during the mid-Cretaceous (i.e., OAEs and LIPs volcanism), the osmium isotopic records in the sedimentary sequence, and the scope of this study.

In Chapter II, I reconstructed a continuous marine Os isotopic record from upper Aptian to lower Albian (~118–110 Ma) encompassingOAE1b using Tethyan and Pacific sedimentary records. The Os isotopic record showed the several unradiogenic shifts during the lower part of OAE1b, which could represent massive submarine volcanic events at the Kerguelen Plateau. Since these unradiogenic shifts correspond to the biotic crises of planktonic foraminifera, massive volcanic events could have triggered severe biotic crises through ocean acidification. Besides, Os isotopic ratio showed radiogenic shifts during the upper part of OAE1b implying the enhanced continental weathering caused by intensive global warming.

In Chapter III, I conducted continuous high-resolution Os and C isotopic measurements using Tethyan sedimentary record covering the entire Aptian (~120–113 Ma). From the paleontological information and carbon isotopic ratios of carbonate ($\delta^{13}C_{carb}$), I identified the previously undescribed black shale horizons in the early Aptian (*Leupoldina cabri* planktonic foraminiferal Zone and Ap7 of carbon isotopic segment) and named it as the "Wezel Level". The Os isotopic ratio showed unradiogenic shifts at two black shale horizons of The Wezel and Fallot Levels during the early to mid-Aptian.

The sedimentary ages of these events roughly correspond to the formation ages of Ontong Java, Manihiki, and Hikurangi Plateaus, which once formed a single large oceanic Plateau called “Ontong Java Nui”. Thus, I concluded that the deposition of black shale horizons during Aptian was related to the enhanced submarine volcanic events at the OJN. This result implies that the massive volcanic events at the OJN could have continued for about 5 million years.

In Chapter IV, I reconstructed the Os isotopic record of the pelagic deep-sea sedimentary record of Goshikinohama bedded chert. Goshikinohama bedded chert provides a rare opportunity to examine the redox condition at the deep-sea Pacific basin during Aptian OAE1a. However, the exact stratigraphic interval of OAE1a has not been precisely constrained because of the lack of reliable stratigraphic indicators. The new Os isotopic data showed characteristic unradiogenic shifts at two purple chert horizons. These Os isotopic variations could represent the massive input of mantle-derived unradiogenic Os through the volcanic activity at the OJN, which can be correlated to the OAE1a interval. Since most of the OAE1a sequence is composed of red chert rich in hematite, oxic conditions prevailed at the deep-sea Pacific basin even during the OAE1a. However, the two purple beds with the especially unradiogenic Os isotopic values are slightly enriched in redox-sensitive elements (V, Cr, and U). These facts imply that the two especially intensive phases of the OJN volcanism caused especially strongly reducing conditions, which may have extended to the deep-sea Pacific Basin.

In Chapter V, I reconstructed continuous marine Os isotopic record during the Hauterivian to Barremian encompassing the first mid-Cretaceous OAE, called Faraoni Level. The Os isotopic ratio showed cyclic radiogenic shifts from 0.7 to 0.9 paced by the 400 kyr eccentricity, which represents the cyclic enhancement of continental weathering. Combining clay mineral composition in the Tethyan sedimentary sequence, I concluded that eccentricity-paced intensification of monsoonal activity caused the cyclic increase in continental weathering. Since Faraoni Level is not accompanied by the unradiogenic shifts, I concluded that this event is unrelated to the massive volcanic events.

In Chapter VI, I measured Os isotopic ratios of Albian to Turonian sedimentary rock samples deposited in pelagic Tethys and Indian Oceans. Combining these data with previous chapters, I reconstructed a continuous long-term Os isotopic record across the mid-Cretaceous. The compiled Os isotopic record suggests that hydrothermal activity was enhanced during Aptian, late Albian, and latest Cenomanian, which likely represent the enhanced hydrothermal activity associated with submarine LIPs volcanism. Besides, mid-Cretaceous OAE can be classified into two types: (1) OAEs accompanied by unradiogenic Os isotopic shifts (OAE1a, Wezel and Fallot Events, and OAE2) and (2) OAEs which are

not accompanied by unradiogenic shifts (OAE1c and OAE1d). The former OAEs were global events and caused by the increase in the primary productivity triggered by the massive LIPs volcanism. On the other hand, the latter OAEs have been mainly reported from the Tethyan region and were caused by the ocean stratification induced by the enhancement of monsoonal activity. The warmest interval during the mid-Cretaceous does not correspond to the enhanced hydrothermal activity but corresponds to the interval of the subaerial LIPs volcanism and circum-Pacific volcanic episodes. These data suggest that subaerial eruptions and following outgassing may have played an important role in the regulation of the mid-Cretaceous climate.

In Chapter VII, I summarized the doctoral dissertation. Subsequently, I compiled the Os isotopic variations during the Phanerozoic massive volcanic events and discussed the relationship between the location of LIPs volcanism and marine osmium isotopic variations. Finally, I described the problems and future perspectives of osmium isotopic studies using the sedimentary sequence.

Acknowledgments

I expressed my sincere gratitude to advisory committee members of my dissertation, Profs. Eiichi Tajika, Tsuyoshi Iizuka, Masayuki Ikeda, Tsuyoshi Komiya and Junichiro Kuroda. This study is conducted under the guidance of the supervisor, Prof. Junichiro Kuroda at Atmosphere and Ocean Research Institute (AORI). I am deeply indebted to Profs. Rodolfo Coccioni and Fabrizio Frontalini at the Urbino University, Italy, for their fruitful advice to my research and careful guidance of my manuscripts. I cannot complete this work without their help. I thank Drs. Andrea Mazzoli and Amr S. Zaky for their assistance in sampling sedimentary rocks in Italy. Sincere gratitude is expressed to Drs. Kenji Matsuzaki and Norikatsu Akizawa at AORI for their advice on my preliminary manuscript. I am deeply grateful to Drs. Katsuhiko Suzuki, Tatsuo Nozaki, and Toshihiro Yoshimura, and Yukari Ohtsuki at Japan Agency for Marine Earth-Science and Technology (JAMSTEC) for their assistance with Re-Os analysis. I would like to thank Dr. Maria Luisa Tejada at JAMSTEC and Dr. Takashi Sano at the National Museum of Nature and Science for the advice on the Ontong Java volcanism. Sincere gratitude is expressed to Prof. Akira Ishikawa at the Tokyo Institute of Technology for the advice of Os isotopic analysis and valuable comments on my research. I wish to thank Prof. Kotaro Shirai, Dr. Kentaro Tanaka, and Noriko Izumoto at AORI, and Dr. Saburo Sakai at JAMSTEC for the help with carbon isotopic analysis of carbonate. I am thankful to Drs. Naohiko Ohkouchi, and Ogawa O., Nanako at JAMSTEC for the support with organic geochemical analysis. I am obliged to Drs. Takazo Shibuya and Motoko Igisu at JAMSTEC for their assistance with Raman analysis. I thank Dr. Satoshi Takahashi at the University of Tokyo for the assistance of Scanning Electron Microscope (SEM) and valuable advice for my research. Sincere gratitude is offered to Dr. Takashi Toyofuku at JAMSTEC for the assistance of SEM analysis. This study is supported by the Profs. Luigi Jovane, Jairo F. Savian, and Ricardo I. F. Trindade. I thank Dr. Silvia Gardin at Centre de Recherche en Paléontologie-Paris for the paleontological advice. I would like to thank Prof. Rie Hori at Ehime University for the constructive comments on my manuscript. Also, I warmly thank the members of the Department of Ocean Floor Geoscience in AORI for the advice on my research. This study was financially supported by Grant-in-aid for JSPS Research Fellow (19J20708). Parts of the sedimentary rock samples are provided by International Ocean Discovery Program (IODP) (Sample request numbers: 071305-IODP, 072558-IODP, 073623-IODP, 075591-IODP, 076411-IODP, 089443-IODP).

Contents of the doctorate dissertation

CHAPTER I

General Introduction

I-1. Conventional vs. Precise views of the mid-Cretaceous world

The Cretaceous Period is a geological interval from ~145 Ma to 66 Ma and consists of the two Epochs (i.e., Early and Late Cretaceous) and twelve Stages (i.e., Berriasian, Valanginian, Hauterivian, Barremian, Aptian, Albian, Cenomanian, Turonian, Coniacian, Santonian, Campanian, and Maastrichtian) (Gale et al., 2020). The middle part of the Cretaceous ranging from the late Barremian to early Turonian experienced dramatic environmental perturbations, such as the extremely warm climate (e.g., Huber et al., 2018) repeated oceanic anoxic events (e.g., Leckie et al., 2002), massive magmatic episodes (e.g., Coffin and Eldholm, 2005), and biotic crises of marine organisms (e.g., Leckie et al., 2002) (Fig. I-1). The term "mid-Cretaceous" has been often used to describe this distinctive geological interval with large environmental perturbations. Since it is regarded as a potential analog of future environmental perturbations, the understanding of the mid-Cretaceous world has attracted wide attention (e.g., Beerling et al., 2011). However, mid-Cretaceous is a vague term and its definition is slightly different from study to study. In this dissertation, "mid-Cretaceous" is defined as the geological interval from the late Barremian to early Turonian (121–93 Ma).

The mid-Cretaceous earth environment was different from the present earth in many aspects. The super-continent, Pangea, started to break up into Laurasia and Gondwana during the latest Triassic (e.g., Müller et al., 2016) and further broke up into smaller pieces of continents (i.e., North America, Eurasia, South America, Africa, Australia-Antarctica, and Indian blocks) during the mid-Cretaceous (Fig. I-2a) (e.g., Scotese and Golonka, 1997). Mg/Ca ratio of seawater during the mid-Cretaceous was considered lower (calcite ocean: Mg/Ca<2) than the present and favorable condition for the marine organism making calcite tests (e.g., rudists, calcareous nannofossils, and planktonic foraminifera) (Ries, 2010). As the result, chalk and limestones, rich in planktonic foraminifera and calcareous nannofossils, were deposited in the wide sedimentary settings including "Terrain Crétacé" in the Paris Basin which was the origin of the word "Cretaceous" (Gale et al., 2020 and reference therein).

The mid-Cretaceous is generally believed to be a hot greenhouse world (e.g., Huber et al., 2018). The sea-surface temperature of the Atlantic Ocean during the Cenomanian to Turonian (~100–90 Ma) reached 34°C (e.g., Moriya et al., 2007), which was more than 5°C warmer than the present ocean at the same latitude. Several studies have revealed that such warm conditions prevailed even in the polar regions (Fig. I-1) (e.g., Spicer and Herman, 2010; Herman et al., 2016; Klages et al., 2020). This warm climate was likely sustained by high pCO_2 up to several thousand ppm (Fig. I-1) (e.g., Hong and Lee, 2012; Wang, Y. et al., 2014 and references therein) that has been attributed to the active

degassing associated with oceanic crustal production (Fig. I-1) (e.g., Larson, 1991; Hong and Lee, 2012).

However, these typical features actually represent the only short geological interval from the Cenomanian to Turonian in mid-Cretaceous (100–90 Ma) and mid-Cretaceous climate was more variable than generally believed. Before describing the objectives of this study, I would like to update our current knowledge about (1) temperature, (2) pCO_2, and (3) hydrothermal activity during the mid-Cretaceous.

I-1.1. Temperature variations during the mid-Cretaceous

The seawater temperature during the mid-Cretaceous has been estimated from the various proxies (e.g., oxygen isotope ratio ($\delta^{18}O_{carb}$) of calcareous fossils, TEX_{86} index, and composition of calcareous nannofossil assemblages: Bottini and Erba, 2018; Huber et al., 2018; Steining et al., 2020). These proxies suggest that the early half of the mid-Cretaceous (from upper Barremian to early Albian: 121–113 Ma) is characterized by a relatively cool climate except for the earliest Aptian OAE1a (discussed in Chapter I-1.2). For example, $\delta^{18}O$ of well-preserved foraminifera recovered from the Atlantic region show that the latest Aptian (~118–113 Ma) sea-surface and bottom water temperatures are 10–14℃ and 8–10℃, respectively (Huber et al., 2011), which are 10–16 ℃ and 4–6℃ cooler than present-day condition at the same latitude. The cool climate during the late Aptian is also supported by other geochemical proxies, such as the oxygen isotopic ratios of belemnite (Bodin et al., 2015) and TEX_{86} index (McAnena et al., 2013) (Fig. I-3c). Besides, glendonite and dropstones, suggesting the presence of cold bottom water and ice drafts, have been reported from the Barremian and late Aptian to earlies Albian sedimentary record of the Arctic and Antarctic region (Figs. I-1, 2a, and 3c) (e.g., Herrle et al., 2015; Rodríguez-López et al., 2016; Vickers et al., 2019). Based on these pieces of evidence, the late Aptian is considered as one of the coolest intervals during the mid-Cretaceous and called as “Aptian cold snap” (Fig. I-3c).

The sea surface temperature (SST) estimated from the $\delta^{18}O$ of calcareous fossils and TEX_{86} index started to increase abruptly from the Aptian-Albian boundary (~113 Ma) (Fig. I-3c) (e.g., McAnena et al., 2013; Bodin et al., 2015). At the same time, the glendonite disappeared from the arctic sedimentary record, which suggests the onset of warming in the polar regions. The SST kept increasing during Albian and took the highest value from the upper Cenomanian to Turonian (Fig. I-3c) (Huber et al., 2011, 2018; Friedrich et al., 2012; Steining et al., 2020). Arctic temperature variation estimated from the Climate Leaf Analysis Multivariate Program (CLAMP) using north arctic leaves also indicates that atmospheric temperature started to rise from the Albian and took highest

values at the Cenomanian (Spicer and Herman, 2010; Herman et al., 2016).

Despite some debates on the reliability and interpretations of these proxies (Pearson et al., 2001; Huber et al., 2011; Tierney, 2014), most studies support the idea that the early half of the mid-Cretaceous (118–113 Ma) was characterized by a relatively cooler climate and, at least, seasonal polar ice could have existed. On the other hand, the conventional mid-Cretaceous characteristics of "extremely high temperature" occurred only during Cenomanian–Turonian interval (100–90 Ma).

I-1.2. pCO_2 during the mid-Cretaceous

The mid-Cretaceous temperature variations are likely modulated by the variation of atmospheric CO_2 concentrations. The paleo-pCO_2 has been reconstructed by several methods, such as fossil plant stomata, stable carbon isotopes of paleosol, stable carbon isotopes of fossil liverworts, boron isotopes of marine carbonate, alkenones, and modeling calculations (Wang, Y. et al., 2014 and reference therein). Most of the studies agree that mid-Cretaceous pCO_2 were low during the Aptian and highest during the Cenomanian–Turonian interval (Wang, Y. et al., 2014). Since these trends are consistent with the temperature variations of the mid-Cretaceous, pCO_2 was considered as the most important factor to control the mid-Cretaceous climate. However, the estimated paleo-pCO_2 values have large variations depending on the methods and studies (from ~500 to several thousand ppm: Hong and Lee, 2012; Wang, Y. et al., 2014 and references therein) and no consensus has been achieved. Considering the lowest estimate of pCO_2 values during Barremian to Aptian are close to the modern values (Fig. I-1), the extremely high pCO_2 cannot characterize the entire mid-Cretaceous.

I-1.3. Estimated hydrothermal intensity

The long-term pCO_2 variations during the mid-Cretaceous are considered regulated by the hydrothermal activity associated with the oceanic crustal production (e.g., Larson, 1991) and subduction of carbonate sediments (Barnes et al., 1978). Since these factors are mainly controlled by the oceanic crustal spreading rate, its accurate estimation is essential for understanding the mid-Cretaceous climate variation. The mid-Cretaceous oceanic crustal production rate has been mainly estimated from (1) the sea-level changes (e.g., Mills et al., 2017), (2) reconstructed plate motions (e.g., Larson, 1991; Rowley, 2002; Demicco, 2004; Cogné and Humler, 2006; Seton et al., 2009; Müller et al., 2016), and (3) paleo-seawater Sr isotopic ratios (e.g., Blättler et al., 2011; Pogge von Strandmann et al., 2013; Adloff et al., 2021).

The first method is based on the idea that the changes in the seafloor spreading rate

and ridge volume influenced sea-level fluctuations due to the eustacy (Gaffin, 1987). However, this method cannot estimate the influence of sea-level change caused by the glacial formation, and the short-term hydrothermal events associated with the formation of a large oceanic plateau. Besides, most of the papers are based on the old sea-level reconstruction of Vail et al. (1977a,b) and no fundamental revision has been done (Mills et al., 2017). These papers describe large sea-level changes over 100 m. However, since there were no large and long-lasting ice sheets during the mid-Cretaceous, it is difficult to explain the triggering mechanism of such large sea-level changes. Indeed, Vail et al. (1977a,b) admitted that the amplitude of the sea-level change has large uncertainties because it is difficult to estimate the local orogenic deformation, tectonic subsidence, and excessive sedimentary loading. Thus, further updates of sea-level information are essential for the reliable and quantitative reconstruction of seafloor spreading rate during the mid-Cretaceous using this method.

The second method estimated oceanic crustal production rate based on the reconstructed past plate motions (e.g., Larson, 1991; Rowley, 2002; Demico, 2004; Cogné and Humler, 2006; Seton et al., 2009; Müller et al., 2016). Since the oceanic plate record paleomagnetic reversals, it is possible to determine the ages of the oceanic plate and estimate the past oceanic crustal production rate. However, the reconstructed oceanic crustal production rates in these papers have large variations, and some reconstructions contradicted the rapid oceanic crustal production at the ridges during the mid-Cretaceous (e.g., Rowley, 2002; Cogné and Humler, 2006). These contradictions seem to be derived from the differences in the calculation methods of ocean floor spreading rate and the subducted areas (Cogné and Humler, 2006). Besides, the temporal resolution of the mid-Cretaceous oceanic crustal production rate is not good due to the difficulties in determining the oceanic crustal ages during the Cretaceous normal superchron that lacks polarity reversal (Hasley et al., 1968; Gale et al., 2020).

The last strategy is the proxy-based reconstruction of hydrothermal activity associated with oceanic crustal production. Marine $^{87}Sr/^{86}Sr$ values represent the balance between continental derived Sr with radiogenic values (0.71106: Peucker-Ehrenbrink and Fiske, 2019) and hydrothermal derived Sr with less radiogenic values (0.7035: Peucker-Ehrenbrink and Fiske, 2019). Thus, paleo-marine strontium isotopic ratio ($^{87}Sr/^{86}Sr$) variation could represent the relative intensity of hydrothermal activity which potentially reflects the paleo-oceanic crustal production rate (Figs. I-1 and 3d). Less radiogenic paleo-marine $^{87}Sr/^{86}Sr$ values during the mid-Cretaceous could suggest the enhanced oceanic crustal production and associated hydrothermal activity than present (Antonelli et al., 2017). Especially, $^{87}Sr/^{86}Sr$ showed the most rapid unradiogenic shift during the

Aptian, which implies the pronounced oceanic crustal production interval (Fig. I-3) (e.g., Bralower et al., 1997). $^{87}Sr/^{86}Sr$ values back to the background values during the Albian to Cenomanian which implies the weakening of hydrothermal activity (Fig. I-3). However, because of the long residence time of Sr (~3 million years), this proxy also has a problem in the time resolution. In addition, the precise quantitative estimation of past hydrothermal activity and plate production is difficult because of the lack of precise continental weathering information and uncertainties in the Sr system in the ocean.

To summarize the above discussions, hydrothermal activity during the mid-Cretaceous has been estimated by several methods. However, the estimated values are highly variable depending on methods and studies. Based on the Sr isotopic data, hydrothermal activity associated with the oceanic crustal production was most intensive during Aptian (Fig. I-3d). However, due to the long residence time of Sr in the ocean (~1.9–3.4 million years: Hodel et al., 1990), marine $^{87}Sr/^{86}Sr$ cannot record rapid changes in the hydrothermal activity (~10^5 years scale). Thus, for high-resolution hydrothermal reconstructions, the development of more reliable indicators of hydrothermal activity with shorter residence time is required.

I-1.4. Current picture of the mid-Cretaceous climate

Combining the discussions from Chapter I-1.2–I-1.3, the Barremian to earliest Albian (~122 to 113 Ma) was characterized by relatively low pCO_2 and a relatively cool climate (Fig. I-3c). The temperature and pCO_2 started to increase from the Aptian–Albian boundary (~113 Ma) and took the highest value during Cenomanian–Turonian (~100–90 Ma) (Fig. I-3c). The $^{87}Sr/^{86}Sr$ variations suggest that hydrothermal activity associated with the oceanic crustal production was enhanced during the Aptian characterized by the cool climate and weaken during Cenomanian when the highest temperature was achieved (Fig. I-3d). These pieces of evidence imply that the Cretaceous climate was highly variable and the long-believed typical mid-Cretaceous image of "*hot-house world supported by extremely high pCO_2 maintained by the enhanced oceanic crustal production*" seems not true in many respects.

I-2. Oceanic Anoxic Events

One of the characteristic events during the mid-Cretaceous is the oceanic anoxic events (OAEs). OAEs are defined as the episodic phases of organic-carbon burial under the various oceanic setting at the same time (Schlanger and Jenkyns, 1976). Normally, the pelagic deep-sea water in the present ocean is well-oxygenated due to the oceanic

circulations and organic matter is easily re-mineralized by O_2. Thus, the total organic carbon contents (TOC) in the pelagic deep-sea sediments are low (<0.5 wt%) except for the high productivity area, such as upwelling zones, shelf areas, and arctic regions (Seiter et al., 2004). However, at some timings in the earth's history, worldwide depositions of dark-colored organic-rich sediments have been reported (e.g., Schlanger and Jenkyns, 1976). In some cases, these organic-rich intervals with extremely high TOC (~up to 30 wt% in case of Cretaceous sedimentary record: Schlanger and Jenkyns, 1976) have been observed not only at the coastal areas but also in the pelagic mid-Pacific regions (e.g., Schlanger and Jenkyns, 1976; Sliter, 1999; Price, 2003). Especially, well-laminated dark-colored organic-rich sedimentary rocks are specifically termed as “black shale”. Since the organic matter is easily decomposed under the usual oxic oceanic condition, the bottom water was considered depleted in oxygen worldwide during the major OAEs (Schlanger and Jenkyns, 1976). The presence of pyrite and redox-sensitive elements and lack of bioturbation in these organic-rich sediments further support the possibility of oxygen-depleted bottom-water and/or water column conditions (e.g., Kuroda et al., 2005; Scopelliti et al., 2006). Originally, the term “Oceanic Anoxic Event” was used to indicate the worldwide oxygen-depleted condition which caused the deposition of organic-rich sediments (Schlanger and Jenkyns, 1976). However, at present, OAE is used to indicate the worldwide deposition of organic-rich sediments, which does not necessarily require the oxygen-depleted oceanic condition.

From the first suggestion of the idea of OAEs in Schlanger and Jenkyns (1976), many OAEs have been reported throughout the Phanerozoic era (Fig. I-4) and especially many OAEs have been identified in the mid-Cretaceous Tethyan sedimentary sequence (e.g., OAE1a, Noir, and Fallot events, OAE1b, OAE1c, OAE1d, and OAE2) (Figs. I-2 and 4). In them, the most pronounced mid-Cretaceous OAEs are the earliest Aptian OAE1a and the latest Cenomanian OAE2. These OAEs continued ~1.4 and 0.7 Myr, respectively (Gale et al., 2020), and the thick organic-rich sediments are not only reported from the Tethyan region (e.g., Coccioni et al., 1987; Schlanger and Jenkyns, 1976 and reference therein) but also Atlantic and the shallow Pacific region (Fig. I-3b) (e.g., Schlanger and Jenkyns, 1976; Sliter, 1999; Price, 2003), which indicates that these events are truly world-wide events. On the other hand, other smaller OAEs (e.g., OAE1b, OAE1c, and OAE1d) characterized by thinner organic-rich sediments are only reported in the Tethys and Atlantic regions (Fig. I-3b) and considered regional events. These minor organic-rich horizons are different from major mid-Cretaceous OAEs of OAE1a and OAE2 not only in lithologies but also in organic geochemical features. The organic matter deposited during the major OAEs (OAE1a and 2) is mainly composed of Type II kerogen derived

from marine primary producers while other black shales (e.g., OAE1c and 1d) are mainly composed of type III kerogen that is derived from terrigenous organic matter (Erbacher et al., 1996). In addition, the Tethyan sedimentary record contains numerous regional not-named astronomical-paced thin-black shales that are reported in the Valanginian–Barremian, Albian, and late Cenomanian intervals that are paced by the short-eccentricity cycles (Fig. I-3a) (Mitchell et al., 2008; Lanci et al., 2010; Franceschi et al., 2011). These facts imply that the mid-Cretaceous OAEs are the amalgam of the different oceanic anoxic events with different origins and features.

The depositions of major organic-rich intervals roughly correspond to the biotic crises of marine planktons (Leckie et al., 2002), changes in the lithologies (e.g., Coccioni and Premoli Silva, 2015; Coccioni, 2020), and the perturbations of carbon cycles (Menegatti et al., 1998) (Figs. I-2b and 3). Therefore, the worldwide depositions of organic-rich sediments are believed to have caused a significant impact on the marine environment. The triggering mechanism of OAEs has been actively debated and one of the candidates for the triggering factors of OAEs is the massive volcanic events forming large igneous provinces.

I-3. Large Igneous Provinces

One of the most drastic events during the mid-Cretaceous is the repeated massive volcanic episodes associated with the formations of large igneous provinces (LIPs). LIPs are defined as the massive basaltic plateau with areal extents >0.1 Mkm^2 and igneous volume >0.1 Mkm^3 and a large proportion of the basaltic plateaus was formed during a short geological interval (~1–5 Myr) (Bryan and Ernst, 2008). These basaltic plateaus are considered derived from the mantle plumes and repeatedly formed throughout the earth's history (Fig. I-5a) (Eldholm and Coffin, 2000). During the massive volcanic event forming LIPs, enormous amounts of volatiles and CO_2 could have been released into the atmosphere-ocean systems which could have directly and/or indirectly caused the environmental perturbations, such as global warming (e.g., Bond and Sun, 2020), ocean-acidification (e.g., Gutjahr et al., 2017), ocean eutrophication, and oceanic anoxia (e.g., Erba et al., 2015). Indeed, the timing of the major Phanerozoic LIPs formations roughly corresponds to the major extinction of marine biota and the occurrences of OAEs (Fig. I-5b) and their causal linkages have been intensively debated so far.

During mid-Cretaceous, especially many submarine LIPs formations have been reported (e.g., Paranà-Etendeka LIPs, Ontong Java Plateau, Manihiki Plateau, Hikurangi Plateau, Kerguelen Plateau, Madagascar, Agulhas, Caribbean Plateaus) (Fig. I-5a). Since the estimated formation ages of major mid-Cretaceous LIPs (e.g., Ontong Java, Kerguelen,

and Caribbean Plateaus) roughly correspond to the sedimentary ages of major OAEs (OAE1a: ~120 Ma, OAE1b: ~113 Ma, and OAE2: ~94 Ma), these OAEs have been ascribed to the massive volcanic events forming LIPs (e.g., Larson and Erva, 1999; Leckie et al., 2002; Kuroda et al., 2007). The typically proposed mechanism of OAEs triggered by the massive volcanic event is as follows (Fig. I-6). Massive volcanic events released a large amount of greenhouse gases into the atmosphere that caused global warming. Subsequently, continental weathering was accelerated, and nutrients were supplied into the ocean. As a result, primary production increased, and oxygen was consumed by decomposing the organic matter, which lead to oceanic anoxia.

In order to prove the causal linkages between LIPs volcanic events and environmental perturbations, the accurate chronological correlations of these events are essential. The formation age of the mid-Cretaceous LIPs is mainly determined by the ^{39}Ar-^{40}Ar of basaltic rock samples. However, this method is sometimes accompanied by large uncertainties up to several million years. For example, the estimated formation ages of Ontong Java Plateau using the ^{39}Ar-^{40}Ar method range from 122–129 Ma and each data has a large error from 2–9 myr (Olierook et al., 2019). These values can be easily altered by the secondary alteration of the basaltic rock (e.g., Baksi et al., 2007), ^{40}K decay constant, and inter-calibration values (Olierook et al., 2019). Besides, we can access the only surface of basaltic samples and it is impossible to obtain a deeper part of the basaltic plateaus.

In addition, the ages of the mid-Cretaceous sedimentary sequence also contain large uncertainties. For example, the latest Geologic Time Scale (GTS) 2020 defined the Barremian-Aptian boundary, when the Ontong Java Plateau was formed, at 121.4 Ma (Gale et al., 2020) that was ~5 million years younger than the previous version of GTS 2012 (126.3 Ma: Ogg et al., 2012). Thus, it is difficult to precisely correlate the ^{39}Ar-^{40}Ar ages of LIPs basalt and sedimentary ages recording environmental perturbations using these conventional ways. One of the possible solutions for their precise age correlations is to trace the volcanic signals recorded in the sedimentary record. The LIPs volcanism could have caused the isotopic perturbations in many elements (e.g., ^{87}Sr/^{86}Sr, ^{187}Os/^{188}Os, δ^{13}C, and δ^{34}S) (e.g., Bralower et al., 1997; Tejada et al., 2009; Laakso et al., 2020) and released massive volcanic materials (e.g., volcanic ashes), which were recorded in the same sedimentary sequence that records the environmental perturbation. Thus, by extracting volcanic information from the sedimentary records, these events can be stratigraphically correlated.

I-4. Osmium isotopic ratio

Recent studies on the paleo-marine Os isotopic record have provided clues on the relationship between the volcanic events at the submarine LIPs volcanism and the oceanic anoxic events. Os isotopic ratio represents the ratio of radiogenic Os (^{187}Os) derived from the radioactive decay of ^{187}Re and unradiogenic ^{188}Os. Mantle and extraterrestrial materials have less radiogenic ^{187}Os/^{188}Os values (~0.12: Levasseur et al., 1999) because of their relatively low ^{187}Re/^{188}Os values (Fig. I-7a). On the other hand, due to the greater incompatibility of Re than Os, continental crust tends to have higher ^{187}Re/^{188}Os and more radiogenic ^{187}Os/^{188}Os values than mantle (e.g., Peucker-Ehrenbrink and Blum, 1998; Peucker-Ehrenbrink and Jahn, 2001; Lassiter, 2003). Besides, the sediments deposited under the oxygen-depleted condition tend to have high ^{187}Re/^{188}Os (e.g., Selby and Creaser, 2003; Yamashita et al., 2007). As the result, riverine Os derived from old granitoid and old organic-rich sedimentary rocks exposed on land has more radiogenic ^{187}Os/^{188}Os values (~1.4) than that of the mantle and extraterrestrial materials (Fig. I-7a) (Peucker-Ehrenbrink and Ravizza, 2000). Marine Os isotopic ratios mainly reflect the balance of Os input flux from extraterrestrial material (~17.6 t/kyr) and mantle/hydrothermal (~108.3 t/kyr) with unradiogenic Os isotopic values (~0.12) (Levasseur et al., 1999), and riverine Os input (~295 t/kyr) with radiogenic Os isotopic values (~1.4) (Levasseur et al., 1999; Peucker-Ehrenbrink and Ravizza, 2000). Since marine ^{187}Os/^{188}Os can reflect the relative intensity of hydrothermal/mantle Os input, it has potential as the tracer of massive volcanic events forming LIPs.

The estimated Os concentration in seawater is ~a few to 11 fg g^{-1} (Fig. I-7c) (Sharma et al., 1997; Levasseur et al., 1998; Woodhouse et al., 1999). However, due to its very low concentration in the seawater, this estimated value has relatively large uncertainties. Since the residence time of Os (~8 to 50 kyr: Levasseur et al., 1999; Oxburgh, 2001) is longer than the representative oceanic circulation time, Os isotopic ratio in the present ocean takes relatively constant values ~1.05–1.06 (Sharma et al., 1997; Levasseur et al., 1998; Woodhouse et al., 1999). X-ray Absorption Fine Structure (XAFS) study on the artificial seawater inferred that Os exists in the oxidized form of $OsCl_6^{2-}$, $HOsO_5^-$, and $H_3OsO_6^-$ in the seawater (Fig. I-7b) (Yamashita et al., 2007). However, the direct measurement of the oxidation state of Os in the real seawater is difficult because of its extremely low concentration. Under the reducing condition, Os is removed from the seawater by reducing Os to the insoluble form of Os(IV) and Os(III) and recorded in the sediments (Fig. I-7b) (Yamashita et al., 2007). Several materials have been suggested as candidates for the host phases of Os in the sediments, such as Fe- and Mn- oxides, organic matter, and sulfide (Fig. I-7b) (e.g., Lu et al., 2017; Yamashita et al., 2007; Sekine et al., 2011).

The Os isotopic composition of the surface of the sediment and Fe–Mn crust is almost identical to that of present seawater (Fig. I-7c) (e.g., Burton et al., 1999; Oxburgh, 1998). Besides, $^{187}Os/^{188}Os$ values in the sedimentary rock show quite similar variations if the ages of sedimentary rocks were deposited in the same age (e.g., Oxburgh et al., 2007; Du Vivier et al., 2014). Therefore, it is empirically known that Os isotopic information in the sedimentary record mainly reflects hydrogenous information. However, since sediment contains siliciclastic minerals derived from continents, sedimentary Os isotopic information actually represents the mixture of terrigenous and hydrogenous fractions. Organic-rich sediments deposited under the reducing condition are generally regarded as a good material for the paleo-marine Os isotopic record because it has extremely high Os concentrations compared to the terrigenous silicates (e.g., Selby and Creaser, 2003). However, Re-Os analysis of old organic-rich sedimentary rocks has a critical problem. Since organic-rich sediments tend to have high $^{187}Re/^{188}Os$ values, the measured (present-day) $^{187}Os/^{188}Os$ of old organic-rich sediments tend to take higher values (> 1) than the original Os isotopic values (~0.2–1.0) due to the in-situ radioactive decay of ^{187}Re into ^{187}Os. Thus, a large age correction is required to obtain the initial $^{187}Os/^{188}Os$ values. This implies that if the original proportions of Re and Os in the sedimentary rocks were altered by the secondary alteration and/or weathering, it is impossible to estimate the initial Os isotopic ratios precisely. Indeed, some of the previous studies reported that initial Os isotope values of old sedimentary rocks with high $^{187}Re/^{188}Os$ showed unrealistically low (< 0.0) and high initial Os isotopic values (> 1.5) caused by the secondary alterations (e.g., Choen and Coe, 2002; Nozaki et al., 2019; Liu and Selby, 2021).

On the other hand, sedimentary rocks deposited under the oxidized condition tend to take low $^{187}Re/^{188}Os$. Since the differences between measured (present-day) and age-corrected (initial) $^{187}Os/^{188}Os$ values of these sedimentary rocks are relatively small, they are less influenced by the secondary alteration of the Re-Os system. Therefore, these materials are considered suitable for the reconstruction of paleo-marine Os isotopic records older than Cenozoic when the well-preserved oceanic cores are limited. However, due to their extremely low Os concentrations, Os isotopic information recorded in these materials is easily influenced by the contamination of radiogenic Os included in the silicate minerals. Thus, for the reconstruction of the paleo-marine Os isotopic record, it is important to use multiple sedimentary records and check whether their variation pattern represents global signals or not.

Paleo-marine Os isotopic ratios have been intensively investigated during the Cenozoic (Fig. I-8) (Peucker-Ehrenbrink and Ravizza, 2012). In the case of the mid-Cretaceous, the Os isotopic ratios of the sediments during OAE1a and OAE2 have been

intensively investigated so far (Turgeon and Creaser, 2008; Tejada et al., 2009; Bottini et al., 2012; Du Vivier et al., 2014, 2015; Sullivan et al., 2020; Percival et al., 2021). These studies have revealed that the Os isotopic ratios showed pronounced less radiogenic shifts during these OAEs (Fig. I-8). Since the radiometric ages of the Ontong Java Plateau and Caribbean Plateau roughly correspond to the Os isotopic excursions of OAE1a and OAE2, they are interpreted to reflect the massive submarine volcanism associated with the formation of LIPs. These studies strongly support the hypothesis that massive volcanic events caused these mid-Cretaceous OAEs. However, almost all of the mid-Cretaceous Os isotopic studies focus on short geological intervals around the OAE1a and OAE2 and there have been no continuous Os isotopic data covering other mid-Cretaceous OAEs.

I-5. Objectives of this study

This study aims to establish a continuous and high-resolution Os isotopic stratigraphy throughout the mid-Cretaceous. Mid-Cretaceous is typically believed to be a "*hot-house world supported by high pCO_2 maintained by the enhanced oceanic crustal production*" (e.g., Larson, 1991). However, this typical Cretaceous image has not been proved due to the lack of reliable long-term high-resolution hydrothermal data. Since Os isotopic data in the sedimentary record have the potential to provide high-resolution paleo-hydrothermal information, this study could validate the long-believed typical Cretaceous image described above. The understanding of the cause of the extremely high temperature during the mid-Cretaceous (~100–90 Ma) is important not only for the comprehension of the evolution of the earth ecosystem but also for the prediction of future Anthropocene environmental perturbations.

Os isotopic ratios in the sedimentary sequence have the potential as a tracer of massive volcanic events forming large igneous provinces. Previous studies have constrained the duration of major volcanic events at the Ontong Java and Caribbean Plateaus from the sedimentary Os isotopic record (Turgeon and Creaser, 2008; Tejada et al., 2009). However, there are still a lot of LIPs whose exact duration has not been constrained so far. This study aims to detect all massive volcanic pulses during the mid-Cretaceous using Os isotopic record and examined the relationship between the LIPs formation and the contemporaneous environmental perturbations.

From the first proposal of the concept of OAE in 1976 (Schlanger et al., 1976), a lot of articles focusing on the relationship between OAEs and volcanic events (Turgeon and Creaser, 2008; Tejada et al., 2009) and biotic crises (e.g., Erba et al., 1994) have been published. However, there has been no fundamental improvement in the understanding of mid-Cretaceous OAEs and their influence earth environment for a decade. One of the

causes is that most of the previous paleontological and geochemical studies including Os isotopic records focus on the short geological interval (~a few million years) across the two global oceanic anoxic events of OAE1a and OAE2. However, in order to fully understand the differences in oceanic environments during the major mid-Cretaceous OAEs and normal oceanic conditions, long-term background information is essential. Besides, the mid-Cretaceous sedimentary sequence records many other organic-rich intervals (i.e., Faraoni, Wezel, and Fallot events, OAE1b, OAE1c, and OAE1d). However, it is uncertain whether all mid-Cretaceous OAEs are caused by the conventionally proposed triggering mechanism, "the LIPs volcanism caused the global warming which led to the OAEs". Thus, another motivation of this study is the acquisition of the background Os isotopic variations and the validation of the above hypothesis on the triggering mechanism of OAEs.

The last purpose of this study is to establish a standard Os isotopic curve throughout the mid-Cretaceous. Generally, stratigraphic correlations of mid-Cretaceous sediments are conducted by magnetostratigraphy, biostratigraphy (e.g., ammonite, coccolith, planktonic foraminifera, and radioralia), and chemostratigraphy (e.g., $\delta^{13}C$, $^{87}Sr/^{86}Sr$, and $\delta^{34}S$). However, since most of the mid-Cretaceous is located within the normal superchron (Hasley et al., 1968; Gale et al., 2020) where no magnetic reversal exists, magnetostratigraphy cannot be applied for mid-Cretaceous stratigraphic correlations. Biostratigraphy (e.g., ammonite, radioralia, coccolith, and foraminifera) is another powerful tool for stratigraphic correlations. However, fossils with calcareous tests are rare and poorly preserved in the organic-rich sediments (e.g., OAE1a, OAE1b, and OAE2 intervals: Coccioni and Luciani, 2004; Coccioni et al., 2014; Coccioni 2020) and the sedimentary record which was deposited below carbonate compensation depth (CCD). Besides, since the possibility of species localization cannot be ruled out completely, it is important to combine biostratigraphy with other chemostratigraphy. Carbon isotopic stratigraphy using carbonate is also a useful tool, but it cannot be applied to the sedimentary rock samples with extremely low calcium carbonate content, such as deep-sea pelagic chert and black shale layers. Besides, carbon isotopic stratigraphy using organic matter can be susceptible to the source of organic matter especially in the case of the low TOC samples. Sr isotopic stratigraphy can be applied when the well-preserved carbonate/phosphate samples are available. However, it can produce a very gradual curve because of its long-residence time of ~3 myr and is not suitable for high-resolution stratigraphic correlations.

On the other hand, Os isotope records of the sedimentary rocks are very useful for the stratigraphic correlations. Os isotopic ratios in the ocean can trace the changes in Os

isotopic shift of ~10^4 years order because of its relatively short residence time in the ocean (~8 to 50 kyr: Levasseur et al., 1999; Oxburgh, 2001). Besides, since the residence time of Os is longer than the typical ocean circulation time (~1 kyr: Broecker and Pend, 1982), it is homogeneous in the ocean. In addition, Os isotopic stratigraphy can be potentially used in various lithologies including deep-sea chert sequence. Therefore, the Os isotopic variation presented in this study will contribute to the establishment of the new strong chemostratigraphy during the mid-Cretaceous.

I-6. Outline of This Dissertation

In this chapter (Chapter I), I summarized the mid-Cretaceous climate and environmental perturbations, and osmium isotope systems in the ocean. In Chapter II, I reconstructed high-resolution Os isotopic records across the Aptian-Albain boundary (~113 Ma) using two distant pelagic sedimentary records, Umbria–Marche, Italy, and DSDP Site 463 deposited at the mid-Pacific Mountains. Based on the Os isotopic records, I discussed the relationship between the biotic crisis during OAE1b and massive subaerial volcanic events at the Kerguelen Plateau in the Indian Ocean. In Chapter III, a continuous Os isotopic record covering the entire Aptian was reconstructed using the Tethyan sedimentary record collected from the Umbria–Marche Basin. Subsequently, I discussed the relationship between the volcanic events forming the Ontong Java Nui and several Aptian oceanic anoxic events (OAE1a, Wezel, and Fallot Events). In Chapter IV, I conducted Os isotopic analysis of Goshikinohama bedded chert exposed at Kochi Prefecture that could record the paleo-redox condition at the deep-sea Pacific basin during early to mid-Aptian OAEs. From the Os isotopic variations, I tried to constrain the OAE1a interval in the Goshikinohama bedded chert and discuss the changes in the redox condition at the pelagic deep-sea Pacific basin during the massive volcanic events at the Ontong Java Nui. In Chapter V, I conducted the Os isotopic analysis around Hauterivian–Barremian boundary including the first major Cretaceous OAEs, called Faraoni Event. From the newly discovered orbital-paced Os isotopic fluctuations, I tried to reveal the changes in the continental weathering pattern and their relation to the monsoonal activity. In Chapter VI, Os isotopic variations from Albian to Cenomanian were reconstructed using sedimentary rock samples from the Umbria–Marche Basin and ODP Site 763B. By combining Os isotopic data presented in this dissertation and that of previous research, I reconstructed a continuous mid-Cretaceous marine Os isotopic record and constrained the timing of massive volcanic events. Based on these data, I discussed the relationship between massive volcanic events and long-term mid-Cretaceous environmental perturbations. In Chapter VII, I summarize the Ph.D. dissertation and describe the

problems and future perspectives of Os isotopic studies.

Figures of Chapter I

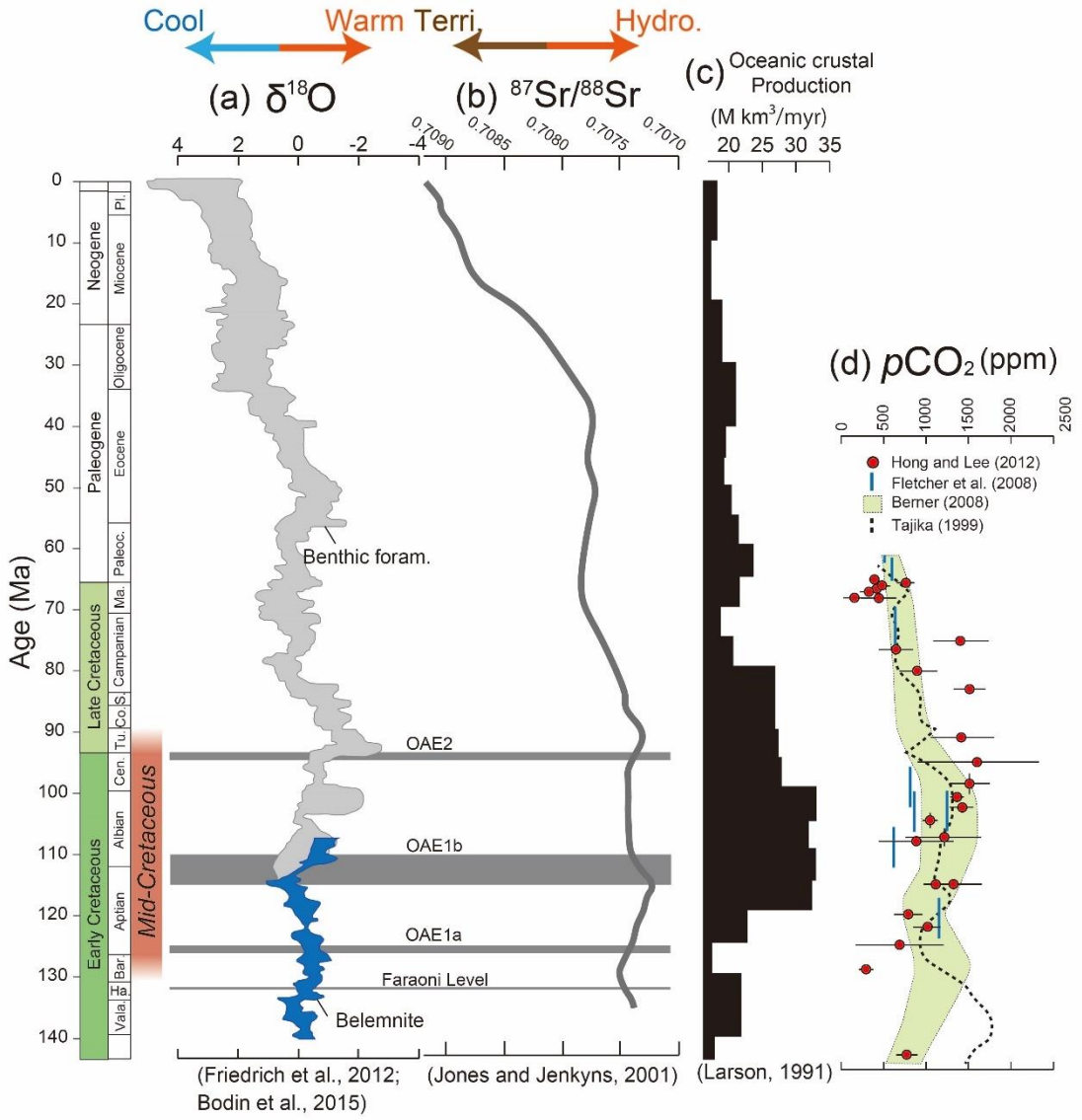

Figure I-1. The compilation of oxygen and strontium isotopic ratios, oceanic crustal production, and pCO_2 : (a) Oxygen isotope ratio of benthic foraminifera and belemnite (Friedrich et al., 2012; Bodin et al., 2015), (b) strontium isotope ratio (Jones and Jenkyns, 2001), (c) oceanic crustal production rate (Larson, 1991), and (d) pCO_2 (Tajika, 1999; Berner, 2008; Fletcher et al., 2008; Hong and Lee, 2012).

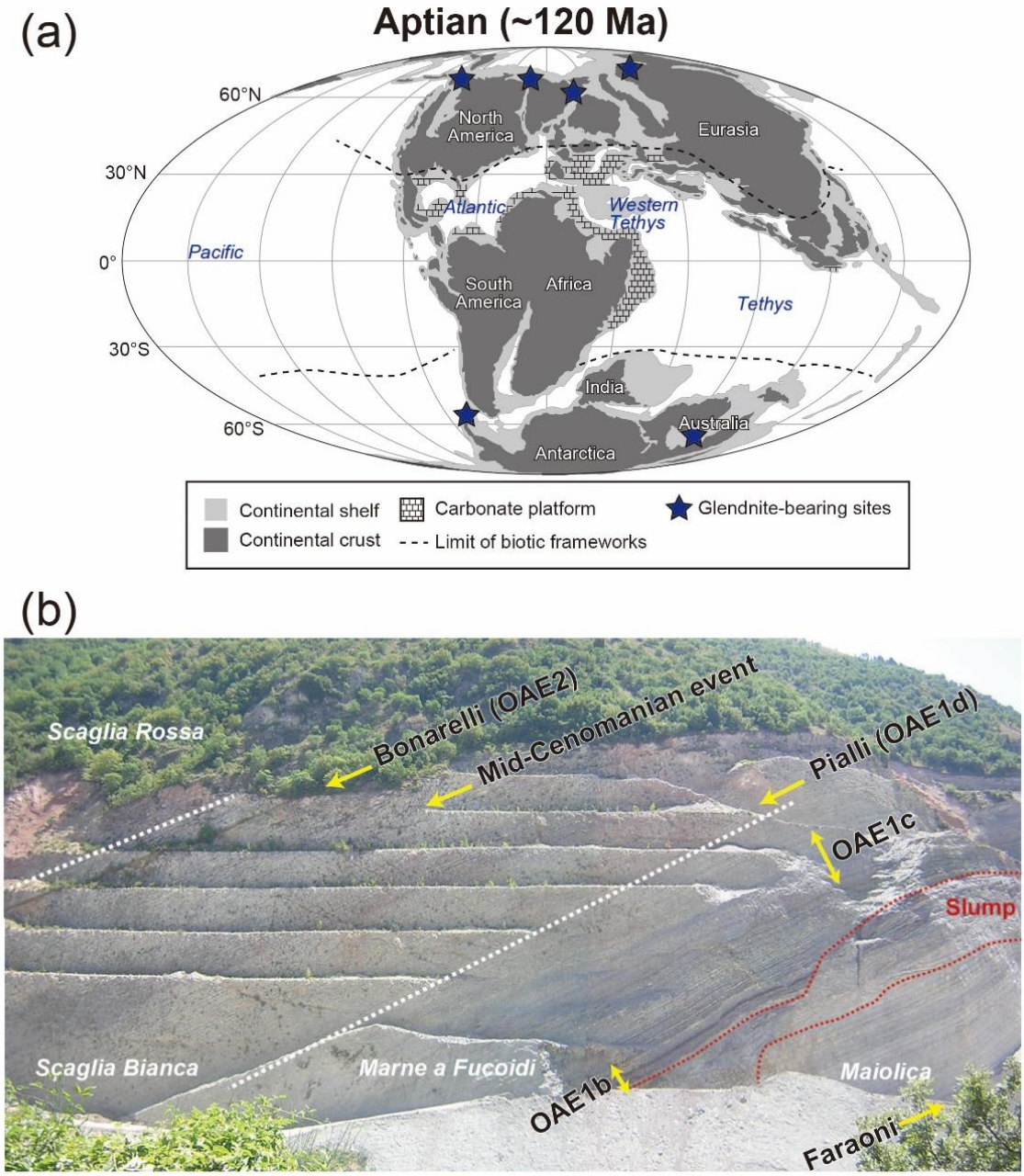

Figure I-2. Paleogeography and the Tethyan outcrop covering the mid-Cretaceous: (a) Paleogeography of 120 Ma (earliest Aptian) after Matsumoto et al. (2020). The distribution of carbonate sediments is after Takashima et al. (2007). Glendonite-bearing sites are after Vickers et al. (2019). (b) Mid-Cretaceous Tethyan carbonate sequence at the Vispi Quarry, central Italy, which was deposited in the Umbria–Marche Basin. The original photo was provided by Assoc. Prof. Junichiro Kuroda at the Atmosphere and Ocean Research Institute, the University of Tokyo.

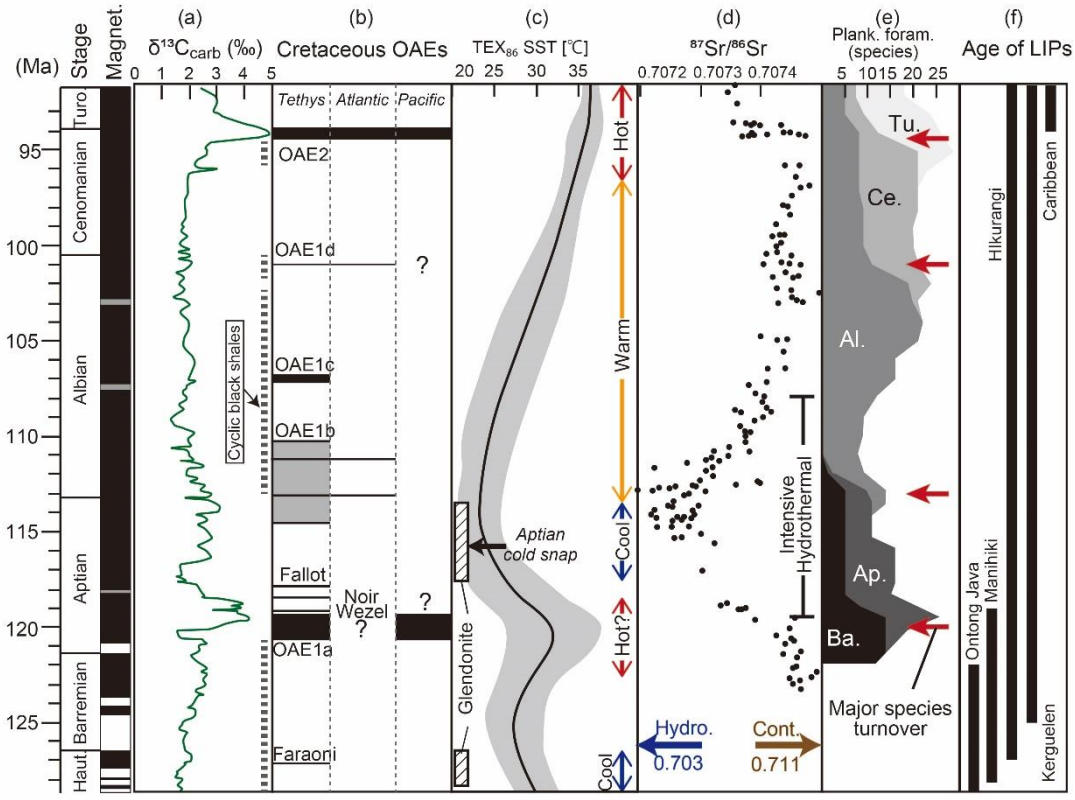

Figure I-3. Compilation of geological events during the mid-Cretaceous: (a) carbon isotope ratio of carbonate (Gale et al., 2020), (b) distribution of organic-rich sediments during mid-Cretaceous OAEs, (c) temperature variation during the mid-Cretaceous based on TEX_{86} index (Steinig et al., 2020), (d) Sr isotope record (Bralower et al., 1997), (e) number of planktonic foraminiferal species (Leckie et al., 2002; Kuroyanagi et al., 2020), and (f) age of LIPs (Sinton et al., 1998; Hoernle et al., 2010; Olierook et al., 2019; Jiang et al., 2021). Dark gray dashed lines in (a) represent the interval of cyclic deposition of thin black shale layers at the Umbria–Marche Basin. The glendonite occurrence interval in (c) is based on Herrle et al. (2015) and Vickers et al. (2019). Haut.—Hauterivian, Ba.—Barremian species, Ap.—Aptian species, Al.—Albian species, Ce.—Cenomanian species, and Tu.—Turonian species.

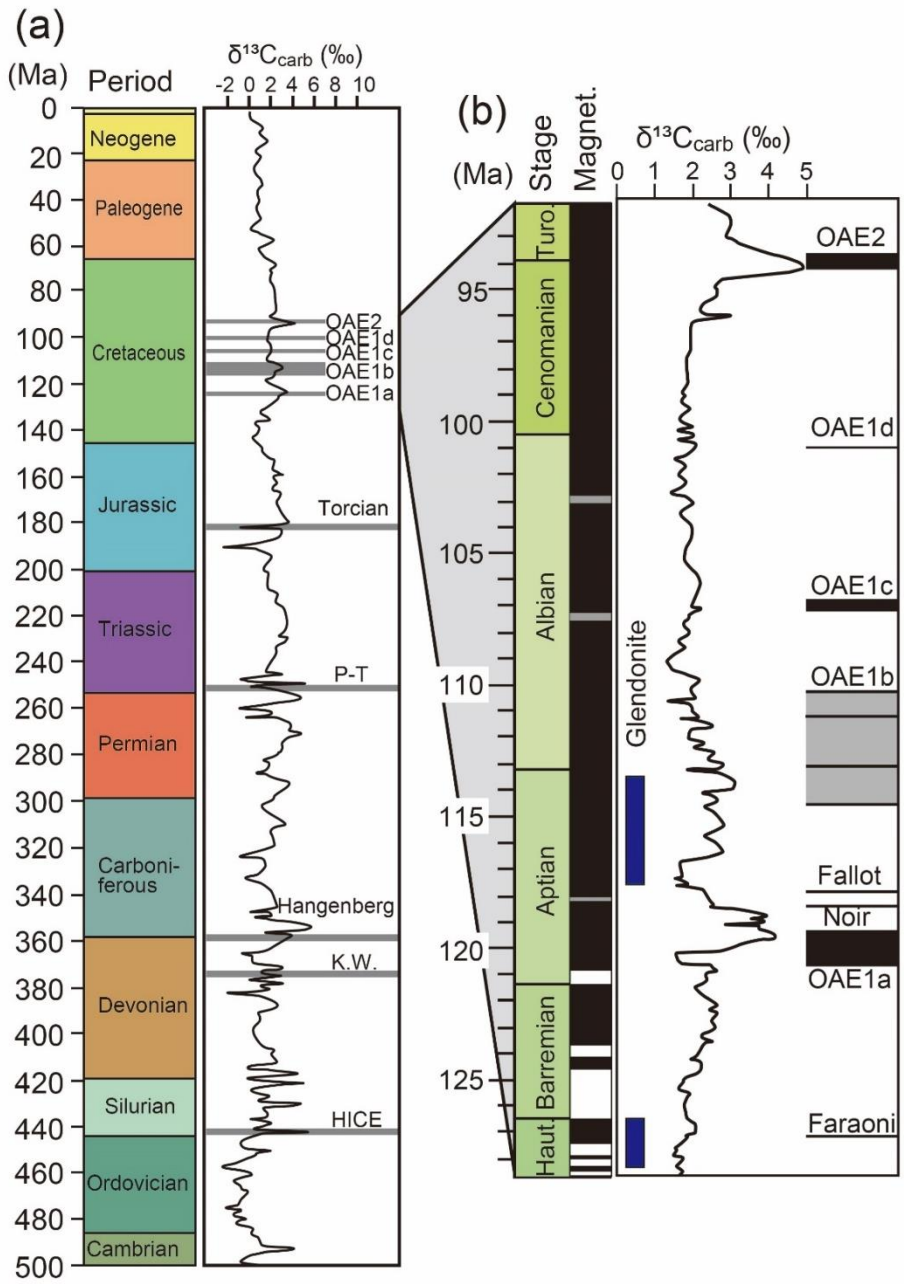

Figure I-4. Major oceanic anoxic events (OAEs) throughout the Phanerozoic era: (a) Carbon isotope ratio and timing of major OAEs modified from Bergman et al. (2021) and (b) close-up of mid-Cretaceous interval after Gale et al. (2020). Haut.—Hauterivian, and Turo. —Turonian.

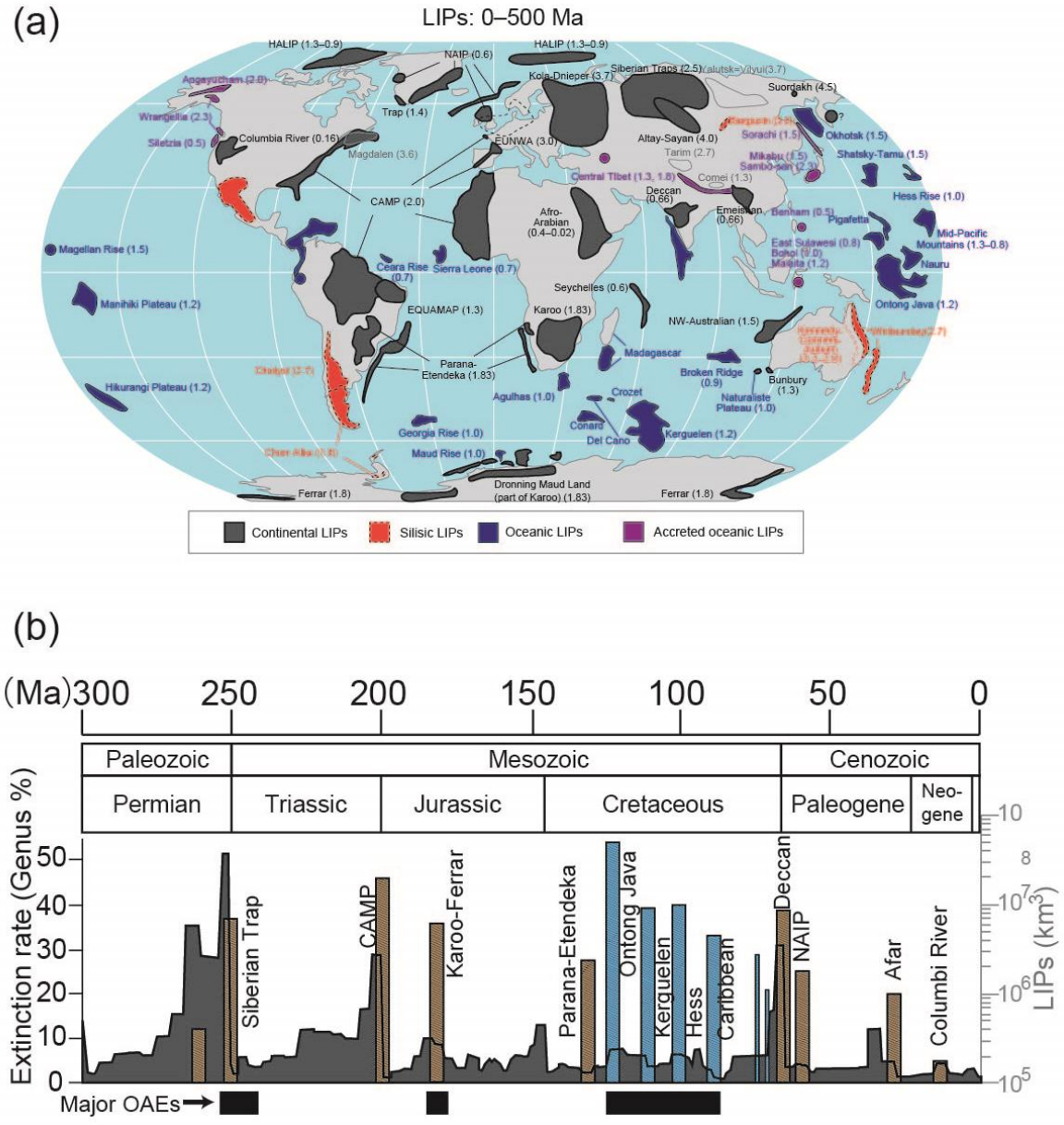

Figure I-5. The distribution and the timing of large igneous provinces (LIPs) formations: (a) Distribution of large igneous provinces modified from Ernst et al. (2021) and (b) extinction rate of genus, the timing of major LIPs formation, and timing of major OAEs modified from Guex et al. (2016).

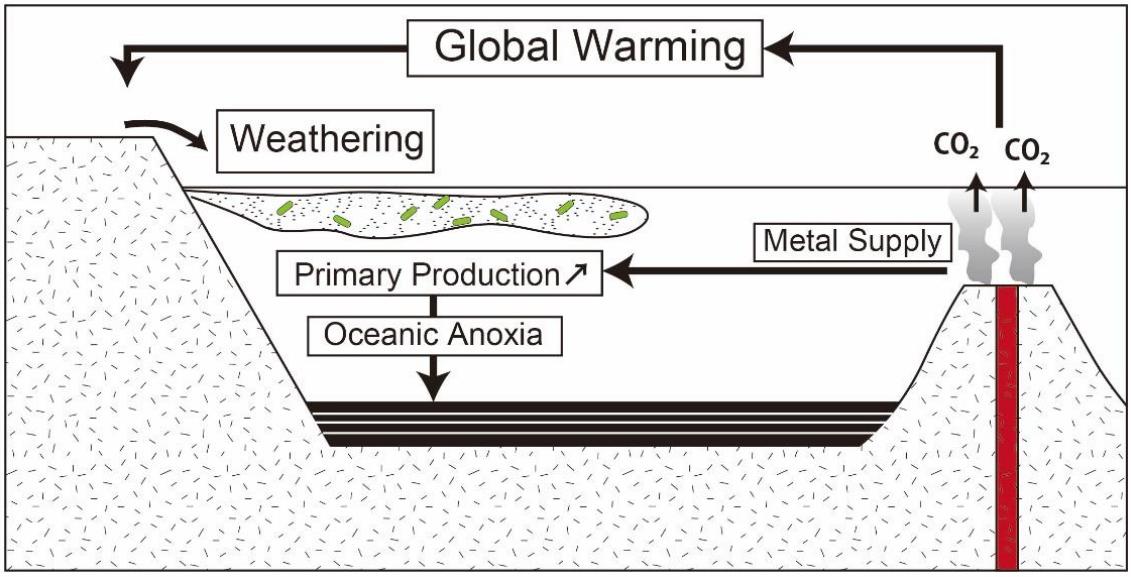

Figure I-6. Schematic image of triggering mechanism of oceanic anoxic events.

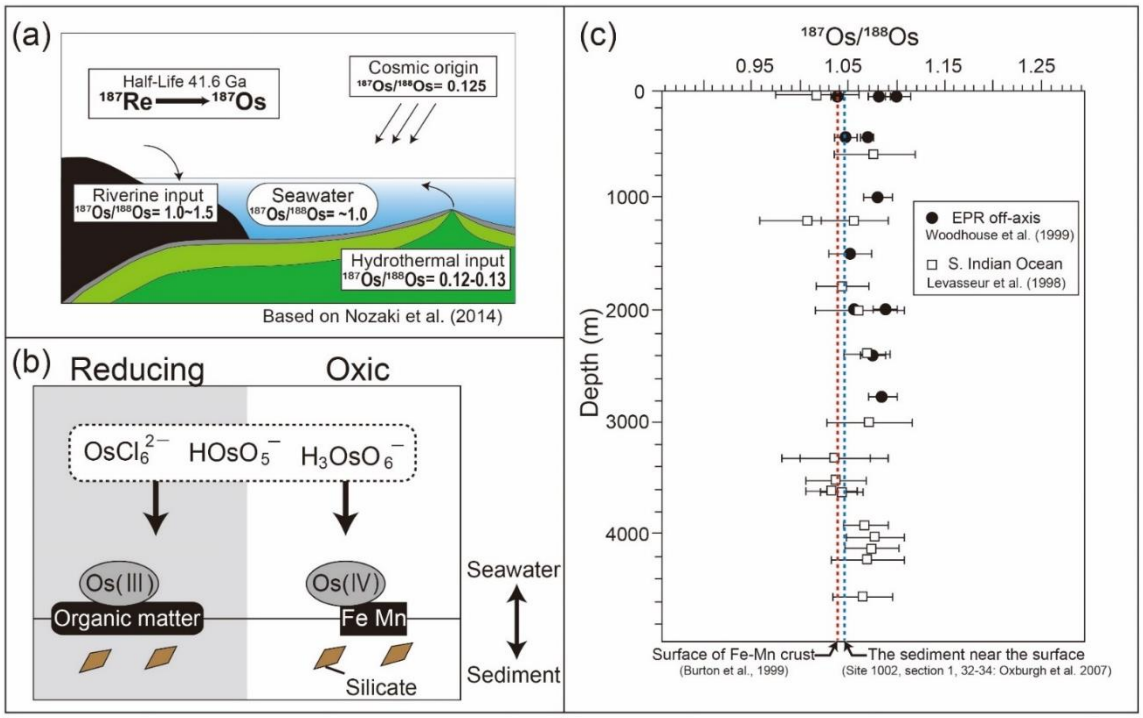

Figure I-7. Os cycle and isotopic system in the present ocean: (a) Os isotopic systems in the present ocean modified from Nozaki et al. (2014), (b) oxidation state of Os in the ocean and host materials in the sediments based on Yamashita et al. (2007), and (c) Os isotopic variations in the ocean after Peucker-Ehrenbrink and Hannigan (2000). Os isotopic data are from Levasseur et al. (1998), Burton et al. (1999), Woodhouse et al. (1999), and Oxburgh et al. (2007).

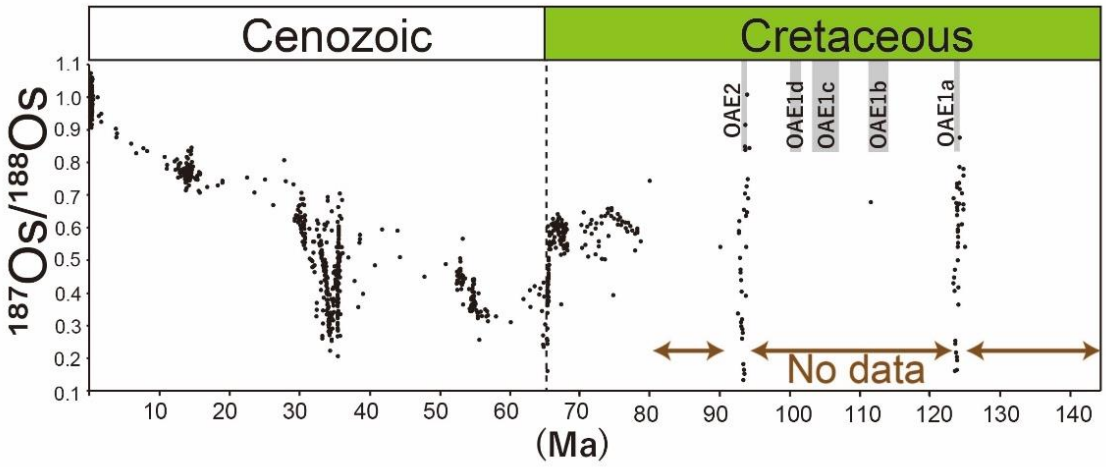

Figure I-8. Compilation of Os isotopic variation modified from Peucker-Ehrenbrink and Ravizza, (2012).

CHAPTER II

Marine Os isotopic evidence for multiple volcanic episodes during Cretaceous Oceanic Anoxic Event 1b

This chapter is published at *Scientific Reports*

II-1. Abstract of Chapter II

The Aptian–Albian boundary was marked by one of the major oceanic perturbations during the Cretaceous, called Oceanic Anoxic Event (OAE) 1b. Extensive volcanic episodes at the Southern Kerguelen Plateau have been suggested as the trigger of OAE1b, but compelling evidence remains lacking. Here, I reconstructed the temporal variations of marine Os isotopic ratios across the Aptian–Albian boundary in the Tethyan and Pacific pelagic sedimentary records to elucidate the causal links between OAE1b, the biotic turnover, and volcanic episodes. The new Os isotopic records show two negative spikes that correlate with a period of planktonic foraminiferal turnover across the Aptian–Albian boundary during OAE1b and suggest multiple submarine volcanic events. By comparing the new Os isotopic profile with carbon isotopic compositions of carbonate, $CaCO_3$ content, and the relative abundances of agglutinated foraminifera, I conclude that ocean acidification caused by the massive release of CO_2 through extensive volcanic episodes could have promoted the major planktonic foraminiferal turnover during OAE1b.

II-2. Introduction

The mid-Cretaceous (Barremian–Turonian) was punctuated by repeated Oceanic Anoxic Events (OAEs) (Chapter I-2), which represent intervals of global and episodic burial of organic-rich sediments on the seafloor under oxygen-deficient bottom waters. Several organic-rich sedimentary deposits are recorded in the uppermost Aptian to the lower Albian, mainly in the Tethys and Atlantic Oceans (Leckie et al., 2002; Herrle et al., 2004; Trabucho Alexandre et al., 2010; Coccioni et al., 2014; Sabatino et al., 2018) (Fig. II-1). In particular, four prominent black shale horizons (113/Jacob, Kilian, Urbino/Paquier, and Leenhardt equivalent levels) have been identified as the sedimentary expression of OAE1b (Coccioni et al., 2014). OAE1b is characterized by (1) an exceptionally long duration (~ 3.8 Myr) with intermittent occurrences of oxygen-depleted bottom water conditions, (2) a global carbon-cycle perturbation, and (3) a major marine biotic turnover (Coccioni et al., 2014). In particular, planktonic foraminifera experienced one of the most significant turnovers in their evolutionary history, where large, heavily calcified planktonic foraminifera of the Aptian were replaced by small, weakly calcified taxa characteristic of the Albian (Huber et al., 2011; Petrizzo et al., 2012; Coccioni et al., 2014; Ferraro et al., 2020). Since ^{40}Ar–^{39}Ar ages of the Southern Kerguelen Plateau basalt (Fig. II-1) (109.2–119.0 Ma) (Coffin et al., 2002) roughly correspond to the duration of OAE1b (~110.5–114.5 Ma), volcanic episodes associated with the break-up of Gondwana have been suggested as the trigger of OAE1b (Leckie et al., 2002; Trabucho Alexandre et al., 2011; Sabatino et al., 2018). However, the issue remains debated because of the large

chronological uncertainties of the ^{40}Ar–^{39}Ar ages of the basaltic rocks and the ages of the sedimentary sequences. Marine osmium (Os) isotopic records ($^{187}Os/^{188}Os$) reflect the balance between the continental Os flux ($^{187}Os/^{188}Os \approx 1.0–1.5$) and mantle/hydrothermal and extraterrestrial Os fluxes ($^{187}Os/^{188}Os \approx 0.12–0.13$) to the global ocean (Levasseur et al., 1999). Thus, $^{187}Os/^{188}Os$ values of paleo-seawater preserved in sedimentary rocks represent a robust proxy to constrain the timing of massive input of unradiogenic Os through submarine hydrothermal or volcanic eruption (Chapter I-4). Here, I present late Aptian to early Albian paleo-marine Os isotopic variations in the Poggio le Guaine (PLG) record (central Italy, deposited in the central to western Tethys) (Figs. II-1 and 2) and Deep Sea Drilling Program (DSDP) Site 463 (western Mid-Pacific mountains, central Pacific Ocean) (Figs. II-1 and 3) to constrain the timing of extensive volcanic episodes during OAE1b. For the Os isotopic analysis of organic-rich sedimentary rock samples of the PLG section, I preferentially used borehole core (Coccioni et al., 2012) samples drilled near the PLG section because initial Os isotopic information of these rocks are easily altered by weathering.

II-3. Lithological description

II-3.1. The Poggio le Guaine section in the Umbria–Marche Basin

A representative Tethyan pelagic sedimentary sequence crops out at the Umbria–Marche basin in Central Italy (Figs. II-1 and 2). The sedimentary sequence of this basin was deposited in the pelagic environment of the Tethys Ocean at middle to lower bathyal depths of about 1000–1500 m (Coccioni et al., 2014 and reference therein) and the paleolatitude was estimated to be about 20°N (Coccioni et al., 2014) (Fig. II-1). Since the sedimentary rock rarely contains coarse silicate minerals derived from rivers, the sedimentary sequence is suitable for paleo-environmental reconstruction. The sedimentary sequences of this basin cover the long time range from Tithonian (Jurassic) to Lutetian (Paleocene) and can be subdivided into four formations in the ascending order: Maiolica (Tithonian to early Aptian), Marne a Fucoidi (early Aptian to latest Albian), Scaglia Bianca (latest Albian to earliest Turonian), and Scaglia Rossa Formations (early Turonian to early Lutetian) (Fig. I-2b) (Coccioni and Galeotti, 2003).

The sedimentary rock samples of this study were collected from the Poggio le Guaine (PLG) section, which belongs to the Marne a Fucoidi Formation on the Monte Nerone ridge (Figs. II-2 and 4). This section (Figs. II-1 and 2) is one of the most continuous sedimentary successions encompassing OAE1b (Coccioni et al., 2014). Detailed foraminiferal and carbon isotopic studies have revealed that the Poggio le Guaine (PLG) section covers from the upper Aptian to lower Albian and contains the OAE1b interval

continuously (Coccioni et al., 2014). Sedimentary rocks of the PLG section are mainly composed of biogenic calcite (foraminifera and coccolith), biogenic silica (radiolaria), and fine clay minerals (Fig. II-5a-c). Since coarse silicate fragments are rare throughout this section (Fig. II-5a–c), this sedimentary sequence was considered deposited in a pelagic environment. The pre-OAE1b interval mainly comprises reddish or olive-grey argillaceous limestone and marlstone enriched in heavily calcified large planktonic foraminifera (Figs. II-4a, 5a, 6a, and 7), whereas the OAE1b interval is characterized by a cyclic alternation of olive to greenish-grey marlstone/mudstone and black shale (Figs. II-4b,c, 6a, and 7) where the size and abundance of planktonic foraminifera decreased (Figs. II-5b and 7). The 113/Jacob, Kilian, Urbino/Paquier, and Leenhardt equivalent levels are the regional sedimentary expression of OAE1b sub-events (Coccioni et al., 2014) (Figs. II-4, 5c, and 6). The 113/Jacob equivalent level is the first organic-rich sediment during OAE1b. A distinctive sequence of alternating reddish and black shales, called Monte Nerone interval, occurs between the Kilian and Urbino/Paquier equivalent levels (Figs. II-6 and 8). Above 15.42 m stratigraphic level in the section (pink line in Figs. II-6 and 7), small, weakly calcified Albian planktonic foraminiferal taxa appear followed by the abrupt decrease in the number of large (>250 μm), heavily calcified Aptian planktonic foraminifera (Coccioni et al., 2014). The heavily calcified planktonic foraminifera characteristic of Aptian never appeared above the thick black shale horizon called Kilian level (16.97–17.37 m) (Coccioni et al., 2014) (Figs. II-4 and 7). This major planktonic foraminiferal species turnover is accompanied by a significant increase in the radiolarian abundance (Coccioni et al., 2014) and a decrease in calcium carbonate ($CaCO_3$) content (Fig. II-7). The Kilian equivalent level is punctuated by a major negative carbon isotopic excursion (CIE) (Fig. II-7) coupled with a marked decrease of $CaCO_3$ content and the dominance of agglutinated foraminiferal taxa (Coccioni et al., 2014) (Fig. II-7). The drilling site of the PLG-core is located 400 m northwest of the PLG Section (Coccioni et al., 2012). The upper Aptian–lower Albian sedimentary and biostratigraphic record of PLG core is well correlated to that of the PLG section. Therefore, the geochemical data of the outcrop and borehole core can be confidently combined.

II-3.2. DSDP Site 463

The DSDP Site 463 is located in the western Mid-Pacific Mountains and consists of 822.5 m-thick Cenozoic to Mesozoic pelagic carbonate sediments (Fig. II-3) (Thiede et al., 1981). The upper Aptian to lower Albian sedimentary interval was deposited at about 15°S (Fig. II-3) (Thiede et al., 1981). DSDP Site 463 consists of vari-colored limestone with some chert layers. Bioturbation is common throughout the DSDP Site 463 cores 58–

62 (Fig. II-9). The upper Aptian to lower Albian sedimentary sequence lacks organic-rich sediments (Price, 2003) and does not exhibit any marked lithological changes.

II-4. Methods

II-4.1. Stable carbon and oxygen isotopic compositions of carbonate.

Stable carbon ($\delta^{13}C_{carb}$) and oxygen isotopic compositions ($\delta^{18}O_{carb}$) of carbonate were measured in 39 samples from the PLG section and 68 samples from DSDP Site 463 using a GV IsoPrime instrument at the Japan Agency for Marine-Earth Science and Technology (JAMSTEC). The isotopic compositions are expressed in delta notation as per-mil variations relative to Vienna Peedee Belemnite (VPDB). Analytical errors (1σ) on $\delta^{13}C_{carb}$ and $\delta^{18}O_{carb}$ were estimated to be within 0.1‰ and 0.2‰, respectively on the basis of repeated measurements of in-house standard materials (Supplementary Tables S1 and S2). The isotopic analytical method is detailed by Toyofuku et al. (2011).

II-4.2. Stable carbon isotopic compositions of organic matter and total organic carbon contents (TOC).

I determined total organic carbon contents (TOC) and organic stable carbon isotopic compositions ($\delta^{13}C_{org}$) for sedimentary rock samples from the PLG section and 11 sedimentary rock samples from the PLG core. Powdered and weighed samples were decalcified with 2 M HCl, rinsed with purified water using a MilliQ Water purification system. After evaporation to dryness, these samples were weighed to calculate the change in weight during decalcification. These samples were wrapped in a Sn cup for measurements. Carbon contents and $\delta^{13}C_{org}$ were measured at JAMSTEC via the online system of isotope-ratio mass spectrometry (DeltaPlus XP; Finnigan, Waltham, MA, USA) coupled to a Flash EA 1,112 Automatic Elemental Analyzer through a ConFlo III interface (Ohkouchi et al., 2005). Analytical errors (1σ) on $\delta^{13}C_{org}$ are better than 0.37‰ based on repeated measurements of the in-house standard (L-Tyrosine) (Supplementary Tables S3 and S4).

II-4.3. Rhenium and osmium analysis.

I used CrO_3-H_2SO_4 digestion (Selby and Creaser, 2003) and inverse aqua regia digestion methods to extract Re and Os from the samples. Samples for Re-Os analyses varied from 0.1 to 1 g depending on the expected concentration of Os in the samples. In fact, organic-rich black shale samples generally show high Os and Re concentrations and marl/limestone samples with low TOC shows lower Os and Re concentrations. After spiking using ^{190}Os- and ^{185}Re-rich solutions, each sample was sealed in a Carius tube

(Shirey and Walker, 1995) with 4 mL of CrO_3-H_2SO_4 (0.2 g CrO_3 per 1 mL of 4 N H_2SO_4) or inverse aqua regia (mixture of 1 mL of 30 wt% HCl and 3 mL of 68 wt% HNO_3) digestion solutions. The sample solutions were heated at 240 °C for 48 h. Through this process, Os and Re were completely extracted from the samples as $Os(VIII)O_4$ and $Re(VII)O_4^-$, respectively, and isotopic equilibrium between the spike and sample was achieved. The supernatant (leachate) was separated from the residue by centrifugation. After removing the residue, Os was separated from the leachate with 3 mL of carbon tetrachloride (CCl_4) in three successive extractions. The volatile $Os(VIII)O_4$ was reduced to non-volatile $Os(IV)Br_6^{2-}$ by adding 3 mL of 9 N HBr. Extracted Os was purified by micro-distillation (Birck et al., 1997). Re was separated from the leachate through the following two steps: (1) 2 mL of Bio-Rad AG1-X8 anion exchange resin (100–200 mesh) and (2) 0.3 mL of Bio-Rad AG1-X8 anion exchange resin (100–200 mesh). Os abundances and isotopic compositions were determined by negative thermal ionization mass spectrometry (Thermal Electron TRITON) (Kuroda et al., 2010 and references therein) at JAMSTEC (Japan) and Re abundances and isotopic compositions by quadrupole inductively coupled plasma mass spectrometry (iCapQ) at JAMSTEC using in-house Re standards. All data were corrected for procedural blanks, whose respective averages were 0.57 pg Os and 5.4 pg Re. The average of $^{187}Os/^{188}Os$ of the procedural blank is 0.13. Instrumental reproducibility (standard error) was monitored based on replicate analyses of the in-house standard for $^{187}Os/^{188}Os = 0.106838 \pm 0.000015$ (2σ) (Nozaki et al., 2012). The ^{187}Re decays to ^{187}Os in sediments with a decay constant of 1.666×10^{-11} yr^{-1} (Smoliar et al., 1996). Therefore, the initial $^{187}Os/^{188}Os$ of sediments ($^{187}Os/^{188}Os_i$) was calculated as:

$$^{187}Os/^{188}Os_i = {}^{187}Os/^{188}Os_m - [\exp\{\lambda \times \text{age (yr)}\} - 1] \times {}^{187}Re/^{188}Os_m \quad \text{(II-1)}$$

Here, λ is the decay constant, and the subscript 'm' indicates measured values. For the sedimentary rock samples from the PLG section and PLG core, ages used for the correction were 119 Ma from 0 to 6 m in the section, 117 Ma from 6 to 9 m, 115 Ma from 9 to 12 m, 114 Ma from 12 to 15 m, 113 Ma from 15 to 20 m, 112 Ma from 20 to 23 m, and 111 Ma from 23 to 26 m. In the DSDP Site 463 core, ages used for the correction were 114 Ma for DSDP Site 463, cores 62–61 and 113 Ma for DSDP Site 463, cores 61–58 (Supplementary Tables II-S5 and S6). These ages were determined based on Coccioni et al. (2014) and Huang et al., (2010).

II-4.4. Major elemental composition of bulk sedimentary rock samples.

The powdered samples and lithium tetraborate flux ($Li_2B_4O_7$, MERCK) were heated at 110 °C for more than 12 h. Dried powdered samples were weighed and heated at 950 °C for 7 h. After measurement of their weight to calculate the loss of ignition, about 0.4 g samples and exactly ten-times larger amounts of $Li_2B_4O_7$ were mixed and heated to make glass beads. They were analyzed by ZSX Primus II XRF spectrometer (Rigaku) installed in Atmosphere and Ocean Research Institute (AORI), the University of Tokyo, Japan to determine major elemental composition. The result is described in Supplementary Table II-S7.

II-4.5. Calculation of Os fluxes using a simple box model.

I calculated the changes in the Os flux through hydrothermal activities and continental weathering using a zero-dimensional box model based on Tejada et al. (2009). This model assumes the ocean to be a unique Os reservoir, and its Os content and isotopic composition to reflect the balance between continental input, hydrothermal input related to oceanic crustal production and volcanic eruptions at the Southern Kerguelen Plateau, extraterrestrial input, and a sedimentary sink. These relationships are described as:

$$dM_{ocean}/dt = F_{cont} + F_{hydr} + F_{cosm} + F_{Kerg} - F_{sed} \quad \text{(II-2)}$$

$$d(M_{ocean}R_{ocean})/dt = F_{cont}R_{cont} + F_{hydr}R_{hydr} + F_{cosm}R_{cosm} + F_{Kerg}R_{Kerg} - F_{sed}R_{sed} \quad \text{(II-3)}$$

where M, F, and R indicate the amount, flux, and isotopic ratio ($^{187}Os/^{188}Os$) of Os, and the subscripts ‘ocean’, ‘cont’, ‘hydr’, ‘cosm’, ‘Kerg’, and ‘sed’ represent the oceanic reservoir, continental input, hydrothermal input, extraterrestrial input, input from the Southern Kerguelen Plateau, and sedimentary output, respectively. Since the isotopic fractionation of Os is negligible between sediments and seawater, I assumed that R_{sed} coincides with R_{ocean}. Then, the above equations can be combined as:

$$dR_{ocean}/dt = [F_{cont}(R_{cont} - R_{ocean}) + F_{hydr}(R_{hydr} - R_{ocean}) + F_{cosm}(R_{cosm} - R_{ocean}) + F_{Kerg}(R_{Kerg} - R_{ocean})]/M_{ocean} \quad \text{(II-4)}$$

Here, I used the present-day values of F_{cont} = 295 t/kyr, R_{cont} = 1.54 (Esser and Turekian, 1993; Levasseur et al., 1999), R_{hydr} = 0.126 (Allègre and Luck, 1980), F_{cosm} = 17.6 t/kyr, and R_{cosm} = 0.126 (Allègre and Luck, 1980; Levasseur et al., 1999) for the steady background conditions below the Jacob level. The steady background oceanic condition is R_{ocean} = 0.54, and I set F_{hydr} to 532.7 t/kyr to match this value because several studies have suggested that hydrothermal activities associated with the production of oceanic crust in the Cretaceous were more active than today (e.g., Müller et al., 2008). For the

output parameters, I assumed that R_{sed} varies proportionally to R_{ocean}, and set the coefficient of proportionality at 0.056 following Tejada et al. (2009). Since there are no Os isotopic data available for Southern Kerguelen Plateau basalts, I used the isotopic composition of Kerguelen Archipelago lavas ($^{187}Os/^{188}Os = 0.16$) (Reisberg et al., 1993; Yang et al., 1998) for R_{Kerg}. At a steady-state, F_{Kerg} is considered to be 0 t/kyr. Only Os isotopic values from the PLG section were used for R_{ocean} because the PLG section is more continuous and spans a longer time interval than DSDP Site 463. Detailed parameter values throughout the cores are listed in Supplementary Table II-S8.

II-5. Results

II-5.1. Stable carbon and oxygen isotopic compositions of carbonate

The results of $\delta^{13}C_{carb}$ and $\delta^{18}O_{carb}$ analyses are listed in Supplementary Tables S1 and S2. Considering the relatively linear correlation between $\delta^{13}C_{carb}$ and $\delta^{18}O_{carb}$ of the PLG section (Fig. II-10), these values might have experienced diagenetic alternation to some extent. Also, the fluctuation of $\delta^{13}C_{carb}$ is larger than that of the DSDP Site 463, which might be derived from diagenetic alternation. However, since the smoothed trend of $\delta^{13}C_{carb}$ at PLG section (Coccioni et al., 2014) is quite similar to that of other sections (e.g., Vocontian Basin in southeast France, DSDP Site 545 at Mazagan Plateau, and ODP Site 1049 at Blake Nose: Herrle et al., 2004; Sabatino et al., 2018), major trends of $\delta^{13}C_{carb}$ variation is considered to be preserved. The $\delta^{13}C_{carb}$ and $\delta^{18}O_{carb}$ records of the DSDP Site 463 don't show a clear correlation, which implies that $\delta^{13}C_{carb}$ values of these samples have not experienced the post-depositional alteration. Here, one sample (523.07 mbsf, core 59, section 4, 7 to 11cm) showing extremely low $\delta^{13}C_{carb}$ and $\delta^{18}O_{carb}$ values is excluded from the discussions as outliers (Fig. II-10).

The $\delta^{13}C_{carb}$ values of the PLG section were 1.7–3.4‰ (Fig. II-6a) and consistent with those presented in Coccioni et al. (2014). Although the $\delta^{13}C_{carb}$ values of DSDP Site 463 (2.4–4.6‰; Fig. II-6b) are higher than those at PLG section by ~ 1‰, their temporal variation is quite similar. The $\delta^{13}C_{carb}$ record at DSDP Site 463 shows a negative CIE at ~ 539 m below seafloor (mbsf), just above the *Schackoina cepedai* acme at 539.8 mbsf (Fig. II-6b). Since the *S. cepedai* acme at the PLG section falls ~ 1.2 m below the 113/ Jacob equivalent level (the first organic-rich horizon in the Tethys region during OAE1b) which is marked by a negative CIE (Coccioni et al., 2014) (Fig. II-6), I correlate the CIE in the Pacific Ocean with the 113/Jacob equivalent level (Fig. II-6). A more distinct negative CIE (~ 1‰) occurs at 529.33 mbsf, just above the lowest occurrence of *Microhedbergella renilaevis* (529.56 mbsf). Since these features are consistent with those recorded across the Kilian equivalent level, which records the demise of the Aptian

planktonic foraminifera in the PLG section, I correlate this CIE at DSDP Site 463 to that of the Kilian level (Fig. II-6).

II-5.2. Re-Os data

II-5.2.1. PLG section

Re-Os data of PLG section are listed in Fig. II-11 and Supplementary Table II-S5. Most of the present-day measured $^{187}Os/^{188}Os$ values ($^{187}Os/^{188}Os_m$) range between 0.4 and 0.7 (Fig. II-11). However, $^{187}Os/^{188}Os_m$ of Kilian and Urbino level showed higher values between 1.1 and 3.8, which reflects the effect of additional ^{187}Os decayed from ^{187}Re after deposition. Initial $^{187}Os/^{188}Os$ values ($^{187}Os/^{188}Os_i$) of most limestone, marlstone, and shale samples range from 0.5 to 0.7 (Fig. II-11). However, in the PLG section, $^{187}Os/^{188}Os_i$ of organic-rich samples show a different trend between outcrop samples and borehole core samples. An outcrop sample of Kilian level and Urbino level shows particularly high $^{187}Os/^{188}Os_i$ values of 1.37 and 2.25 respectively which exceeds far beyond the possible range of Phanerozoic marine Os isotopic composition ($^{187}Os/^{188}Os$ ~0.2 to 1.5). On the other hand, PLG-core samples show much lower values of 0.4 to 0.73 at the Kilian level and 0.63 to 0.66 at the Urbino level respectively. These features are evident in the cross plot of measured $^{187}Os/^{188}Os$-$^{187}Re/^{188}Os$ (Fig. II-12). All PLG-core samples are scattered around the isochron of 114 Ma. However, black shale samples collected from the outcrop are apparently out of this trend. Those unusually higher $^{187}Os/^{188}Os_i$ values in the PLG outcrop could reflect the post-depositional alternation caused by weathering. Peucker -Ehrenbrink and Hannigan, (2000) and Georgiev et al. (2012) showed that weathering of organic- and Re-rich samples could change their $^{187}Os/^{188}Os_i$ values because of the different post-depositional mobilities between Os and Re. This time, large Re loss or addition of Os occurred during diagenesis or weathering. This effect is crucial to the samples with high Re concentration which require large in-situ radiogenic growth correction. In the PLG section, the sedimentary rocks upper than the extinction interval of planktonic foraminifera are fragile and TOC and Re concentrations are higher than pre-OAE1b intervals. I concluded that fragile black shale, marlstone, and mudstone samples with high TOC and Re/Os ratios are susceptible to weathering. Hereafter, I exclude four outcrop samples with high-Re concentrations at 15.5 msl, 17.1 msl, 25.28 msl, and 26 msl from the further discussions (Fig. II-12). Only limestone, mudstone, and marlstone samples with low-Re concentrations whose differences of measured and initial $^{187}Os/^{188}Os$ are less than 0.01 are considered here.

II-5.2.2. DSDP Site 463

Os and Re concentrations and isotopic ratio data are listed in Fig. II-13 and Supplementary Table II-S6. Age correction does not affect $^{187}Os/^{188}Os_i$ too much because of the low Re concentration throughout this core. Therefore, $^{187}Os/^{188}Os_m$ and $^{187}Os/^{188}Os_i$ show similar variations.

II-5.2.3. Rhenium and osmium records across the Aptian/Albian boundary

A study by Selby and Creaser (2003) has proposed that digestion with CrO_3-H_2SO_4 properly extracts Re and Os in a hydrogenous fraction of sediments, while digestion with inverse aqua regia dissolved Re and Os in terrigenous fractions of sediments. Here I tested both digestion methods for some samples of the PLG section and found no significant differences in the initial $^{187}Os/^{188}Os$ values ($^{187}Os/^{188}Os_i$) (Figs. II-11 and 14). This correspondence of $^{187}Os/^{188}Os$ values between these methods suggests that Os derived from the terrigenous material is minor in these samples and inverse aqua regia adequately extracts Re and Os in the hydrogenous fractions of sediments. However, Re concentrations dissolved by the inverse aqua regia are a little lower than those dissolved by CrO_3–H_2SO_4 (Figs. II-11 and 14). Since the aqua regia dissolves not only a hydrogenous fraction but also silicate minerals and extracts more Re from sediments, the cause of these differences is corundum. However, these differences are too small to affect $^{187}Os/^{188}Os_i$.

The trends and most of the $^{187}Os/^{188}Os_i$ of the two distant sites (PLG and DSDP Site 463) are quite similar. This similarity also suggests that the $^{187}Os/^{188}Os_i$ records reflect hydrogenous Os information strongly though there might be slight contamination of silicate materials.

At the PLG section, the total organic carbon content (TOC) values of pre-OAE1b range from 0.01 to 0.04% and averages 0.03% (Fig. II-15 and Table II-S3). The TOC values of black shale horizons during OAE1b are higher than other horizons. In particular, TOC values across the Jacob and Urbino equivalent levels show extremely high values (up to 8%). Other black shale intervals (i.e., Kilian equivalent level, Monte Nerone interval, and Leenhardt equivalent level) reveal lower concentrations of TOC (up to 0.65%). TOC values of sedimentary rocks from the DSDP Site 463 are 0.04–0.12% and I could not find organic-rich intervals (Supplementary Table II-S4). I conducted Re-Os analysis of limestone, marlstone, mudstone, and black shale samples collected from the PLG record (outcrop and core) and limestone and marlstone samples of the DSDP Site 463 (Figs. II-6, 11, and 13, and Tables II-S5 and S6). Considering the positive correlations between TOC and Re, Os concentrations throughout the PLG section, these elements are derived from the hydrogenous fraction associated with organic matters (Fig. II-16)

(Ravizza et al., 1991; Creaser et al., 2002). Since there are no clear relationships between other elements (e.g., Fe and Mn), the contribution of Os and Re derived from other fractions (such as ferromanganese oxides) (Yamashita et al., 2007) is considered minor (Fig. II-17 and Table II-S7). Most of the PLG core samples were treated with aqua regia digestion. However, for some samples of the PLG section, I applied both CrO_3-H_2SO_4 and inverse aqua regia to check whether the method extracts hydrogenous fractions or not. On the basis of these results, I could not find any significant differences in $^{187}Os/^{188}Os_i$ (Figs. II-12 and 14), which supports the approach to successfully extract the hydrogenous information.

II-6. Discussions

II-6.1. Osmium isotopic records across the Aptian–Albian boundary.

In the pre-OAE1b interval, $^{187}Os/^{188}Os_i$ values (i.e., initial $^{187}Os/^{188}Os$ values, corrected for the radioactive decay of ^{187}Re to ^{187}Os) range from 0.52 to 0.57 (average 0.54) in the PLG section and from 0.49 to 0.51 (average 0.50) at DSDP Site 463 (Figs. II-6 and 7). These values are slightly lower than the pre-OAE1a values of the lower Aptian (~ 0.7) (Tejada et al., 2009) and pre-OAE2 values of the upper Cenomanian (~ 0.7) (Turgeon and Creaser, 2008). Since several seawater temperature proxies (belemnite oxygen isotopic ratios, the organic palaeothermometer TEX_{86}, and the existence of glendonites at higher latitudes) suggest a cooler climate during the Late Aptian than during the Early Aptian and Late Cenomanian (McAnena et al., 2013; Bodin et al., 2015; Herrle et al., 2015), these low $^{187}Os/^{188}Osi$ values may reflect weak continental weathering under cool climatic conditions.

The $^{187}Os/^{188}Os_i$ values began to fluctuate immediately after the onset of OAE1b (i.e. the deposition of the Jacob level) in the PLG section. The first sharp negative spike of $^{187}Os/^{188}Os_i$ values appears a few centimeters below the major planktonic foraminiferal turnover (15.48 m; the pink line in Fig. II-6) at the PLG section. A similar Os isotopic spike can be also recognized at the DSDP Site 463 (531.08 mbsf: Fig. II-6a). The $^{187}Os/^{188}Os_i$ values again sharply decline in the lower part of the Kilian level in the PLG section, then rapidly increase to 0.73 (Fig. II-6a). Although the pattern of $^{187}Os/^{188}Os_i$ variations is quite similar between the two sites, the amplitude of $^{187}Os/^{188}Os_i$ variations at the Kilian equivalent level at DSDP Site 463 (0.54–0.62) is much smaller than that in the PLG Section (0.40–0.73) (Fig. II-6b). Considering the long residence time of Os in the present ocean (10–100 kyr) (Levasseur et al., 1998, 1999), the significant difference in the range of $^{187}Os/^{188}Os_i$ values between these two localities is a conundrum. Borehole core samples from both sites are fresh, and the influence of weathering seems

insignificant. I consider active bioturbation or a small hiatus around the Kilian equivalent horizon at DSDP Site 463 to be the most probable explanation of the decreased $^{187}Os/^{188}Os_i$ variations there. Indeed, the amplitude of the negative $\delta^{13}C_{carb}$ spike at the Kilian equivalent level of DSDP Site 463 (~ 1‰) is also smaller than the one at the PLG section (> 2‰), which also implies the mixing of sediments or the existence of minor hiatus during Kilian event. The sedimentary expression of the Kilian level at the PLG section is a 40 cm-thick black shale with minor bioturbation (Coccioni et al., 2014) whereas that of DSDP Site 463 is bioturbated lime/marlstone thinner than 20 cm (Figs. II-5e and 9). Therefore, I consider the Os isotopic variations in the PLG section to be less disturbed and to better reflect the initial Os isotopic signature of seawater than those at the DSDP Site 463. The two sharp declines of $^{187}Os/^{188}Os_i$ values to ~ 0.4 (Figs. II-6 and 7) can be explained either by (1) rapid declines in continental weathering, (2) large meteorite impacts, or (3) increases in hydrothermal activity. Here, I apply a simple box model calculation to evaluate these possibilities. The first one requires an abrupt 35% decrease in radiogenic continental Os within a few hundred thousand years (Supplementary Table II-S8), probably through rapid cooling events. However, no such abrupt cooling of the climate has yet been reported. Instead, intensive warming was reported at the Kilian equivalent level in the Atlantic Ocean (McAnena et al., 2013; Herrle et al., 2015), which, on the contrary, would have accelerated chemical weathering. Decreased continental weathering, therefore, seems unlikely as the cause of the decreased $^{187}Os/^{188}Os_i$ values. Although a meteorite impact could explain the sharp decline of $^{187}Os/^{188}Os_i$ values, neither a large meteorite crater nor tektites have been reported in correspondence with this stratigraphic interval. Therefore, extensive volcanic events on the Southern Kerguelen Plateau (Coffin et al., 2002), which could have released a large amount of unradiogenic Os through hydrothermal activities, seems the most reasonable explanation. This box-model calculation shows Kerguelen volcanic episodes at that time promoted a 60–90% increase in the unradiogenic Os flux through hydrothermal activities. The $^{187}Os/^{188}Os_i$ values abruptly increase from 0.40 to 0.73 in the upper part of the Kilian level in the PLG section (Fig. II-6). Based on this box-model calculation, this abrupt increase in $^{187}Os/^{188}Os_i$ values can be explained by either a 41% decrease in the hydrothermal Os flux associated with the oceanic crustal production or a 67% increase in the continental weathering rate. Considering the intensive warming during the Kilian event (McAnena et al., 2013; Huber et al., 2018), a rapid increase in the radiogenic Os flux through continental weathering appears plausible. Based on the characteristics of Kerguelen lava flows, a large part of the volcanic plateau was emplaced subaerially, and the submarine eruption was short-lived (Frey et al., 2003). I interpret this radiogenic

$^{187}Os/^{188}Os_i$ shift as a later eruptive phase when active CO_2 degassing via subaerial eruptions enhanced continental weathering and weakened the hydrothermal input of unradiogenic Os. Similar radiogenic $^{187}Os/^{188}Os_i$ shifts have not been reported yet for other Cretaceous OAEs (OAE1a: Tejada et al. (2009) and OAE2: Turgeon and Creaser (2008)). This might be ascribed to the entirely submarine volcanic eruptions of the Ontong Java Plateau and Caribbean Plateau, which triggered OAE1a and OAE2, respectively, and continuously supplied a large amount of unradiogenic Os through hydrothermal activities throughout the eruptions.

The $^{187}Os/^{188}Os_i$ values above the Kilian equivalent level (average 0.63 both in the PLG section and at the DSDP Site 463) are higher than the pre-OAE1b background values (0.54 in the PLG section and 0.50 at the DSDP Site 463) (Fig. II-6). Planktonic foraminifera oxygen isotopic records in the Atlantic Ocean (Ocean Drilling Program Site 1049) indicate a rise in seawater temperature after the Aptian–Albian transition relative to the pre-OAE1b interval (Huber et al., 2011). Furthermore, the disappearance of glendonite from Arctic sediments (Herrle et al., 2015) supports a warming climate after the Aptian–Albian boundary, which could have sustained high continental weathering rates and high marine $^{187}Os/^{188}Os_i$ values. The radiogenic strontium isotopic ratio ($^{87}Sr/^{86}Sr$) of seawater also continuously declined from the early to late Aptian, with an incipient increase above the Aptian–Albian boundary (Bralower et al., 1997). Such trends suggest a larger contribution of continental weathering during OAE1b (early Albian) than during the pre-OAE1b interval (late Aptian). After the initial sharp declines of $^{187}Os/^{188}Os_i$ values to ~ 0.4, $^{187}Os/^{188}Os_i$ values fluctuated throughout OAE1b from 0.53 to 0.68 in the PLG section and from 0.58 to 0.71 at DSDP Site 463 (Fig. II-6). Considering the protracted volcanic eruptions of the Southern Kerguelen Plateau (Coffin et al., 2002), extended minor eruptions after the main volcanic pulse might have caused fluctuations of the continental weathering rate and/ or the hydrothermal Os influx, eventually contributing to the prolonged perturbation of the Os cycle (Fig. II-6).

II-6.2. Major planktonic foraminiferal turnover

The two volcanic Os isotopic signals correspond to the major planktonic foraminiferal turnover interval characterized by the extinction of large, heavily ornamented calcified planktonic foraminifera and the speciation of smaller thin, weakly calcified species that lack ornamentation in the PLG Section (Coccioni et al., 2014; Ferraro et al., 2020). These volcanic horizons are accompanied by abrupt decreases in $CaCO_3$ content and the poor preservation of calcareous microfossil tests, which means the dissolution of $CaCO_3$ on the seafloor. Moreover, the relative abundance of

agglutinated benthic foraminifera, which is resilient to ocean acidification, increased at the same time in the Tethys region (Coccioni et al., 2014) (Fig. II-7). These features suggest a shallowing of the carbonate compensation depth (CCD) (Dias et al., 2010; Kawahata et al., 2015; Pettit et al., 2015) at these volcanic horizons. A massive input of volcanic CO_2 could have prompted ocean acidification, potentially leading to dwarfism of planktonic foraminifera and shallowing of the CCD. Positive relationships among pH, test thickness, and growth rates of foraminifera have been documented in laboratory experiments and geological observations (Barker et al., 2002, Allison et al., 2010; Davis et al., 2017). Therefore, the drastic turnover and reduction in the size of planktonic foraminifera may reflect a decline in pH caused by the massive release of volcanic CO_2 (Fig. II-7). Indeed, since acidified condition prevents the growth of ornamentation and spines of foraminifera (Barker et al., 2002; Davis et al., 2017; Khanna et al., 2013), the lack of ornamentation in smaller Albian species (Coccioni et al., 2014) might reflect adaptation to the acidified oceanic condition. No major extinction of calcareous nannoplankton has been reported during OAE1b. Marine organisms with extremely small calcified tests might have been less influenced by ocean acidification (Bolton et al., 2016; McClelland et al., 2016), probably, because of their more efficient proton pumping systems in the carbon pools inside their cells relative to larger calcareous shell-forming organisms (Henehan et al., 2017). The large negative $\delta^{13}C_{carb}$ spike at the Kilian equivalent level implies a more intensive volcanic input of ^{13}C-depleted CO_2 than during the first volcanic pulse at the beginning of the biotic turnover (Fig. II-18). The resulting intensive climatic warming and subsequent massive input of nutrients into the ocean through continental weathering could have triggered increased primary production, leading to oceanic anoxia in the Tethyan and Atlantic Oceans (Fig. II-18). No evidence of an O_2-depleted environment has yet been reported for the first volcanic pulse. Furthermore, O_2-depleted conditions during the Kilian event (i.e., during the latest stage of the biotic turnover) were limited to the Tethyan and the Atlantic Oceans. These facts might imply that oceanic anoxia was not the direct trigger of the major marine biota turnover during OAE1b and possibly, the ocean acidification induced by volcanic events could have contributed to the biotic crisis. This conclusion suggests that oceanic anoxia and the extinction of marine biota are different phenomena that should be separately discussed.

II-7. Conclusions of Chapter II

Here, I presented continuous marine Os isotopic variation across the Aptian–Albian boundary at Tethyan pelagic section (PLG section) and Pacific sediments (DSDP Site

463). I found two sharp negative shifts around the Aptian–Albian boundary, which suggest submarine volcanic eruptions. Since these intervals correspond to the major planktonic foraminiferal species turnover and neither of them correspond to global oceanic anoxia, I concluded this turnover was likely caused by ocean acidification triggered by two major volcanic events.

Figures of Chapter II

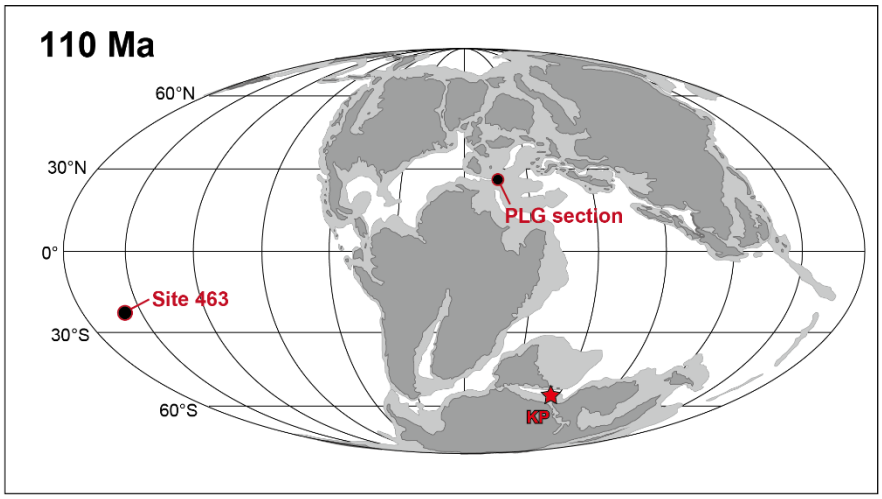

Figure II-1. Paleogeographic reconstruction at 110 Ma based on Sabatino et al. (2018): Red circles represent the locations of the PLG section and DSDP Site 463. The red star indicates the Southern Kerguelen Plateau (KP). The map was created using Illustrator CS5.5 (https ://www.adobe .com/products/illustrator.html).

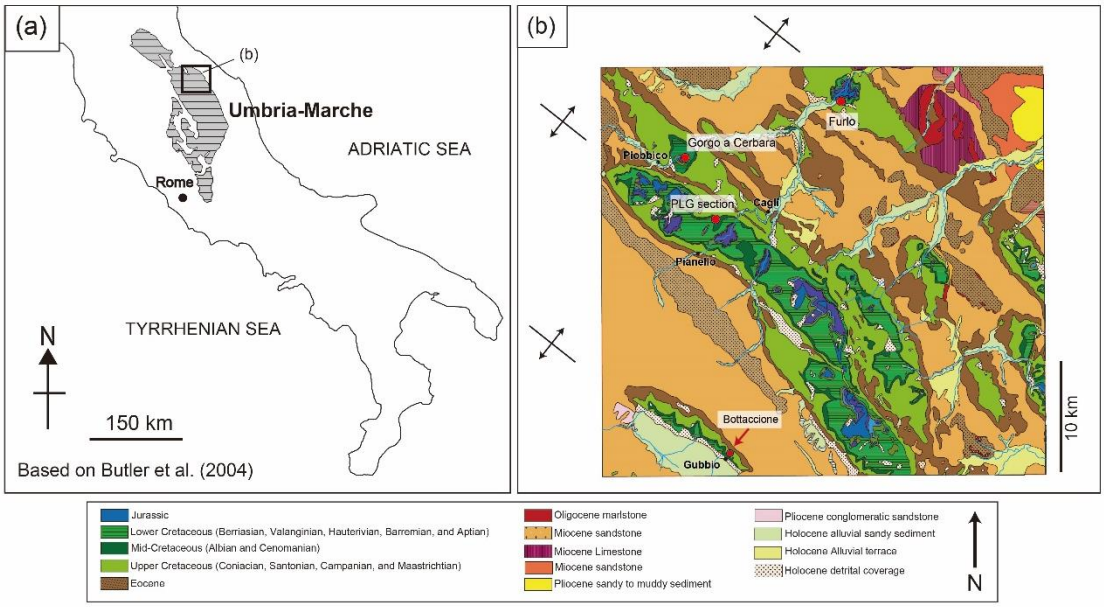

Figure II-2. **The sampling sites of Umbria–Marche Basin:** (a) The location of the Umbria–Marche Basin after Butler et al. (2004). (b) Geological map of the Umbria–Marche basin modified from Cresta et al. (1989).

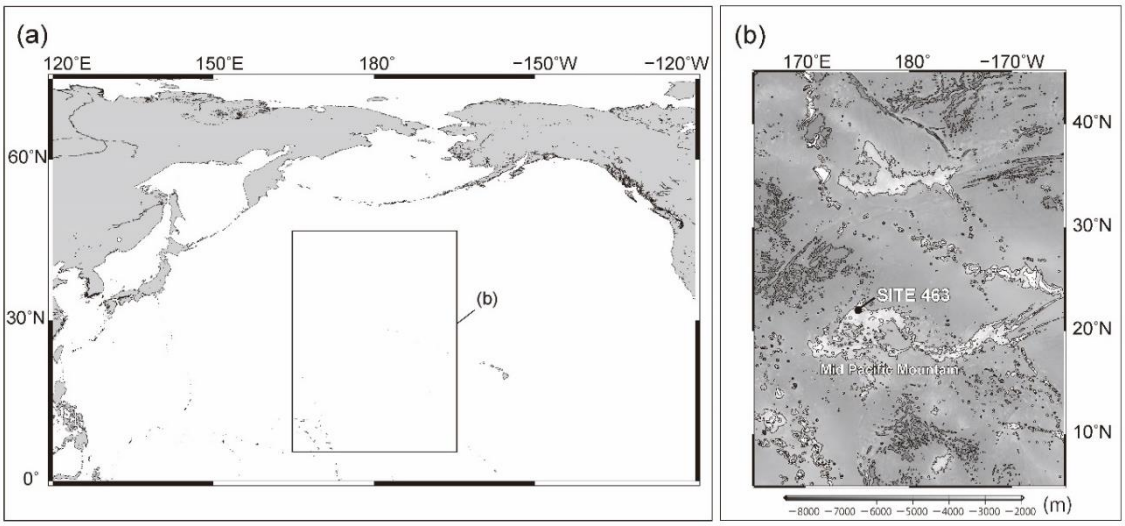

Figure II-3. Drilling site of the DSDP Site 463

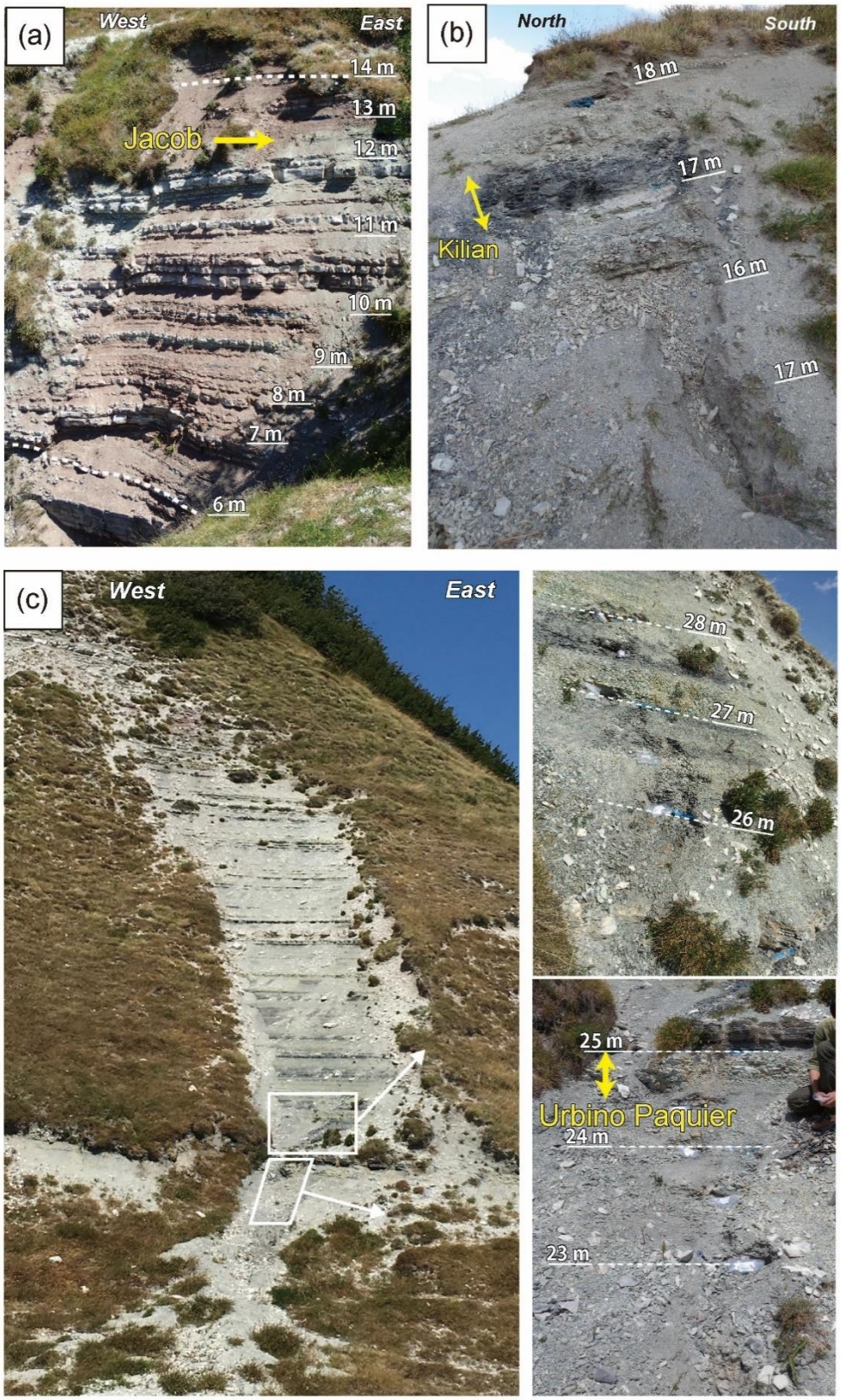

Figure II-4. Outcrop images of the Poggio le Guaine section.

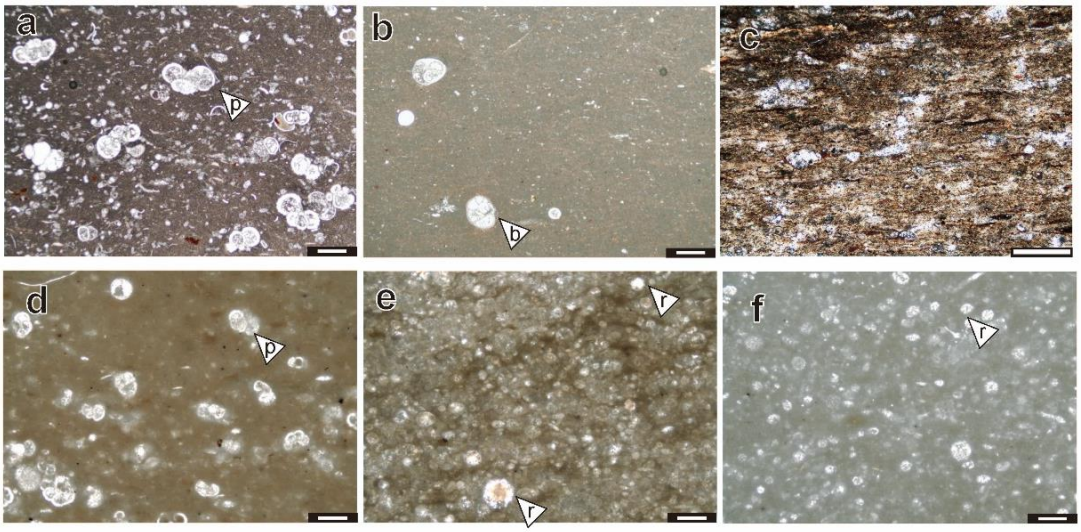

Figure II-5. Thin sectional images of PLG section and DSDP Site 463: (a) limestone at 12 m, PLG section, (b) marlstone at 16 m, PLG section, (c) black shale (Urbino level) at 25.28 m, PLG section, (d) DSDP Site 463, core 62, Sect. 1, 80–82 cm (538.3 mbsf), (e) DSDP Site 463, core 62, Sect. 1, 133–138 cm (529.3 mbsf : Kilian equivalent interval), (f) DSDP Site 463, core 59, Sect. 2, 116–118 cm (521.16 mbsf). p planktonic foraminifera, b benthic foraminifera, r radiolaria. All scale bars are 200 μm.

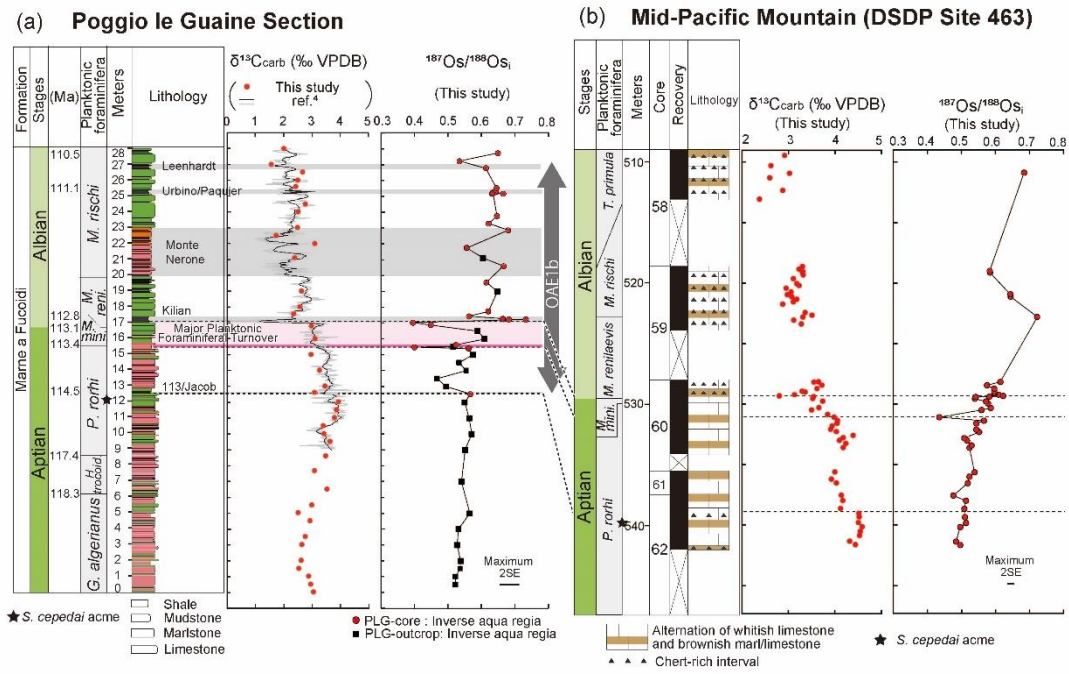

Figure II-6. Carbon and Os isotopic variations at (a) the PLG section and (b) DSDP Site 463: Grey and black lines in the $\delta^{13}C_{carb}$ profile in (a) are the $\delta^{13}C_{carb}$ values of Coccioni et al. (2014). Dashed horizontal lines mark the 113/Jacob equivalent level, the onset of the planktonic foraminiferal turnover, and the Kilian equivalent level. The pink-shaded band in (a) highlights the planktonic foraminiferal turnover. Grey shaded areas in (a) indicate prominent shale horizons. Star marks the *S. cepedai* acme. The lithology of the PLG section consists of shale, mudstone, marlstone, and limestone rich in planktonic foraminifera and calcareous nannofossils. The color of the lithological column in (a) represents the color of sediments. The lithology of DSDP Site 463 consists of alternations of white/brownish limestone and brownish marlstone with minor chert layers. Triangles in (b) represent chert-rich intervals. *G.—Globigerinelloides, H.—Hedbergella, P.—Paraticinella, M.—Microhedbergella, S.—Schackoina.*

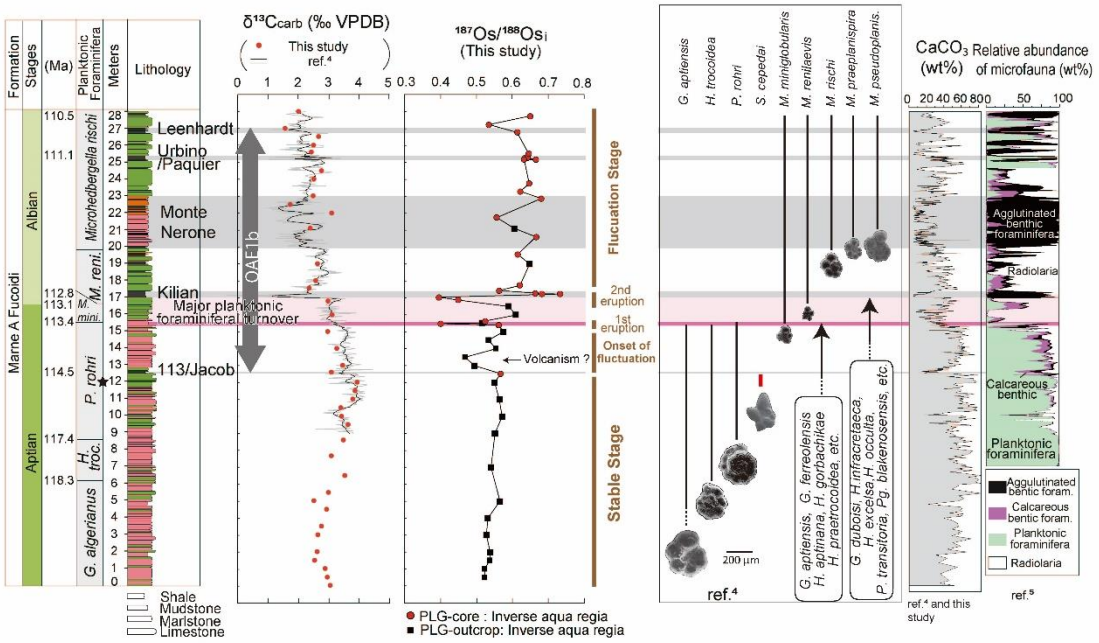

Figure II-7. Interpretation of Os isotopic variations and environmental changes during OAE1b in the context of the lithological, geochemical, and biological profiles reported in Fig. II-4: (a) Oceanic conditions during the pre- OAE1b interval; (b) the first volcanic eruption at the extinction level; and (c) the second volcanic eruption at the Kilian level.

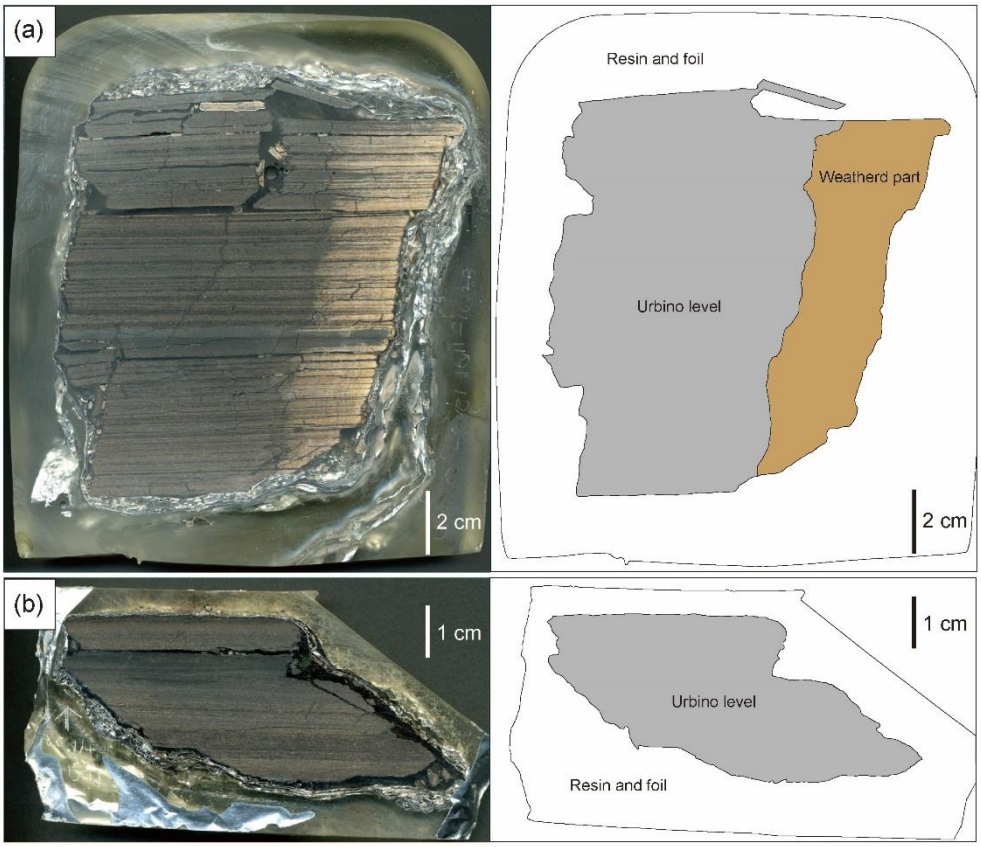

Figure II-8. Slabs of the Urbino/Paquier equivalent horizon of the Poggio le Guaine section: (a) 25.11–25.13 m, (b) ~25.28 m. The brownish part in (a) is an apparently weathered part.

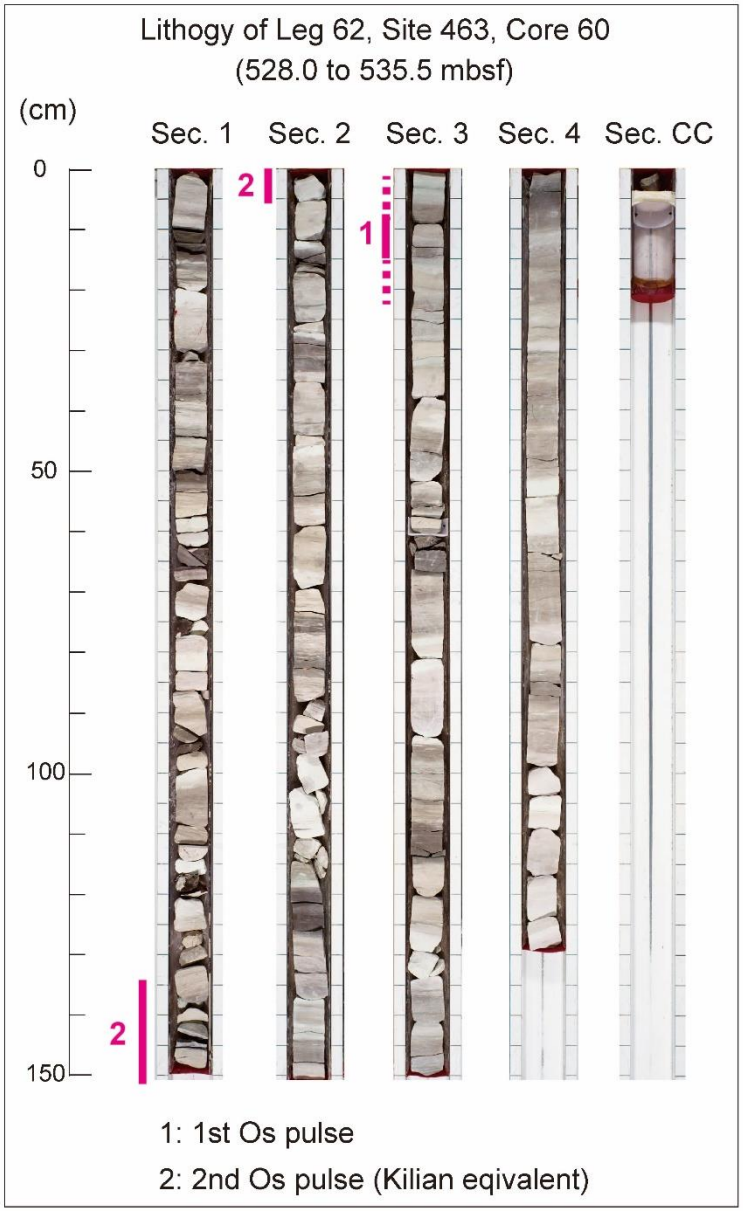

Figure. II-9. Lithological image of DSDP Site 463, core 60: The image is cited from http://deepseadrilling.org/cores/leg062/463.60R.PDF. Lithology consists of whitish limestone and brownish marlstone alternated with some chert layers.

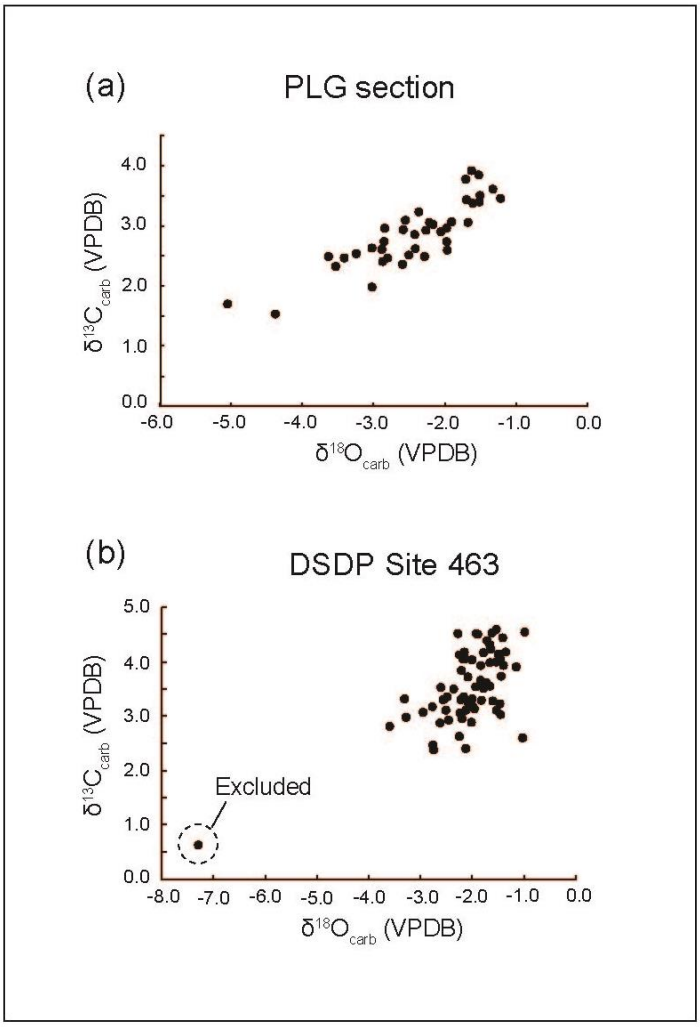

Figure II-10: **Cross plot of $\delta^{13}C_{carb}$ and $\delta^{18}O_{carb}$ of sedimentary rock samples from (a) the PLG section and (b) the DSDP Site 463**

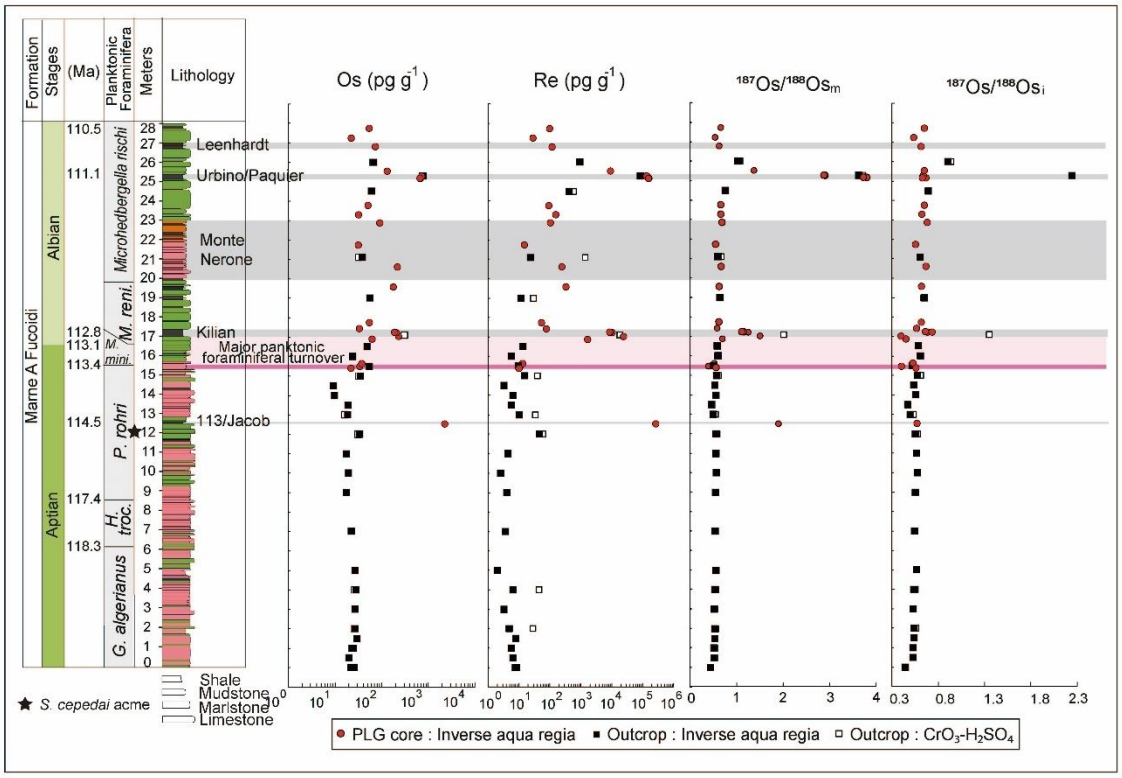

Figure II-11. Os and Re concentration, $^{187}Os/^{188}Os_m$, and $^{187}Os/^{188}Os_i$ at the PLG section and core.

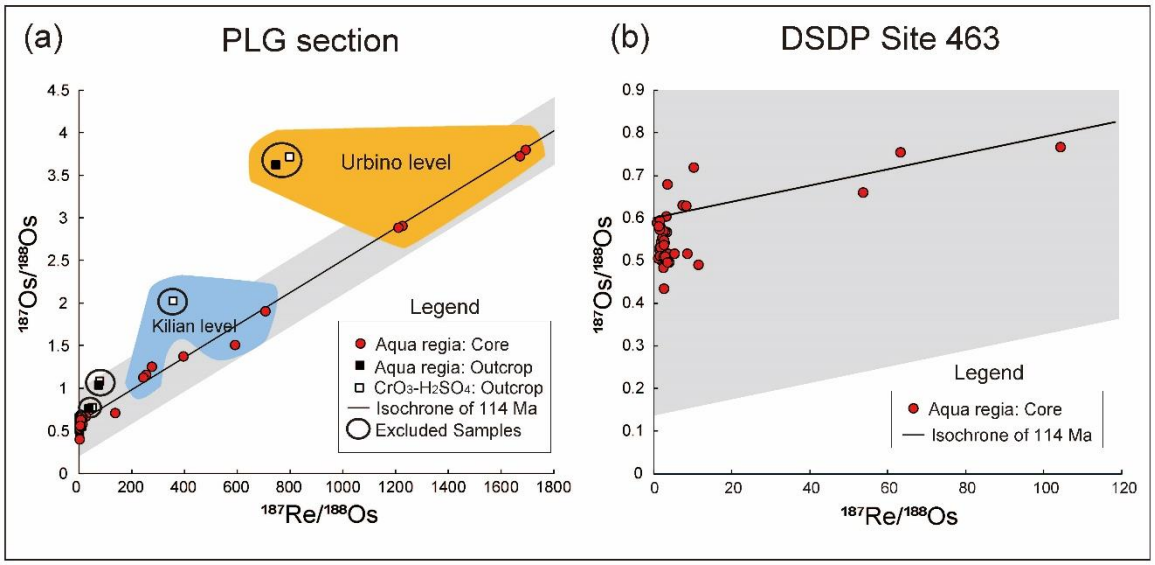

Figure II-12. Cross plot of $^{187}Re/^{188}Os$-$^{187}Os/^{188}Os_m$ of the PLG section and PLG core, and the DSDP Site463: Points in the orange area represent the Urbino/Paquier equivalent level, and points in the blue area represents the Kilian equivalent level.

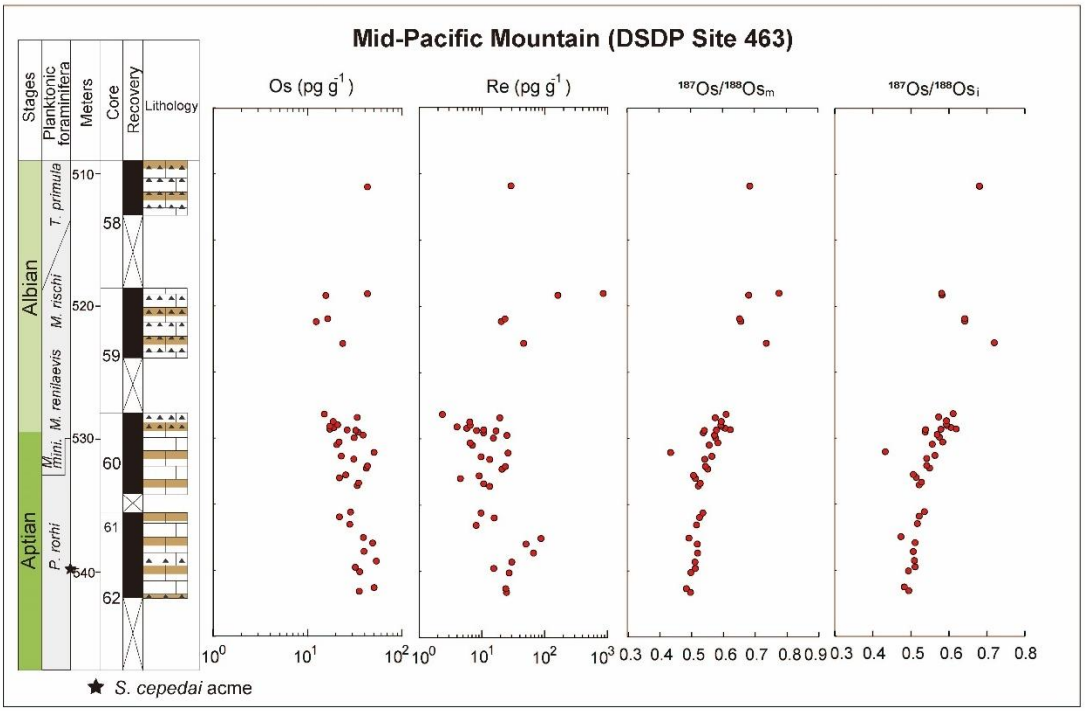

Figure II-13. The Os and Re concentration, $^{187}Os/^{188}Os_m$, and $^{187}Os/^{188}Os_i$ at the DSDP Site 463.

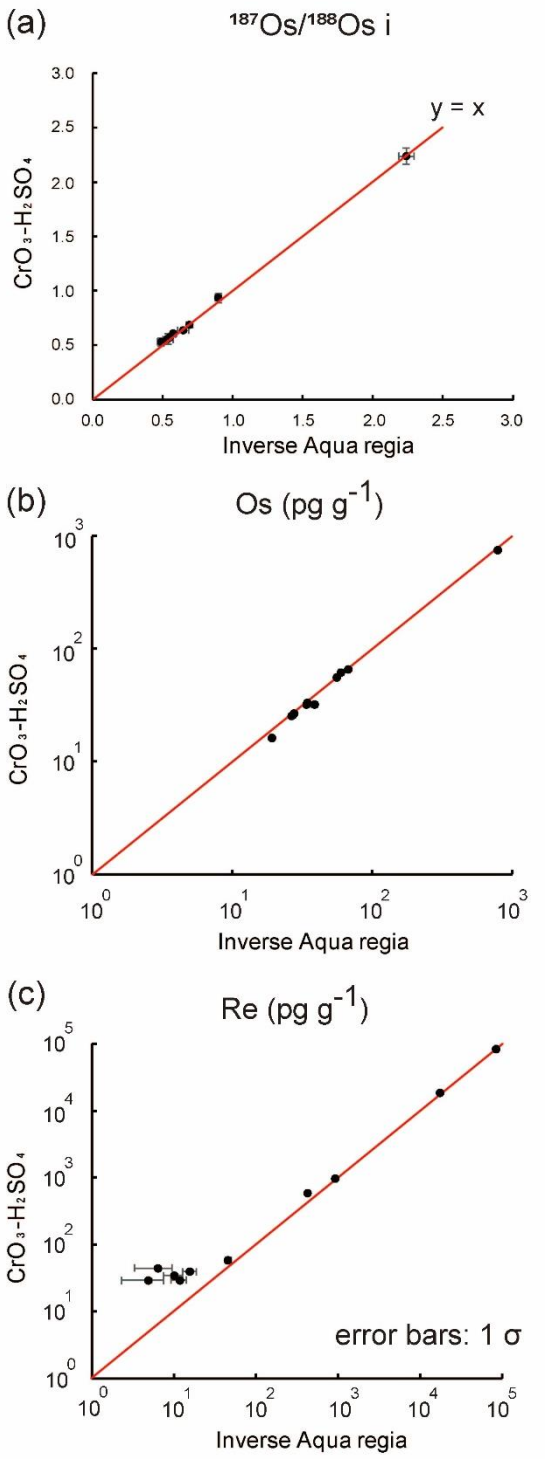

Figure II-14. Comparison of $^{187}Os/^{188}Os_i$ and Os and Re concentrations of sedimentary rock samples of the PLG section treated with inverse aqua regia and CrO_3–H_2SO_4.

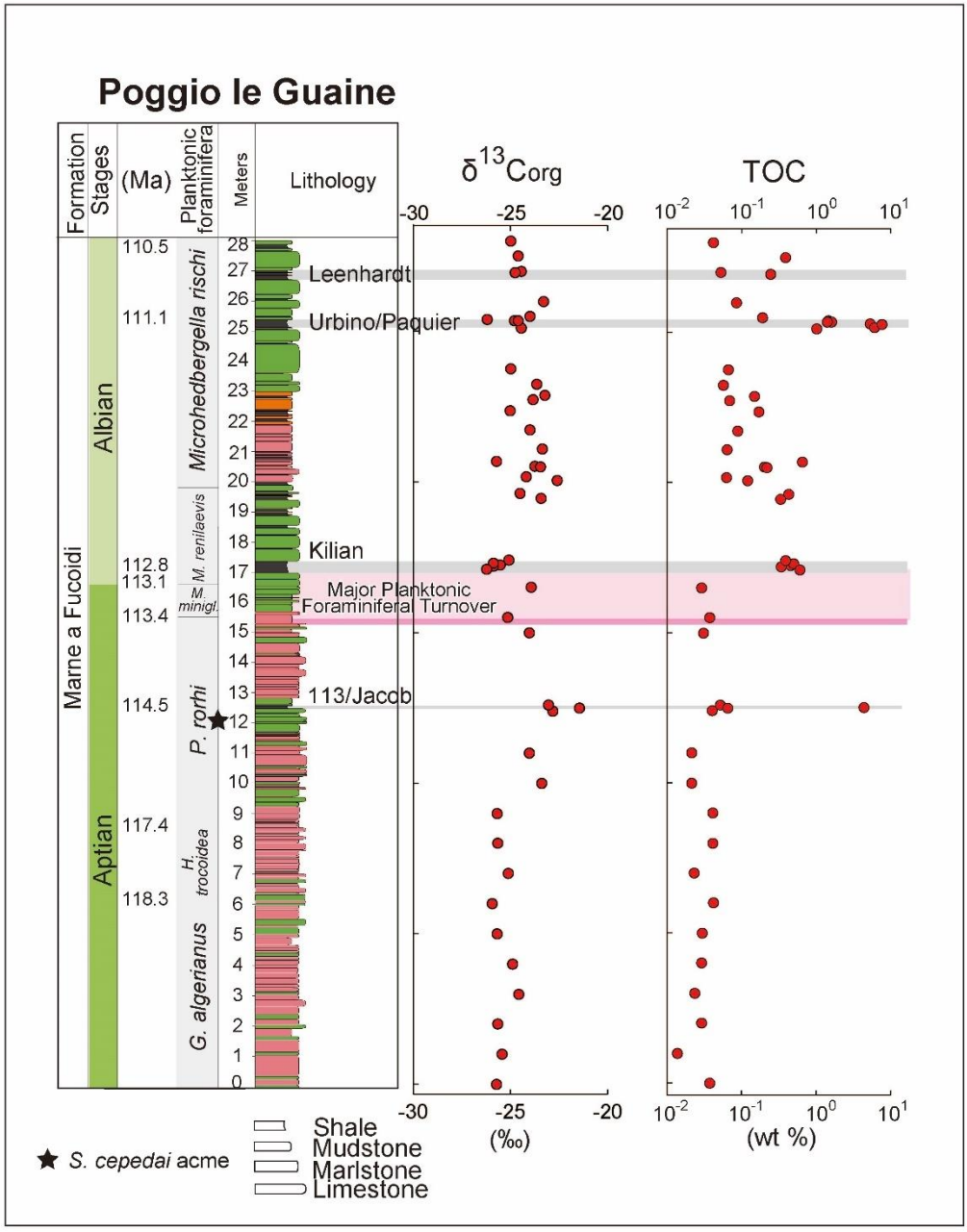

Figure II-15: The $\delta^{13}C_{org}$ and TOC records at the PLG section.

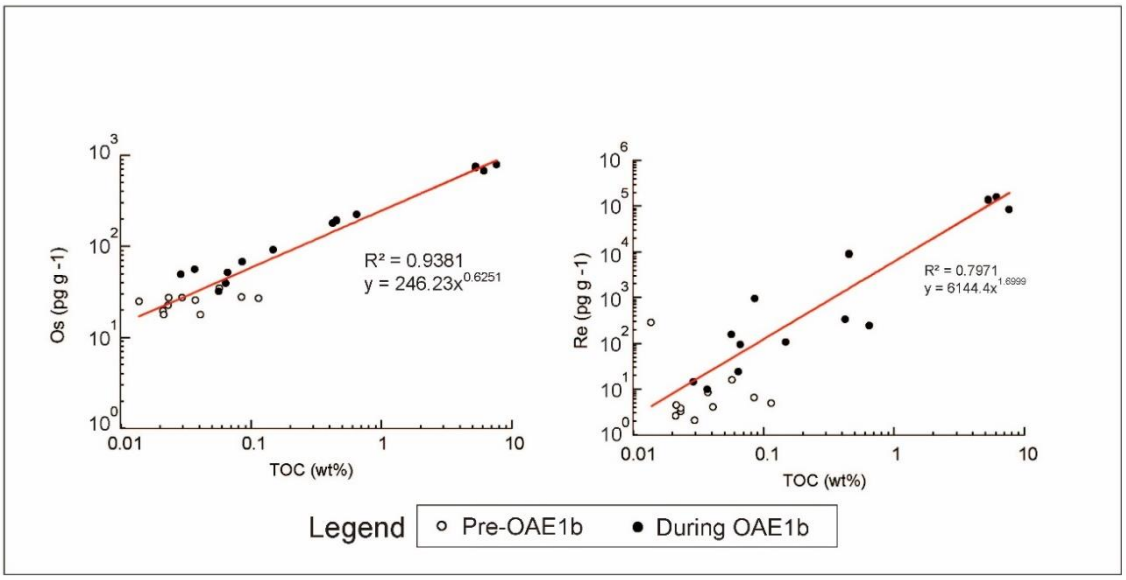

Figure II-16. Cross plots of Os and Re concentrations against TOC of the PLG section: Black circles represent the sedimentary rock samples from the OAE1b interval and white ones represent the sedimentary rock samples from the pre-OAE1b. Red lines show the approximate curves of plotted data containing both black and white circles.

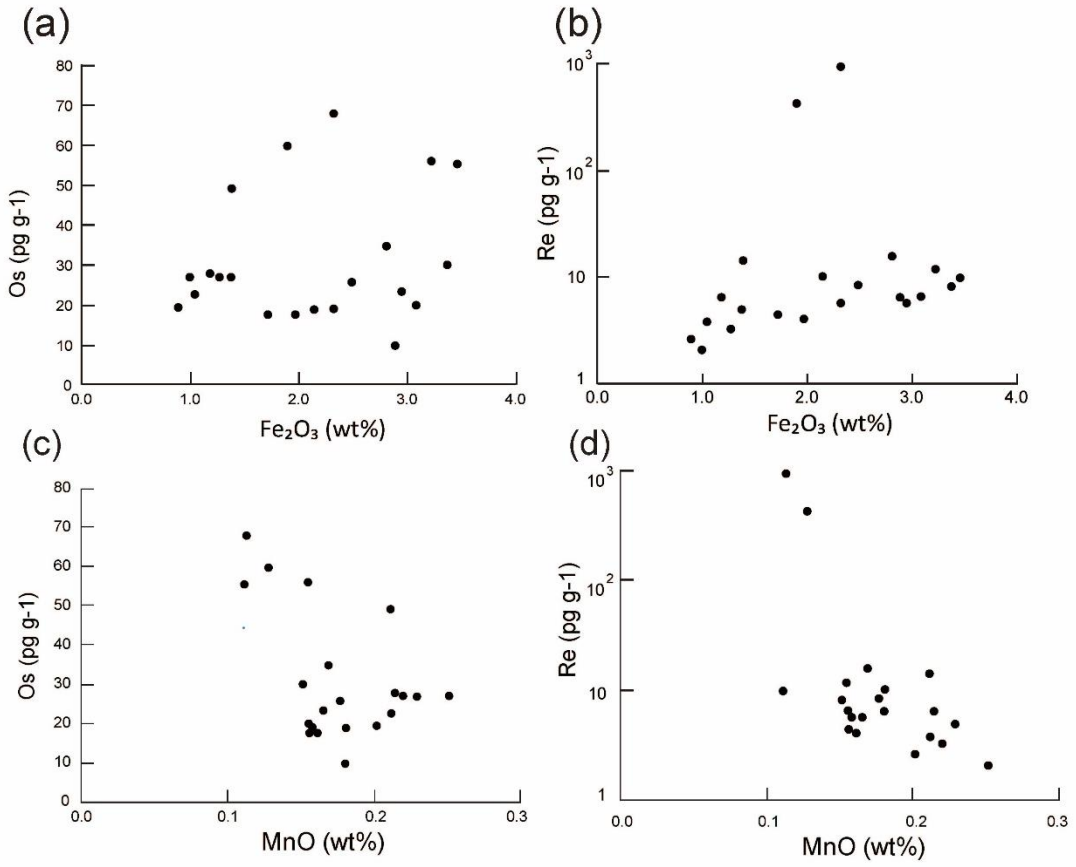

Figure II-17. Cross plots of (a) Fe_2O_3 (wt%)–Os (pg g^{-1}), (b) Fe_2O_3 (wt%)–Re (pg g^{-1}), (c) MnO (wt%)–Os (pg g^{-1}), and (d) MnO (wt%)–Re (pg g^{-1}).

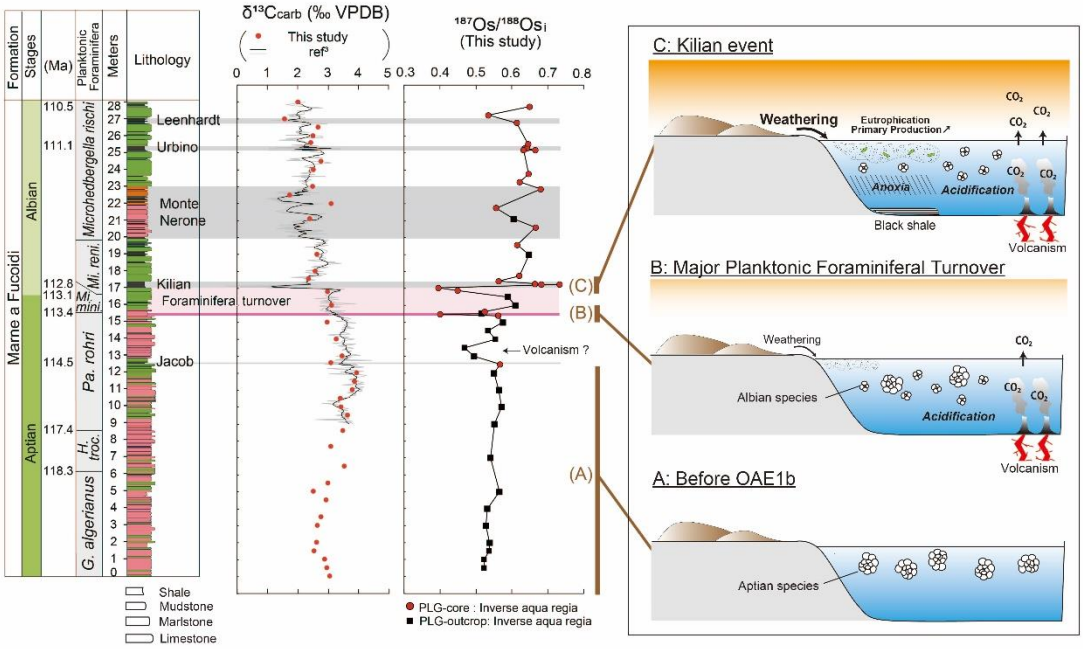

Figure II-18. Interpretation of Os isotopic variations and environmental changes during OAE1b in the context of the lithological, geochemical, and biological profiles reported in Fig. 4: (a) Oceanic conditions during the pre- OAE1b interval; (b) the first volcanic eruption at the extinction-level; and (c) the second volcanic eruption at the Kilian level.

Supplementary Tables of Chapter II

Name (Date SampleID)	Depth (msl)	Date	$\delta^{13}C$ (‰VPDB)	1σ for $\delta^{13}C$	$\delta^{18}O$ (‰VPDB)	1σ for $\delta^{18}O$
171229 PLG-9.0	0	2017/12/29	3.024	0.005	-2.164	0.012
171229 PLG-8.5	0.5	2017/12/29	2.931	0.004	-2.269	0.006
171229 PLG-8.0	1	2017/12/29	2.862	0.004	-2.421	0.017
171229 PLG-7.5	1.5	2017/12/29	2.512	0.006	-2.499	0.009
171229 PLG-7.0	2	2017/12/29	2.598	0.004	-1.962	0.012
171229 PLG-6.0	3	2017/12/29	2.616	0.009	-2.415	0.012
171229 PLG-5.5	3.5	2017/12/29	2.740	0.004	-1.979	0.007
171229 PLG-4.5	4.5	2017/12/29	2.909	0.004	-2.051	0.012
171229 PLG-4.0	5	2017/12/29	2.488	0.005	-2.282	0.010
171229 PLG-3.5	5.5	2017/12/29	2.969	0.005	-1.978	0.009
171229 PLG-2.5	6.5	2017/12/29	3.508	0.007	-1.506	0.015
171229 PLG-1.35	7.65	2017/12/29	3.059	0.007	-2.210	0.009
171229 PLG-0.4	8.6	2017/12/29	3.459	0.005	-1.217	0.009
171229 PLG-0.5	9.5	2017/12/29	3.614	0.004	-1.325	0.013
171229 PLG+1.0	10	2017/12/29	3.402	0.008	-1.519	0.015
171229 PLG+1.5	10.5	2017/12/29	3.381	0.009	-1.604	0.011
171229 PLG+2.0	11	2017/12/29	3.775	0.004	-1.705	0.019
171229 PLG+2.5	11.5	2017/12/29	3.845	0.007	-1.530	0.014
171229 PLG+3.0	12	2017/12/29	3.921	0.006	-1.626	0.015
171230 PLG+3.6	12.6	2017/12/30	3.063	0.004	-1.674	0.010
171230 PLG+4.0	13	2017/12/30	3.436	0.003	-1.700	0.019
171230 PLG+5.0	14	2017/12/30	3.239	0.005	-2.363	0.012
171230 PLG+6.0	15	2017/12/30	2.940	0.011	-2.581	0.02
171230 PLG+7.0	16	2017/12/30	3.092	0.004	-2.551	0.011
171230 PLG+7.8	16.8	2017/12/30	2.959	0.007	-2.846	0.013
171230 PLG+8.55	17.55	2017/12/30	2.330	0.011	-3.534	0.015
171230 PLG+9.0	18	2017/12/30	2.544	0.005	-3.244	0.009
171230 PLG+10.0	19	2017/12/30	2.609	0.006	-2.886	0.009
171230 PLG+14.0	23	2017/12/30	2.464	0.008	-2.802	0.011
171230 PLG+150	24	2017/12/30	2.491	0.010	-3.627	0.017
171230 PLG+15.5	24.5	2017/12/30	2.735	0.003	-2.856	0.018
171230 PLG+16.6	25.6	2017/12/30	2.405	0.013	-2.877	0.03
171230 PLG+17.0	26	2017/12/30	2.470	0.006	-3.410	0.02
171230 PLG+17.5	26.5	2017/12/30	2.640	0.004	-3.023	0.015
171230 PLG+18.0	27	2017/12/30	1.535	0.007	-4.380	0.017
171230 PLG+19.0	28	2017/12/30	1.984	0.007	-3.027	0.02
171230 PLG+12.10	21.1	2017/12/30	2.363	0.012	-2.595	0.05
171230 PLG+13.0	22	2017/12/30	3.069	0.008	-1.907	0.03
171230 PLG+13.5	22.5	2017/12/30	1.707	0.017	-5.046	0.06

Supplementary Table II-S1. Stable carbon and oxygen isotopic composition of carbonate from the PLG section.

Name	Sample ID	Depth	Date	$\delta^{13}C$	1σ for $\delta^{13}C$	$\delta^{18}O$	1σ for $\delta^{13}C$	Remarks
(Date Site_Core-Section_Top(cm)-Bottom(cm))		(mbsf)		(‰VPDB)		(‰VPDB)		
181001 463_56-1_30-34	463-2-56-1-2	490.3	2018/10/1	2.404	0.011	-2.134	0.02	
181001 463_57-2_70-72	463-2-57-2-3	500.2	2018/10/1	2.470	0.007	-2.766	0.011	
180404 463_58-1_46-48	463-1-58-1-1	509.46	2018/4/4	2.922	0.005	-2.462	0.015	
181001 463_58-1_131-135	463-2-58_1_4	510.31	2018/10/1	2.624	0.015	-2.252	0.017	
180404 463_58-2_44-50	463-1-58-2-1	510.94	2018/4/4	3.025	0.002	-1.453	0.007	
180919 463_58-2_83-86	463-1-58-2-2	511.33	2018/9/19	2.596	0.007	-1.031	0.013	
180404 463_58-3_40-42	463-1-58-3-2	512.36	2018/4/4	2.881	0.005	-2.027	0.011	
181001 463_58-3_107_111	463-1-58-3-3	513.07	2018/10/1	2.375	0.010	-2.748	0.012	
180404 463_59-1_14_18	463-1-59-1-1	518.64	2018/4/4	3.299	0.003	-2.574	0.009	
180404 463_59-1_36_38	463-1-59-1-2	518.86	2018/4/4	3.227	0.004	-2.073	0.013	
180404 463_59-1_54_56	463-1-59-1-3	519.04	2018/4/4	3.311	0.002	-2.008	0.007	
180422 463_59-1_68_71(2)	463-1-59-1-4	519.18	2018/4/22	3.300	0.007	-2.558	0.009	
180422 463_59-1_83-86(2)	463-1-59-1-5	519.33	2018/4/22	3.315	0.004	-3.313	0.016	
180404 463_59-1_115-119	463-1-59-1-6	519.65	2018/4/4	3.109	0.003	-2.136	0.003	
180404 463_59-2_6-9	463-1-59-2-1	520.06	2018/4/4	3.177	0.004	-2.777	0.008	
180404 463_59-2_21-26	463-1-59-2-2	520.21	2018/4/4	3.225	0.005	-1.466	0.009	
180422 463_59-2_44-48(2)	463-1-59-2-3	520.44	2018/4/22	2.948	0.007	-2.203	0.008	
180404 463_59-2_74-78	463-1-59-2-4	520.74	2018/4/4	3.057	0.004	-2.241	0.006	
180404 463_59-2_96-98	463-1-59-2-5	520.96	2018/4/4	2.976	0.003	-3.276	0.010	
180404 463_59-2_116-118	463-1-59-2-6	521.16	2018/4/4	3.071	0.0018	-2.954	0.006	
180404 463_59-2_135-137	463-1-59-2-7	521.35	2018/4/4	3.177	0.003	-1.992	0.009	
180422 463_59-3_6-9(2)	463-1-59-3-1	521.56	2018/4/22	3.104	0.006	-2.511	0.008	
180422 463_59-3_25-27(2)	463-1-59-3-2	521.75	2018/4/22	2.874	0.002	-2.626	0.007	
180822 463_59-3_95-97(2)	463-1-59-3-3	522.45	2018/8/22	3.361	0.003	-2.168	0.008	
180404 463_59-3_118-120	463-1-59-3-4	522.68	2018/4/4	3.510	0.006	-1.784	0.004	
180404 463_59-3_133-135	463-1-59-3-5	522.83	2018/4/4	3.309	0.002	-2.223	0.013	
180404 463_59-4_7-11	463-1-59-4-1	523.07	2018/4/4	0.631	0.004	-7.283	0.007	Excluded from the discussion
180822 463_59-4_7-11(2)	463-1-59-4-1	523.07	2018/8/22	3.110	0.004	-1.536	0.007	
180404 463_59-CC_10-13	463-1-59-CC-1	523.4	2018/4/4	3.280	0.003	-1.615	0.009	
180404 463_60-1_18-20	463-1-60-1-1	528.18	2018/4/4	3.647	0.002	-1.842	0.007	
180822 463_60-1_20-22(2)	463-1-60-1-2	528.2	2018/8/22	3.551	0.004	-1.659	0.007	
180404 463_60-1_44-46	463-1-60-1-3	528.44	2018/4/4	3.715	0.005	-2.086	0.012	
180404 463_60-1_73-75	463-1-60-1-4	528.73	2018/4/4	3.613	0.003	-1.734	0.007	
180822 463_60-1_94-99(2)	463-1-60-1-5	528.94	2018/8/22	3.296	0.003	-1.825	0.012	
180404 463_60-1_100-102	463-1-60-1-6	529	2018/4/4	3.355	0.003	-2.489	0.005	
180919 463_60-1_122-127	463-2-60-1-2	529.22	2018/9/19	3.129	0.006	-1.969	0.012	
180404 463_60-1_133-138	463-2-60-1-7	529.33	2018/4/4	2.806	0.004	-3.594	0.011	
180919 463_60-1_138-141	463-2-60-1-3	529.38	2018/9/19	3.539	0.005	-1.936	0.010	
180406 463_60-2_6-8	463-1-60-2-1	529.56	2018/4/6	3.521	0.003	-2.611	0.009	
180406 463_60-2_27-29	463-1-60-2-2	529.77	2018/4/6	3.734	0.004	-1.449	0.007	
180406 463_60-2_82-85	463-1-60-2-5	530.32	2018/4/6	3.650	0.007	-1.848	0.015	
180406 463_60-2_100-103	463-1-60-2-6	530.5	2018/4/6	3.497	0.005	-2.368	0.012	
180822 463_60-2_136-138(2)	463-1-60-2-7	530.86	2018/8/22	3.839	0.005	-2.219	0.009	
180822 463_60-3_8-12(2)	463-1-60-3-1	531.08	2018/8/22	3.980	0.006	-1.662	0.007	
180406 463_60-3_36-40	463-1-60-3-2	531.36	2018/4/6	4.051	0.003	-2.140	0.010	
180406 463_60-3_58-59	463-1-60-3-3	531.58	2018/4/6	4.043	0.003	-2.187	0.014	
180919 463_60-3_80-82	463-2-60-3-1	531.8	2018/9/19	3.936	0.003	-1.839	0.010	
180919 463_60-3_111-117	463-2-60-3-2	532.11	2018/9/19	3.907	0.007	-1.152	0.017	
180919 463_60-3_130-134	463-2-60-3-3	532.3	2018/9/19	4.028	0.007	-1.458	0.010	
180919 463_60-4_10-13	463-2-60-4-1	532.6	2018/9/19	4.391	0.006	-1.718	0.010	
180919 463_60-4_30-32	463-2-60-4-2	532.8	2018/9/19	4.173	0.005	-2.156	0.009	
181001 463_60-4_52-54	463-2-60-4-3	533.02	2018/10/1	4.093	0.004	-2.163	0.009	
180919 463_60-4_77-79	463-2-60-4-4	533.27	2018/9/19	4.232	0.008	-1.657	0.011	
180919 463_60-4_110-117	463-2-60-4-6	533.6	2018/9/19	4.177	0.009	-1.358	0.008	
180919 463_61-1_12-15	463-2-61-1-1	535.62	2018/9/19	4.001	0.008	-1.547	0.009	
180919 463_61-1_70-72	463-2-61-1-2	536.2	2018/9/19	3.927	0.009	-1.399	0.006	
180919 463_61-1_103-105	463-2-61-1-3	536.53	2018/9/19	4.028	0.007	-2.004	0.011	
180919 463_62-1_3-5	463-2-62-1-1	537.53	2018/9/19	4.138	0.010	-1.506	0.015	
180822 463_62-1_47-49(2)	463-1-62-1-1	537.97	2018/8/22	4.168	0.005	-1.792	0.008	
180822 463_62-1_114-116	463-2-62-1-2	538.64	2018/8/22	4.119	0.007	-2.255	0.007	
180822 463_62-2_5-7	463-2-62-2-1	539.05	2018/8/22	4.514	0.002	-2.281	0.008	
180822 463_62-2_32-35	463-2-62-2-2	539.32	2018/8/22	4.521	0.004	-1.918	0.004	
180822 463_62-2_80-81	463-2-62-2-3	539.8	2018/8/22	4.505	0.006	-1.901	0.005	
180822 463_62-2_113-115	463-2-62-2-4	540.13	2018/8/22	4.589	0.009	-1.546	0.01	
180822 463_62-3_2-9	463-2-62-3-1	540.52	2018/8/22	4.543	0.005	-0.988	0.007	
180822 463_62-3_35-42	463-2-62-3-2	540.85	2018/8/22	4.529	0.007	-1.620	0.007	
180822 463_62-3_83-88	463-2-62-3-3	541.33	2018/8/22	4.312	0.008	-1.658	0.013	
180822 463_62-3_111-113	463-2-62-3-4	541.61	2018/8/22	4.438	0.005	-1.424	0.007	

Supplementary Table II-S2. Stable carbon and oxygen isotopic composition of carbonate from DSDP Site 463.

Sample ID	Lab ID	Core or Outcrop	lithology	Depth (msl)	Date	$\delta^{13}C$ (‰VPDB)	C wt.% (TOC) (wt%)
PLG-9	HM-C-16	Outcrop	marlstone	0	2018/7/23	-25.7	0.04
PLG-8	HM-C-17	Outcrop	marlstone	1	2018/7/12	-25.4	0.01
PLG-7	HM-C-18	Outcrop	marlstone	2	2018/7/12	-25.7	0.03
PLG-6	HM-C-19	Outcrop	marlstone	3	2018/7/12	-24.6	0.02
PLG-5	HM-C-20	Outcrop	marlstone	4	2018/7/12	-24.9	0.03
PLG-4	HM-C-21	Outcrop	marlstone	5	2018/7/23	-25.7	0.03
PLG-3	HM-C-22	Outcrop	marlstone	6	2018/7/12	-26.0	0.04
PLG-2	HM-C-23	Outcrop	marlstone	7	2018/7/12	-25.1	0.02
PLG-1	HM-C-24	Outcrop	marlstone	8	2018/7/12	-25.7	0.04
PLG0	HM-C-25	Outcrop	marlstone	9	2018/7/12	-25.7	0.04
PLG+1.0	HM-C-26	Outcrop	marlstone	10	2018/7/12	-23.4	0.04
PLG+2.0	HM-C-27	Outcrop	marlstone	11	2018/7/12	-24.1	0.02
PLG+3.4	HM-C-28	Outcrop	marlstone	12.4	2018/7/12	-22.8	0.04
PLG+3.5①	HM-C-29	Outcrop	black shale	12.5	2018/7/12	-21.5	0.06
PLG+3.5③	HM-C-30-1	Outcrop	black shale	12.52	2018/7/23	Too large	4.4
PLG+3.5③	HM-C-30-2	Outcrop	black shale	12.52	2018/8/8-7	-19.4	6.1
PLG+3.5③	HM-C-30-3	Outcrop	black shale	12.52	2018/8/8-7	-19.1	5.1
PLG+3.5③	HM-C-30-4	Outcrop	black shale	12.52	2018/8/8-7	-18.8	5.2
PLG+3.6	HM-C-31	Outcrop	marlstone	12.6	2018/7/23	-23.1	0.05
PLG+6.0	HM-C-32	Outcrop	marlstone	15	2018/7/23	-24.0	0.03
PLG+6.5	HM-C-33	Outcrop	marlstone	15.5	2018/7/23	-25.2	0.04
PLG+7.5	HM-C-08	Outcrop	marlstone	16.5	2018/7/23	-23.9	0.03
PLG+8.1	HM-C-34	Outcrop	black shale	17.1	2018/7/23	-26.3	0.60
PLG+8.2	HM-C-35	Outcrop	black shale	17.2	2018/7/23	-25.9	0.34
PLG-C_64.49	HM-C-15	Core	black shale	17.24	2018/7/23	-25.6	0.45
PLG+8.3	HM-C-36	Outcrop	black shale	17.3	2018/7/23	-25.9	0.49
PLG+8.4	HM-C-37	Outcrop	black shale	17.4	2018/7/23	-25.1	0.39
PLG+10.45	HM-C-49	Outcrop	black shale	19.45	2018/7/23	-23.5	0.33
PLG-C62.11-62.2	HM-C-14	Core	marlstone	19.62	2018/7/23	-24.5	0.42
PLG-C61.67-61.73	HM-C-13	Core	black shale	20.06	2018/7/23	-22.6	0.12
PLG_C61.56-61.59	HM-C-12	Core	marlstone	20.17	2018/7/12	-24.2	0.11
PLG+11.5	HM-C-50	Outcrop	mudstone	20.5	2018/7/23	-23.5	0.22
PLG-C_61.2	HM-C-11	Core	black shale	20.53	2018/7/23	-23.8	0.20
PLG-C_61.05-61.2	HM-C-10	Core	black shale	20.68	2018/7/23	-25.7	0.65
PLG+12.10	HM-C-48	Outcrop	mudstone	21.1	2018/7/23	-23.4	0.06
PLG-C_60.00-60.15	HM-C-09	Core	marlstone	21.73	2018/7/12	-24.0	0.09
PLG-C_59.37-59.38	HM-C-07	Core	marlstone	22.36	2018/7/23	-25.0	0.17
PLG-C_58.99	HM-C-06	Core	marlstone	22.74	2018/7/23	-23.9	0.07
PLG-C_58.86-58.87	HM-C-05	Core	black shale	22.87	2018/7/12	-23.3	0.15
PLG-C_58.48-58.40	HM-C-04	Core	marlstone	23.25	2018/7/12	-23.7	0.06
PLG-C_57.97	HM-C-03	Core	marlstone	23.76	2018/7/23	-25.0	0.07
PLG+16.12	HM-C-38	Outcrop	black shale	25.12	2018/7/23	-24.5	1.0
PLG-C_56.56-56.58	HM-C-02-1	Core	black shale	25.17	2018/7/23	Too large	6.1
PLG-C_56.56-56.58	HM-C-02-2	Core	black shale	25.17	2018/8/8-7	-23.5	8.1
PLG-C_56.56-56.58	HM-C-02-3	Core	black shale	25.17	2018/8/8-7	-23.3	7.5
PLG-C_56.56-56.58	HM-C-02-4	Core	black shale	25.17	2018/8/8-7	-24.6	7.0
PLG+16.28	HM-C-39-1	Outcrop	black shale	25.28	2018/7/23	Too large	7.7
PLG+16.28	HM-C-39-2	Outcrop	black shale	25.28	2018/8/8-7	-23.2	5.7
PLG+16.28	HM-C-39-3	Outcrop	black shale	25.28	2018/8/8-7	-23.0	5.2
PLG+16.28	HM-C-39-4	Outcrop	black shale	25.28	2018/8/8-7	-23.1	6.7
PLG-C_56.44-56.48	HM-C-01-1	Core	black shale	25.29	2018/7/23	Too large	5.3
PLG-C_56.44-56.48	HM-C-01-2	Core	black shale	25.29	2018/8/8-7	-23.6	5.7
PLG-C_56.44-56.48	HM-C-01-3	Core	black shale	25.29	2018/8/8-7	-22.5	5.8
PLG-C_56.44-56.48	HM-C-01-4	Core	black shale	25.29	2018/8/8-7	-23.0	4.6
PLG+16.35	HM-C-40-1	Outcrop	black shale	25.35	2018/7/12	Too small	-
PLG+16.35	HM-C-40-3	Outcrop	black shale	25.35	2018/7/23	-24.8	1.6
PLG+16.35	HM-C-40-2	Outcrop	black shale	25.35	2018/7/12	-24.6	1.4
PLG+16.4	HM-C-42	Outcrop	black shale	25.4	2018/7/23	-26.2	1.5
PLG+16.5	HM-C-41	Outcrop	black shale	25.5	2018/7/23	-24.0	0.19
PLG+17	HM-C-44	Outcrop	black shale	26	2018/7/23	-23.3	0.09
PLG+17.95	HM-C-45	Outcrop	marlstone	26.95	2018/7/23	-24.8	0.25
PLG+18	HM-C-46	Outcrop	marlstone	27	2018/7/23	-24.5	0.05
PLG+18.5	HM-C-47	Outcrop	black shale	27.5	2018/7/23	-24.6	0.39
PLG+19	HM-C-43	Outcrop	marlstone	28	2018/7/23	-25.0	0.04

Supplementary Table II-S3. Total organic carbon content and stable carbon isotopic composition of organic matter at the PLG section and core.

Sample ID	Lab ID	Depth (mbsf)	$\delta^{13}C$ (‰VPDB)	C wt.% (TOC) (wt%)
463_58-1_46-48	HM 1	509.46	-26.5	0.06
463_59-1_14-18	HM 2	518.64	-27.0	0.04
463_59-3_95-97	HM 3	522.45	-26.5	0.07
463_59-4_7-11	HM 4	523.07	-27.5	0.12
463_59-CC_10-13	HM 5	523.4	-26.6	0.02
463_60-2_82-85	HM 6	530.32	-27.0	0.51
463_60-2_27-29	HM 7	529.77	-27.1	0.10
463_60-3_8-12	HM 8	531.08	-27.0	0.12
463_60-4_90-93	HM 9	531.08	-27.1	0.08
463_60-4_110-117	HM 10	533.6	-27.6	0.10
463_61-1_12-15	HM 11	535.62	-27.0	0.05
462_61-1_103-105	HM 12	536.53	-27.0	0.09
463_62-2_113-115	HM 13	540.13	-27.1	0.07
463_62-3_83-88	HM 14	541.33	-27.0	0.07
463_62-3_111-113	HM 15	541.98	-27.4	0.07

Supplementary Table II-S4. Total organic carbon content and stable carbon isotopic composition of organic matter at the DSDP Site 463.

Sample Name	Lithology	Depth (msl)	Age (Ma)	Digestion liquid	Core/ outcrop	Os conc (pg g-1)	1SD	1SE	187Os/ 188Osm	1SD	1SE	Re conc (pg g-1)	1SD	1SE	187Re/ 188Os	1SD	1SE	187Os/ 188Osi	1SD	1SE
PLG-9.0	Marlsrtone	0	119	In. aqua regia	Outcrop	25.7	1.8	0.3	0.45	0.09	0.03	8.4.E+00	1.7.E+00	4.E-01	1.64	0.4	0.08	0.44	0.09	0.03
PLG-9	Marlsrtone	0	119	In. aqua regia	Outcrop	22.15	0.16	0.02	0.448	0.009	0.003	7.8.E+00	1.3.E+00	3.E-01	1.76	0.3	0.06	0.445	0.009	0.003
PLG-8.5	Marlsrtone	0.5	119	In. aqua regia	Outcrop	19.98	0.3	0.05	0.526	0.018	0.005	6.5.E+00	1.3.E+00	3.E-01	1.64	0.3	0.07	0.522	0.018	0.005
PLG-8	Marlsrtone	1	119	In. aqua regia	Outcrop	23.37	0.2	0.03	0.526	0.009	0.003	5.7.E+00	1.1.E+00	3.E-01	1.22	0.2	0.06	0.523	0.009	0.003
PLG-7.5	Marlsrtone	1.5	119	In. aqua regia	Outcrop	29.95	0.2	0.04	0.540	0.011	0.003	8.1.E+00	1.3.E+00	3.E-01	1.37	0.2	0.05	0.537	0.011	0.003
PLG-7.0	Marlsrtone	2	120	CrO_3-H_2SO_4	Outcrop	25.57	0.5	0.08	0.567	0.03	0.011	2.88.E+01	3.E+00	6.E-01	5.7	0.5	0.12	0.56	0.03	0.011
PLG-7.0	Marlsrtone	2	120	In. aqua regia	Outcrop	26.9	0.9	0.14	0.540	0.05	0.016	4.9.E+00	1.7.E+00	4.E-01	0.9	0.3	0.07	0.54	0.05	0.016
PLG-6.0	Marlsrtone	3	119	In. aqua regia	Outcrop	27.02	0.5	0.07	0.529	0.03	0.008	3.3.E+00	1.7.E+00	4.E-01	0.61	0.3	0.07	0.528	0.03	0.008
PLG-5.0	Marlsrtone	4	120	CrO_3-H_2SO_4	Outcrop	26.61	0.3	0.05	0.566	0.009	0.003	4.47.E+01	3.E+00	7.E-01	8.6	0.6	0.13	0.55	0.009	0.003
PLG-5.0	Marlsrtone	4	120	In. aqua regia	Outcrop	27.84	0.3	0.05	0.534	0.011	0.004	6.4.E+00	1.8.E+00	4.E-01	1.2	0.3	0.07	0.53	0.011	0.004
PLG-4.0	Marlsrtone	5	119	In. aqua regia	Outcrop	27.02	0.3	0.05	0.566	0.02	0.007	2.1.E+00	1.7.E+00	4.E-01	0.39	0.3	0.07	0.565	0.02	0.007
PLG-2.0	Marlsrtone	7	117	In. aqua regia	Outcrop	22.59	0.3	0.05	0.542	0.017	0.005	3.8.E+00	1.8.E+00	4.E-01	0.85	0.4	0.09	0.541	0.017	0.005
PLG0.0	Marlsrtone	9	117	In. aqua regia	Outcrop	17.6	0.2	0.03	0.554	0.015	0.005	4.0.E+00	1.8.E+00	4.E-01	1.17	0.5	0.11	0.551	0.016	0.005
PLG+1.0	Marlsrtone	10	115	In. aqua regia	Outcrop	19.38	0.13	0.02	0.573	0.011	0.003	2.6.E+00	1.7.E+00	4.E-01	0.68	0.5	0.10	0.571	0.011	0.003
PLG+2.0	Marlsrtone	11	115	In. aqua regia	Outcrop	17.57	0.16	0.03	0.566	0.016	0.005	4.4.E+00	1.8.E+00	4.E-01	1.28	0.5	0.11	0.564	0.016	0.005
PLG+3.0	Limestone	12	115	CrO_3-H_2SO_4	Outcrop	31.78	0.4	0.06	0.591	0.012	0.004	5.83.E+01	3.E+00	8.E-01	9.4	0.6	0.13	0.57	0.012	0.004
PLG+3.0	Limestone	12	115	In. aqua regia	Outcrop	34.2	0.5	0.08	0.564	0.03	0.009	4.61.E+01	2.E+00	5.E-01	6.8	0.4	0.08	0.55	0.03	0.009
PLG-C-69.20	Black shale (Jacob)	12.53	114	In. aqua regia	Core	2275	43	7	1.908	0.04	0.012	2.70.E+05	1.E+04	2.E+03	705	28	6	0.567	0.07	0.016
PLG+4.0	Marlsrtone	13	114	CrO_3-H_2SO_4	Outcrop	16.24	0.4	0.08	0.550	0.03	0.009	3.44.E+01	3.E+00	6.E-01	10.8	0.8	0.18	0.53	0.03	0.009
PLG+4.0	Marlsrtone	13	114	In. aqua regia	Outcrop	18.9	0.3	0.09	0.50	0.02	0.014	1.01.E+01	1.8.E+00	4.E-01	2.7	0.5	0.11	0.495	0.02	0.014
PLG+4.5	Marlsrtone	13.5	114	In. aqua regia	Outcrop	19.03	0.10	0.015	0.471	0.005	0.002	5.7.E+00	1.6.E+00	4.E-01	1.50	0.4	0.10	0.469	0.005	0.002
PLG+5	Limestone	14	114	In. aqua regia	Outcrop	9.75	0.14	0.02	0.561	0.018	0.005	6.4.E+00	1.3.E+00	3.E-01	3.33	0.7	0.16	0.555	0.018	0.005
PLG+5.5	Marlstone	14.5	114	In. aqua regia	Outcrop	9.30	0.11	0.017	0.537	0.015	0.005	3.2.E+00	1.7.E+00	4.E-01	1.8	0.9	0.2	0.534	0.015	0.005
PLG+6.0	Marlstone	15	113	CrO_3-H_2SO_4	Outcrop	32.94	0.4	0.06	0.617	0.02	0.005	3.95.E+01	3.E+00	7.E-01	6.1	0.5	0.11	0.61	0.016	0.005
PLG+6.0	Marlstone	15	113	In. aqua regia	Outcrop	34.74	0.4	0.07	0.579	0.02	0.007	1.57.E+01	2.E+00	5.E-01	2.3	0.3	0.07	0.57	0.02	0.007
PLG-C-66.35	Mudstone	15.38	113	In. aqua regia	Core	22.17	0.17	0.03	0.567	0.015	0.004	1.03.E+01	1.5.E+00	3.E-01	2.36	0.3	0.08	0.563	0.015	0.004
PLG-C-66.25	Mudstone	15.48	113	In. aqua regia	Core	33.92	0.3	0.05	0.403	0.008	0.003	1.07.E+01	3.E+00	6.E-01	1.58	0.4	0.09	0.400	0.008	0.003
PLG+6.5	Mudstone	15.5	113	In. aqua regia	Outcrop	55.4	1.0	0.15	0.516	0.016	0.005	9.7.E+00	2.E+00	5.E-01	0.9	0.2	0.05	0.514	0.016	0.005
PLG-C-66.10	Mudstone	15.63	113	In. aqua regia	Core	38.02	0.4	0.07	0.528	0.016	0.005	1.32.E+01	3.E+00	6.E-01	1.77	0.4	0.08	0.524	0.016	0.005
PLG+7.0	Marlstone	16	113	In. aqua regia	Outcrop	24.01	0.3	0.05	0.61	0.02	0.007	5.8.E+00	2.E+00	5.E-01	1.2	0.5	0.11	0.610	0.02	0.007
PLG+7.5	Marlstone	16.5	113	In. aqua regia	Outcrop	49.1	1.0	0.15	0.59	0.03	0.008	1.41.E+01	3.E+00	6.E-01	1.5	0.3	0.07	0.589	0.03	0.008
PLG-C-64.85	Marlstone	16.88	113	In. aqua regia	Core	62.9	0.7	0.10	0.706	0.013	0.004	1.660.E+03	8.E+01	1.7.E+01	136.7	6.5	1.4	0.449	0.018	0.005
PLG-C-64.85(2)	Marlstone	16.88	113	In. aqua regia	Core	58.3	0.2	0.03	0.737	0.005	0.002	1.636.E+03	8.E+01	1.8.E+01	146.0	7	1.6	0.462	0.015	0.003
PLG-C-64.85(3)	Marlstone	16.88	113	In. aqua regia	Core	57.0	0.4	0.06	0.746	0.011	0.003	1.631.E+03	6.E+01	1.5.E+01	148.9	6	1.3	0.465	0.016	0.004
PLG-C-64.70	Black shale (Kilian)	17.03	113	In. aqua regia	Core	233.3	2	0.3	1.506	0.02	0.008	2.42.E+04	4.E+02	1.E+02	590	12	3	0.395	0.03	0.009
PLG+8.1	Black shale (Kilian)	17.1	113	CrO_3-H_2SO_4	Outcrop	308	7	1.0	2.021	0.05	0.016	1.823.E+04	2.E+02	5.E+01	356	9	1.5	1.35	0.06	0.016
PLG-C-64.50	Black shale (Kilian)	17.23	113	In. aqua regia	Core	205.2	5	0.8	1.251	0.06	0.018	1.023.E+04	2.E+02	5.E+01	275	9	2	0.733	0.06	0.018
PLG-C-64.49	Black shale (Kilian)	17.24	113	In. aqua regia	Core	192	6	0.9	1.16	0.09	0.03	8.93.E+03	3.E+02	6.E+01	254	11	2	0.68	0.09	0.03
PLG-C-64.49	Black shale (Kilian)	17.24	113	In. aqua regia	Core	194.0	1.6	0.3	1.124	0.02	0.007	8.68.E+03	1.9.E+02	4.E+01	243.4	6	1.3	0.665	0.03	0.008
PLG-C-64.30	Marlstone	17.43	113	In. aqua regia	Core	33.7	0.3	0.04	0.585	0.008	0.003	7.71.E+01	4.E+00	9.E-01	11.65	0.6	0.13	0.563	0.008	0.003
PLG-C-64	Marlstone	17.73	113	In. aqua regia	Core	55.47	0.3	0.05	0.631	0.008	0.003	5.49.E+01	1.8.E+00	4.E-01	5.08	0.2	0.04	0.621	0.008	0.003
PLG+10.0	Marlstone	19	113	CrO_3-H_2SO_4	Outcrop	55.6	2	0.3	0.642	0.04	0.012	2.93.E+01	3.E+00	6.E-01	2.7	0.3	0.05	0.64	0.04	0.012
PLG+10.0	Marlstone	19	113	In. aqua regia	Outcrop	56.0	0.7	0.11	0.649	0.017	0.005	1.17.E+01	1.8.E+00	4.E-01	1.1	0.2	0.04	0.65	0.017	0.005
PLG-C-62.11-62.2	Black shale	19.575	113	In. aqua regia	Core	179.3	5	0.7	0.63	0.04	0.011	3.344.E+02	7.E+01	1.7.E+01	10	2	0.5	0.615	0.04	0.011
PLG-C-61.05-61.2	Mudstone	20.6025	112	In. aqua regia	Core	221.5	5	0.7	0.68	0.04	0.012	2.438.E+02	6.E+01	1.3.E+01	5.7	1.4	0.3	0.666	0.04	0.012
PLG+12.10	Mudstone	21.1	112	In. aqua regia	Outcrop	39.0	1.5	0.2	0.611	0.06	0.019	2.34.E+01	4.E+00	8.E-01	3.1	0.5	0.11	0.60	0.06	0.019
PLG-C-60-60.15	Mudstone	21.73	112	In. aqua regia	Core	31.80	0.3	0.05	0.562	0.012	0.004	1.54.E+01	1.3.E+00	3.E-01	2.47	0.2	0.05	0.557	0.012	0.004
PLG-C-58.86-58.87	Mudstone	22.865	112	In. aqua regia	Core	91.4	1.0	0.16	0.691	0.016	0.005	1.054.E+02	5.E+00	1.2.E+00	6.0	0.3	0.07	0.680	0.016	0.005
PLG-C-58.4-58.48	Mudstone	23.29	111	In. aqua regia	Core	31.98	0.3	0.04	0.668	0.017	0.005	1.557.E+02	7.E+00	1.5.E+00	25.1	1.1	0.2	0.622	0.017	0.005
PLG-C-57.97	Marlstone	23.76	111	In. aqua regia	Core	51.27	0.4	0.07	0.66	0.007	0.003	9.23.E+01	6.E+00	1.4.E+00	9.3	0.6	0.14	0.646	0.007	0.003
PLG+15.5	Marlstone	24.5	111	CrO_3-H_2SO_4	Outcrop	61.9	1.6	0.2	0.777	0.02	0.007	5.85.E+02	1.4.E+01	3.E+00	49	1.7	0.3	0.69	0.02	0.007
PLG+15.5	Marlstone	24.5	111	In. aqua regia	Outcrop	59.7	0.9	0.15	0.762	0.02	0.007	4.250.E+02	6.E+00	1.4.E+00	37.1	0.8	0.15	0.69	0.02	0.007
PLG-C-56.56-56.58	Black shale (Urbino)	25.16	111	In. aqua regia	Core	673	6	1.0	3.80	0.05	0.016	1.600.E+05	5.E+03	1.1.E+03	1693	54	12	0.67	0.11	0.03
PLG-C-56.56-56.58	Black shale (Urbino)	25.16	111	In. aqua regia	Core	673.6	4	0.6	3.728	0.04	0.013	1.591.E+05	3.E+03	7.E+02	1672	34	7	0.633	0.08	0.019
PLG-C-56.44-56.48	Black shale (Urbino)	25.27	111	In. aqua regia	Core	749	6	1.0	2.90	0.05	0.015	1.399.E+05	1.8.E+03	4.E+02	1225	19	4	0.635	0.06	0.017
PLG-C-56.44-56.48	Black shale (Urbino)	25.27	111	In. aqua regia	Core	729	10	1.5	2.884	0.06	0.019	1.347.E+05	1.5.E+03	3.E+02	1211	21	4	0.64	0.07	0.02
PLG+16.28	Black shale (Urbino)	25.28	111	CrO_3-H_2SO_4	Outcrop	744	6	1.0	3.716	0.05	0.014	8.40.E+04	1.4.E+03	3.E+02	798	15	3	2.24	0.06	0.016
PLG+16.28	Black shale (Urbino)	25.28	111	In. aqua regia	Outcrop	788	9	1.3	3.62	0.07	0.02	8.392.E+04	8.E+02	1.8.E+02	747	11	2	2.24	0.07	0.02
PLG-C-56.20	Marlstone	25.53	111	In. aqua regia	Core	131.2	0.8	0.12	1.374	0.013	0.004	9.23.E+03	1.5.E+03	3.E+02	394	65	14	0.65	0.12	0.03
PLG+17.0	Marlstone	26	111	CrO_3-H_2SO_4	Outcrop	65.9	0.6	0.09	1.081	0.02	0.006	9.62.E+02	4.E+01	8.E+00	79	3	0.7	0.93	0.02	0.006
PLG+17.0	Marlstone	26	111	In. aqua regia	Outcrop	67.9	1.7	0.3	1.035	0.04	0.012	9.33.E+02	2.E+01	5.E+00	74.0	3	0.5	0.90	0.04	0.012
PLG-C-54.95	Black shale (Leenhardt)	26.78	111	In. aqua regia	Core	73.5	2	0.4	0.629	0.04	0.012	1.187.E+02	8.E+01	1.7.E+01	8	5	1.2	0.614	0.04	0.012
PLG-C-54.50	Marlstone	27.23	111	In. aqua regia	Core	22.31	0.4	0.06	0.547	0.019	0.006	2.86.E+01	3.E+00	6.E-01	6.5	0.6	0.14	0.534	0.019	0.006
PLG-C-54.00	Marlstone	27.73	111	In. aqua regia	Core	54.32	0.6	0.09	0.666	0.02	0.006	9.87.E+01	3.E+00	7.E-01	9.4	0.3	0.07	0.649	0.02	0.006

Supplementary Table II-S5. Re- and Os data of the PLG section

Sample Name	Lithology	Depth	Age	Digestion liquid	Os conc	1SD	1SE	187Os/188Os$_m$	1SD	1SE	Re conc	1SD	1SE	187Re/188Os	1SD	1SE	187Os/188Os$_i$	1SD	1SE
		(mbsf)	(Ma)		(pg g-1)						(pg g-1)								
463_58-2_44-50	Limestone	510.94	113	In. aqua regia	42.22	0.4	0.05	0.686	0.010	0.0015	28.8	1.3	0.3	3.52	0.17	0.04	0.679	0.010	0.0015
463_59-1_54-56	Limestone	519.04	113	In. aqua regia	42.29	0.3	0.04	0.777	0.008	0.0012	845	28	6.3	104.3	4	0.8	0.580	0.010	0.0019
463_59-1_68-71	Limestone	519.18	113	In. aqua regia	15.50	0.17	0.03	0.683	0.012	0.0019	161.2	3	0.6	53.72	1.1	0.2	0.581	0.013	0.0019
463_59-2_96-98	Marlstone	520.96	113	In. aqua regia	16.20	0.16	0.02	0.654	0.012	0.0018	23.1	3	0.7	7.35	1.0	0.2	0.641	0.013	0.0019
463_59-2_116-118	Limestone	521.16	113	In. aqua regia	12.38	0.12	0.018	0.657	0.013	0.0019	20.1	1.6	0.4	8.35	0.7	0.15	0.641	0.013	0.0019
463_59-3_133-135	Limestone	522.83	113	In. aqua regia	23.43	0.16	0.02	0.738	0.012	0.0018	46.2	3	0.6	10.26	0.6	0.14	0.719	0.012	0.0018
463_60-1-18_20	Limestone	528.18	113	In. aqua regia	14.94	0.3	0.05	0.612	0.03	0.005	2.3	1.2	0.3	0.80	0.4	0.09	0.611	0.035	0.005
463_60-1_44-46	Limestone	528.44	113	In. aqua regia	33.02	0.19	0.03	0.577	0.009	0.0014	19.0	1.2	0.3	2.94	0.19	0.04	0.572	0.009	0.0014
463_60-1_73-75	Limestone	528.73	113	In. aqua regia	18.50	0.3	0.04	0.597	0.018	0.003	6.4	2	0.5	1.75	0.6	0.14	0.593	0.018	0.003
463_60-1_100-102	Limestone	529	113	In. aqua regia	20.56	0.4	0.05	0.596	0.03	0.004	6.5	3	0.6	1.62	0.6	0.14	0.593	0.029	0.004
463_60-1_110-115	Limestone	529.1	113	In. aqua regia	17.18	0.13	0.019	0.596	0.011	0.0016	4.0	1.1	0.2	1.19	0.3	0.07	0.594	0.011	0.0016
463_60-1_122-127	Limestone	529.22	113	In. aqua regia	18.87	0.15	0.02	0.608	0.009	0.0014	5.7	1.1	0.2	1.55	0.3	0.07	0.605	0.009	0.0014
463_60-1_133-138	Marlstone	529.33	113	In. aqua regia	17.08	0.2	0.03	0.625	0.02	0.003	10.5	2	0.5	3.16	0.7	0.16	0.619	0.020	0.003
463_60-1_138-141①	Marlstone	529.38	113	In. aqua regia	26.00	0.2	0.03	0.582	0.010	0.0015	8.1	1.1	0.2	1.60	0.2	0.05	0.579	0.010	0.0015
463_60-1_138-141②	Marlstone	529.41	113	In. aqua regia	31.73	0.14	0.02	0.544	0.005	0.0008	16.6	1.2	0.3	2.66	0.2	0.04	0.539	0.005	0.0008
463_60-2_6-8	Limestone	529.56	113	In. aqua regia	33.67	0.12	0.019	0.540	0.004	0.0007	10.6	2	0.6	1.59	0.4	0.08	0.537	0.004	0.0007
363_60-2_27-29	Marlstone	529.77	113	In. aqua regia	37.93	0.3	0.05	0.575	0.010	0.0015	24.8	3	0.7	3.34	0.4	0.09	0.569	0.010	0.0015
463_60-2_46-49	Limestone	529.96	113	In. aqua regia	30.65	0.16	0.02	0.579	0.005	0.0007	15.0	1.2	0.3	2.50	0.2	0.05	0.575	0.005	0.0007
463_60-2_82-85	Marlstone	530.32	113	In. aqua regia	21.34	0.4	0.06	0.586	0.03	0.005	6.4	1.4	0.3	1.54	0.3	0.08	0.583	0.031	0.005
463_60-2_100-103	Limestone	530.5	113	In. aqua regia	20.26	0.2	0.03	0.559	0.013	0.002	7.0	3	0.6	1.77	0.7	0.15	0.556	0.013	0.002
463_60-3_8-12	Marlstone	531.08	113	In. aqua regia	49.64	0.4	0.06	0.438	0.006	0.0010	25.8	1.7	0.4	2.61	0.18	0.04	0.433	0.006	0.0010
463_60-3_36-40	Limestone	531.36	113	In. aqua regia	22.50	0.2	0.03	0.567	0.011	0.0016	9.7	1.3	0.3	2.19	0.3	0.06	0.563	0.011	0.0016
463_60-3_58-59	Limestone	531.58	113	In. aqua regia	30.47	0.18	0.03	0.545	0.007	0.0010	13.3	3	0.6	2.21	0.5	0.10	0.541	0.007	0.0010
463_60-3_111-117	Marlstone	532.11	113	In. aqua regia	42.15	0.4	0.05	0.547	0.012	0.0018	23.3	1.4	0.3	2.81	0.17	0.04	0.541	0.012	0.0018
463_60-3_130-134	Limestone	532.3	113	In. aqua regia	41.27	0.2	0.03	0.554	0.007	0.0010	20.8	1.3	0.3	2.57	0.16	0.03	0.549	0.007	0.0010
463_60-4_30-32	Limestone	532.8	113	In. aqua regia	25.06	0.3	0.04	0.510	0.013	0.002	8.9	1.1	0.2	1.80	0.2	0.05	0.506	0.013	0.002
463_60-4_52-54	Limestone	533.02	113	In. aqua regia	21.62	0.13	0.02	0.516	0.007	0.0010	4.6	0.9	0.2	1.07	0.2	0.05	0.514	0.007	0.0010
463_60-4_90-93	Limestone	533.4	113	In. aqua regia	34.03	0.2	0.03	0.530	0.009	0.0013	10.6	0.8	0.19	1.58	0.13	0.03	0.527	0.009	0.0013
463_60-4_110-117	Limestone	533.6	113	In. aqua regia	32.87	0.17	0.03	0.525	0.007	0.0010	13.3	0.8	0.18	2.05	0.13	0.03	0.521	0.007	0.0010
463_61-1_12-15	Limestone	535.62	114	In. aqua regia	28.03	0.11	0.016	0.539	0.006	0.0010	9.6	0.8	0.19	1.74	0.15	0.03	0.536	0.006	0.0010
463_61-1_47-49	Marlstone	535.97	114	In. aqua regia	21.54	0.18	0.03	0.528	0.010	0.0015	15.6	1.5	0.3	3.66	0.4	0.08	0.521	0.010	0.0015
463_61-1_103-105	Marlstone	536.53	114	In. aqua regia	27.65	0.19	0.03	0.519	0.008	0.0013	8.0	1.2	0.3	1.47	0.2	0.05	0.516	0.008	0.0013
463_62-1_3-5	Limestone	537.53	114	In. aqua regia	38.20	0.2	0.03	0.496	0.006	0.0009	86.7	1.9	0.4	11.45	0.3	0.06	0.474	0.006	0.0009
463_62-1_47-49	Marlstone	537.97	114	In. aqua regia	47.73	0.4	0.06	0.521	0.011	0.0017	50.1	1.8	0.4	5.32	0.2	0.04	0.511	0.011	0.0017
463_62-1_114-116	Marlstone	538.64	114	In. aqua regia	38.61	0.15	0.02	0.522	0.004	0.0006	65.4	2	0.5	8.57	0.3	0.07	0.506	0.004	0.0006
463_62-2_32-35	Limestone	539.32	114	In. aqua regia	52.41	0.4	0.06	0.514	0.011	0.0017	29.6	1.4	0.3	2.86	0.14	0.03	0.508	0.011	0.0017
463_62-2_80-81	Marlstone	539.8	114	In. aqua regia	31.66	0.11	0.016	0.516	0.005	0.0008	15.4	1.4	0.3	2.46	0.2	0.05	0.511	0.005	0.0008
463_62-2_113-115	Marlstone	540.13	114	In. aqua regia	35.13	0.18	0.03	0.501	0.005	0.0008	27.0	1.3	0.3	3.89	0.19	0.04	0.494	0.005	0.0008
463_62-3_83-88	Limestone	541.33	114	In. aqua regia	49.52	0.3	0.04	0.487	0.006	0.0010	23.8	1.1	0.2	2.42	0.11	0.03	0.483	0.006	0.0010
463_62-3_111-113	Marlstone	541.61	114	In. aqua regia	34.73	0.3	0.04	0.501	0.008	0.0012	24.3	1.3	0.3	3.54	0.2	0.04	0.494	0.008	0.0012

Supplementary Table II-S6. Re- and Os data of the DSDP Site 463

Sample Name	Section	Depth	Na2O	MgO	Al2O3	SiO2	P2O5	K2O	CaO	TiO2	Cr2O3	MnO	Fe2O3	NiO	LOI
		(m/mbsf)	wt%	wt%	wt%	wt%	wt%	wt%	wt%	wt%	wt%	wt%	wt%	wt%	
PLG-9	PLG	0 m	0.27	1.40	6.91	34.44	0.06	1.78	27.53	0.25	0.01	0.18	2.49	0.01	24.21
PLG-8.5	PLG	0.5 m	0.22	1.60	7.72	35.86	0.06	2.14	25.47	0.28	0.01	0.16	3.08	0.01	22.77
PLG-8	PLG	1 m	0.22	1.63	7.78	36.96	0.06	2.17	24.75	0.29	0.01	0.17	2.95	0.01	22.35
PLG-7.5	PLG	1.5 m	0.24	1.91	8.55	37.54	0.05	2.33	23.36	0.34	0.01	0.15	3.37	0.01	21.57
PLG-7	PLG	2 m	0.12	1.01	4.13	23.22	0.05	1.02	36.78	0.14	0.00	0.23	1.37	0.00	31.24
PLG-6	PLG	3 m	0.12	1.04	4.63	26.09	0.05	1.16	34.60	0.15	0.01	0.22	1.27	0.00	29.79
PLG-5	PLG	4 m	0.17	1.10	4.94	27.18	0.06	1.18	33.82	0.15	0.01	0.21	1.18	0.00	29.23
PLG-4	PLG	5 m	0.11	0.87	3.33	21.09	0.04	0.60	38.81	0.09	0.00	0.25	0.99	0.00	32.79
PLG-2	PLG	7 m	0.10	0.79	3.23	24.50	0.05	0.74	37.03	0.09	0.00	0.21	1.04	0.00	31.42
PLG0	PLG	9 m	0.13	1.09	5.12	32.44	0.09	1.36	30.46	0.15	0.01	0.16	1.97	0.00	26.45
PLG1	PLG	10 m	0.08	0.80	3.11	21.02	0.06	0.69	39.22	0.10	0.00	0.20	0.89	0.00	33.02
PLG2	PLG	11 m	0.16	0.97	4.64	28.57	0.07	0.95	33.35	0.13	0.00	0.16	1.72	0.00	28.58
PLG4	PLG	13 m	0.12	1.06	5.19	29.29	0.13	1.28	31.95	0.16	0.01	0.18	2.14	0.00	27.68
PLG4.5	PLG	13.5 m	0.16	1.09	5.60	30.84	0.10	1.31	30.98	0.16	0.01	0.16	2.32	0.00	26.85
PLG5	PLG	14 m	0.14	1.23	6.42	34.70	0.08	1.59	27.46	0.20	0.01	0.18	2.89	0.00	24.30
PLG6	PLG	15 m	0.18	1.31	6.97	41.68	0.09	1.66	23.29	0.21	0.01	0.17	2.81	0.00	21.09
PLG6.5	PLG	15.5 m	0.24	1.86	9.91	51.85	0.09	2.53	14.33	0.44	0.02	0.11	3.46	0.01	14.49
PLG7.5	PLG	16.5 m	0.15	0.96	5.36	41.90	0.06	1.08	25.45	0.13	0.01	0.21	1.38	0.00	22.56
PLG10	PLG	19 m	0.18	1.45	7.95	48.23	0.10	1.85	18.37	0.21	0.01	0.15	3.22	0.01	17.35
PLG15.5	PLG	24.5 m	0.19	1.24	7.63	46.07	0.09	1.57	20.97	0.23	0.01	0.13	1.90	0.01	19.19
PLG17	PLG	26 m	0.22	1.64	9.36	48.62	0.09	1.93	17.67	0.26	0.01	0.11	2.32	0.01	16.87
463_60-4_90-93	Site 463	533.4 mbsf	0.21	0.57	1.70	18.10	0.08	0.05	42.28	0.24	0.00	0.02	0.99	0.00	34.88
463_60-4_110-117	Site 463	533.6 mbsf	0.11	0.45	1.38	23.65	0.06	0.03	39.63	0.17	0.00	0.03	0.74	0.00	33.17
463_61-1_12-15	Site 463	535.62 mbsf	0.07	0.29	0.82	18.49	0.06	0.04	43.32	0.09	0.00	0.03	0.36	0.00	35.73
463_61-1_103-105	Site 463	526.53 mbsf	0.00	0.36	1.06	17.92	0.04	0.00	43.52	0.10	0.00	0.03	0.50	0.00	35.75
463_62-2_113-115	Site 463	540.13 mbsf	0.15	0.43	1.36	12.64	0.05	0.06	45.91	0.07	0.00	0.03	0.47	0.00	37.89
463_62-3_83-88	Site 463	541.33 mbsf	0.15	0.48	1.71	17.40	0.06	0.05	43.00	0.06	0.00	0.03	0.55	0.00	35.60
463_62-3_111-113	Site 463	541.61 mbsf	0.13	0.33	1.20	20.56	0.05	0.06	42.15	0.04	0.00	0.02	0.37	0.00	34.67

Supplementary Table II-S7. Major elemental composition of sedimentary rock samples of the PLG section and the DSDP Site 463.

Interval	Depth at PLG (msl)	Age interval (Ma)	R_{ocean}	M_{ocean} (t)	F_{cont} (t/ky)	F_{Kerg} (t/ky)	Remarks
Steady state	1~12.5	~5	0.54	1.51×10^{4}	295.0	0	Steady state
After jacob level	~13.5	~0.5	0.47	1.41×10^{4}	239.7	0	Decrease in continental weathering
			0.47	1.85×10^{4}	295.0	191.0	Hydrothermal activities at the SKP
Extinction horizon	15.48	<0.1	0.40	1.32×10^{4}	191.1	0	Decrease in continental weathering
			0.40	2.39×10^{4}	295.0	493.4	Hydrothermal activities at the SKP
Extinction horizon to Kilian level			0.58	1.57×10^{4}	330.2	0	Increase in continental weathering
Lower Kilian level	16.88-17.03	~0.6	0.40	1.32×10^{4}	191.1	0	Decrease in continental weathering
			0.40	2.75×10^{4}	330.2	660.5	Hydrothermal activities at the SKP
Upper Kilian level	~17.24	~0.6	0.73	1.86×10^{4}	493.2	0	Increase in continental weathering
Upper than Kilian level	17.24-	~2	0.62	1.64×10^{4}	368.5	0	Increase in continental weathering

Supplementary Table II-S8. Parameters and the results of Os-box model calculation.

CHAPTER III

Long-term Aptian marine osmium isotopic record of Ontong Java Nui activity

This chapter is published at *Geology*

Abstract of Chapter III

The early to mid-Aptian was punctuated by episodic phases of organic-carbon burial in various oceanographic settings, which are possibly related to massive volcanism associated with the emplacement of the Ontong Java, Manihiki, and Hikurangi oceanic plateaus in the southwestern Pacific Ocean inferred to have formed a single plateau called Ontong Java Nui. Sedimentary osmium (Os) isotopic compositions are one of the best proxies for determining the timing of voluminous submarine volcanic episodes. However, available Os isotopic records during the interval are limited to a narrow interval in the earliest Aptian, which is insufficient for the reconstruction of long-term hydrothermal activity. I document the early to mid-Aptian Os isotopic record using pelagic Tethyan sediments deposited in the Poggio le Guaine (Umbria–Marche Basin, Italy) to precisely constrain the timing of massive volcanic episodes and to assess their impact on the marine environment. The new Os isotopic data reveal three shifts to unradiogenic values, two of which correspond to black shale horizons in the lower to mid-Aptian, namely the Wezel (herein named) and Fallot Levels. These Os isotopic excursions are ascribed to massive inputs of unradiogenic Os to the ocean through hydrothermal activity. Combining the new Os isotopic record with published data from the lowermost Aptian organic-rich interval in the Gorgo a Cerbara section of the Umbria-Marche Basin, it can be inferred that Ontong Java Nui volcanic eruptions persisted for ~5 m.y. during the early to mid-Aptian.

III-1. Introduction

Oceanic anoxic events (OAEs) are major perturbations of the global carbon cycle, accompanied by the deposition of organic-rich sediments in various oceanographic settings (Chapter I-2). The early to mid-Aptian (Early Cretaceous) was marked by episodic burial of organic-rich sediments in the Tethyan region (Coccioni et al., 1987, 2012; Herrle et al., 2004) (Fig. I-3), a gradual long-term decrease in the diversity of planktonic foraminifera (Coccioni, 2020), and a decline in the size of calcareous nannoplankton (Bottini and Faucher, 2020). The Selli Level, recognized not only in the Tethyan region but also in the Pacific Ocean (Fig. I-3), is one of the most studied Cretaceous organic-rich intervals and records the earliest Aptian OAE (OAE1a) (Coccioni et al., 1987; Price, 2003). In the Tethyan region, several minor organic-rich intervals occur above the Selli Level (Fig. I-3) (Herrle et al., 2004; Coccioni et al., 2012). However, their significance in the geologic record is unclear because they are observed only in the Tethys at present and are poorly studied.

Radiometric ages of Ontong Java Plateau (OJP, southwestern Pacific Ocean) basalts (125–119 Ma; Mahoney et al., 1993; Tejada et al., 2002) roughly correspond to the

depositional ages of the Selli Level (ca. 121–120 Ma; Malinverno et al., 2012), and massive volcanic episodes associated with the plateau emplacement have been ascribed as the trigger of the OAE1a and the associated marine biotic crises (e.g., Erba, 1994). Available geochemical data and radiometric ages of the Manihiki Plateau and the Hikurangi Plateau suggest that these plateaus, as well as the OJP, were part of a larger oceanic plateau, known as Ontong Java Nui (OJN) (Taylor, 2006; Chandler et al., 2012). As discussed in the Chapter I-4, marine Os isotopic ($^{187}Os/^{188}Os$) information recorded in the sedimentary rocks can be applied to identify episodic submarine volcanic events (Turgeon and Creaser, 2008; Tejada et al., 2009; Bottini et al., 2012; Du Vivier et al., 2014). Early Cretaceous marine Os isotopic records are, however, limited to a short interval from the latest Barremian to the earliest Aptian (Tejada et al., 2009; Bottini et al., 2012), too short to trace the major OJN volcanic pulses ranging from early to mid-Aptian (Taylor, 2006). To assess the links between massive eruptions forming OJN and environmental perturbations in the early to mid-Aptian, this study extends the marine Os isotopic record to the entire Aptian using pelagic sediments collected from the Poggio le Guaine section (43°32'29.06"N, 12°34'51.09"E) and core (43°32'42.72"N, 12°32'40.92"E) in the Umbria-Marche Basin (central Italy) of the western Tethys (Coccioni et al., 2012, Figs. III-1 and S1).

III-2. Materials

The sedimentary rock samples for Os and C isotopic analyses were collected from the Poggio le Guaine (PLG) section and the PLG core drilled nearby, located on the Monte Nerone ridge of the Umbria–Marche Basin in central Italy (Coccioni et al., 2012; Figs. III-1 and S1). The upper Barremian to lowermost Aptian interval belongs to the Maiolica Formation and consists of white limestone with cyclic intercalation of black shale layers (Fig. III-2) (Coccioni et al., 2012; Savian et al., 2016). The ~2 m-thick organic-rich Selli Level, which is the regional expression of OAE1a, occurs at the base of the Marne a Fucoidi Formation (0 m in Fig. III-2: Coccioni et al., 1987; Coccioni, 2020). Above the Selli Level, the main lithologies of the lower to mid-Aptian stage are greenish-gray mud/marlstone, reddish marlstone, and minor siliceous sediments. A 20 cm-thick black shale horizon occurs ~1 m above the Selli Level and a 6 cm-thick black shale horizon occurs ~10 m above the Selli Level (Figs. III-2 and S2). The lithology of the PLG core is comparable to that of nearby outcrops, namely the PLG (Coccioni et al., 2014) and Gorgo a Cerbara sections (Coccioni et al., 1987). I correlated the three sedimentary records with biostratigraphy, chemostratigraphy (Os and $\delta^{13}C_{carb}$), and lithological features. The sedimentary rock samples were collected from just above the Selli Level to ~11 m above

it in the PLG core (Coccioni et al., 2012). Sedimentary rock samples were also collected from the lowermost part of the PLG section that overlaps with the uppermost parts of the studied interval in the PLG core (Matsumoto et al., 2020). Since the black shales at ~3 and ~12 m of the composite depth scale were fractured during the drilling activity, these were not used for Os and C isotopic analyses. Instead, marlstone samples from just above and below the black shale horizons were used.

III-3. Methods

Cleaned samples were dried and powdered in an agate mill. After spiking, Re and Os in the hydrogenous fraction of the carbonate rocks were extracted using inverse aqua regia digestion. Abundances and isotopic compositions of Os were determined by negative thermal ionization-mass spectrometry (TRITON, Thermo Fisher Scientific, USA) at the Japan Agency for Marine-Earth Science and Technology (JAMSTEC, Japan). The Re abundances were determined by a quadrupole inductively coupled plasma-mass spectrometer (iCAP Qc, Thermo Fisher Scientific, USA) at JAMSTEC. The average procedural blank of Os was 0.5±0.3 pg and $^{187}Os/^{188}Os$ was 0.11±0.03. The average Re procedural blank was 4±2 pg. Initial $^{187}Os/^{188}Os$ values (Os_i) were calculated from the measured $^{187}Os/^{188}Os$ and $^{187}Re/^{188}Os$ values, the age-depth model of the sediments (Supplementary Table III-S1), and the ^{187}Re decay constant (1.666×10^{-11} yr^{-1}; Smoliar et al., 1996). The detailed measuring methods are described in Chapter II-4.3. A marlstone sample at 4.1 m showed an extremely whitish color and had an anomalous high Os_i (~1.35) value. Since these samples could have experienced different diagenesis or alteration compared to other samples, it was considered to be an outlier and discarded thereof (Fig. III-S3, Supplementary Table III-S1).

The stable carbon isotope ratio of carbonate ($\delta^{13}C_{carb}$) was determined using isotope ratio-mass spectrometry (Delta V plus, Thermo Fisher Scientific, USA), equipped with an automated carbonate reaction device (GasBench II, Thermo Fisher Scientific, USA), at the Atmosphere and Ocean Research Institute, University of Tokyo (Japan). All isotope values are reported using delta notation with respect to PeeDee Belemnite (PDB), based on an NBS-19 value of −2.20‰ for $\delta^{18}O$ and +1.95‰ for $\delta^{13}C$. External reproducibility was estimated from the repeated analysis of the NBS-19 standard within an analysis batch and the typical values are better than 0.05‰ and 0.08% for $\delta^{18}O$ and $\delta^{13}C$, respectively (1 SD) (Table SupplementaryIII-S2). Detailed analytical conditions are reported in Shirai et al. (2018).

Changes in the Os flux through hydrothermal activities were calculated using a simple box model based on Tejada et al. (2009). A detailed explanation of the box

modeling of Os is described in Chapter II-4.4.

I calculated the changes in the Sr flux through hydrothermal activities using a simple box model after Blättler et al. (2011). Like the box modeling of Os, the relationship of Sr flux can be described as:

$$\frac{dM_{ocean}}{dt} = F_{cont} + F_{hydr} + F_{diag} + F_{OJN} - F_{sed} \quad (\mathrm{III}-1)$$

$$\frac{d(M_{ocean}R_{ocean})}{dt} = F_{cont}R_{cont} + F_{hydr}R_{hydr} + F_{diag}R_{diag} + F_{OJN}R_{OJN} - F_{sed}R_{sed} \quad (\mathrm{III}-2)$$

$$\frac{dR_{ocean}}{dt} =$$

$$\frac{[F_{cont}(R_{cont}-R_{ocean})+F_{hydr}(R_{hydr}-R_{ocean})+F_{OJN}(R_{OJN}-R_{ocean})+F_{diag}(R_{diag}-R_{ocean})]}{M_{ocean}} \quad (\mathrm{III}-3)$$

where M, F, and R indicate the amount, flux, and isotopic ratio of Sr ($^{87}Sr/^{86}Sr$), and the subscripts 'ocean', 'cont', 'hydr', 'diag', 'OJN', and 'sed' represent the oceanic reservoir, continental input, hydrothermal input, diagenetic input, input from the OJN, and sedimentary output, respectively. I used M_{ocean}=1.05×10^{13} t, R_{cont},=0.7115, R_{hydr},=0.7033, R_{diag},=0.7084, F_{cont}=1.59×10^{9} t/kyr, F_{hydro}=1.62×10^{9} t/kyr, F_{diag}=0.30×10^{9} t/kyr (Palmer and Edmond, 1989; Blättler et al., 2011). In addition, I set R_{sed} and F_{sed} as R_{sed}=R_{ocean} and F_{sed}=M_{ocean}×3.33×10^{-4} t/kyr.

III-4. Results

The carbonate $\delta^{13}C$ ($\delta^{13}C_{carb}$) record of Poggio le Guaine core shows the highest values (4.7‰) just above the Selli Level, which is followed by a continuous decline to 3.1‰ toward the top of the studied interval in segment Ap10, at ~13 m on the composite depth scale (Figs. III-2 and S4; Supplementary Table III-S1). This trend is consistent with the $\delta^{13}C_{carb}$ records from the Gorgo a Cerbara section of the Umbria–Marche Basin and from the Vocontian Basin (southeastern France) (Herrle et al., 2004; Li et al., 2016). By integrating the new available $\delta^{13}C_{carb}$ data with those from the Poggio le Guaine and Gorgo a Cerbara sections (Coccioni et al., 2014; Li et al., 2016; Savian et al., 2016; Matsumoto et al., 2020), I constructed a composite $\delta^{13}C_{carb}$ record (Fig. III-2) in which 21 carbon isotopic segments (Ap1 to Al6) can be identified, following Menegatti et al. (1998) and Herrle et al. (2004). Os and Re concentrations vary from 18 to 153 pg g^{-1} and from 3 to 7100 pg g^{-1}, respectively (Fig. S3; Supplementary Table S2). Age-corrected $^{187}Os/^{188}Os$ (Os_i) values above the Selli Level range from 0.27 to 0.55, with distinct excursions to unradiogenic values at the levels of two black shales at ~3 m and ~12 m (Fig. III-2).

III-5. Discussions

The black shale horizon at 12 m on the composite depth scale near the boundary between the Ap9 and Ap10 carbon isotopic segments and within the *Globigerinelloides algerianus* planktonic foraminiferal zone can be correlated to the Fallot Level in the Serre Chaitieu section of the Vocontian Basin (Herrle et al., 2004). The black shale horizon located at ~3 m on the composite depth scale falls in the Ap7 carbon isotopic segment and the *Leupoldina cabri* planktonic foraminiferal zone, which cannot be correlated to any named early Aptian black shales. At the present state of knowledge, a similar and coeval horizon is recorded in the Piobbico and Cismon cores (Tornaghi et al., 1989; Erba et al., 1999) and Gargano Promontory (Luciani et al., 2001) in Italy, but on the basis of the available stratigraphic data, it could also be recognized in the Vocontian Basin (Kößler et al. 2001; Herrle et al., 2004; Heimhofer et al., 2006), in southern Spain (De Gea et al., 2003; Quijano et al., 2012: Aguado et al., 2014), in northeastern Tunisia (Elkhazri et al., 2013) and in central Turkey (Hu et al., 2012). Thus, I propose to name this undescribed black shale horizon as the "Wezel Level" with a help of Prof. Rodolfo Coccioni at The University of Urbino.

Upper Barremian Os_i values from the Umbria-Marche Basin fluctuate around 0.7 and gradually decrease to 0.4 at ~44 cm below the Selli Level (Fig. III-2; Tejada et al., 2009). Upward, Os_i values increase to 0.7 again before decreasing sharply to 0.2 in the lower part of the Selli Level (Fig. III-2; Tejada et al., 2009). Based on the correspondence between the sedimentary age of the Selli Level (ca. 120–121 Ma; Malinverno et al., 2012) and the radiometric age of the OJP (125–119 Ma; Mahoney et al., 1993; Tejada et al., 2002), these two Os isotopic declines likely mark massive volcanic episodes during OJP emplacement (Tejada et al., 2009). Os_i values increase to 0.5 above the Selli Level (~2.4 m in Fig. III-2), which may represent an interruption in submarine volcanic activity. However, Os_i values drop to 0.27 around the Wezel Level (Fig. III-2), recover back to 0.5, and show a small shift to unradiogenic values of 0.40 ~1 m above the Wezel Level. A similar shift to unradiogenic Os_i values of 0.36 is observed around the Fallot Level equivalent.

I estimated the unradiogenic Os input required to explain Osi variations using a box model, assuming constant continental weathering (cf. Tejada et al., 2009). The three Os isotopic excursions, at the Wezel Level, 1 m above the Wezel Level, and at the Fallot Level equivalent, would have required at least ~3100, ~850, and ~1150 t/k.y. increases in the unradiogenic Os input, respectively (Fig. III-3). These values are 7.5, 2.1, and 2.6 times higher than the steady hydrothermal Os input associated with oceanic plate

production of the uppermost Barremian (Fig. III-3). To explain these negative Os isotopic shifts solely by a decrease in the flux of continental Os, a reduction of ~60%–80% of continental-derived Os would be required. Given that continental weathering rates rose during the early Aptian (e.g., Blättler et al., 2011), this possibility is unlikely. The sedimentary ages of the early to mid-Aptian Os isotopic excursions (ca. 121–116.3 Ma; Malinverno et al., 2012) roughly correspond to the radiometric ages of the OJP (125–119 Ma; Mahoney et al., 1993; Tejada et al., 2002) and the Manihiki Plateau (126–117.9 Ma; Ingle et al., 2007; Timm et al., 2011), so the most probable source of unradiogenic Os is the hydrothermal activity associated with the emplacement of these plateaus. The weathering of the young basaltic plateau could be another candidate for the unradiogenic Os source. However, most of OJN was emplaced under submarine conditions, and subaerial weathering is considered to be unlikely to cause the large unradiogenic Os_i shift (e.g., Shipboard Scientific Party, 2001), despite evidence of subaerial eruption on OJN (Thordarson, 2004).

The most probable trigger for the black shale deposition is global warming promoted by the massive release of volcanic gases associated with the emplacement of OJN. Global warming could have enhanced the continental weathering supplying nutrients into the ocean and, in turn, stimulated the primary productivity that ultimately led to the local marine anoxia and the subsequent deposition of the Wezel and Fallot Levels. These levels are currently reported only in Tethyan regions, possibly because the depositional environment may have been susceptible to nutrient supply from riverine input and upwelling. The Sedimentary thickness of organic-rich interval and $\delta^{13}C_{carb}$ excursion at the Wezel (~20 cm and at most −1‰) and Fallot Levels (~6 cm and none) are smaller than at the Selli Level (~2 m and −2‰). The negative $\delta^{13}C$ excursion during OAE1a is ascribed to the thermogenic methane released from sill intrusion into marine organic-rich sediments (Adloff et al., 2021). Considering the smaller unradiogenic Os shifts at the Wezel and Fallot Levels (Fig. III-3), the perturbations of the carbon cycle at these horizons may have been limited compared to that at the Selli Level. At each of the Wezel Level and the Fallot Level equivalent, the initial decline in Osi occurs ~60 cm below the onset of deposition of black shale horizons, which corresponds to ~200 k.y. (Fig. III-3; Supplementary Table III-S1). A shorter time lag (~59 k.y.) between unradiogenic Osi shift and the onset of positive $\delta^{13}C_{carb}$ excursion (i.e., the potential organic-carbon burial) is observed during OAE2 (Jones et al., 2021). The time lag could represent the required time from the onset of the volcanic outgassing to the outbreak of oceanic anoxia. Smaller Os isotopic shifts than at OAE2 around the Wezel and Fallot Levels imply decreased volcanic eruptions that may have led to tempered environmental perturbations and longer time lags.

Above the Fallot Level equivalent, Osi shows stable values of ~0.55 to the end of Aptian (Matsumoto et al., 2020), lower than the latest Barremian pre-OAE1a values (~0.7) (Tejada et al., 2009), though estimated Barremian values have large variations (0.4–0.9) (Bottini et al., 2012). Because the oceanic crustal production rate during the Aptian is considered higher than that of the Barremian (Eldholm and Coffin, 2000), the intensified hydrothermal activity associated with plate production may have contributed to the low steady Os_i values. Another possibility is that small-magnitude but continuous volcanism after the main volcanic pulse at OJN released unradiogenic Os into the ocean. Indeed, the basaltic rocks at the northeastern plateau margin (Rapuhia Scarp) on the Hikurangi Plateau show younger ages (118–96 Ma; Hoernle et al., 2010) than the peak ages of the OJP and Manihiki Plateau, which may support this possibility.

Marine strontium isotopic ratios ($^{87}Sr/^{86}Sr$) represent the balance between radiogenic Sr input from continents and unradiogenic Sr input through hydrothermal activity. Although $^{87}Sr/^{86}Sr$ varies like Os_i, the residence time of Sr is much longer (~2.5 m.y.; Hodell et al., 1990) than that of Os (8–10 k.y.; Oxburgh, 2001), which makes the change in marine $^{87}Sr/^{86}Sr$ more gradual than that of Os_i. The global marine $^{87}Sr/^{86}Sr$ curve shows a marked decline toward unradiogenic values during the early Aptian (Fig. III-3; Bralower et al., 1997), which supports enhanced hydrothermal activity induced by the submarine volcanic episodes. Although their timing is concordant, the increase in the input of unradiogenic Os is more drastic (2.6–16 times higher) compared to that of Sr (~15% increase) owing to their different geochemical behaviors. The Os_i fluctuations continued for ~5 m.y. during the early to mid-Aptian, which could reflect a long-term submarine volcanic eruption at OJN. The Os isotopic fluctuations during the early to mid-Aptian correspond to stepwise declines in the planktonic foraminiferal diversity, the demise of nannoconids, and a decrease in the shell size of nannofossils at least in the Umbria-Marche Basin (Fig. III-2; Erba, 1994; Bottini and Faucher, 2020; Coccioni, 2020). Because calcareous organisms are strongly influenced by ocean acidification (Erba et al., 2010; Bottini and Faucher, 2020; Matsumoto et al., 2020), the biotic changes have been ascribed to at least local lowering of pH caused by the massive volcanic outgassing. After the three major Os isotopic declines, an increase in the heavily calcified planktonic foraminiferal species (Coccioni et al., 2014) and a blooming of nannoconids (*Nannoconus truitti* acme, Fig. III-2; Coccioni et al., 2014) are reported, suggesting a weakening of the acidified conditions caused by volcanic activity at OJN. These pieces of evidence imply that the volcanic episodes at OJN could have had an impact on marine ecosystems at least locally from the latest Barremian to the mid-Aptian, potentially through marine anoxia and acidification.

III-6. Conclusions

The new Os isotopic record from the Poggio le Guaine in the Umbria-Marche Basin provides evidence of several Os isotopic shifts to unradiogenic values around two black shale horizons, namely the Wezel Level and the Fallot Level equivalent in the lower to mid-Aptian. Considering the lack of large-scale subaerial exposure on OJN, the Os isotopic variations are attributed to massive inputs of unradiogenic Os through hydrothermal activity. Integrating the Os isotopic data with published data from the late Barremian to early Aptian of the Gorgo a Cerbara section, I infer that intensive hydrothermal activity continued for ~5 m.y. during the early to mid-Aptian and was associated with the deposition of three major organic-rich intervals in the Tethyan region (Selli Level, Wezel Level, and Fallot Level equivalent). Considering the consistency of radiometric ages of OJN with the sedimentary ages of the Os isotopic shifts, the most probable cause for these volcanic signals is submarine volcanic eruptions at OJN.

Figures of Chapter III

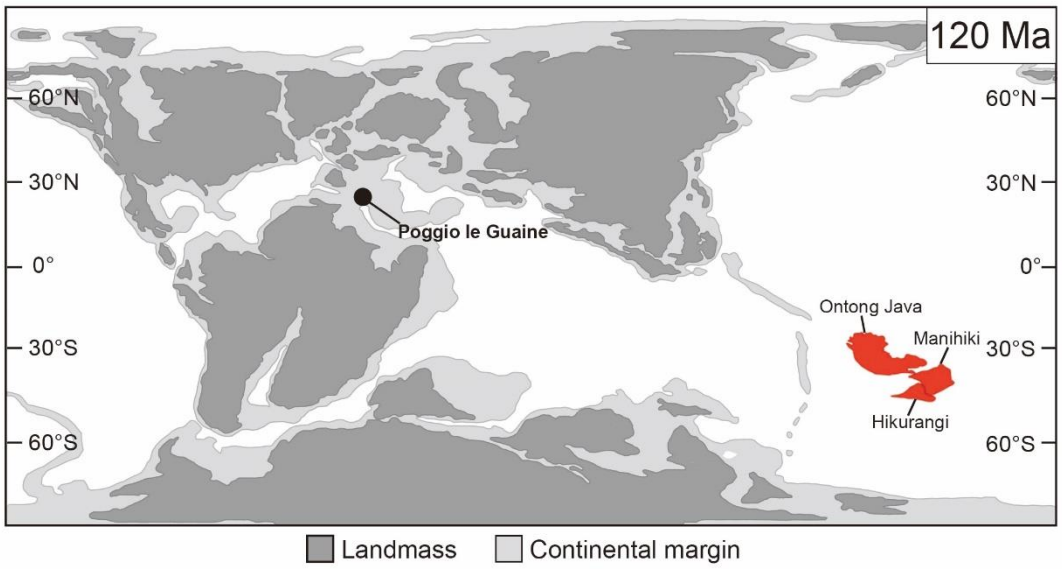

Figure III-1. Paleogeography at 120 Ma based on Chandler et al. (2012), showing the location of the studied Poggio le Guaine section (Umbria-Marche Basin, Italy).

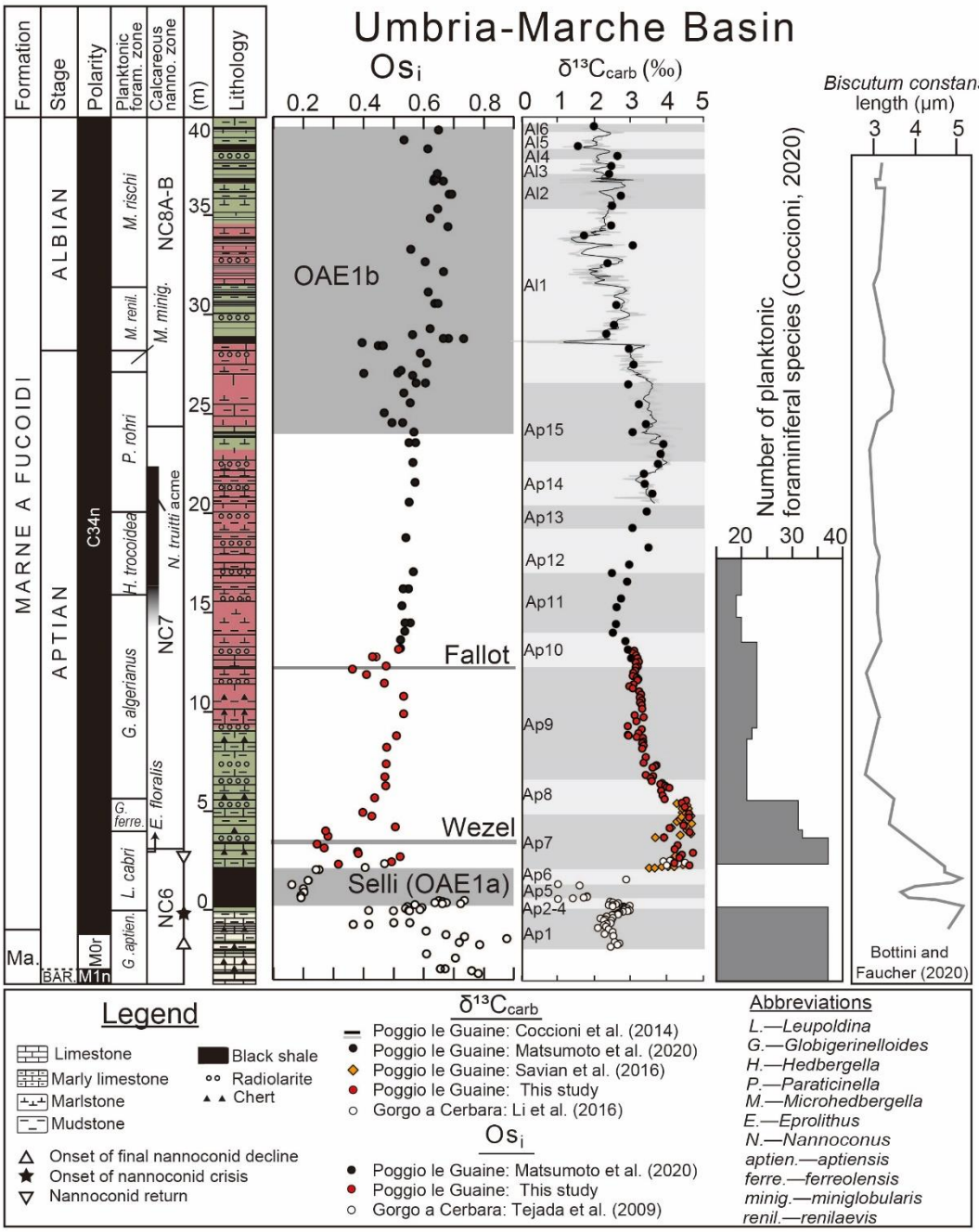
Umbria-Marche Basin
Formation
Stage
Polarity
Planktonic foram. zone
Calcareous nanno. zone
(m)
Lithology
MARNE A FUCOIDI
ALBIAN
APTIAN
Ma.
C34n
M0r
M1n
BAR.
M. rischi
M. renil.
M. minig.
P. rohri
H. trocoidea
G. algerianus
G. ferre.
E. floralis
L. cabri
G. aptien.
NC8A-B
NC7
NC6
N. truitti acme
Osi
0.2 0.4 0.6 0.8
δ13Ccarb (‰)
0 1 2 3 4 5
OAE1b
Fallot
Wezel
Selli (OAE1a)
Al6
Al5
Al4
Al3
Al2
Al1
Ap15
Ap14
Ap13
Ap12
Ap11
Ap10
Ap9
Ap8
Ap7
Ap6
Ap5
Ap2-4
Ap1
Number of planktonic foraminiferal species (Coccioni, 2020)
20 30 40
Biscutum constans length (μm)
3 4 5
Bottini and Faucher (2020)
Legend
Limestone
Marly limestone
Marlstone
Mudstone
Black shale
Radiolarite
Chert
Onset of final nannoconid decline
Onset of nannoconid crisis
Nannoconid return
δ13Ccarb
Poggio le Guaine: Coccioni et al. (2014)
Poggio le Guaine: Matsumoto et al. (2020)
Poggio le Guaine: Savian et al. (2016)
Poggio le Guaine: This study
Gorgo a Cerbara: Li et al. (2016)
Osi
Poggio le Guaine: Matsumoto et al. (2020)
Poggio le Guaine: This study
Gorgo a Cerbara: Tejada et al. (2009)
Abbreviations
L.—Leupoldina
G.—Globigerinelloides
H.—Hedbergella
P.—Paraticinella
M.—Microhedbergella
E.—Eprolithus
N.—Nannoconus
aptien.—aptiensis
ferre.—ferreolensis
minig.—miniglobularis
renil.—renilaevis

←Figure III-2. Late Barremian to early Albian $^{187}Os/^{188}Os$ (Os_i) and carbonate $\delta^{13}C$ ($\delta^{13}C_{carb}$) records in the Poggio le Guaine (PLG) section and core and the Gorgo a Cerbara section of the Umbria–Marche Basin (Italy): Chronostratigraphy is after Gale et al. (2020). Litho-, magneto-, and biostratigraphy are after Coccioni et al. (2012, 2014) and Coccioni (2020), and this study. Colors used in the lithological column are the schematic colors of the sedimentary rocks based on Coccioni et al. (2012). Os_i is from Tejada et al. (2009), Matsumoto et al. (2020), and this study. Gray horizontal bars in the Os_i plot represent the intervals of oceanic anoxia. $\delta^{13}C_{carb}$ is after Coccioni et al. (2014), Li et al. (2016), Savian et al. (2016), Matsumoto et al. (2020), and this study. Gray and black lines in $\delta^{13}C_{carb}$ plots represent the raw and smoothed curves of $\delta^{13}C_{carb}$ at the PLG record, respectively (Coccioni et al., 2014). The number of planktonic foraminiferal species at the Gorgo a Cerbara section is after Coccioni (2020). Variation of *Biscutum constans* size in the Cismon (southern Alps, Italy) and Piobbico (central Italy) cores is from Bottini and Faucher (2020). Ma.—Maiolica; BAR—Barremian; foram.—foraminiferal; nanno.—nannofossil; OAE—Oceanic Anoxic Event.

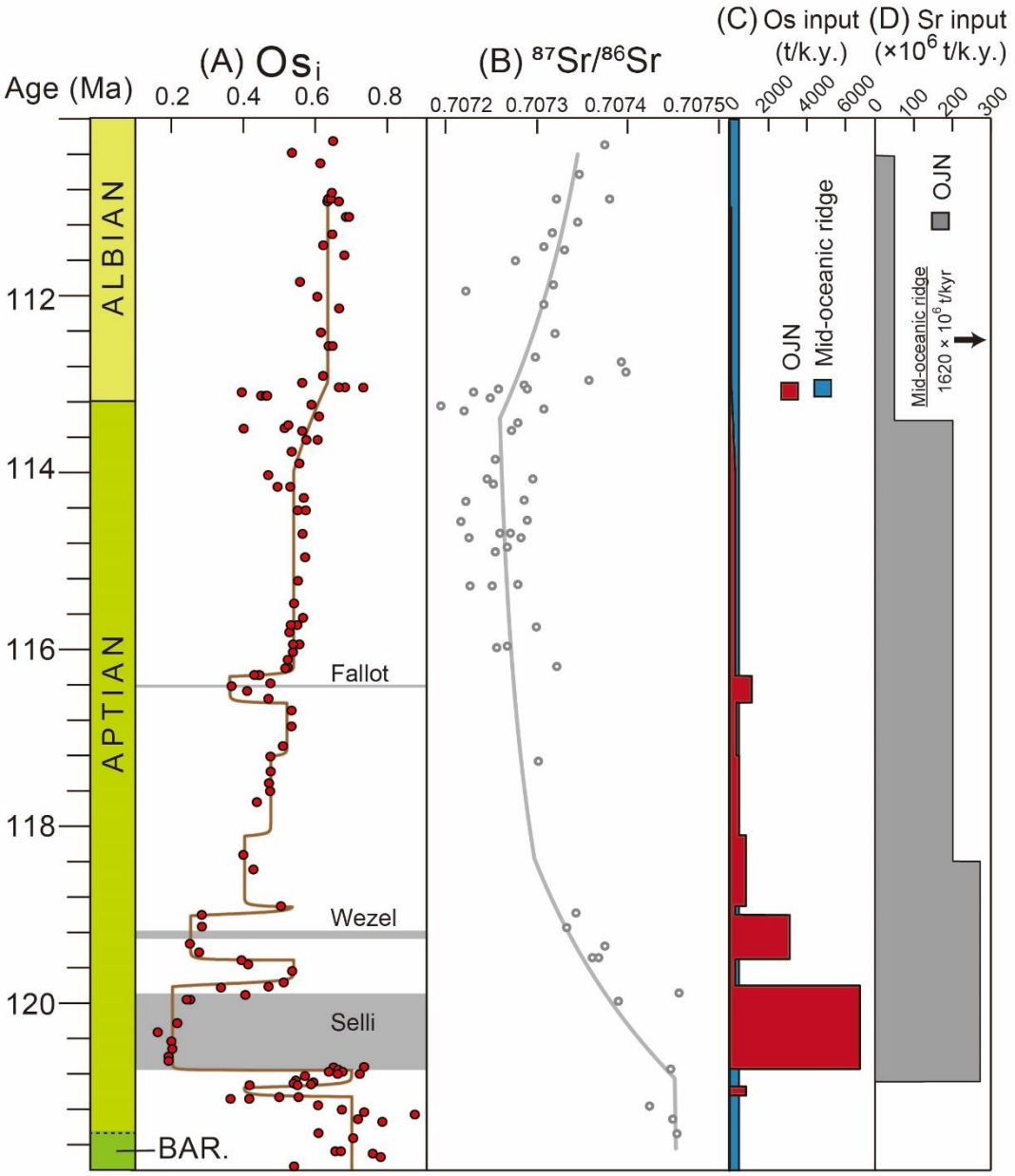

Figure III-3: (A) $^{187}Os/^{188}Os$ (Os_i) and (B) $^{87}Sr/^{86}Sr$ variations, and (C) unradiogenic Os and (D) unradiogenic Sr inputs from Ontong Java Nui volcanism: Solid lines in A and B represent the estimated Os_i and $^{87}Sr/^{86}Sr$ variations caused by the hydrothermal Os and Sr input described in C and D. Os_i is based on Tejada et al. (2009), Matsumoto et al. (2020), and this study. Gray horizontal bars in A represent the intervals of oceanic anoxia. $^{87}Sr/^{86}Sr$ data are from Bralower et al. (1997). Time scale is according to Gale et al. (2020) (Fig. III-S4 and Table III-S3). BAR.—Barremian; OJN—Ontong Java Nui.

Supplementary Figures of Chapter III

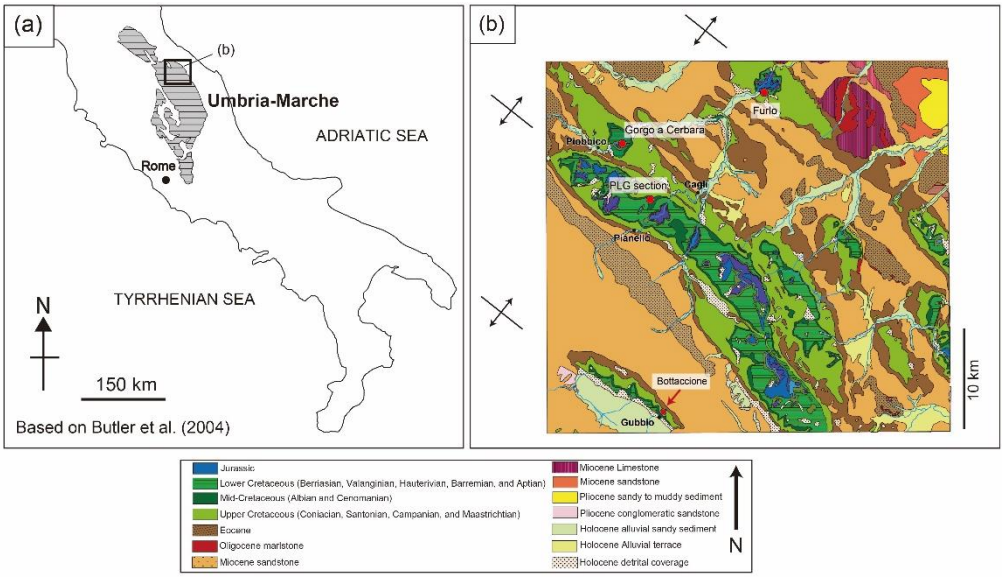

Figure III-S1. Geological map of Poggio le Guaine (PLG) revised from Matsumoto et al. (2020): PLG section is located at lat. 43°32’29.06” N, long. 12°34’51.09” E and the drilling site of the PLG core is located at lat. 43°32'42.72" N; long. 12°32'40.92" E. The location of the Gorgo a Cerbara section is also shown.

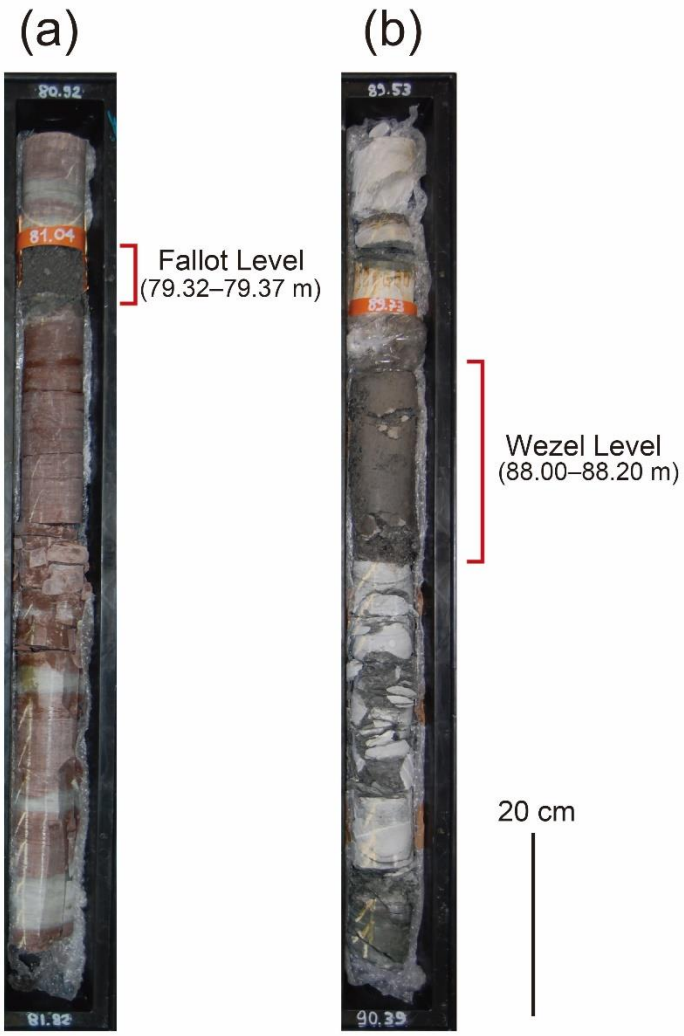

Figure III-S2: Core images of (a) Fallot Level and (b) Wezel Level in Poggio le Guaine core.

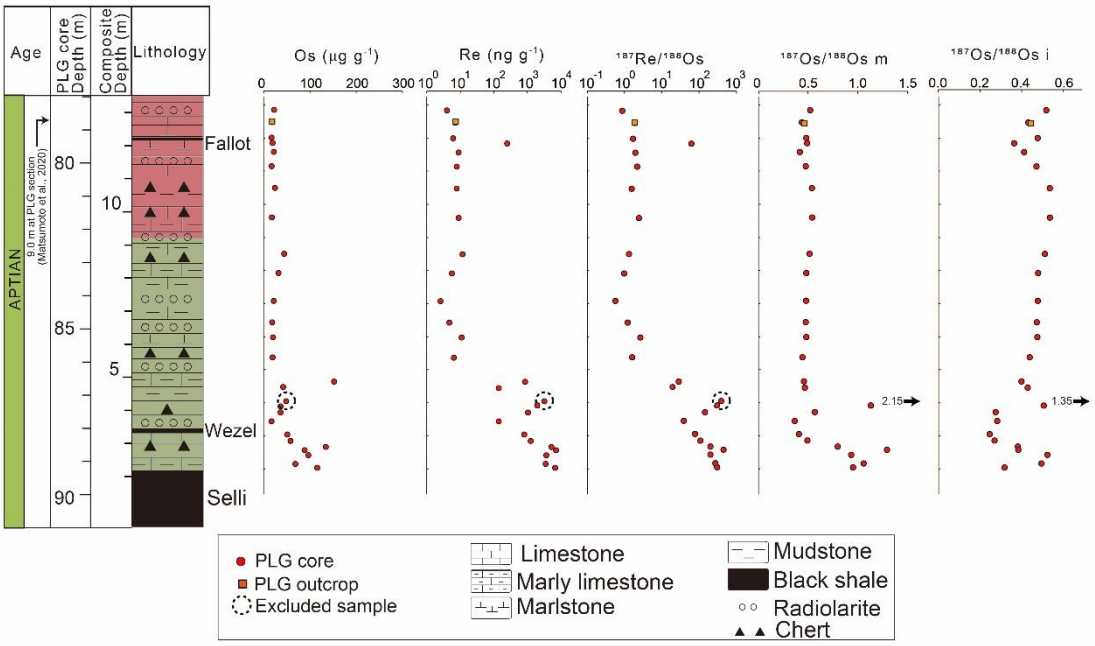

Figure III-S3. Os and Re data of sedimentary rock samples of PLG record.

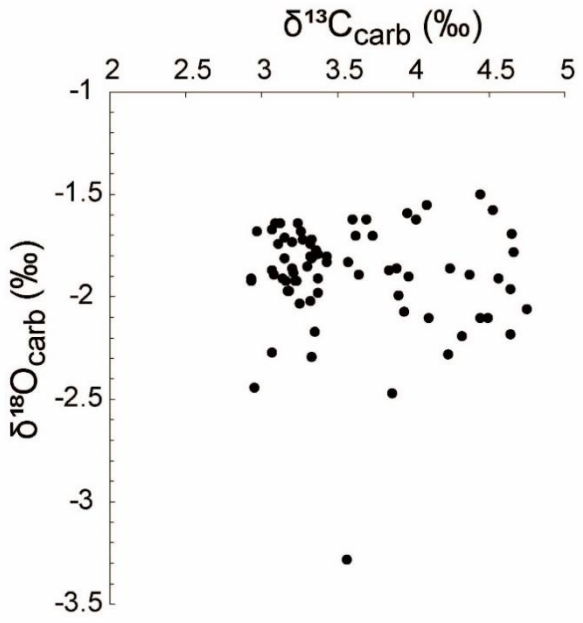

Figure III-S4: Cross plot of $\delta^{13}C_{carb}$ and $\delta^{18}O_{carb}$ of sedimentary rock samples of the Poggio le Guaine core.

Supplementary Tables of Chapter II

Sample Name	Lithology	δ^{13}C-PDB (‰)	δ^{18}O-PDB (‰)	δ^{13}C-1SD (‰)	δ^{18}O-1SD (‰)	Depth (Core) (m)	Depth (Composit) (m)
PLG-C 90.98	Marlstone	4.65	-1.69	0.09	0.05	89.20	2.34
PLG-C 90.85	Marlstone	4.23	-2.28	0.06	0.05	89.08	2.46
PLG-C 90.58	Mudstone	4.37	-1.89	0.06	0.05	88.82	2.72
PLG-C 90.42	Marlstone	4.44	-2.1	0.06	0.05	88.67	2.87
PLG-C 90.32	Mudstone	4.75	-2.06	0.06	0.05	88.57	2.97
PLG-C 90.13	Marlstone	4.24	-1.86	0.06	0.05	88.39	3.15
PLG-C 89.93	Marlstone	4.32	-2.19	0.06	0.05	88.19	3.35
PLG-C 89.53	Marlstone	3.94	-2.07	0.06	0.05	87.80	3.74
PLG-C 89.26	Marlstone	4.66	-1.78	0.06	0.05	87.53	4.01
PLG-C 89.06	Marlstone	4.1	-2.1	0.06	0.05	87.33	4.21
PLG-C 88.92	Marlstone	4.49	-2.1	0.06	0.05	87.19	4.35
PLG-C 88.52	Marlstone	4.64	-1.96	0.06	0.05	86.79	4.75
PLG-C 88.33	Mudstone	4.64	-2.18	0.06	0.05	86.60	4.94
PLG-C 87.99	Marlstone	4.53	-1.57	0.07	0.07	86.26	5.28
PLG-C 87.79	Marlstone	4.44	-1.5	0.08	0.05	86.06	5.48
PLG-C 87.67	Marlstone	4.56	-1.91	0.08	0.05	85.94	5.60
PLG-C 87.60	Mudstone	3.96	-1.59	0.08	0.05	85.87	5.67
PLG-C 87.41	Marlstone	3.9	-1.99	0.08	0.05	85.68	5.86
PLG-C 87.17	Marlstone	3.86	-2.47	0.08	0.05	85.44	6.10
PLG-C 87.03	Marlstone	4.09	-1.55	0.08	0.05	85.30	6.24
PLG-C 86.99	Marlstone	4.02	-1.62	0.08	0.05	85.26	6.28
PLG-C 86.92	Mudstone	3.97	-1.9	0.08	0.05	85.19	6.35
PLG-C 86.84	Marlstone	3.84	-1.87	0.08	0.05	85.11	6.43
PLG-C 86.79	Mudstone	3.89	-1.86	0.08	0.05	85.06	6.48
PLG-C 86.68	Marlstone	3.6	-1.62	0.08	0.05	84.95	6.59
PLG-C 86.54	Marlstone	3.57	-1.83	0.06	0.05	84.81	6.73
PLG-C 86.44	Marlstone	3.64	-1.89	0.06	0.05	84.71	6.83
PLG-C 86.38	Mudstone	3.43	-1.83	0.06	0.05	84.65	6.89
PLG-C 86.17	Marlstone	3.56	-3.28	0.06	0.05	84.44	7.10
PLG-C 86.01	Marlstone	3.62	-1.7	0.06	0.05	84.28	7.26
PLG-C 85.94	Mudstone	3.69	-1.62	0.06	0.05	84.21	7.33
PLG-C 85.89	Marlstone	3.73	-1.7	0.06	0.05	84.16	7.38
PLG-C 85.77	Mudstone	3.37	-1.79	0.06	0.05	84.04	7.50
PLG-C 85.48	Marlstone	3.43	-1.8	0.06	0.05	83.75	7.79
PLG-C 85.05	Mudstone	3.33	-2.29	0.06	0.05	83.32	8.22
PLG-C 84.90	Marlstone	3.37	-1.91	0.06	0.05	83.17	8.37
PLG-C 84.78	Marlstone	3.33	-1.72	0.08	0.05	83.05	8.49
PLG-C 84.70	Mudstone	3.36	-1.77	0.08	0.05	82.97	8.57
PLG-C 84.51	Marlstone	3.35	-2.17	0.08	0.05	82.78	8.76
PLG-C 84.40	Mudstone	2.95	-2.44	0.08	0.05	82.67	8.87
PLG-C 84.36	Mudstone	2.93	-1.92	0.08	0.05	82.63	8.91
PLG-C 84.27	Marlstone	3.23	-1.92	0.08	0.05	82.54	9.00
PLG-C 84.08	Marlstone	3.32	-2.02	0.08	0.05	82.35	9.19
PLG-C 83.92	Mudstone	2.93	-1.91	0.08	0.05	82.19	9.35
PLG-C 83.67	Marlstone	3.17	-1.97	0.08	0.05	81.94	9.60
PLG-C 83.47	Mudstone	3.37	-1.98	0.08	0.05	81.74	9.80
PLG-C 83.37	Marlstone	3.12	-1.64	0.08	0.05	81.64	9.90
PLG-C 83.05	Mudstone	3.33	-1.81	0.06	0.05	81.32	10.22
PLG-C 82.86	Mudstone	3.32	-1.74	0.06	0.05	81.13	10.41
PLG-C 82.73	Marlstone	3.27	-1.72	0.06	0.05	81.00	10.54
PLG-C 82.61	Marlstone	3.32	-1.8	0.06	0.05	80.88	10.66
PLG-C 82.48	Marlstone	3.26	-1.68	0.06	0.05	80.75	10.79
PLG-C 82.32	Marlstone	3.3	-1.85	0.06	0.05	80.59	10.95
PLG-C 82.15	Mudstone	3.25	-2.03	0.06	0.05	80.44	11.10
PLG-C 82.01	Mudstone	3.07	-2.27	0.06	0.05	80.28	11.26
PLG-C 81.91	Mudstone	2.97	-1.68	0.06	0.05	80.18	11.36
PLG-C 81.82	Mudstone	3.09	-1.64	0.06	0.05	80.09	11.45
PLG-C 81.61	Marlstone	3.2	-1.86	0.06	0.05	79.88	11.66
PLG-C 81.56	Marlstone	3.22	-1.92	0.06	0.05	79.83	11.71
PLG-C 81.47	Marlstone	3.18	-1.97	0.08	0.05	79.74	11.80
PLG-C 81.35	Marlstone	3.07	-1.87	0.08	0.05	79.66	11.88
PLG-C 81.23	Marlstone	3.08	-1.89	0.08	0.05	79.50	12.04
PLG-C 81.12	Marlstone	3.14	-1.91	0.08	0.05	79.39	12.15
PLG-C 80.96	Marlstone	3.15	-1.81	0.08	0.05	79.23	12.31
PLG-C 80.92	Marlstone	3.21	-1.88	0.08	0.05	79.19	12.35
PLG-C 80.71	Marlstone	3.15	-1.71	0.08	0.05	78.98	12.56
PLG-C 80.67	Marlstone	3.24	-1.64	0.08	0.05	78.94	12.60
PLG-C 80.49	Marlstone	3.2	-1.73	0.08	0.05	78.76	12.78
PLG-C 80.35	Marlstone	3.16	-1.92	0.08	0.05	78.62	12.92
PLG-C 80.23	Marlstone	3.07	-1.67	0.08	0.05	78.50	13.04
PLG-C 80.12	Marlstone	3.11	-1.74	0.08	0.05	78.39	13.15

Supplementary Table III-S1. Carbon and oxygen isotopic ratios of carbonate of the sedimentary rock samples of Poggio le Guaine.

Sample Name	Lithology	Os	1SD	$^{187}Os/^{188}Os$ m	1SD	Re	1SD	$^{187}Re/^{188}Os$	1SD	Osi	1SD	Age	Depth(core)	Depth(composit)	Comments
		(pg g^{-1})				(pg g^{-1})						(Ma)	(m)	(m)	
PLG core															
PLG-C 90.98	Marlstone	116.8	0.5	0.952	0.007	6.74.E+03	6.E+01	308	3	0.337	0.009	119.8	89.20	2.3	
PLG-C 90.85	Marlstone	69.5	0.4	1.058	0.010	3.52.E+03	9.E+01	274	7	0.512	0.019	119.8	89.08	2.5	
PLG-C 90.58	Mudstone	97.6	0.4	0.933	0.006	3.66.E+03	1.8.E+02	199	9.9	0.535	0.02	119.6	88.82	2.7	
PLG-C 90.42	Marlstone	89.6	0.6	1.295	0.013	7.14.E+03	1.7.E+02	442	11	0.413	0.03	119.6	88.67	2.9	
PLG-C 90.32	Mudstone	135.2	0.9	0.796	0.011	5.21.E+03	9.E+01	202	4	0.394	0.013	119.5	88.57	3.0	
PLG-C 90.13	Mudstone	59.1	0.4	0.490	0.007	1.257.E+03	1.8.E+01	107	2	0.276	0.008	119.4	88.39	3.2	
PLG-C 89.93	Marlstone	52.1	0.3	0.404	0.007	8.06.E+02	1.3.E+01	77.2	1.3	0.251	0.007	119.3	88.19	3.3	Just below Wezel Level
PLG-C 89.53	Marlstone	18.0	0.2	0.361	0.013	1.41.E+02	3.E+00	38.7	1.1	0.284	0.013	119.1	87.80	3.7	Just above Wezel Level
PLG-C 89.26	Marlstone	37.6	0.18	0.565	0.006	1.045.E+03	1.6.E+01	142	2	0.284	0.008	119.0	87.53	4.0	
PLG-C 89.06	Marlstone	36.5	0.30	1.131	0.019	2.046.E+03	1.9.E+01	305	4	0.504	0.02	118.9	87.33	4.2	
PLG-C 88.92	Marlstone	49.6	0.19	2.156	0.013	3.20.E+03	1.7.E+02	393	21	1.377	0.05	118.8	87.19	4.4	Excluded
PGL-C 88.52	Marlstone	43.1	0.39	0.464	0.010	1.54.E+02	1.0.E+01	17.9	1.2	0.427	0.011	118.5	86.79	4.8	
PLG-C 88.33	Mudstone	153.4	0.7	0.454	0.003	8.53.E+02	1.1.E+01	27.9	0.4	0.399	0.003	118.3	86.60	4.9	
PLG-C 87.60	Mudstone	20.4	0.2	0.440	0.011	6.E+00	1.0.E+01	2	3	0.437	0.012	117.7	85.87	5.7	
PLG-C 86.99	Marlstone	21.2	0.14	0.479	0.007	1.1.E+01	8.E+00	2.6	1.8	0.474	0.008	117.6	85.26	6.3	
PLG-C 86.54	Marlstone	19.5	0.18	0.473	0.009	4.7.E+00	1.1.E+00	1.2	0.3	0.471	0.009	117.5	84.81	6.7	
PLG-C 85.89	Marlstone	22.8	0.14	0.476	0.007	3.E+00	5.E+00	0.6	1.0	0.475	0.007	117.4	84.16	7.4	
PLG-C 85.05	Mudstone	35.0	0.3	0.477	0.013	6.E+00	2.E+00	0.9	0.3	0.475	0.010	117.2	83.32	8.2	
PLG-C 84.47	Mudstone	45.5	0.2	0.512	0.005	1.17.E+01	1.0.E+00	1.30	0.11	0.509	0.005	117.1	82.74	8.8	
PLG-C 83.37	Marlstone	18.6	0.1	0.538	0.007	8.9.E+00	1.0.E+00	2.4	0.3	0.533	0.007	116.9	81.64	9.9	
PLG-C 82.48	Marlstone	25.4	0.2	0.536	0.009	8.E+00	9.E+00	1.6	1.8	0.533	0.010	116.7	80.75	10.8	
PLG-C 81.82	Marlstone	18.3	0.10	0.473	0.007	7.8.E+00	1.0.E+00	2.2	0.3	0.469	0.007	116.6	80.09	11.4	
PLG-C 81.35	Marlstone	23.1	0.14	0.414	0.006	9.E+00	6.E+00	1.9	1.3	0.410	0.007	116.5	79.66	11.9	
PLG-C 81.12	Marlstone	20.3	0.12	0.487	0.007	2.50.E+02	5.E+00	62.1	1.4	0.366	0.008	116.4	79.39	12.1	Just below Fallot Level
PLG-C 80.96	Marlstone	18.1	0.10	0.478	0.007	6.1.E+00	1.2.E+00	1.7	0.3	0.475	0.007	116.4	79.23	12.3	Just above Fallot Level
PLG-C 80.49	Marlstone	18.9	0.14	0.433	0.008	7.1.E+00	1.3.E+00	1.9	0.4	0.430	0.008	116.3	78.76	12.8	
PLG-C 80.12	Marlstone	23.6	0.2	0.518	0.015	4.E+00	6.E+00	0.9	1.2	0.516	0.015	116.2	78.39	13.1	
PLG section													Depth (outcrop)		
PLG-9	Marlstone	22	0.16	0.448	0.009	7.8.E+00	1.3.E+00	1.8	0.29	0.445	0.009	116.3	9 m	12.5	

Supplementary Table III-S2. Os and Re isotopic data of the sedimentary rock samples of Poggio le Guaine.

Horizons	Age (Ma)	Depth (m)
LO *M. renilaevis*	113.2	28.2
HO *G. algerianus*	116.9	15.0
LO *G. algerianus*	118.3	5.6
HO *L. cabri*	118.6	4.4
LO *L. cabri*	120.5	0.2
Top of CM0r	121.0	-1.0
Base of CM0r	121.4	-2.8

Note1. G.=Globigerinelloides, L.=Leupoldina, P.=Paraticinella, M.=Microhedbergella,
Note2. Age is based on Gale et al. (2020)
Note3. Depth is based on Coccioni (2020), and Matsumoto et al. (2020).

Supplementary Table III-S3. Age model of Poggio le Guaine.

CHAPTER IV

Re-examination of the OAE1a interval in the pelagic deep-sea chert (Goshikinohama chert) from Japanese accretionary complex based on Os isotopic record, and new insight into the redox condition of deep-sea Pacific Basin

Abstract of Chapter IV

The early Aptian oceanic anoxic event (OAE) 1a is one of the largest OAEs in the Cretaceous and the organic-rich sediments have been reported at various sedimentation depths (up to ~3000 m below sea level) worldwide. Since the sedimentation age of organic-rich interval corresponds to the radiometric ages of Ontong Java Nui basalts, their causal linkage has been debated. Although the OAE1a interval in the Tethyan sedimentary records has been intensively studied, the exact extent of oceanic anoxia in the Pacific has yet to be constrained because of the lack of the well-dated deep-sea Pacific sedimentary sequence. Goshikinohama bedded chert is one of the Pacific pelagic sedimentary sequences deposited at depths deeper than carbonate compensation depth (~4000 m) and covers the time interval from Valanginian to Cenomanian. However, the stratigraphic level equivalent to OAE1a in the Goshikinohama bedded chert determined in the previous studies have slight uncertainties due to the low-resolution radiolarian biostratigraphy and carbon isotopic data. Here, to further constrain the exact OAE1a interval, I present $^{187}Os/^{188}Os$ record of the sedimentary sequence of the Goshikinohama bedded chert and correlate it to other well-studied Tethyan and Pacific sedimentary sequences. Subsequently, I discussed the changes in the redox condition of the deep-sea Pacific basin during OAE1a. $^{187}Os/^{188}Os$ of the Goshikinohama bedded chert showed a sharp unradiogenic shift that can be correlated to the other sites representing OAE1a. Major lithology of the Goshikinohama bedded chert is red bedded chert with an extremely low concentration of total organic carbon (TOC) event during the OAE1a interval, implying the persistent oxic bottom water condition at the deep-sea Pacific basin. However, two thin purple chert beds during OAE1a are characterized by the slight enrichment of redox-sensitive elements (e.g., V, Cr, and U), suggesting the temporary reducing and acidified condition during OAE1a. Since the two purple beds are accompanied by the especially unradiogenic Os isotopic values, the especially intensive volcanic events at the OJN could have occurred twice during OAE1a which could have resulted in the strongly reducing and acidified oceanic conditions extending to the deep-sea Pacific Basin.

IV-1. Introduction

The earliest Aptian oceanic anoxic event (OAE) 1a is one of the largest OAEs in the Cretaceous (Chapter 1-3). Thick organic-rich interval has been reported not only from the Tethyan region (e.g., Coccioni et al., 1987) but also shallow carbonate sequence on the oceanic plateaus at the Pacific Ocean (Fig. I-3) (Schlanger and Jenkyns, 1976; Price, 2003). Since these layers are characterized by the lack of bioturbations and the high total organic carbon content (TOC) (e.g., Price, 2003; Li et al., 2016), the reducing condition

could have prevailed in various oceanographic settings (coastal and pelagic environment of Tethys and Pacific Oceans). Radiometric ages of Ontong Java, Manihiki, and Hikurangi Plateaus in the Pacific Ocean, which once formed a single large oceanic plateau called Ontong Java Nui (OJN), (129–118 Ma; Mahoney et al., 1993; Tejada et al., 2002; Taylor, 2006; Chandler et al., 2012; Olierook et al., 2019), roughly correspond to the depositional ages of the OAE1a (~121–120 Ma: Gale et al., 2020). Thus, the massive volcanic events associated with the formation of OJN are considered as the triggering factors of OAE1a (Chapter III). The proposed triggering mechanism of OAE is as follows. The greenhouse gases released from the OJN volcanism caused global warming and following enhanced continental weathering. Nutrients (e.g., phosphorous) were supplied into the ocean which stimulated the primary production. As the result, the decomposition of organic matter consumed dissolved oxygen and finally led to the thickening of the oxygen minimum zone (OMZ) up to ~3000 m below sea level (e.g., Schlanger and Jenkyns, 1976). Indeed, model calculations revealed that (1) the ocean stagnation, (2) lower oxygen solubility, (3) increase in the riverine phosphorous flux caused by the global warming can cause the decrease in the oxygen concentration in seawater and, especially, the last factor is the most critical (e.g., Ozaki et al., 2011, 2013). In their modeling, the most pronounced oxygen-depleted condition could have occurred between 200–3000 mbsf (Ozaki et al., 2011). In addition to these effects, the trace metal input through a hydrothermal activity could have contributed to the increase in primary productivity (Leckie et al., 2002; Erba et al., 2015). The volcanic gases released from the OJN volcanism also caused the ocean acidification and the shallowing of lysocline and carbonate compensation depth (CCD) (Erba et al., 2010), which could have caused the biotic crises of marine calcareous planktons (calcareous nannofossils and planktonic foraminifera) (e.g., Erba, 1994; Matsumoto et al., 2021). However, most studies on OAE1a are limited to the shallow marine carbonate sequence, especially in the Tethyan region. On the other hand, the knowledge about the redox condition in the Pacific region, which occupied a large portion of the ocean floor, is limited. For better constraints of the nutrient input, increase in the temperature, and pCO_2 during OAE1a, the comprehension of the precise extent of oceanic anoxia at the Pacific regions is essential.

Goshikinohama bedded chert is the Cretaceous pelagic deep-sea sedimentary sequence exposed at the Yokonami Peninsula, Kochi-Prefecture, Shikoku, Japan (Okamoto et al., 1991). Since the sedimentary sequence was deposited under the CCD, it could provide a rare opportunity to examine the redox condition at the deep-sea Pacific basin (Fig. IV-1). However, due to the low-resolution radioralian biostratigraphy and carbon isotopic variations of organic matter ($\delta^{13}C_{org}$) in the Goshikinohama bedded chert,

there remain slight uncertainties in constraining the OAE1a interval (Fig. IV-2) (Ihoriya et al., 2009; Kuroda et al., 2015).

Recently, the osmium isotope ratio ($^{187}Os/^{188}Os$) of the sedimentary record has attracted attention as a useful chemostratigraphy. The marine Os isotopic values are homogeneous in the ocean and vary with age depending on the balance of the three major Os sources (continental material, mantle, and extraterrestrial material). Thus, paleo-marine Os isotopic variations recorded in the sedimentary sequence can be used for the stratigraphic correlation (see Chapter I-4).

Here, I reconstructed the Os isotopic variation of the late Barremian to early Aptian part of the Goshikinohama bedded chert to constrain the exact stratigraphic interval corresponding to OAE1a. In addition, combining the new Os isotopic data with the lithological and geochemical features revealed in the previous studies, I discussed the detailed paleo-redox variation in the Pacific deep-sea basin during OAE1a.

IV-2. Geological setting of the Goshikinohama bedded chert and stratigraphic comparison with other sites

Sedimentary rock samples are collected from the Goshikinohama bedded chert located in the Shimanto accretionary belt exposed at the Yokonami Peninsula, Kochi Prefecture, Shikoku, Japan (Okamura et al., 1991). The ~200 m lithological sequences are composed of pillow lava, chert, varicolored shale, greenstone and divided into three blocks (Okamura et al., 1991). The sampling site is the southernmost part of the Goshikinohama chert blocks which consists of an alternation of reddish chert and shale with characteristic purple chert and shale at ~6.1 and ~4.8 m of stratigraphic depth. Since the sedimentary sequence contains abundant radiolaria, and lacks coarse siliciclastic material and $CaCO_3$, the section is considered deposited at pelagic deep-seafloor under the CCD. Based on the compilations of paleo-depths of calcareous and non-calcareous sediments in the Pacific DSDP cores, the paleo-CCD at Pacific regions during the Cretaceous is ~4000 m (Van Andel, 1975). Thus, the Goshikinohama bedded chert could have been deposited below 4000 m. Paleo-magnetographic studies on the basaltic rock beside the chert sequence have suggested that the sedimentary sequence was once located at a low latitude of the Pacific Ocean (Kodama et al., 1983). Several paleontological and carbon isotopic studies have proposed that the southern part of the Goshikinohama bedded chert covers the early Aptian OAE1a (Ihoriya et al., 2009; Kuroda et al., 2015). Ihoriya et al (2009) and Kuroda et al. (2015) reported many radioralian species from the Goshikinohama bedded chert. However, there are no geological ages that can conformably explain all of the occurrences of these species. Thus, we excluded the

conferred species for the determination of the sedimentary ages of the Goshikinohama bedded chert. In addition, Ihoriya et al. (2009) reported high abundances of species belonging into the radioralian genus *Thanarla* from the Goshikinohama bedded chert and used them for the stratigraphic correlations. *Thanarla brouweri*, which occurs from upper Barremian to early Albian in the Tethyan region (U.A.1–11: O'Dogherty et al., 1994), was reported throughout the section (Ihoriya et al., 2009). *Thanarla lacrimula* (upper Barremian to mid-Aptian, U.A.1–6: O'Dogherty et al., 1994) occurs from ~7.5 to 5.7 m, *Thanarla pacifica* (upper Barremian to mid-Aptian, U.A.1–6: O'Dogherty et al., 1994) occurs from ~10.1 to 4.4 m, and *Thanarla pseudodecora* (upper Barremian to mid-Aptian, U.A.1–4: O'Dogherty et al., 1994) occurs from ~6.3 to 4.4 m at the Goshikinohama bedded chert (Fig. IV-2) (Ihoriya et al., 2009). Combining these radiolarian data, I concluded that the stratigraphic interval from 10.0 to 4.4 m of the studied section falls in the U.A. 1–4 (the late Barremina to the early Aptian) and stratigraphic interval 4.4 to 0.0 m correspond to U.A.1–10 (upper Barremian to lower Albian) (Fig. IV-2). The Selli Level is located in the U.A.1–2 (O'Dogherty et al., 1994), but it is difficult to constrain the stratigraphic interval corresponding to the Selli Level in the Goshikinohama bedded chert solely by the radiolarian biostratigraphy. Ihoriya et al. (2009) and Kuroda et al. (2015) tried to further constrain the stratigraphic interval of OAE1a using $\delta^{13}C_{org}$. However, the fluctuations of $\delta^{13}C_{org}$ data are very large and the $\delta^{13}C_{org}$ values of these two papers are inconsistent (Fig. IV-2). Considering the extremely low TOC (<0.03%) (Ihoriya et al., 2009; Kuroda et al., 2015), contamination or the heterogeneity in the sedimentary rocks could have contributed to the large fluctuations and their inconsistency.

During OAE1a, most of the Pacific and Tethyan sections show an increase in the TOC (e.g., Li et al., 2016; Price, 2003). In the Pacific region, pronounced organic-rich sediments have been observed at DSDP Site 317 (>200 m of paleo depth: Schlanger et al., 1976), DSDP Site 463 (sedimentation depth is unknown: Price et al., 2003), ODP Site 866 (a few m of paleo-depth: Sager et al., 1993; Arnaud et al., 1995), ODP Site 1207 (~1300 m of paleo depth: Bralower et al., 2002), ODP Site 1213 (~2800 m of paleo depth: Bralower et al., 2002), and Calera Limestone (sedimentation depth is unknown: Robinson, S.A. et al., 2008) during OAE1a (Figs. IV-1 and 3). Although no TOC data are available at DSDP Site 167 (~400 m of paleodepth: Winterer, 1973), dark laminated sediments have been observed during the earliest Aptian. However, since the sedimentary sequence consists of the red bedded chert and lacks the anoxic signature, Ihoriya et al. (2009) concluded that the anoxic condition did not reach the Pacific deep-seafloor during OAE1a.

IV-3. Methods

Sedimentary rock samples were crushed into small pieces and washed ultrasonically in deionized water. After being heated to dryness, rock fragments without quartz veins were carefully picked up under microscopic observation. After ultrasonic cleaning with deionized water again, the selected rock fragments were powdered in an aluminum rod mill. After spiking with ^{190}Os- and ^{185}Re-rich solutions, Re and Os of chert and shales were extracted with the inverse aqua regia digestion method. Os abundances and isotopic compositions were determined by negative thermal ionization-mass spectrometry (N-TIMS) (TRITON, Thermo Fisher Scientific, USA) at the Japan Agency for Marine-Earth Science and Technology (JAMSTEC, Japan). The abundances of Re were determined by 1) a quadrupole inductively coupled plasma-mass spectrometer (iCAP Qc, Thermo Fisher Scientific, USA) and 2) TIMS (TRITON, Thermo Fisher Scientific, USA) at JAMSTEC. Initial ^{187}Os/^{188}Os values (^{187}Os/^{188}Os$_i$) were calculated from the measured ^{187}Os/^{188}Os and ^{187}Re/^{188}Os values using the sedimentation age (120 Ma) and the ^{187}Re decay constant (1.666×10^{-11} yr^{-1}; Smoliar et al., 1996). The average procedural blank of Os and Re abundances were 1.9±0.7 pg and 26±11 pg and ^{187}Os/^{188}Os was 0.18±0.04. The detailed method is described in Kuroda et al. (2010) and Chapter II-4.3.

IV-4. Results

Os and Re concentration of the studied section ranges from 0.3 to 12 pg g^{-1} and 0.5 to 200 pg g^{-1} (Supplementary Table IV-S1). Measured values of osmium isotopic values (^{187}Os/^{188}Os$_m$) range from 0.14 to 0.87 and initial osmium isotopic values (^{187}Os/^{188}Os$_i$) range from 0.16 to 0.54 (Supplementary Table IV-S1). The ^{187}Os/^{188}Os$_i$ of the lowermost part of the section takes relatively unradiogenic values around 0.3. Then the ^{187}Os/^{188}Os$_i$ showed a radiogenic shift to 0.4–0.5 at 7–8 m (Fig. IV-2). The ^{187}Os/^{188}Os$_i$ showed the sudden drop at 6.5 m and took especially unradiogenic values (0.16–0.19) at ~6.3 and 4.9m, which corresponds to the characteristic purple chert beds. After ^{187}Os/^{188}Os$_i$ showed a temporal radiogenic shift at 4 m, ^{187}Os/^{188}Os$_i$ shows another radiogenic shift to ~0.17. ^{187}Os/^{188}Os$_i$ showed the radiogenic shift to 0.37 at the top of the section.

IV-5. Discussions

IV-5.1. Stratigraphic correlation of the Goshikinohama bedded chert with other Tethyan and Pacific sections.

The ^{187}Os/^{188}Os$_i$ data show a large unradiogenic shift from ~0.4 to 0.15 at ~6.5 m (Fig. IV-2). Based on the radiolarian biostratigraphy, this unradiogenic Os isotopic shift occurs during the late Barremian to early Aptian. Given that a similar sharp unradiogenic

Os isotopic shift has been reported from the early Aptian OAE1a interval in Tethyan and Pacific record (Fig. IV-4: Tejada et al., 2009; Bottini et al., 2012; Percival et al., 2021), I consider that the unradiogenic shift of $^{187}Os/^{188}Os_i$ at 6.5 m most likely represents to the onset of OAE1a. The unradiogenic Os isotopic shift is interpreted as the massive input of unradiogenic Os through hydrothermal activity associated with the formation of the OJN (Tejada et al., 2009; Bottini et al., 2012). $^{187}Os/^{188}Os_i$ values took two especially unradiogenic values at 6.3 and 4.9 m (Figs. IV-2 and 4). Similar Os isotopic features can be observed in Cismon core, DSDP Site 463, and Cau cores during OAE1a (Fig. IV-4) (Bottini et al., 2012; Martínez-Rodríguez et al., 2021). The two especially unradiogenic shifts of the $^{187}Os/^{188}Os_i$ values are not evident at the Gorgo a Cerbara section and PLG record, which may be ascribed to the low data density in the upper part of the Selli Level or regional heterogeneity of Os isotopic composition. The two unradiogenic Os isotopic shifts during OAE1a imply that especially enhanced volcanic events and associated hydrothermal activity occurred twice during the main phase of OJN volcanism.

The $^{187}Os/^{188}Os_i$ values show a temporal radiogenic shift at ~4 m in the Goshikinohama bedded chert which likely marks the end of OAE1a reported in the Tethyan region (Tejada et al., 2009; Matsumoto et al., 2021a). $^{187}Os/^{188}Os_i$ values show another unradiogenic shift at ~1–3 m in the Goshikinohama bedded chert. In the Tethyan region, another unradiogenic Os isotopic shift was reported around the Wezel Level which is located just above the Selli Level (Matsumoto et al., 2021a). Therefore, I propose to correlate the unradiogenic Os isotopic shift around 1–3 m to the Wezel Level (Fig. IV-4). Throughout the section, $^{187}Os/^{188}Os_i$ values of the Goshikinohama bedded chert show less radiogenic values than the Os isotopic ratio reported in other sections (Fig. IV-4). The local heterogeneity of Os isotopic composition in the deep-sea Pacific basin is a candidate for less radiogenic Os isotopic values at the Goshikinohama bedded chert. However, considering the very small Os isotopic variations in the water column in the present ocean (Levasseur et al., 1998; Woodhouse et al., 1999), this possibility is unlikely. Also, the contamination of Os contained in clay minerals may explain less radiogenic Os isotopic values at the Goshikinohama bedded chert. However, since there are no meaningful correlations between the Os isotopic data and Al concentrations presented in Kuroda et al. (2015), contamination of Os in the clay minerals cannot fully explain the differences in Os isotopic variations. Owing to the slow sedimentation rate and low Os abundance, the pelagic chert could be susceptible to the input of extraterrestrial materials with extremely unradiogenic values (~0.12) (Ravizza and McMurtry, 1993). Thus, the relatively large fluctuations and unradiogenic values of Os isotopic ratios at the Goshikinohama bedded chert can be ascribed to the influence of the relative contribution

of cosmic dust.

Based on the Os isotopic variations, I concluded that OAE1a is located at ~7–4 m in the studied section (Fig. IV-4). However, I acknowledge that the Os isotopic variation of the Goshikinohama bedded chert is not completely consistent with the contemporaneous Os isotopic record obtained from other sections. Indeed, Kuroda et al. (2015) pointed out the possibility of the secondary alteration of the geochemical composition of the Goshikinohama-bedded chert during the accretion to Japan. Besides, due to the very low Os concentrations of pelagic bedded chert sequence, it is still uncertain whether pelagic bedded chert sequences are reliable as the recorder of hydrogenous Os isotopic information. Furthermore, the reconstructed Os isotopic variation patterns during the upper Barremian are highly diversified from section to section (Fig. IV-4). Considering the long residence time of Os in the ocean, such large variations cannot be explained only by the local heterogeneity. As discussed in Chapter I-4, Os isotopic variations of the outcrop samples are easily altered by the weathering or the secondary alteration, which may be the most probable cause of the Os isotopic variations of upper Barremian records. Therefore, the reconstruction of reliable global standard Os isotopic stratigraphy during the Barremian is necessary to determine the sedimentary ages of lower part of the Goshikinohama bedded chert sequence. In addition, to further confirm the reliability of the stratigraphic correlations of our Os isotopic information, additional Os isotopic analysis of the Goshikinohama bedded chert over the longer time range (Barremian to Cenomanian) and correlating it with the global standard curve (Matsumoto et al., 2022) will be necessary.

IV-5.2. Redox condition in the Pacific deep-sea basin during OAE1a

The two especially unradiogenic Os isotopic values (i.e., enhanced hydrothermal activity) during OAE1a correspond to the characteristic purple chert and shale intervals (~4.7 m and 6.3m) in the Yokonami chert (Fig. IV-4). In the most Japanese Triassic chert sequences, purple chert sometimes appears during the massive volcanic events (e.g., Carnian and Triassic–Jurassic boundary: Fujisaki et al., 2016; Nakada et al., 2014), when marine Os isotopic record took the extremely unradiogenic Os isotopic values (Kuroda et al., 2015; Tomimatsu et al., 2021). The cause of the purple chert formation has not been fully understood. Abrajevitch et al. (2013) suggested that color changes implied the changes in the morphology or stoichiometry of hematite grains caused by ocean acidification. Besides, Ikeda et al. (2015) reported the decrease in the hematite content in the purple chert compared to the reddish chert, which was ascribed to the dissolution of hematite caused by the ocean acidification. Thus, coincidences of especially unradiogenic

Os isotopic values and purple chert intervals imply that especially pronounced volcanic episodes at the OJN could have occurred twice during OAE1a, which may have led to the acidified condition in the deep-sea Pacific Basin.

The compilation of the Pacific sedimentary record suggests that the oxygen-depleted condition could have prevailed from ~3000 m to near sea level in the Pacific region (Fig. IV-3). On the other hand, the possible OAE1a interval of the Goshikinohama bedded chert showed reddish color suggesting the presence of hematite under the oxidized condition (Ihoriya et al., 2009). Also, TOC of the reddish chert sequence was extremely low throughout the studied interval, which suggests the absence of strongly reducing conditions at the deep-sea Pacific Basin during most of the Barremian to Aptian transition interval (Ihoriya et al., 2009; Kuroda et al., 2015). Since due to the lack of evidence of the oxygen-depleted condition, Ihoriya et al. (2009) concluded that oxygen-depleted condition did not reach the deep-sea Pacific Basin. However, the two purple chert layers during OAE1a (YO-58 from 4.66 m and YO-84 at 6.11 m) showed the slight enrichment of redox-sensitive elements (V, Cr, and U) (Fig. IV-5: Kuroda et al., 2015), which are taken into the sediments under the reducing condition (Tribovillard et al., 2006). Based on the elemental concentration data of the Goshikinohama bedded chert presented in Kuroda et al. (2015), I calculated the enrichment factors of these elements defined as follows:

$$X_{EF}=(X_{sample}/Al_{sample})/(X_{UCC}/Al_{UCC}) \qquad \text{(IV-1)}$$

, where X and Al are the concentrations of element X and Al. The highest enrichment factors of purple chert layers are V_{EF}=5.6, Cr_{EF}=12, and U_{EF} =16 (Fig. IV-5). The OJN volcanism released massive volcanic ashes and altered tuffaceous beds have been widely reported from many Pacific sedimentary records during OAE1a (e.g., Price, 2003). Therefore, contamination of the OJN ash may have contributed to the enrichment of these elements. However, the enrichment factors of these elements in the OJN basalt are V_{EF} = 2.9, Cr_{EF} = 3.4, and U_{EF} = 0.04 (calculated from Fitton and Godard, 2004), which are well below the maximum enrichment factors of these elements in the Goshikinohama bedded chert. Therefore, I concluded that the enrichment of V, Cr, and U at the purple chert of Goshikinohama bedded chert likely represents the temporal weak reducing condition at the deep-sea Pacific Basin. Although Re is also one of the redox-sensitive elements and enriched under the reducing condition (e.g., Algeo and Li, 2020), I did not measure YO-58 and 84 in this study and no pronounced enrichment appears in Figure IV-2. Considering the enrichment that occurred during the unradiogenic shifts of $^{187}Os/^{188}Os_i$,

two especially intensive volcanic episodes at the OJN may have caused the especially reducing oceanic condition that could have reached the deep-sea Pacific Basin deeper than 4000 m below sea level.

IV-6. Conclusion

I reconstructed $^{187}Os/^{188}Os$ profile of the sedimentary sequence of the Goshikinohama bedded chert and tried to constrain the exact position of the OAE1a interval. The $^{187}Os/^{188}Os$ of the Goshikinohama bedded chert showed the characteristic unradiogenic shifts which could be correlated to the OAE1a. Since most of the sedimentary sequence during OAE1a consists of red bedded chert containing hematite, the Pacific deep-sea floor remained oxidized even during the OAE1a. However, two purple chert-shale sequences during OAE1a corresponds to the slight enrichment of redox-sensitive elements (V, Cr, and U), suggesting the temporal weakly reducing and acidified condition in the Pacific deep-sea floor (>4000 m below sea level) during the OAE1a. Since the two purple chert-shale sequences are characterized by the especially unradiogenic Os isotopic shifts, the changes in the deep-sea redox condition could be related to the enhanced phases of volcanic episodes associated with the formation of the Ontong Java Nui.

Figures of Chapter IV

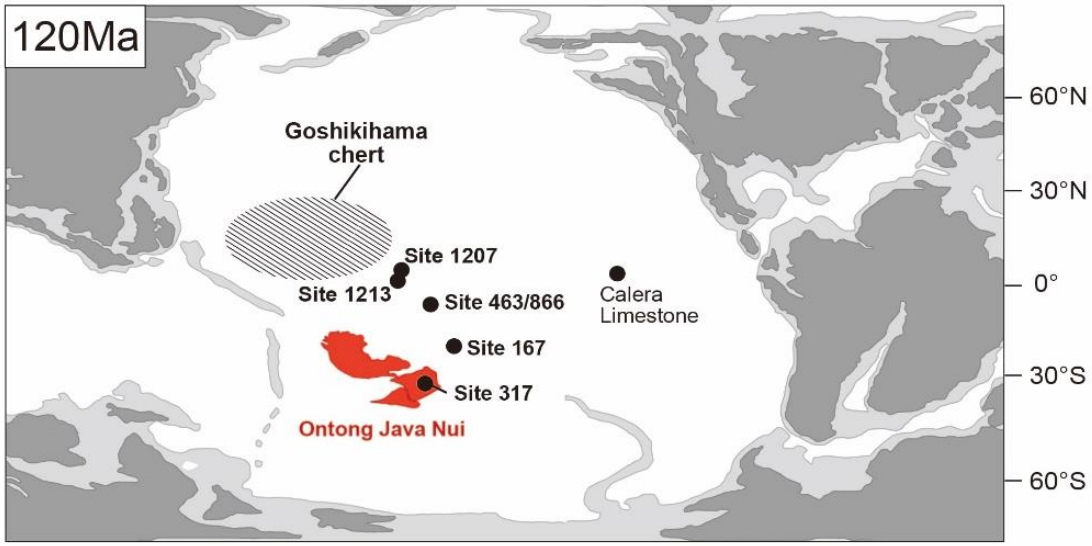

Figure IV-1. Paleogeography of 120 Ma is based on Chandler et al. (2012) and Erba et al. (2015).

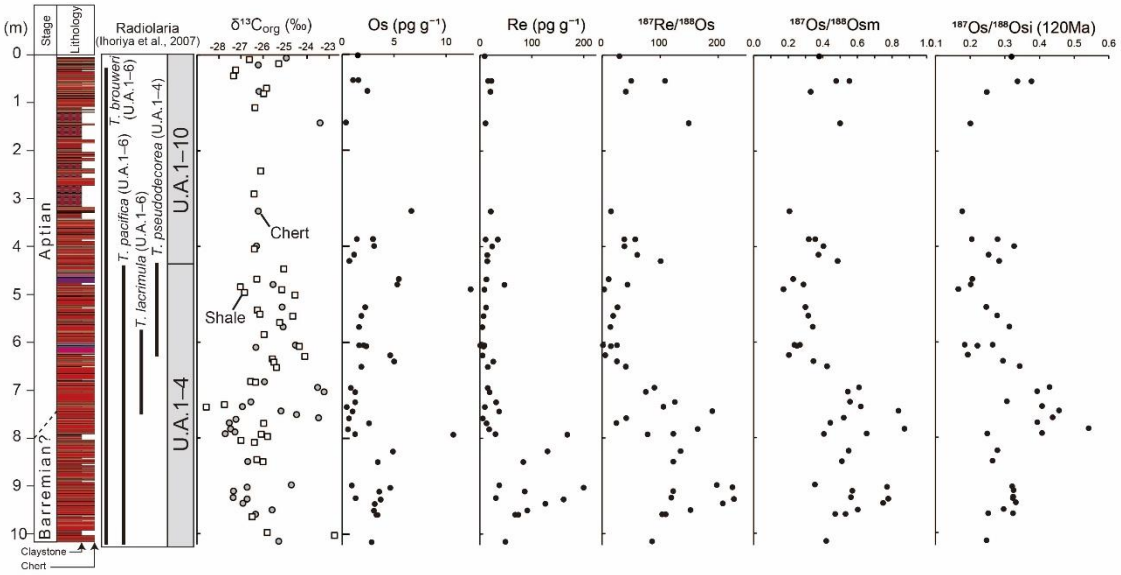

Figure IV-2. Occurrences of radiolaria, Os and Re abundances, $^{187}Re/^{188}Os$, measured Os isotopic ratio ($^{187}Os/^{188}Os_m$), and initial Os isotopic ratio ($^{187}Os/^{188}Os_i$) of Goshikinohama bedded chert: Lithology and occurrences of radiolaria are based on the Ihoriya et al. (2009).

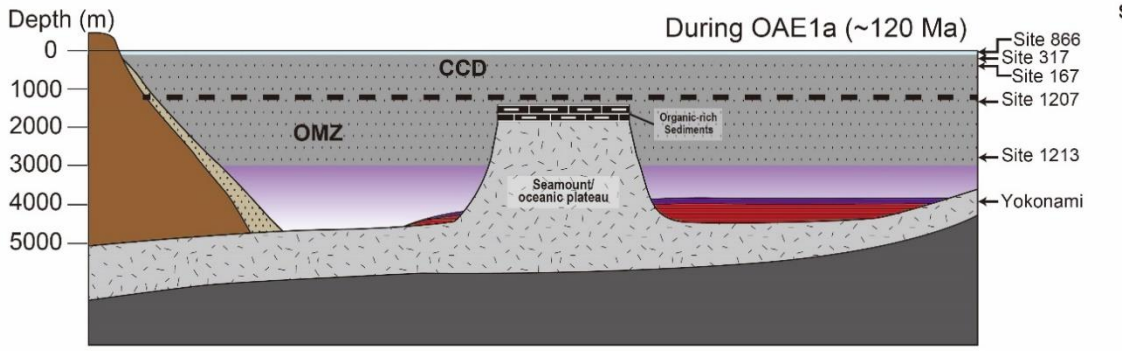

Figure IV-3. Schematic diagram of the paleoceanographic condition of the Pacific Ocean of 120Ma: The depth profile of DSDP Site 167 (~400 m of paleodepth: Winterer, 1973), DSDP Site 317 (>200 m of paleo depth: Schlanger et al., 1976), 866 (a few m of paleo depth: Sager et al., 1993), Site 1207 (~1300 m of paleo depth: Bralower et al., 2002), and 1213 (~2800 m of paleo depth: Bralower et al., 2002).

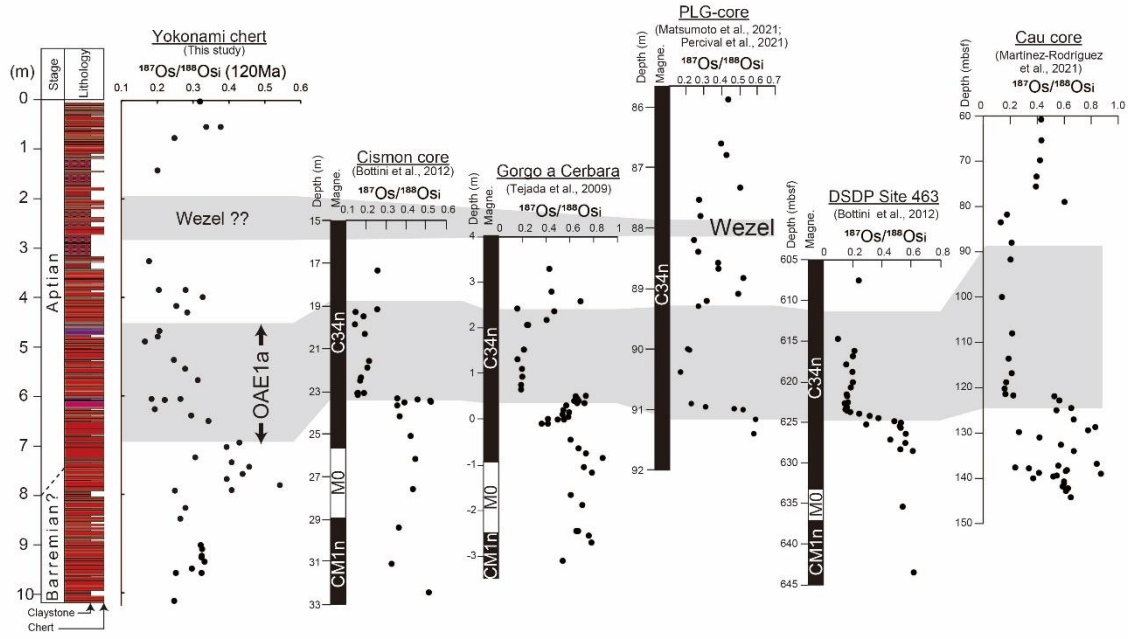

Figure IV-4. Stratigraphic correlation among the Goshikinohama chert, Cismon core, Gorgo a Cerbara section, PLG core, and DSDP Site 463 using Os isotopic ratio: Os isotopic data is from Tejada et al. (2009) (Gorgo a Cerbara section), Bottini et al. (2012) (Cismon core and DSDP Site 463), Percival et al. (2021) (PLG-core), Matsumoto et al. (2021) (PLG core), and Martínez-Rodríguez et al. (2021) (Cau core).

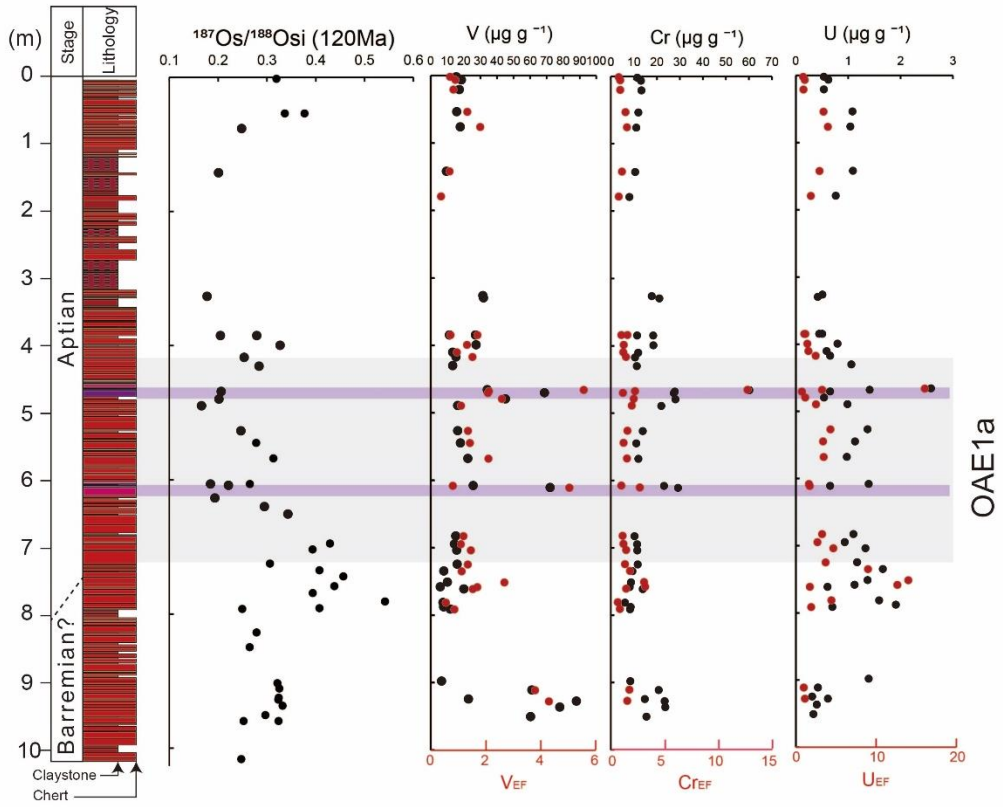

Figure IV-5. $^{187}Os/^{188}Os_i$ and V, Cr, U abundances of sedimentary rock of Goshikinohama chert: V, Cr, and U abundances are from Kuroda et al. (2015).

Supplementary Tables of Chapter IV

Sample ID	Lithology	Os	1SD	$^{187}Os/^{188}Os_m$	1SD	Re	1SD	$^{187}Re/^{188}Os$	1SD	$^{187}Os/^{188}Os_i$	1SD	Depth	Age	Equipment for Re measurement
		(pg g-1)				(pg g-1)						(m)	(Ma)	
YO-128	Chert	2.85	0.06	0.420	0.010	49.1	-	86.2	1.5	0.248	0.011	10.161	120	TIMS
YO-123	Chert	3.40	0.07	0.472	0.011	74.1	-	109.6	0.9	0.252	0.011	9.596	120	TIMS
YO-123-2	Chert	3.32	0.09	0.53	0.02	68	13	104	19	0.32	0.04	9.596	120	ICP-MS
YO-122	Chert	3.06	0.03	0.602	0.006	91.3	-	152.4	0.7	0.297	0.006	9.506	120	TIMS
YO-121	Chert	3.15	0.04	0.749	0.009	125.9	-	208.2	1.9	0.332	0.010	9.366	120	TIMS
YO-120	Chert	3.70	0.12	0.78	0.02	161.3	-	227	5	0.32	0.02	9.276	120	TIMS
YO-120	Chert	3.70	0.12	0.78	0.02	161.3	-	227	5	0.32	0.02	9.276	120	TIMS
YO-119	Chert	1.31	0.03	0.563	0.011	30.6	-	119.2	1.1	0.324	0.011	9.246	120	TIMS
YO-117	Chert	3.59	0.06	0.571	0.006	86.3	-	122.6	1.6	0.325	0.007	9.111	120	TIMS
YO-115	Chert	4.64	0.07	0.771	0.011	199.8	-	225	3	0.321	0.012	9.03	120	TIMS
YO-112	Chert	3.43	0.04	0.510	0.008	83.4	-	122.8	1.0	0.265	0.009	8.493	120	TIMS
YO-110	Chert	4.89	0.06	0.550	0.008	130.3	-	135.3	0.7	0.279	0.008	8.273	120	TIMS
YO-106/107-3	Shale	10.71	0.12	0.41	0.01	168	43	78	20	0.25	0.04	7.923	120	ICP-MS
YO-106	Chert	1.26	0.03	0.65	0.05	30.0	-	122.7	1.2	0.41	0.05	7.913	120	TIMS
YO-104	Chert	0.57	0.03	0.87	0.05	17.8	-	164.8	1.5	0.54	0.05	7.813	120	TIMS
YO-103	Chert	2.59	0.14	0.44	0.08	13	2	25	5	0.39	0.08	7.688	120	ICP-MS
YO-101	Chert	0.67	0.03	0.52	0.03	5.5	1.8	42	14	0.44	0.04	7.583	120	ICP-MS
YO-99	Chert	1.02	0.02	0.84	0.03	37	5	190	26	0.46	0.06	7.438	120	ICP-MS
YO-98	Chert	0.452	0.008	0.62	0.03	9.3	1.5	106	17	0.41	0.04	7.348	120	ICP-MS
YO-97	Chert	1.26	0.08	0.56	0.03	31.2	-	125	3	0.31	0.03	7.248	120	TIMS
YO-96	Chert	1.26	0.02	0.545	0.013	19	3	75	11	0.39	0.03	7.038	120	ICP-MS
YO-95	Chert	0.84	0.03	0.61	0.02	14.8	-	90.1	0.8	0.43	0.02	6.948	120	TIMS
YO-90	Chert	1.86	0.05	0.42	0.02	15	3	41	7	0.34	0.03	6.508	120	ICP-MS
YO-88	Chert	5.01	0.11	0.346	0.014	26	2	25	2	0.295	0.015	6.398	120	ICP-MS
YO-86	Chert	4.63	0.08	0.204	0.010	5.0	1.0	5.2	1.0	0.194	0.010	6.27	120	ICP-MS
YO-83	Chert	2.34	0.03	0.251	0.007	7.1	1.2	15	3	0.221	0.009	6.08	120	ICP-MS
YO-82	Chert	1.65	0.09	0.24	0.03	8.7	-	25.58	0.13	0.18	0.03	6.06	120	TIMS
YO-82-2	Chert	2.08	0.04	0.268	0.009	0.6	0.8	1.3	1.8	0.265	0.010	6.06	120	ICP-MS
YO-75	Chert	1.64	0.02	0.342	0.010	4.7	1.3	14	4	0.313	0.013	5.68	120	ICP-MS
YO-70	Chert	1.85	0.06	0.316	0.014	7.1	-	19.0	0.2	0.278	0.014	5.448	120	TIMS
YO-67	Chert	2.22	0.03	0.299	0.007	11.9	1.2	26	3	0.246	0.009	5.268	120	ICP-MS
YO-62	Chert	12.36	0.08	0.173	0.003	8.7	1.2	3.4	0.5	0.166	0.003	4.895	120	ICP-MS
YO-61	Chert	5.32	0.07	0.289	0.006	47.1	-	43.6	0.3	0.201	0.006	4.795	120	TIMS
YO-59	Chert	5.45	0.08	0.229	0.006	12.6	1.5	11.3	1.4	0.206	0.007	4.68	120	ICP-MS
YO-49	Chert	0.70	0.02	0.49	0.03	14.1	1.2	101	9	0.28	0.03	4.303	120	ICP-MS
YO-48	Chert	1.17	0.03	0.37	0.01	14.2	1.2	61	5	0.253	0.018	4.173	120	ICP-MS
YO-44	Chert	3.08	0.03	0.404	0.005	23.7	-	38.3	0.2	0.327	0.005	3.993	120	TIMS
YO-42	Chert	2.97	0.04	0.319	0.011	34.3	1.4	57	2	0.205	0.012	3.848	120	ICP-MS
YO-42R	Chert	1.42	0.06	0.36	0.02	11.0	-	38.2	0.4	0.28	0.02	3.848	120	TIMS
YO-33	Chert	6.67	0.09	0.208	0.007	21	3	15.2	1.9	0.177	0.008	3.263	120	ICP-MS
YO-22	Chert	0.37	0.03	0.50	0.07	10.9	1.3	149	21	0.20	0.09	1.421	120	ICP-MS
YO-14	Chert	2.44	0.06	0.330	0.015	20.1	1.5	41	3	0.248	0.017	0.763	120	ICP-MS
YO-10	Chert	1.05	0.06	0.55	0.04	22.4	-	108.4	1.0	0.34	0.04	0.538	120	TIMS
YO-10-2	Chert	1.57	0.02	0.477	0.009	15.7	-	50.3	0.2	0.377	0.009	0.538	120	TIMS
YO-1	Chert	1.52	0.03	0.379	0.011	9.1	-	29.8	0.2	0.319	0.011	0.02	120	TIMS

Supplementary Table IV-S1. Re-Os data of the sedimentary rock samples recovered from the Goshikinohama bedded chert

CHAPTER V

Osmium isotopic evidence for eccentricity-paced increases in continental weathering during the latest Hauterivian, Early Cretaceous

This chapter is published at *Geochemistry, Geophysics, Geosystems*

Abstract of Chapter V

The 405-kyr eccentricity cycle is a consistent orbital parameter throughout the Phanerozoic that is associated with long-term variations in global continental weathering. However, a lack of reliable geological evidence has hampered the understanding of the relation between the 405-kyr eccentricity cycle and continental weathering during the Cretaceous. Os isotopic ratios ($^{187}Os/^{188}Os$) of the sedimentary record reflect the balance between radiogenic Os derived from continental weathering and Os derived from unradiogenic sources (e.g., hydrothermal activity, weathering of mafic rocks, and extraterrestrial sources). This ratio is therefore considered as a good proxy for the evaluation of short-term changes in continental weathering patterns. To trace orbital-paced continental weathering, this study reconstructs the marine Os isotopic records in upper Hauterivian to lower Barremian (Lower Cretaceous) carbonate rocks in central Italy, where previous studies have reported that variations in clay mineral composition are paced by the 405-kyr cycle. The new Os isotopic record documents periodic oscillations of $^{187}Os/^{188}Os$ between 0.7 and 0.9 that correspond to the 405-kyr Earth's eccentricity cycle. Because the sedimentary interval with radiogenic $^{187}Os/^{188}Os$ values (~0.9) corresponds to a time interval characterized by a humid climate in areas surrounding the Tethys, variations in the $^{187}Os/^{188}O$ values likely reflect cyclic changes in continental weathering caused by eccentricity-paced intensification of monsoonal activity at low latitudes. This variation could have been further amplified by increased input of radiogenic Os from Paleozoic shale and Precambrian crust at higher latitudes that resulted from a latitudinal shift of the intertropical convergence zone.

V-1. Introduction

Changes in continental weathering and their association with variations in monsoonal activity related to orbital cycles have been widely reported throughout the Phanerozoic (e.g., Clemens et al., 1991; Wehausen and Brumsack, 2002; Moiroud et al., 2012; Martinez et al., 2013, 2015; Ikeda et al., 2017). The intensity of continental weathering during the Quaternary has been commonly linked to monsoonal activity, and the growth and retreat of polar ice sheets that are paced by astronomical cycles (Clemens et al., 1991; Oxburgh et al., 2007; Vance et al., 2009; Wang, P. 2009; Elderfield et al., 2012). However, during periods when the continents were ice-free, such as during the Mesozoic, monsoonal activity was the predominant influence on global-scale chemical weathering (Kutzbach and Gallimore, 1989; Wang, P. 2009; Ikeda et al., 2017, 2020). During the Permian and Triassic, for instance, global geochemical cycles were controlled by "mega-monsoons", the intensity of which was modulated by precession and eccentricity cycles

(Kutzbach and Gallimore, 1989; Ikeda et al., 2017, 2020). In contrast, monsoonal intensity was proposed to have weakened during the Cretaceous, as the break-up of the supercontinent Pangea changed the relationship between continents and the ocean (Wang, P. 2009). However, studies of monsoonal activity during the Cretaceous and its influence on the global geochemical cycle are limited. Recently, 405-kyr eccentricity cycles have been recognized in the Tethyan sedimentary record through changes in gamma ray spectrometry and clay mineral composition (e.g., kaolinite/chlorite ratio) of Valanginian to Barremian (Lower Cretaceous) sedimentary records (Moiroud et al., 2012; Martinez et al., 2013, 2015). Because kaolinite is formed under humid conditions (Martinez et al., 2015), these cycles have been interpreted as eccentricity-paced occurrences of humid conditions in which intensified monsoonal activity enhanced continental weathering (Charbonnier et al., 2016). However, because clay mineral composition was also strongly influenced by the regional, geological, and environmental setting of the Tethyan region, it is unclear whether these changes reflected global variations of monsoonal activity.

The radiogenic isotopic composition of osmium ($^{187}Os/^{188}Os$) reflects the balance between radiogenic Os input from continental materials with high $^{187}Os/^{188}Os$ values (~1–1.5) and unradiogenic Os input with low $^{187}Os/^{188}Os$ values (~0.1–0.2) from hydrothermal activity, weathering of mafic rocks, and extraterrestrial input (Levasseur et al., 1999). Isotopic variations of Os among these sources represent the differences in $^{187}Re/^{188}Os$. Since Re is more incompatible than Os, continental crust tends to have higher $^{187}Re/^{188}Os$ than mantle due to the differentiation process. Additionally, organic-rich marine sedimentary rocks deposited under the reducing conditions have high $^{187}Re/^{188}Os$ ratios (Dubin and Peucker-Ehrenbrink, 2015). Due to the β-decay of ^{187}Re into ^{187}Os with a half-life of 41.6 Gyr (Smoliar et al., 1996), these rocks tend to have higher $^{187}Os/^{188}Os$ values than mantle or extraterrestrial material. Consequently, Os supplied from continental crust and the subaerially exposed old organic-rich sedimentary rocks have higher $^{187}Os/^{188}Os$ values than mantle or extraterrestrial material. Considering its geologically short residence time in the ocean (10–100 kyr: Levasseur et al., 1998, 1999), which is longer than the representative timescale of oceanic circulation, Os is regarded as a useful tracer of orbital-scale changes for global continental weathering rate (e.g., Oxburgh et al., 2007; Sekine et al., 2011; Percival et al., 2016). To investigate orbital-scale weathering conditions and their relationship to monsoonal activity during Early Cretaceous, I reconstruct an Os isotopic record from the latest Hauterivian to the earliest Barremian, an interval in which natural gamma radiation and clay mineral composition display a distinct cyclicity in the Tethyan sedimentary record (e.g., Moiroud et al., 2012; Martinez et al., 2015).

The studied sequence covers the oldest prominent oceanic anoxic event (OAE) of the Cretaceous (uppermost Hauterivian), the Faraoni Level (Cecca et al., 1994), which is dated at ~127 Ma (Martinez et al., 2015, 2020). The Faraoni Level is widely traceable in the Tethyan and Atlantic region (e.g., Cecca et al., 1994; Baudin, 2005; Baudin and Riquier, 2014; Rodríguez-Tovar and Uchman, 2017). The Faraoni Level is a thin sequence (<1 m) characterized by alternating laminated black shales and micritic white limestones that are easily recognized by a calcareous layer rich in well-preserved ammonites (Cecca et al., 1994). The high organic-carbon content and enrichment in redox-sensitive elements of the black shale layers have been interpreted as the dominance of oxygen-depleted bottom water during the Faraoni OAE (Cecca et al., 1994; Bodin et al., 2007; Charbonnier et al., 2018). Several studies have discussed a relationship between the Faraoni Level and volcanic events associated with the formation of a submarine basaltic plateau (e.g., Baudin, 2005). Because the Os isotopic ratio can be used not only as a proxy of continental weathering but also as a proxy of unradiogenic Os input from hydrothermal activity (Turgeon & Creaser, 2008; Tejada et al., 2009; Matsumoto et al., 2020), these data may offer new and significant insight into the factors triggering the deposition of the Faraoni Level.

V-2. Geological setting

The Maiolica Formation, a well-preserved Upper Jurassic to Lower Cretaceous carbonate succession, crops out in the Umbria-Marche region, in central Italy. The Fiume Bosso section, one of the best-studied exposures of Hauterivian strata in the Umbria-Marche Basin, is located on the eastern limb of the Monte Nerone Anticline (Fig. V-S1) (Cecca et al., 1994; Coccioni et al., 1998). This section represents a pelagic environment of the central Tethys (Fig. V-1) (Godet et al., 2006). It primarily consists of yellowish-gray to medium-gray limestone interbedded with dark shale or chert (Fig. V-S1) (Coccioni et al., 1998). Here the Faraoni Level is represented by thin beds of black shale and limestone totaling ~25 cm in thickness with the ammonite-rich key bed in the middle (Cecca et al. 1994) (Fig. V-2 and S1). Limestone samples were collected from the upper Hauterivian to lower Barremian interval at the Fiume Bosso section (Coccioni et al., 1998).

V-3. Methods

V-3.1. Carbon isotopic ratio of carbonate

Stable carbon and oxygen isotope ratios of carbonate ($\delta^{13}C_{carb}$ and $\delta^{18}O_{carb}$) of powdered 41 limestone samples, three cherty limestone samples, and one chert samples

were measured with an isotope ratio mass spectrometer (Delta V plus, Thermo Fisher Scientific, USA), equipped with an automated carbonate reaction device (GasBench II, Thermo Fisher Scientific, USA), at Atmosphere and Ocean Research Institute, The University of Tokyo (Japan). All isotopic values are reported using delta notation with respect to PeeDee Belemnite. External reproducibility was calculated from the repeated analysis of NBS-19 standard. Typical values are better than 0.05‰ and 0.08‰ for $\delta^{18}O$ and $\delta^{13}C$, respectively. Detailed analytical methods are described in Shirai et al. (2018).

V-3.2. Re-Os analysis

I performed Re-Os analyses on 23 limestone samples and two cherty limestone samples from the study section. Because the black shale in the outcrop is subject to weathering that affects its Re-Os system (Jaffe et al., 2002), I measured the Os isotopic ratio of two limestone samples between the black shale layers in the Faraoni Level (Fig. V-2C). Considering the short duration of the Faraoni Event (~100 kyr: Martinez et al., 2015) and the residence time of Os (10–100 kyr: Levasseur et al., 1998, 1999), I assumed that these samples would fairly represent the marine Os isotopic signature during the deposition of the black shale beds.

I extracted Re and Os from the bulk rock samples with an inverse aqua regia digestion method. Os abundances and isotopic compositions were determined by negative thermal ionization mass spectrometry (Thermal Electron TRITON) (Kuroda et al., 2010 and references therein) at the Japan Agency for Marine-Earth Science and Technology (JAMSTEC), and Re abundances were determined by quadrupole inductively coupled plasma mass spectrometry (iCapQ) at JAMSTEC. All data were corrected for procedural blanks, which averaged 0.33 ± 0.25 pg Os with $^{187}Os/^{188}Os$ of 0.11 ± 0.04 and 2.6 ± 1.3 pg Re. The initial $^{187}Os/^{188}Os$ ($^{187}Os/^{188}Os_i$) was calculated as:

$$^{187}\mathrm{Os}/^{188}\mathrm{Os_i} = {}^{187}\mathrm{Os}/^{188}\mathrm{Os_m} - [\exp\{\lambda \times \mathrm{age(yr)}\} - 1] \times {}^{187}\mathrm{Re}/^{188}\mathrm{Os_m}, \text{ (VI-1)}$$

where λ is the decay constant of 1.666×10^{-11} yr^{-1} and the subscript "m" signifies measured values. The detailed explanation is described in Chapter II-4.3.

To verify that Os isotopic variations resulting from the inverse aqua regia digestion methods reflect hydrogenous fraction, I conducted additional Re-Os measurements using the weak leaching method following Dunlea et al. (2021). In this analysis, 200 mg of limestone samples from the Fiume Bosso section were dissolved in 1 M HCl for 24 h at room temperature. The leachate, separated from the residue using centrifugation, was spiked and sealed in a Carius Tube with 4 ml of inverse aqua regia (mixture of 68 wt% of HNO3 and 1ml of 30 wt% HCl). The succeeding separation procedure was the same as the inverse aqua regia digestion method described above. This digestion method does not

strongly attack silicate minerals and is, therefore, expected to extract Os more accurately from hydrogenous fractions.

V-4. Results

V-4.1. Carbon and oxygen isotopic ratios of carbonate

Nearly all $\delta^{13}C_{carb}$ values in the study section clustered tightly between 1.6‰ and 1.9‰ (Fig. V-2 and Supplementary Table V-S1). The poor correlation between $\delta^{13}C_{carb}$ and $\delta^{18}O_{carb}$ values suggests that samples had not experienced strong diagenetic alteration (Fig. V-3a). One chert sample yielded relatively low $\delta^{13}C_{carb}$ and $\delta^{18}O_{carb}$ values (1.43‰ and –3.93‰, respectively: Fig. V-3a and Supplementary Table V-S1) compared to the limestone samples. Because chert does not undergo the same diagenetic processes as limestone, I excluded this sample from further consideration.

V-4.2. Re-Os analysis

Os and Re abundances, extracted by inverse aqua regia, ranged from 8.0 to 18.9 pg g^{-1} and 10.0 to 71.0 pg g^{-1}, respectively (Fig. V-2 and Supplementary Table V-S2). The Os isotopic ratios of measured values ($^{187}Os/^{188}Os_m$) and initial values ($^{187}Os/^{188}Os_i$) ranged from 0.70 to 0.97 and from 0.68 to 0.93, respectively (Fig. V-2 and Supplementary Table V-S2). $^{187}Os/^{188}Os_i$ oscillated cyclically between ~0.7 and ~0.9 during the uppermost Hauterivian (Fig. V-2). The $^{187}Os/^{188}Os_i$ values of organic-rich sediments with high $^{187}Re/^{188}Os$ ratios are easily disturbed by leaching of Re and Os following oxidation of sedimentary rocks after exposure on land (Jaffe et al., 2002). However, considering the low $^{187}Re/^{188}Os$ of the limestone samples and the small difference between their measured and age-corrected initial $^{187}Os/^{188}Os$ values (at most 6.6%), weathering could not have caused a significant alteration of the original $^{187}Os/^{188}Os$ values. Besides, Selby and Creaser, (2003) proposed that CrO_3–H_2SO_4 is a more appropriate method to extract the hydrogenous fraction of Re-Os information than aqua regia because CrO_3–H_2SO_4 weakly attacked silicate minerals, such as quartz and feldspar. However, the Re-Os information extracted with these two methods is almost identical (Selby and Creaser, 2003; Sekine et al., 2011; Matsumoto et al., 2020). Accordingly, Matsumoto et al. (2020) applied both extraction methods for the Re-Os analysis Cretaceous sedimentary rock samples collected from the Umbria–Marche Basin and the reconstructed $^{187}Os/^{188}Os$ values of both high Os-black shale and low-Os carbonate samples are almost identical. This suggests that Re-Os information extracted using inverse aqua regia digestion methods can mainly reflect the hydrogenous fraction of Re-Os. In addition, the Re-Os variation of the Umbria–Marche sedimentary record is concordant with that outside the Tethyan region, which rules out

the possibility of a strong regional effect (Matsumoto et al., 2020). Because $^{187}Os/^{188}Os_i$ and Os abundance have no more than a weak Pearson linear correlation (Fig. V-3b), simple contamination by radiogenic Os from terrigenous material cannot explain the obtained fluctuation of $^{187}Os/^{188}Os_i$.

Os and Re concentrations obtained by the HCl extraction method are much lower than those obtained by the inverse aqua regia digestion method (Fig. V-2). Although the overall variation patterns seem similar between these methods, measured and initial Os isotopic ratios ($^{187}Os/^{188}Os$) obtained by the HCl extraction method show less radiogenic values than those obtained by the inverse aqua regia digestion method (Fig. V-2). Besides, Os isotopic variations obtained by the HCl extraction method lack some radiogenic peaks (e.g., 8.41 m) that are observed in the Os data extracted by the inverse aqua regia digestion method.

V-5. Discussion

V-5.1. Comparison of Os isotopic variations: the inverse aqua regia vs. weak-leaching methods

One possible reason for the discrepancy in Os isotopic values between the two digestion methods (i.e., inverse aqua regia and 1M HCl) is the different degree of contamination of the radiogenic Os from silicate minerals. The inverse aqua regia more strongly attacks the clay minerals than 1M HCl (Dunlea et al., 2021). Therefore, more radiogenic Os isotopic values obtained by the inverse aqua regia digestion method may be attributed to the higher contamination of radiogenic Os from clay minerals. However, considering Os isotopic ratios do not take radiogenic values during the Faraoni Level, where the enrichment of kaolinite is observed (Fig. V-4) (Moiroud et al., 2012), the contamination of terrestrial radiogenic Os from clay minerals may be substantially insignificant in these samples. Thus, the difference in the degrees of radiogenic Os contamination from clay minerals cannot fully explain the dissimilar Os isotopic trends between these two methods.

Another possibility is the partial dissolution of unradiogenic Os sources (e.g., extraterrestrial materials). Dunlea et al. (2021) revealed that Os isotopic ratio extracted from the pelagic clay samples using extremely weakly acidified conditions (0.05–0.1 M HCl) shows more unradiogenic values than the coeval marine Os isotopic ratios. This difference was interpreted as the dissolution of different Os complexities and Os bearing phases (extraterrestrial materials) or the local unradiogenic Os sources. Thus, the higher partial dissolution from the unradiogenic Os sources in the samples may be able to explain less unradiogenic Os isotopic values resulting from the weak-leaching methods.

The last possibility is the uncertainties in blank corrections. Because of the limited amount of samples (~200 mg) and very low Os concentration of the leachable fraction (4–7 pg g^{-1}), the blank corrections are very critical in the Os isotopic measurement applied by the weak-leaching method. For example, Os isotopic ratios ($^{187}Os/^{188}Os$) before blank corrections ranges between 0.37 and 0.53 while Os isotopic ratio after blank corrections rangers 0.61 and 0.83. Thus, the unknown variations of Os blanks in the measurements may have largely altered Os isotopic values obtained by the HCl digestion method toward less radiogenic values. Since very small errors of estimated Os blank (~0.1 to 0.2 pg) can explain the differences in Os isotopic values between these two digestion methods, I consider that the last factor has the most critical effect. To extract more reliable Re-Os information using this weakly leaching method, it is required to dissolve a larger amount of samples than the present one and reduce the Os procedural blanks.

Since large Os isotopic variations (especially, rapid Os isotopic shift to radiogenic values after the Faraoni Level) could be observed regardless of the digestion methods and overall trends are similar, I consider that Os isotopic variation patterns obtained by the inverse aqua regia digestion method could reflect marine Os isotopic variations. Besides, to apply the weak-leaching method to the limestone samples, further improvement of Os blank and reanalysis under more suitable digestion conditions are essential. Therefore, I mainly use the Os isotopic data acquired by the inverse aqua regia digestion method in the following discussions.

V-5.2. Orbital-scale Os isotopic fluctuations in the uppermost Hauterivian

The $^{187}Os/^{188}Os_i$ values of the uppermost Hauterivian part of the study section vary periodically between ~0.7 and ~0.9 (Fig. V-2). These oscillations are weaker above the stratigraphic height of 12.5 m in the section (Fig. V-2). Recent studies relying on astronomical tuning have shown that the ages of the base of the CM4 geomagnetic polarity chron, the Faraoni Level, and the Hauterivian–Barremian boundary are ~127.1 Ma, 126.7 Ma, and 126.0 Ma, respectively (Fig. V-1: option 2 in Martinez et al., 2015). In addition, the base of the CM5 geomagnetic polarity chron, which is located at the base of the study section, is at 127.7 Ma (Martinez et al., 2015). Assuming a constant sedimentation rate between these tie points, each cycle of Os isotopic fluctuations corresponds to ~400 kyr (Fig. V-2), which is consistent with the eccentricity cycle of 405 kyr. Martinez et al. (2015, 2020) have identified 14 of these 405-kyr cycles (H1 to H13 and H/B) within the Hauterivian section at La Charge-Pommerol in the Vocontian Basin (southeast France) and the Río Argos in the Subbetic Domain (southeast Spain). Five of these cycles (H10, H11, H12, H13, and H/B) are between the base of the CM5 chron and

the Hauterivian–Barremian boundary (Fig. V-2). Therefore, I suggest that $^{187}Os/^{188}Os_i$ fluctuations correspond to the 405-kyr eccentricity cycle. Moreover, Martinez et al. (2015) reported that the eccentricity cycle detected in the magnetic susceptibility record and kaolinite/chlorite contents decreased abruptly in intensity after H12 at the Río Argos section. The similar decreasing trend appears in the Os isotopic record in the study section (Figs. V-2 and 4b). Although Maritnez et al. (2015) presented two options for the age model, the choice of the options does not influence the timing of 405-kyr cycles.

Similar but smaller amplitude oscillations (~0.15) of Os isotopic composition paced by glacial and interglacial cycles have been reported in several Quaternary sedimentary records (e.g., Oxburgh et al., 2007; Lund and Asimow, 2011). These have been mainly explained by changes in hydrothermal intensity due to variations in magma production at mid-ocean ridges caused by sea-level changes (e.g., Lund and Asimow, 2011), changes in surface temperature and precipitation during glacial and interglacial cycles (Oxburgh et al., 2007), and increased radiogenic Os flux from high-latitude rocks exposed by retreating ice sheets (Oxburgh et al., 2007). In all three hypotheses, Os isotopic variation is associated with the waning and waxing of polar ice sheets and ensuing environmental perturbations. However, no evidence has been produced for large ice sheets during the Hauterivian. In addition, although Haq (2014) has reported several high-amplitude sea-level changes during the Early Cretaceous, their timing does not match with those of the Os isotopic fluctuations. I therefore rule out ice sheets as a triggering factor.

V-5.3. Os isotopic fluctuations triggered by eccentricity-paced changes in continental weathering

I propose that cyclic changes in continental weathering intensity regulated by monsoon dynamics paced by Milankovitch cycles may be the cause of the cyclic variations in the Os isotopic record. During the Quaternary, the precession-paced North African summer monsoon and Mediterranean storm track caused cyclic intensifications of precipitation and runoff of continental material around the Mediterranean. Their intensity at perihelion was controlled by the 100-kyr eccentricity cycle (Toucanne et al., 2015). Orbital-paced changes in monsoonal activity have been also proposed to explain the Triassic–Jurassic climate state, when the extremely large thermal contrast between Pangea and the super-ocean Panthalassa created a strong “mega-monsoon” (Kutzbach & Gallimore, 1989; Ikeda et al., 2017). The intensity of the mega-monsoon and the latitudinal shift of intertropical convergence zones (ITCZ) were both strongly influenced by the precession cycle (Ikeda et al., 2017). The eccentricity cycle does not change the total insolation, but it contributes to changes in continental weathering by enhancing the

seasonality changes of the precession cycle (Ikeda et al., 2017). Thus, temperature and precipitation at summertime perihelion were intensified during times of high eccentricity, which in turn enhanced continental weathering. During high eccentricity, this effect was amplified by the contrast between the wet and dry seasons, which accelerates physical and chemical weathering at low latitudes compared to weathering rates during times of low eccentricity (De Vleeschouwer et al., 2020). Assuming that similar climatic changes occurred at low latitudes during the Early Cretaceous, eccentricity-paced intensification of monsoonal activity and precipitation could have periodically enhanced continental weathering and led to an increase in marine $^{187}Os/^{188}Os_i$ values (Fig. V-4). Following the simple box model of Tejada et al. (2009) (see Chapter II-4.4), the radiogenic peaks of $^{187}Os/^{188}Os_i$ (~0.9) would require at most twice as much continental derived radiogenic Os as unradiogenic peaks of $^{187}Os/^{188}Os_i$ (~0.7) (Fig. V-5). The size of this difference in continental weathering is concordant with model calculation results on eccentricity-paced continental weathering during the Miocene Climatic Optimum (Ma et al., 2011). Here, the box model calculation is a very simplified case and does not take into account changes in the Os isotope ratio of riverine Os and the contamination of terrigenous materials. Thus, the actual magnitude of variations of the riverine Os flux could have been smaller than that of the estimation. Within the Hauterivian and Barremian stages, the kaolinite/chlorite ratio in the Río Argos section varies according to the 405-kyr eccentricity cycle, and its variation decreases above the Faraoni Level (Fig. V-4) (Moiroud et al., 2012; Martinez et al., 2015). As a proxy for humid conditions, the record of kaolinite content can be interpreted in terms of summer precipitation according to the 405-kyr eccentricity cycle (Martinez et al., 2015). Considering that the radiogenic peak of $^{187}Os/^{188}Os_i$ corresponds to the peak of the kaolinite-rich interval (Fig. V-4), I infer that intensified monsoonal activity paced by eccentricity promoted an increase in temperature and precipitation at low latitudes during the summer perihelion and enhanced the seasonal wet/dry contrast. Consequently, chemical weathering accelerated at low latitudes and marine $^{187}Os/^{188}Os$ shifted toward radiogenic values as input of continental radiogenic Os increased (Fig. V-4C). Considering that the cyclic enrichment of kaolinite roughly corresponds to the radiogenic Os isotopic peaks, the changes in the clay mineral composition in the sediment rocks may have triggered the cyclic radiogenic Os isotopic peaks. However, pronounced enrichment of kaolinite is reported not only from the radiogenic Os isotopic peaks (~12, 8.5, and 4 m) but also from the Faraoni Level with relatively unradiogenic Os isotopic values ~0.7 (Fig. V-4). Thus, changes in the clay mineral composition in the sediments (e.g., kaolinite content) are unlikely the cause of cyclic Os isotopic shifts to the radiogenic values. Cenozoic 405-kyr eccentricity cycles were commonly accompanied by

fluctuations of $\delta^{13}C_{carb}$ in benthic and planktonic foraminiferal tests that were related to variations in primary productivity (e.g., Wang, P. et al., 2010). However, $\delta^{13}C_{carb}$ in bulk rock samples from the Fiume Bosso section did not show a pronounced variation paced by eccentricity (Fig. V-2). Although Sprovieri et al. (2006) conducted an astronomical tuning using $\delta^{13}C_{carb}$ of bulk rock samples of the Maiolica Formation, they largely underestimated the number of 405-kyr eccentricity cycles in Hauterivian compared to the latest work (Martinez et al., 2015, 2020). Because the limestone samples of the Maiolica Formation were mixtures of planktonic and benthic foraminifers and calcareous nannofossils, changes in their proportions may have obscured subtle orbital-scale carbon isotope fluctuations. Indeed, the $\delta^{13}C_{carb}$ values of benthic foraminifera and bulk rock samples take different values and their detailed variations often do not coincide with each other (e.g., Huber et al., 2011).

Changes in weathering patterns or the source of radiogenic Os caused by ITCZ migration can also influence the marine Os isotopic record. Indeed, it is known that weathering of organic-rich sedimentary rocks with high $^{187}Os/^{188}Os$ (~2.2: Dubin and Peucker-Ehrenbrink, 2015) has the potential to alter the oceanic Os isotopic ratio rapidly. Besides, in Canada, for example, Precambrian shield rocks and Paleozoic organic-rich sediments have extremely radiogenic $^{187}Os/^{188}Os$ values (Huh et al., 2004). Indeed, Precambrian continental rocks and orogenic belts in western and southern Africa may have highly radiogenic $^{187}Os/^{188}Os$ values (Begg et al., 2009). Therefore, during the eccentricity-paced ITCZ migration toward higher latitudes (Ikeda et al., 2020), the increased Os input from more radiogenic sources could have contributed to the increase in marine $^{187}Os/^{188}Os$ values. Although this factor must be important for the changes in the marine Os isotopic record, it is difficult to precisely estimate the influence from precipitation patterns, the resulting changes in local weathering rates, and their contribution to marine $^{187}Os/^{188}Os$ values.

High $^{187}Os/^{188}Os$ values roughly correspond to gray-colored intervals in the study section (Fig. V-2A), which have pronounced enrichments in Re and Os (Fig. V-2). The box-model calculation suggests the cyclic increase in the input of continental Os into the ocean, which could have caused the enrichment of Re and Os to explain the Os isotopic fluctuations. However, increases in the Os concentration by a factor of 2 and Re concentration by a factor of 8 are too large compared to the changes in the marine Os and Re concentration caused solely by the increase in the continental weathering. It is also known that Re and Os concentrations and total organic carbon content are positively correlated (e.g., Selby and Creaser, 2003; Matsumoto et al., 2020). As organic matter is well preserved under reducing conditions, Re and Os enrichments can be interpreted as

the presence of reducing bottom water. In the Quaternary Mediterranean Sea, orbital-paced increases in monsoonal activity cyclically enhanced continental runoff and riverine freshwater supply, which resulted in high primary productivity and marine stratification (Toucanne et al., 2015). The resulting high input of organic carbon to the seafloor and reducing bottom water conditions triggered the periodic deposition of organic-rich sediments paced by the precession and eccentricity cycles (e.g., Hilgen, 1991; Sierro et al., 2000; Toucanne et al., 2015). Therefore, similar riverine fresh water and nutrient input in the Tethys Ocean may have caused the weakly reducing condition in the Tethyan region. However, the depositional setting of Umbria–Marche Basin was considered more pelagic and the degree of reducing condition could be weaker than the Quaternary Mediterranean. Under the assumption that the gray interval (Fig. V-2A) of the Fiume Bosso section corresponds to a humid interval with strong continental weathering (Fig. V-4), I conclude that eccentricity-paced monsoonal activity accelerated the input of freshwater and continental materials including nutrients into the Tethys, leading to reducing bottom water conditions.

The cyclicity of $^{187}Os/^{188}Os_i$ and reducing bottom water conditions weakens and disappears above the Faraoni Level, as do the cyclic variations in the kaolinite/chlorite ratio (Fig. V-4). I interpret these trends as the weakening of monsoonal activity and subsequent decrease in precipitation.

V-5.4. Implication for the Faraoni Level

The eruptions of large igneous provinces (e.g., the Ontong Java, Kerguelen, and Caribbean Plateaus) have been considered as the triggers of major Cretaceous OAEs (e.g., Tejada et al., 2009; Turgeon and Creaser, 2008; Matsumoto et al., 2020; Percival et al., 2021). Signs of these OAEs include sharp negative shifts in $\delta^{13}C_{carb}$ attributed to massive inputs of ^{12}C-rich carbon due to intensive volcanic degassing (e.g., Price, 2003). In the Faraoni Level, $\delta^{13}C_{carb}$ does not display negative excursions (Fig. V-3). Indeed, during the early Aptian OAEs (OAE1a, Wezel, and Fallot) and the late Cenomanian OAE2, sharp excursions of $^{187}Os/^{188}Os$ toward unradiogenic values have been interpreted as the input of unradiogenic Os through massive hydrothermal activity on submarine basaltic plateaus (Turgeon and Creaser, 2008; Tejada et al., 2009; Matsumoto et al., 2021). However, the Os isotopic record shows no $^{187}Os/^{188}Os$ excursion across the Faraoni Level, suggesting the absence of volcanic activity (Fig. V-2). The lack of evidence of volcanic events during the Faraoni Level is also supported by the absence of mercury enrichment caused by the volcanic activity (Charbonnier et al., 2018). These pieces of evidence imply that the Faraoni Level represents an episodic event unrelated to massive volcanic episodes (Fig.

V-2).

V-6. Conclusion

Marine Os isotopic ratios ($^{187}Os/^{188}Os$) in the uppermost Hauterivian sedimentary record at the Fiume Bosso section show cyclic fluctuations that are paced by the 405-kyr orbital eccentricity cycle. During intervals of high eccentricity, the increase in precipitation at low latitudes caused by intensified monsoonal activity accelerated continental weathering. The poleward shift of the ITCZ during those times could also have accelerated Os input from more radiogenic sources, contributing to increased $^{187}Os/^{188}Os_i$ values. During intervals of low eccentricity, decreased summer precipitation caused a weakening of continental weathering. I conclude that oscillations in marine Os isotope ratios can be interpreted as cyclic enhancements of continental weathering and changes in Os sources caused by intensified monsoonal activity. Because the Faraoni Level does not contain an unradiogenic Os isotopic shift, it instead represents an episodic event unrelated to massive volcanic episodes.

Figures of Chapter V

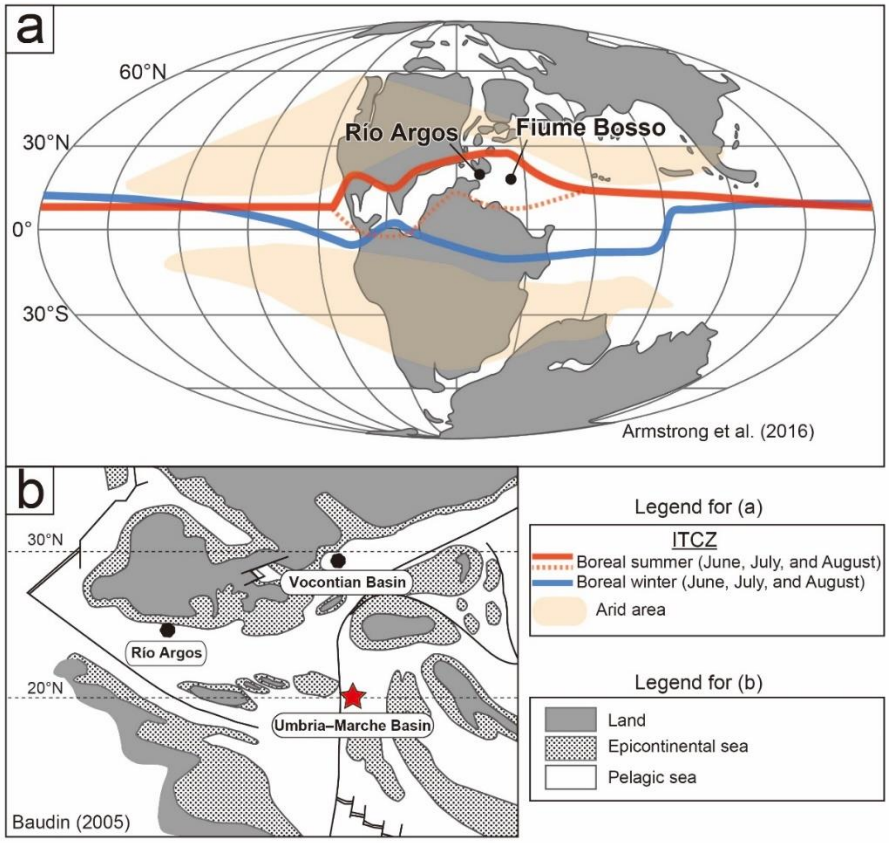

Figure V-1. (a) Paleogeography and intertropical convergence zone (ITCZ) position of the Early Cretaceous based on Armstrong et al. (2016) and (b) detailed paleoceanographic reconstruction modified from Baudin (2005): Red and blue lines represent the position of ITCZ and a dashed red line represents the minor branch of ITCZ.

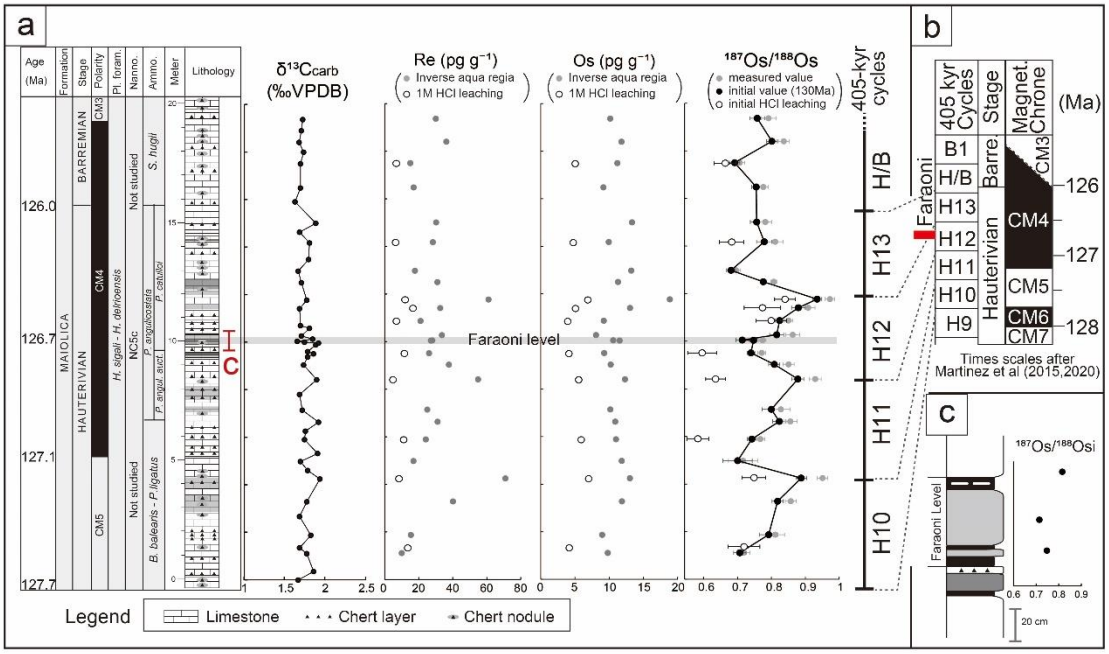

Figure V-2. Os and carbon isotopic data of Fiume Bosso section: (a) Stable carbon isotopic ratio of carbonate ($\delta^{13}C_{carb}$), Re and Os abundances, and $^{187}Os/^{188}Os$ values at the Fiume Bosso section, (b) the 405-kyr eccentricity cycles and magnetostratigraphy, and (c) close-up image of lithology and $^{187}Os/^{188}Os$ values of "C" in Figure VI-2 (a). Stratigraphic column and bio-stratigraphy are from Coccioni et al. (1998). The position of the 405-kyr eccentricity cycle is based on Martinez et al. (2015, 2020).

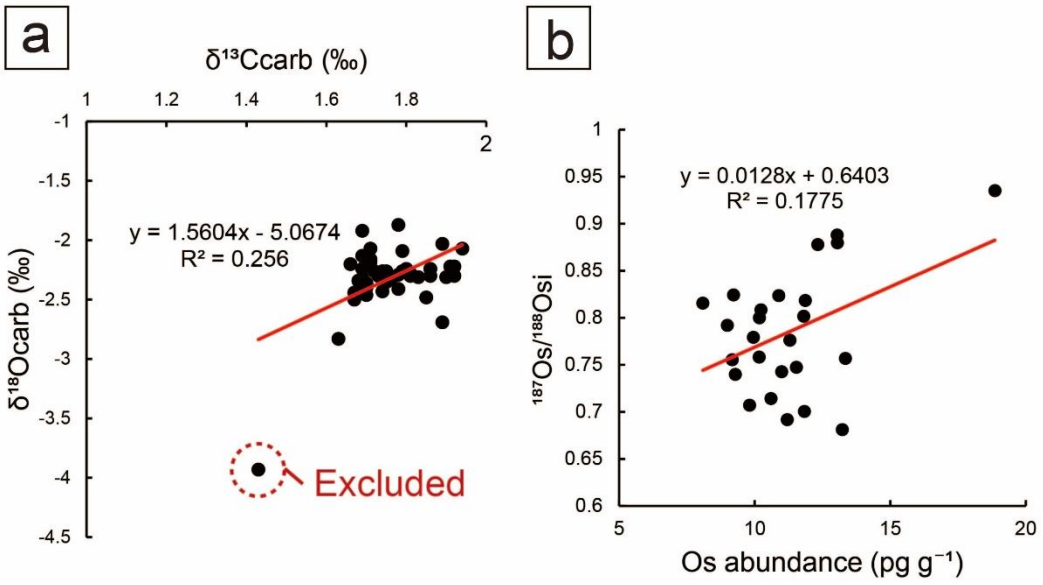

Figure V-3. (a) Cross plot of $\delta^{13}C_{carb}$–$\delta^{18}O_{carb}$, and (b) cross plot of $^{187}Os/^{188}Os_i$–Os abundance: A dashed red circle in (a) represents the excluded sample.

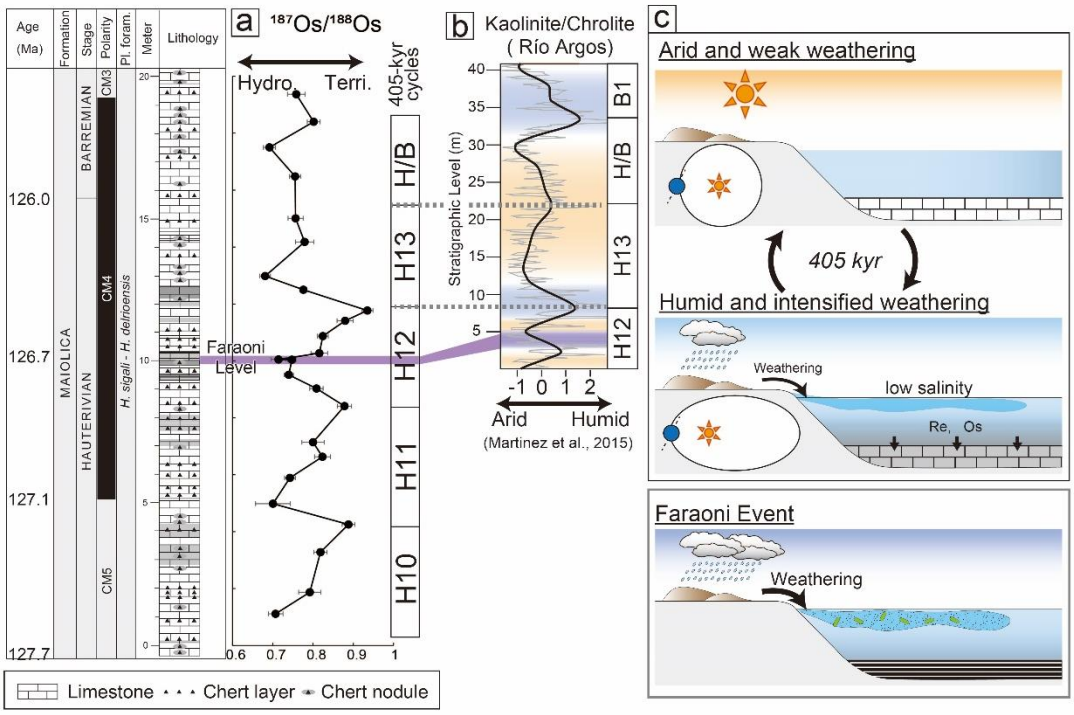

Figure V-4. Os isotopic information and its interpretation: (a) $^{187}Os/^{188}Os$ variation at the Fiume Bosso section, (b) kaolinite/chlorite values at the Río Agros section, Spain (Martinez et al., 2015), and (c) the conceptual model of the 405-kyr cycles of $^{187}Os/^{188}Os$ and clay mineral components.

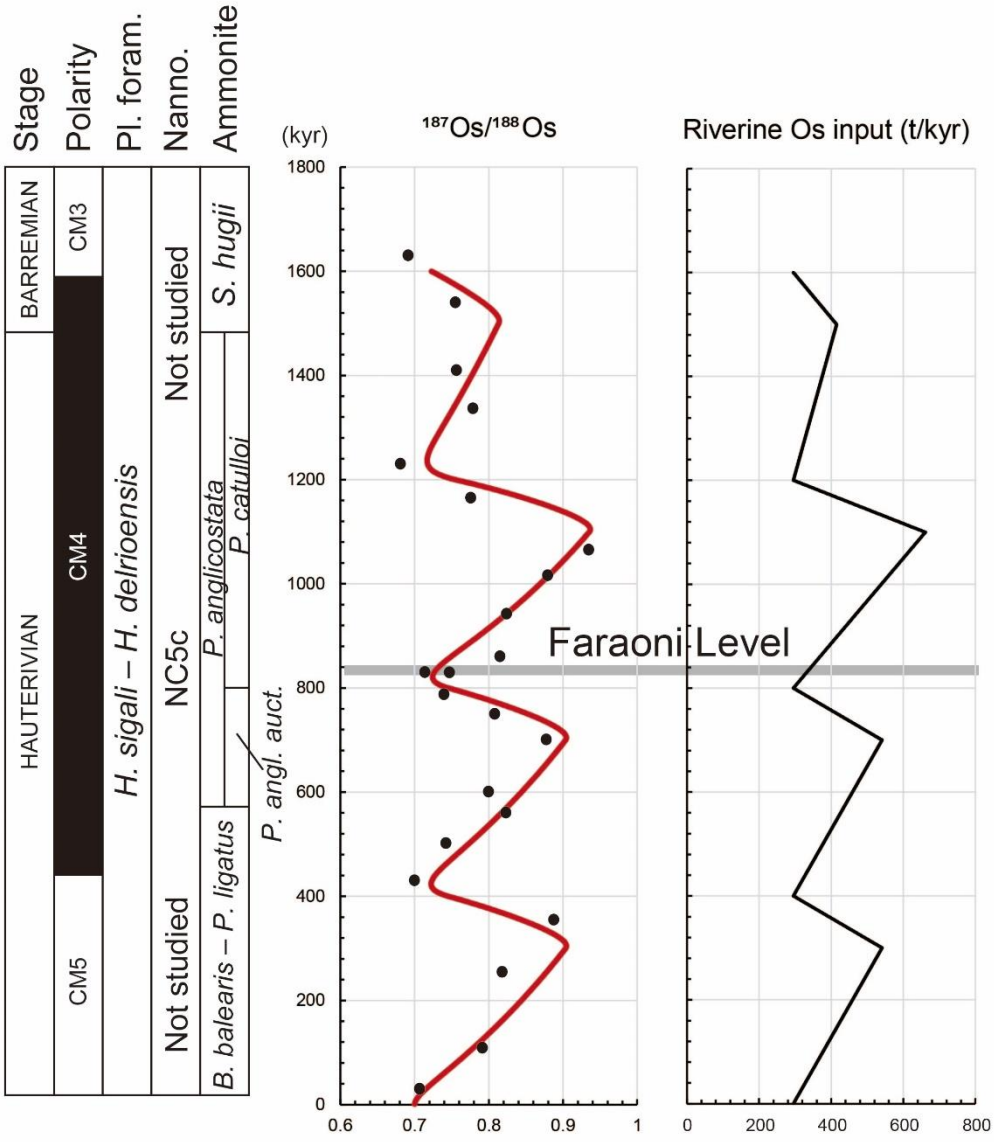

Figure V-5. (a) Reconstructed $^{187}Os/^{188}Os$ values (black circles) and the calculated values (red lines) using a simple box model, and (b) changes in the continental radiogenic Os input. Magnetostratigraphy and biostratigraphy is based on Coccioni et al. (1998). Ages of $^{187}Os/^{188}Os$ are corrected using the 405-kyr eccentricity cycles suggested by Martinez et al. (2015).

Supplementary Figures of Chapter V

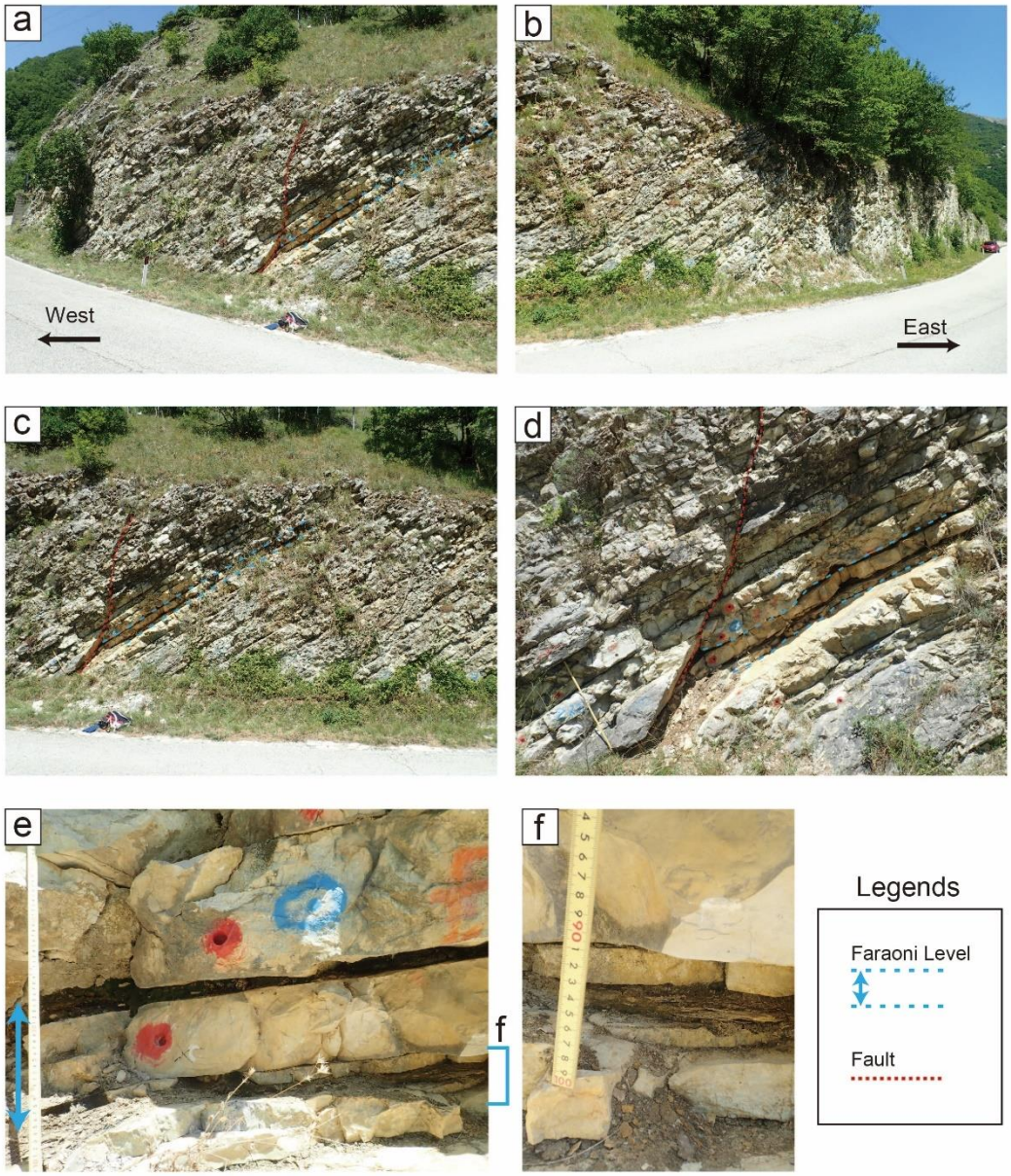

Supplemenmtary Figure V-S1. Outcrop imahes of the Fiume Bosso sections.

Supplementary Tables of Chapter V

ID	Lithology	δ^{13}C-PDB	δ^{18}O-PDB	δ^{13}C-1SD	δ^{18}O-1SD	Depth
		(‰)	(‰)	(‰)	(‰)	(m)
FB01	Limestone	1.67	-2.50	0.08	0.05	0
FB03	Limestone	1.86	-2.24	0.05	0.05	0.35
FB4A	Limestone	1.78	-1.87	0.08	0.05	1.11
FB05	Limestone	1.69	-2.13	0.08	0.05	1.34
FB06	Limestone	1.83	-2.31	0.05	0.05	1.87
FB07	Limestone	1.69	-1.92	0.08	0.05	2.66
FB08	Limestone	1.78	-2.41	0.08	0.05	3.28
FB09	Limestone	1.94	-2.07	0.05	0.05	4.25
FB13	Limestone	1.79	-2.26	0.08	0.05	4.6
FB14	Limestone	1.70	-2.36	0.08	0.05	4.98
FB15	Limestone	1.91	-2.22	0.05	0.05	5.32
FB17	Limestone	1.75	-2.35	0.08	0.05	5.89
FB18	Limestone	1.76	-2.33	0.08	0.05	6.25
FB20	Limestone	1.92	-2.22	0.05	0.05	6.63
FB22	Limestone	1.72	-2.26	0.08	0.05	7.14
FB24	Limestone	1.69	-2.24	0.08	0.05	7.79
FB28	Limestone	1.90	-2.31	0.05	0.05	8.41
FB30	Limestone	1.74	-2.26	0.08	0.05	9.03
FB32	Limestone	1.79	-2.09	0.08	0.05	9.37
FB35	Limestone	1.86	-2.30	0.05	0.05	9.51
FB37	Limestone	1.79	-2.26	0.08	0.05	9.6
FB38	Limestone	1.89	-2.69	0.08	0.05	9.88
FB40	Limestone	1.92	-2.30	0.05	0.05	9.96
FB41	Cherty limestone	1.75	-2.26	0.08	0.05	9.99
FB43	Limestone	1.66	-2.20	0.08	0.05	10.04
FB45	Limestone	1.85	-2.48	0.05	0.05	10.13
FB47	Limestone	1.71	-2.16	0.08	0.05	10.27
FB48	Limestone	1.81	-2.28	0.05	0.05	10.59
FB77	Limestone	1.70	-2.20	0.07	0.07	10.7
FB51*	Chert	1.43	-3.93	0.08	0.05	10.87
FB54	Limestone	1.69	-2.32	0.08	0.05	11.41
FB58	Limestone	1.78	-2.29	0.05	0.05	11.77
FB61	Limestone	1.71	-2.18	0.08	0.05	12.5
FB62	Limestone	1.67	-2.44	0.08	0.05	12.98
FB65	Limestone	1.80	-2.24	0.05	0.05	13.47
FB67	Limestone	1.81	-2.30	0.08	0.05	14.18
FB69	Limestone	1.69	-2.39	0.08	0.05	14.63
FB71	Limestone	1.89	-2.03	0.05	0.05	15.01
FB73	Limestone	1.63	-2.83	0.07	0.07	15.9
FB76	Limestone	1.70	-2.46	0.07	0.07	16.48
FB79	Limestone	1.70	-2.40	0.07	0.07	17.5
FB80	Limestone	1.74	-2.43	0.07	0.07	18
FB84	Cherty limestone	1.68	-2.34	0.07	0.07	18.4
FB86	Limestone	1.71	-2.07	0.07	0.07	18.9
FB87	Cherty limestone	1.73	-2.30	0.07	0.07	19.37

Note. FB51* was excluded from our discussion.

Supplementary Table V-S1. Carbon and oxygen isotopic data of carbonate

Sample ID	Lithology	Os	1sd	$^{187}Os/^{188}Osm$	1sd	Re	1sd	$^{187}Re/^{188}Os$	1sd	$^{187}Os/^{188}Osi$	1sd	Depth	Age
		(pg g-1)				(pg g-1)						(m)	(Ma)
FB4A	Limestone	9.8	0.11	0.718	0.018	10	1.8	5.3	1.0	0.707	0.018	1.11	130
FB6	Limestone	9.0	0.13	0.811	0.028	15	1.5	9.0	0.9	0.792	0.028	1.87	130
FB8	Limestone	11.9	0.10	0.857	0.016	40	2.6	17.8	1.2	0.818	0.016	3.28	130
FB9	Limestone	13.0	0.12	0.951	0.015	71	2.6	29.0	1.1	0.888	0.016	4.25	130
FB14	Limestone	11.8	0.25	0.716	0.043	17	1.5	7.4	0.7	0.700	0.043	4.98	130
FB17	Limestone	11.0	0.10	0.767	0.013	24	2.6	11.4	1.2	0.743	0.013	5.89	130
FB20	Limestone	10.9	0.11	0.856	0.020	31	1.3	15.0	0.7	0.823	0.020	6.63	130
FB22	Limestone	10.2	0.18	0.828	0.028	25	2.4	12.9	1.3	0.800	0.028	7.14	130
FB28	Limestone	12.3	0.10	0.929	0.017	55	1.6	23.7	0.7	0.878	0.018	8.41	130
FB30	Limestone	10.2	0.09	0.851	0.016	38	2.5	19.4	1.3	0.808	0.017	9.03	130
FB35	Limestone	9.3	0.09	0.772	0.011	26	1.2	14.6	0.7	0.740	0.011	9.51	130
FB43	Limestone	11.5	0.07	0.774	0.010	27	1.6	12.3	0.7	0.747	0.010	10.04	130
FB45	Limestone	10.6	0.13	0.744	0.019	28	1.4	13.7	0.7	0.714	0.019	10.13	130
FB47	Limestone	8.1	0.09	0.863	0.021	34	1.5	21.9	1.0	0.816	0.021	10.27	130
FB51	Limestone	9.2	0.05	0.850	0.013	21	1.4	12.0	0.8	0.824	0.013	10.87	130
FB54	Limestone	13.0	0.12	0.908	0.020	33	1.7	13.3	0.7	0.880	0.020	11.41	130
FB58	Limestone	18.9	0.14	0.972	0.014	61	1.6	17.3	0.5	0.935	0.014	11.77	130
FB61	Limestone	11.3	0.06	0.807	0.009	31	1.0	14.4	0.5	0.776	0.009	12.5	130
FB62	Limestone	13.2	0.10	0.696	0.013	18	1.3	6.9	0.5	0.681	0.013	12.98	130
FB67	Limestone	9.9	0.11	0.811	0.023	28	1.9	14.9	1.0	0.779	0.023	14.18	130
FB71	Limestone	13.3	0.12	0.782	0.019	30	1.8	11.8	0.7	0.757	0.019	15.01	130
FB76	Limestone	9.2	0.08	0.776	0.014	17	1.1	9.7	0.6	0.755	0.014	16.48	130
FB79	Limestone	11.2	0.11	0.707	0.015	15	1.7	6.9	0.8	0.692	0.015	17.5	130
FB84	Cherty limestone	11.8	0.08	0.837	0.016	36	1.7	16.1	0.7	0.802	0.016	18.4	130
FB87	Cherty limestone	10.2	0.12	0.792	0.022	30	1.4	15.4	0.8	0.758	0.022	19.37	130

Supplementary Table V-S2. Re-Os data of sedimentary rock samples from the Fiume Bosso section.

Sample ID	Os	1SD	$^{187}Os/^{188}Os_m$	1SD	Re	1SD	$^{187}Re/^{188}Os$	1SD	$^{187}Os/^{188}Os_i$	1SD	Depth	Age
	(pg g-1)				(pg g-1)						(m)	(Ma)
FB05	4.3	0.2	0.75	0.05	14	5	17	6	0.72	0.05	1.34	130
FB09	7.1	0.2	0.76	0.04	9	6	7	5	0.75	0.04	4.25	130
FB17	6.0	0.2	0.59	0.03	12	5	10	4	0.57	0.03	5.89	130
FB28	5.68	0.19	0.64	0.03	6	5	5	5	0.63	0.03	8.41	130
FB35	4.2	0.2	0.62	0.04	12	4	15	5	0.59	0.04	9.51	130
FB51	4.07	0.17	0.82	0.05	8	5	10	6	0.80	0.05	10.87	130
FB54	5.2	0.2	0.81	0.05	17	7	17	7	0.77	0.06	11.41	130
FB58	6.99	0.19	0.86	0.03	13	5	10	4	0.84	0.03	11.77	130
FB67	4.88	0.19	0.69	0.04	7	6	8	7	0.68	0.04	14.18	130
FB79	5.17	0.18	0.67	0.03	7	5	7	5	0.66	0.03	17.5	130

Supplementary Table V-S3. Re-Os data of sedimentary rock samples from the Fiume Bosso section extracted by the weak-leaching methods.

CHAPTER VI

Mid-Cretaceous marine Os isotope stratigraphy

This chapter is published at *Nature Communications*

Abstract of Chapter VI

During the mid-Cretaceous, the earth experienced several dramatic environmental perturbations, including an extremely warm climate and Oceanic Anoxic Events (OAEs). Submarine volcanic episodes associated with the formation of large igneous provinces (LIPs) may have triggered these events. The osmium isotopic ratio ($^{187}Os/^{188}Os$) is a suitable proxy for tracing hydrothermal activity associated with the LIPs formation, but $^{187}Os/^{188}Os$ data from the mid-Cretaceous are limited to short time intervals. Here I provide a continuous high-resolution marine Os isotopic record covering all mid-Cretaceous OAEs. Several mid-Cretaceous OAEs (OAE1a, Wezel and Fallot events, and OAE2) correspond to unradiogenic Os isotopic shifts, suggesting that they were triggered by massive submarine volcanic episodes. However, minor OAEs (OAE1c and OAE1d), which do not show pronounced unradiogenic Os shifts, were likely caused by other factors such as enhanced monsoonal activity. Because the subaerial LIPs volcanic episodes and Circum-Pacific volcanism correspond to the highest temperature and pCO_2 during the mid-Cretaceous, they may have caused the hot mid-Cretaceous climate.

VI.1. Introduction

The mid-Cretaceous (late Barremian to Turonian: ~121 to 90 Ma) is commonly regarded as one of the extremely warm geological intervals of the Phanerozoic Eon (Fig. I-3) (Huber et al., 2018). The oxygen isotopic ratio of carbonate ($\delta^{18}O_{carb}$) and TEX_{86}-Sea Surface Temperature (SST) proxies have revealed that the Cenomanian to Turonian climate was much warmer than that of today (Fig. I-3) (Friedrich et al., 2012; O'Brien et al., 2017; Huber et al., 2018). In addition, palaeobotanical (Herman et al., 2016) and palaeontological data from the Late Cretaceous (Turonian to Coniacian) (Vandermark et al., 2007) suggest that a warm climate prevailed in the Arctic region. The warm climate during the mid-Cretaceous is considered to have been sustained by a high pCO_2 (e.g., ~1500 ppmv during the Cenomanian: Hong and Lee, 2012) derived from active outgassing associated with the production of oceanic crust and/or massive volcanic activity (Larson, 1991).

As discussed in Chapter I-2, this greenhouse world experienced distinctive repeated oceanic anoxic events (OAEs), representing major perturbations in the carbon cycle characterized by deposition of organic-rich sediments in various depositional settings. Many organic-rich lithological intervals have been reported from the mid-Cretaceous Tethyan sedimentary record (Coccioni et al., 2012; Coccioni and Premoli Silva, 2015). The early Aptian OAE1a and latest-Cenomanian OAE2, the most prominent mid-Cretaceous OAEs, were typified by worldwide deposition of thick organic-rich horizons

(Fig. I-3) (Schlanger and Jenkyns, 1976). Additionally, other minor OAEs (e.g., OAE1b, OAE1c, and OAE1d), which have been reported mainly from the Tethys and Atlantic Oceans (Fig. I-3) (Huber et al., 2011; Coccioni et al., 2014, Coccioni and Premoli Silva, 2015, Matsumoto et al., 2021a) and a part of the Pacific region (Robinson, S.A. et al., 2008), are regarded as regional to supra-regional marine anoxic events. As mid-Cretaceous OAEs were often accompanied by intensive marine biotic crises (Leckie et al., 2002), understanding the factors that triggered the OAEs is important for unraveling the evolution of the Cretaceous marine ecosystem.

Massive volcanic events associated with the formation of large basaltic plateaus, called large igneous provinces (LIPs), are the most probable triggering factors of environmental perturbations (Leckie et al., 2002) (see Chapter I-3). Because the radiometric ages of the basaltic plateaus correspond to the sedimentary ages of major OAEs and the species turnovers of marine calcareous plankton, these events are thought to have been linked (Leckie et al., 2002; Erba, 2004; Matsumoto et al., 2020). Although Os isotopic variations ($^{187}Os/^{188}Os$) in the sedimentary record further support a causal linkage between the LIPs volcanism and the onset of marine environmental perturbations (Turgeon and Creaser, 2008; Tejada et al., 2009; Bottini et al., 2012), the Os isotopic record from the mid-Cretaceous is limited to the latest Barremian to early Albian and Cenomanian–Turonian transitional intervals (Matsumoto et al., 2020, 2021; Turgeon and Creaser, 2008; Tejada et al., 2009; Bottini et al., 2012), and these records are not sufficiently long to elucidate the evolution of the prolonged hydrothermal activity associated with volcanic episodes during the mid-Cretaceous. Here, I reconstruct a continuous marine Os isotopic record from the middle Albian to the uppermost Cenomanian using a pelagic sedimentary record from the Umbria–Marche Basin (central Italy) and the borehole core from Ocean Drilling Program (ODP) Site 763 (Exmouth Plateau, southeast Indian Ocean) (Fig. VI-1). Integrating the new data with previously published information, I provide a continuous Os isotopic record from the late Barremian to early Turonian, covering all mid-Cretaceous OAEs, and discuss the long-term hydrothermal record of the mid-Cretaceous.

VI.2. Samples and geological setting

Limestone, marlstone, mudstone, and black shale samples ranging from the middle Albian to the upper Cenomanian were collected from the PLG core (Coccioni et al., 2012) and the Bottaccione section (Coccioni and Premoli Silva, 2015) in the Umbria–Marche Basin (Central Italy). The Umbria–Marche sedimentary record comprises pelagic sedimentary facies of the Tethyan Ocean (Fig. VI-1) and is characterized by a lack of

coarse terrigenous materials. The PLG core is a borehole core drilled near the PLG section (Coccioni et al., 2014) that covers the uppermost Barremian to the lowest Cenomanian. The Bottaccione section is a pelagic sedimentary sequence located in the same basin that includes, for the Cretaceous, the uppermost Albian to the Maastrichtian (Coccioni and Premoli Silva, 2015).

Using lithostratigraphy, biostratigraphy, and carbon and osmium isotopic stratigraphy (Coccioni and Galeotti, 2003; Coccioni et al., 2012; Coccioni and Premoli Silva, 2015), I reconstruct a continuous composite stratigraphic record of the Umbria–Marche Basin during the mid-Cretaceous (Fig. VI-2). The upper Barremian of the composite record belongs to the Maiolica Formation and consists of white cherty limestone cyclically intercalated with thin (~few centimeters) black shale layers (Coccioni et al., 2012). The ~2-m-thick organic-rich interval, known as the Selli Level (Coccioni et al., 1987) occurs around the Barremian–Aptian boundary and records the regional sedimentary expression of OAE1a. Above the Selli Level, the Aptian sedimentary record consists of marly limestone with some black shale layers (e.g., the Wezel and Fallot Levels; Matsumoto et al., 2021a) belonging to the Marne a Fucoidi Formation (Coccioni et al., 2012). The Fallot and Wezel Levels are only reported from the Tethyan Region. However, their accurate extent has not been constrained so far because of the limited geological research focusing on their equivalent intervals outside the Tethyan region. Several pronounced organic-rich intervals (i.e., Jacob, Kilian, Urbino, and Leenhardt Levels), collectively called OAE1b, appear around the Aptian–Albian boundary (Coccioni et al., 2012, 2014). The Albian sediments consist of mudstones intercalated with cyclic thin (~few centimeters) black shale layers (Coccioni et al., 1987, 2012, 2014). A peculiar ~2-m-thick interval in the upper Albian, called the Amadeus segment (Coccioni and Galeotti, 1993), is located in the middle part of OAE1c that spans almost the entire *Biticinella breggiensis* planktonic foraminiferal Zone (Arthur et al., 1990; Coccioni et al., 2012). The muddy interval ends in the upper Albian, and the lithology changes to the white and reddish limestones of the Scaglia Bianca Formation (Coccioni et al., 2015). The last cyclic upper Albian organic-rich layers are known as the Pialli Level (Coccioni, 2001), which represents the regional sedimentary expression of OAE1d (Coccioni and Premoli Silva, 2015). At the end-Cenomanian, a thick organic-rich interval, known as the Bonarelli Level, is the regional sedimentary expression of OAE2 (Coccioni and Premoli Silva, 2015). Osmium and carbon isotopic records from the upper Barremian to lower Albian in the Umbria–Marche Basin have already been reported (Turgeon and Creaser, 2008; Tejada et al., 2009; Coccioni et al., 2014; Li et al., 2016; Savian et al., 2016; Matsumoto et al., 2020, 2021; Percival et al., 2021).

Sedimentary rock samples were also collected from ODP Site 763B in the western part of the central Exmouth Plateau (20°35.21′S, 112°12.51′E, northwestern Australian margin, subtropical Indian Ocean) at 1368 m below the sea surface (Haq et al., 1990). The sediments were deposited at upper bathyal depth (~200–500 m below sea level; Haq et al., 1990) and consist of calcareous claystone to clayey nannofossil chalk. The Aptian–Albian boundary is estimated to lie between cores 37 and 36, but the exact position is uncertain (Fig. VI-2b) (Huber and Leckie, 2011). The Cenomanian–Turonian boundary falls in the gap between cores 23 and 22 (Fig. VI-2b). I collected sedimentary rock samples from ODP Site 763B cores 36 to 21, which cover the middle Albian to lowest Turonian.

VI.3. Method

VI.3.1. Re–Os analysis

Cleaned sedimentary rocks were powdered in an agate mill. After spiking with ^{190}Os- and ^{185}Re-rich solutions, Re and Os of the carbonate rocks were extracted by the inverse aqua regia digestion method. Osmium abundances and isotopic compositions were determined by negative thermal ionization–mass spectrometry (TRITON, Thermo Fisher Scientific, USA) at the Japan Agency for Marine-Earth Science and Technology (JAMSTEC, Japan). The abundances of Re were determined by a quadrupole inductively coupled plasma-mass spectrometer (iCAP Qc, Thermo Fisher Scientific, USA) at JAMSTEC. Initial ^{187}Os/^{188}Os values (^{187}Os/^{188}Os$_i$) were calculated from the measured ^{187}Os/^{188}Os and ^{187}Re/^{188}Os values, the estimated ages (Supplementary Tables VI-S1–S3), and the ^{187}Re decay constant (1.666×10^{-11} yr^{-1} : Smoliar et al., 1996). The average procedural blanks of Os and ^{187}Os/^{188}Os were 0.8 ± 0.5 pg and 0.13 ± 0.04, respectively. The average Re procedural blank was 14 ± 11 pg. Detailed analytical methods are described in Chapter II-4.3.

VI.3.2. Stable carbon isotopic ratio of carbonate

The stable carbon isotope ratio of carbonate ($\delta^{13}C_{carb}$) was measured with an isotope ratio-mass spectrometer (Delta V plus, Thermo Fisher Scientific, USA), equipped with an automated carbonate reaction device (GasBench II, Thermo Fisher Scientific, USA), at the Atmosphere and Ocean Research Institute, University of Tokyo (Japan). Isotopic values are reported in delta notation with respect to PeeDee Belemnite (PDB), based on an NBS-19 value of +1.95‰ for $\delta^{13}C$. External reproducibility was estimated from repeated analysis of the NBS-19 standard (n =20) within an analytical batch; the typical values were better than 0.05‰ and 0.08% for $\delta^{18}O$ and $\delta^{13}C$, respectively (1 SD)

(Supplementary Tables VI-S2 and S3). Detailed explanation is described in Chapter III-3.

VI.4. Results

The $\delta^{13}C_{carb}$ record of sedimentary rock samples from the Umbria–Marche Basin (PLG core and Bottaccione section) shows a gradual decline from ~3‰ in the middle Albian (~40 m: Fig. VI-2) to 2.1‰ in the Pialli Level (~90 m: Fig. 2, Supplementary Tables 1 and 2). The $\delta^{13}C_{carb}$ curve shows a slight positive excursion (~0.4‰: Fig. VI-2) within the Pialli Level (~90 m). Above this level, $\delta^{13}C_{carb}$ shows a gradual positive shift from 2‰ (~110 m) to 3‰ toward the end of Cenomanian (~130 m) (Fig. VI-2a). These data are concordant with those of previous studies (Coccioni and Premoli Silva, 2015; Gambacorta et al., 2015). At ODP Site 763B, $\delta^{13}C_{carb}$ shows a gradual negative shift from ~3‰ at the Aptian–Albian boundary (~520 meters below the sea level [mbsf]) to 1‰ around the Albian–Cenomanian boundary (~434 mbsf) (Fig. VI-2b). The $\delta^{13}C_{carb}$ values of some core samples are highly negative (−2‰ to 0.5‰), which might indicate some diagenetic alteration possibly caused by remineralization of organic matter. The $\delta^{13}C_{carb}$ values increase during the Cenomanian (from 420 to 410 mbsf), which are concordant with the Tethyan sedimentary record (Fig. VI-2b). The $\delta^{13}C_{carb}$ data exhibit a large negative shift from ~2‰ at 410 mbsf to −3‰ at the Cenomanian–Turonian boundary (~380 mbsf) (Fig. VI-2b). Albian–Cenomanian sedimentary rock samples from ODP Site 762C (western part of the Exmouth Plateau) also show highly negative $\delta^{13}C_{carb}$ values, which are interpreted to indicate diagenetic alteration (Falzoni et al., 2016). Although the exact mechanism is unclear at present, it is likely that the carbon isotopic records at ODP Sites 763B and 762C have experienced a similar diagenetic overprint around the Cenomanian–Turonian boundary.

In the Umbria–Marche sedimentary record (PLG core and Bottaccione section), $^{187}Os/^{188}Os_i$ varies from 0.37 to 0.75, except for one sample (BTT450) with an extraordinarily high value (~1.1) and a relatively high $^{187}Re/^{188}Os$ ratio (~10) (Supplementary Tables VI-S3 and 4). Because the Re–Os information of outcrop samples with high Re/Os values can be easily altered by weathering (Matsumoto et al., 2020), I considered this point as an outlier and excluded it from the discussions. The $^{187}Os/^{188}Os_i$ values of ODP Site 763B span from 0.47 to 0.75; this range is concordant with the Tethyan sedimentary record (Figs. VI-2 and 3).

VI.5. Discussion

The composite mid-Cretaceous Os isotopic data reveal that pronounced unradiogenic

shifts (i.e., lower values) occurred during the early to mid-Aptian, late Albian, and end-Cenomanian, and radiogenic shifts took place at the Aptian–Albian boundary and during the Cenomanian (Figs. VI-2 and 3a). As marine Os isotopic ratios ($^{187}Os/^{188}Os$) represent the balance between unradiogenic Os input (mantle and extraterrestrial material) and radiogenic Os input (continental material), these Os isotopic variations reflect changes in the Os fluxes from these sources.

In the uppermost Barremian, $^{187}Os/^{188}Os_i$ exhibits relatively radiogenic values (~0.6 to 0.7) in the Umbria–Marche Basin (Gorgo a Cerbara section and PLG core) and the Pacific record (Deep Sea Drilling Project [DSDP] Site 463) (Figs. VI-2 and 3a) (Tejada et al., 2009; Bottini et al., 2012; Percival et al., 2021). On the contrary, $^{187}Os/^{188}Os_i$ shows sharp drops to ~0.2–0.36 in the lower to mid-Aptian black shales, namely the Selli, Wezel, and Fallot Levels (Figs. VI-2 and 3a) (Tejada et al., 2009; Bottini et al., 2012; Matsumoto et al., 2021; Percival et al., 2021). As the sedimentary ages of these unradiogenic Os isotopic shifts correspond to the radiometric ages of the Ontong Java, Manihiki, and Hikurangi Plateaus, which once formed a single large oceanic plateau called "Ontong Java Nui" (OJN) (Fig. 3a, e), these unradiogenic Os isotopic shifts were likely triggered by a massive input of mantle-derived unradiogenic Os through hydrothermal activity and warm- and low-temperature submarine weathering at OJN (Tejada et al., 2009; Bottini et al., 2012; Matsumoto et al., 2021; Bauer et al., 2021). This possibility is further supported by $^{87}Sr/^{86}Sr$ and sulfur isotopic evidence (Fig. VI-3b, c). Hydrothermal fluid is characterized by unradiogenic $^{87}Sr/^{86}Sr$ and more negative $\delta^{34}S$ values than those of seawater; thus, the unradiogenic $^{87}Sr/^{86}Sr$ values (e.g., Fig. VI-3b) (Bralower et al., 1997) and negative sulfur isotopic ($\delta^{34}S_{barite}$) excursion (Fig. VI-3c) (Paytan et al., 2020) during the early to mid-Aptian further support the hypothesis of enhanced hydrothermal activity and of warm- and low-temperature submarine weathering.

Lechler et al. (2015) suggested that, in addition to hydrothermal activity, subaerial weathering of OJN basalt could have played a significant role in causing large unradiogenic shifts. However, modeling studies have indicated that weathering of a huge amount (~30%–60%) of the Ontong Java Plateau would have been required to explain such large unradiogenic Os isotopic shifts (Tejada et al., 2009). Given that most of the plateau was emplaced under submarine conditions (Shipboard Scientific Party, 2001), I infer that hydrothermal activity was likely the major cause of early to mid-Aptian unradiogenic Os isotopic shifts.

During OAE1b, the $^{187}Os/^{188}Os_i$ values of Tethyan and Pacific sedimentary records show a radiogenic shift from 0.5 to 0.7 (Fig. VI-2) (Matsumoto et al., 2020). The new $^{187}Os/^{188}Os_i$ data from ODP Site 763B also reveal that radiogenic $^{187}Os/^{188}Os_i$ values

prevailed during the early Albian (Figs. VI-2 and 3a). The radiogenic shift of $^{187}Os/^{188}Os_i$ corresponds to the $^{40}Ar/^{39}Ar$ ages of the Kerguelen Plateau basalt (Fig. VI-3) (Coffin et al., 2002; Duncan, 2002; Jiang et al., 2021) and an increase in temperature, as indicated by $\delta^{18}O_{carb}$ of belemnites, the TEX_{86}-SST index, and the demise of glendonite in the Arctic region (Fig. VI-3a, d, e) (McAnena et al., 2013; Bodin et al., 2015; Herrle et al., 2015). Thus, the radiogenic Os isotopic shift during OAE1b has been interpreted as indicating enhanced continental weathering triggered by global warming caused by outgassing from volcanic episodes at the Kerguelen Plateau (Matsumoto et al., 2020). As most of the Kerguelen Plateau was emplaced subaerially at a high latitude in the Indian Ocean, unradiogenic Os inputs from hydrothermal activity and weathering of the basaltic rock were insignificant and did not influence the marine Os isotopic record (Matsumoto et al., 2020). In addition, $^{87}Sr/^{86}Sr$ values show a radiogenic shift during the early Albian (Bralower et al., 1997), which also supports enhanced continental weathering during OAE1b (Matsumoto et al., 2020).

The $^{187}Os/^{188}Os_i$ data exhibit two pronounced unradiogenic shifts during OAE1c (Figs. VI-2 and 3a). These excursions, which were observed in both the Tethyan realm (Umbria–Marche Basin) and at the Indian realm (ODP Site 763B) (Figs. VI-2 and 3), can be ascribed to a decrease in the radiogenic Os input through continental weathering or an increase in the unradiogenic Os input from the mantle or extraterrestrial material. To explain the unradiogenic shifts solely by the decreased continental weathering, a rapid decrease in temperature is required; however, no data support this possibility. Therefore, the two unradiogenic shifts may represent an increase in the input of unradiogenic Os. One of the possible sources of unradiogenic Os is extraterrestrial materials, but the unradiogenic shifts during OAE1c are much longer and smaller (~1 Myr and $^{187}Os/^{188}Os$ ~0.4) than those during massive meteorite impacts (~200 kyr, $^{187}Os/^{188}Os$~0.1 to 0.2) (Ravizza and VanderHaar, 2012). In addition, subaerial basaltic eruptions at low latitudes have not been reported during OAE1c. Thus, the most probable candidate for the unradiogenic shifts during OAE1c is an increase in hydrothermal activity. Indeed, $\delta^{34}S_{barite}$ data show negative values during OAE1c (Fig. VI-3c), which implies hydrothermal sulfur input. However, the $^{87}Sr/^{86}Sr$ values do not show a significant unradiogenic shift, possibly because of the long residence time of Sr (~3 Myr) compared to that of Os (20–50 kyr: Levasseur et al., 1999) and the volatile feature of highly oxidized form of OsO_4.

The estimated ages of the Hikurangi Plateau (Hoernle et al., 2010), Kerguelen Plateau (Coffin et al., 2002; Duncan, 2002; Jiang et al., 2021), Hess Rise (Vallier et al., 1983), and Agulhas Plateau (Parsiegla and Uenzelmann-Neben, 2008) cover the sedimentary

ages of OAE1c (Fig. VI-3). Thus, the hydrothermal activity associated with formation of these oceanic plateaus may have triggered the unradiogenic Os isotopic shifts. However, the age constraints on the Hikurangi Plateau, Hess Rise, and Agulhas Plateau are too poor to conclude when the hydrothermal activity occurred, and further studies are required to determine the exact source of these unradiogenic Os shifts.

After OAE1c, the $^{187}Os/^{188}Os_i$ values gradually shift to be more radiogenic ~0.7 (Fig. VI-3a), which may reflect weakening of hydrothermal activity. This possibility is supported by the sulfur isotopic ratio and strontium isotopic evidence: $\delta^{34}S_{barite}$ shows a positive excursion during the late Albian (Fig. VI-3c) that can be interpreted as a decrease in the hydrothermal sulfur input with low $\delta^{34}S$ (Laakso et al., 2020). The positive excursion of $\delta^{34}S_{barite}$ can be also explained by an increase in sulfur reduction during the early Cenomanian. However, considering the organic-rich sediments are more pronounced during Albian than Cenomanian at the Umbria–Marche Basin, sulfate reduction should also have been more significant during Albian than Cenomanian. Therefore, I consider that the decrease in the volcanic sulfur is a more important factor for explaining the positive $\delta^{34}S$ excursion than the sulfate reduction. The positive excursion of $\delta^{34}S_{barite}$ during the Cenomanian postdates the cessation of the Os isotopic fluctuations (Fig. VI-3a,c). Since the residence time of sulfur in the ocean is longer than Os, the onset of the changes of $\delta^{34}S_{barite}$ could have been more gradual and possibly postdated the radiogenic Os isotopic shift. In addition, $^{87}Sr/^{86}Sr$ show radiogenic values (Fig. VI-3b) that also supports weakening of the input of hydrothermal unradiogenic Sr (Bralower et al., 1997). The $^{187}Os/^{188}Os$ values do not show any significant fluctuation during OAE1d, which likely suggests the absence of intensive submarine volcanism.

The $\delta^{18}O_{carb}$ values of benthic and planktonic foraminifera suggest a temperature increase during the Cenomanian, with the warmest conditions recorded from the Cenomanian to Turonian (Friedrich et al., 2012; Huber et al., 2018). The enhanced chemical weathering caused by the warm climate may have accelerated and intensified inputs in radiogenic continental Os, which may also have contributed to the radiogenic $^{187}Os/^{188}Os_i$ shifts after OAE1c (Fig. VI-3).

Stable radiogenic $^{187}Os/^{188}Os_i$ values during the Cenomanian (~0.7) were followed by a sudden drop just below the OAE2 interval (Fig. VI-3) (Turgeon and Creaser, 2008; Du Vivier et al., 2014). As the sedimentary ages of the unradiogenic shifts correspond to the $^{40}Ar/^{39}Ar$ ages of the Caribbean Plateau (Sinton et al., 1998), the unradiogenic shifts can be explained by an increase in the unradiogenic Os input associated with emplacement of the submarine basaltic plateau. This possibility is further supported by the unradiogenic shift of $^{87}Sr/^{86}Sr$ after OAE2 (Bralower et a., 1997). Although the

weathering of the basaltic plateau may have contributed to the unradiogenic Os isotopic shifts, geological evidence of how much of the plateau was exposed subaerially is still lacking, precluding further discussion of this possibility. $\delta^{34}S_{barite}$ data around OAE2 are scarce, but $\delta^{34}S$ of pyrite and carbonate-associated sulfates (CAS) around OAE2 (Paytan et al., 2020) has been intensively investigated instead. $\delta^{34}S_{CAS}$ and $\delta^{34}S_{pyrite}$ showed a positive excursion (2–4‰) across the OAE2, suggesting an enhanced sulfate reduction (Owens et al., 2013). Considering the global oceanic anoxia and short duration of unradiogenic Os isotopic shift during OAE2 (~600 kyr), the effect of the sulfate reduction could have overwhelmed the effect of volcanic sulfur input.

Previous studies have revealed that the onsets of the major Cretaceous OAEs (OAE1a, Wezel, Fallot, and OAE2) in the Tethyan region correspond to unradiogenic Os isotopic shifts (Turgeon and Creaser, 2008; Tejada et al., 2009; Matsumoto et al., 2020, 2021a), which is compatible with synchronicity between massive submarine volcanism and OAEs. During these OAEs, unradiogenic Os shifts are often accompanied by the negative carbon isotopic excursions (Turgeon and Creaser, 2008; Tejada et al., 2009; Bottini et al., 2012, Percival et al., 2021), implying the volcanic events supply mantle-derived CO_2 with negative carbon isotopic values. Besides, 2 to 16 times increase in the input of mantle-derived Os are required to explain these unradiogenic Os isotopic shifts. Considering that Os could have been supplied in highly volatile oxidized form (OsO_4), enormous amounts of other volatile trace metal elements could have been also injected into the ocean-atmosphere system during the most prominent unradiogenic Os isotopic shifts in these OAEs (OAE1a, Wezel and Fallot events, and OAE2). This possibility supports the linkage between bio-limiting trace metal input and the high productivity (Erba et al., 2015). As explained in Chapter I-3, The massive volcanic events released large quantities of greenhouse gases into the atmosphere that caused an increase in the temperature; as a result, enhanced continental weathering supplied the nutrients to the ocean that led to enhanced primary productivity and ultimately to ocean eutrophication (Erba et al., 2004). In addition, the volcanic activity could have provided iron and other bio-limiting trace metals to the ocean, which might have further stimulated the primary productivity (Erba, 2004). In addition, the warming of the deep-, intermediate-, and surface- ocean could have disrupted the thermocline, which triggered sustained upwelling and maintained the high primary productivity (Erba, 2004). The decomposition of a large amount of organic matter at the seafloor consumed oxygen and thickened the oxygen minimum zones.

The new Os isotopic data revealed that multiple volcanic signals also correspond to the base and top of OAE1c (Figs. VI-2 and 3a); however, the unradiogenic shift does not

cover the most prominent organic-rich interval of the OAE1c, called the Amadeus segments (Figs. VI-2 and 3a). In addition, $^{187}Os/^{188}Os$ values do not show any significant fluctuation during OAE1d, which suggests the absence of intensive submarine volcanic activity. Therefore, I consider that the onsets of OAE1c and OAE1d were unrelated to massive submarine volcanism, unlike other major mid-Cretaceous OAEs. A mercury anomaly has been reported just below the OAE1d horizon at the Youxia section, the eastern Tethys, which has been interpreted as the submarine volcanic eruption at the Kerguelen Plateau (Yao et al., 2021). However, considering the lack of Os isotopic perturbations around OAE1d, this mercury enrichment is probably more related to local perturbation with limited influence on global climate. Major Cretaceous OAEs (OAE1a, Wezel, Fallot, and OAE2) are represented by thick organic-rich intervals, whereas the sedimentary expression of OAE1c and OAE1d in the Umbria–Marche Basin consist of cyclic alternations of thin black shales (Coccioni et al., 2012). Similar cyclic intercalations of thin black shale layers in a carbonate sequence have been observed in the Valanginian–Barremian, Albian, and upper Cenomanian in the Umbria–Marche Basin (Fig. VI-3) (Coccioni and Galeotti, 2003; Coccioni et al., 2012). During the Quaternary, astronomically modulated monsoonal activity cyclically enhanced the hydrology of the Mediterranean Sea at low latitude, which supplied freshwater and nutrients to the peri-continental ocean. The resulting input of terrigenous organic matter, stratification, and slightly enhanced productivity led to oxygen-depleted bottom-water conditions and the deposition of organic-rich sediments dominated by the terrigenous origin (Bornemann et al., 2005; Toucanne et al., 2015). Thus, the lack of the unradiogenic Os isotopic shift and the cyclic deposition of thin black shale layers during OAE1c and OAE1d may suggest a regional-scale weak marine anoxia caused by monsoonal activity modulated by astronomical cycles as proposed by previous studies (Bornemann et al., 2005) rather than an episodic large volcanic event (Yao et al., 2021). The increase in the primary productivity was not significant at the Tethyan region during OAE1d (Bornemann et al., 2005). However, a small positive carbon isotopic excursion during OAE1d suggests a slight increase in the primary production (Fig. VI-2). In addition, organic-rich sediments are reported from the Calera Limestone in California, which was deposited in the Pacific Ocean, and thus the oxygen-depleted condition could have prevailed in the East Pacific as well (Robinson, S.A. et al., 2008). Thus, the latter process can also cause a supra-regional increase in productivity to some extent.

The organic geochemical properties of mid-Cretaceous black shale horizons are also consistent with differences in the origins of mid-Cretaceous OAEs. Erbacher et al.[56] proposed to classify mid-Cretaceous OAEs into two types on the basis of organic

geochemistry and radiolarian occurrences: (1) productivity (P-) OAEs (e.g., OAE1a, OAE1d, and OAE2); and (2) detrital (D-) OAEs (e.g., OAE1c). Organic matter deposited in the Umbria–Marche Basin during OAE1a and OAE2 is close to Type II kerogen, which is derived from marine organisms (Erbacher et al., 1996), whereas organic matter of the OAE1c and OAE1d black shales is classified as Type III kerogen, which has a continental origin (Erbacher et al., 1996). However, OAE1d and part of OAE2 are classified as P-OAE, although their organic matter was identified as Type III kerogen of continental origin (Erbacher et al., 1996). To solve this contradiction, the classification of OAE types should be modified. Thus, on the basis of the organic-geochemistry and Os isotopic data, I here propose to classify the mid-Cretaceous OAEs into: (1) volcanic-induced OAEs triggered by episodic burial of organic-rich sediments derived from marine organisms; and (2) non-volcanic-induced OAEs that are mainly caused by water-mass stratification triggered by freshwater input caused by cyclic intensification of monsoonal activity. The organic matter of monsoon-induced OAEs is mainly composed of terrestrial materials and an increase in the productivity is less significant (Bornemann et al., 2005).

Among the mid-Cretaceous OAEs, OAE1b is a problematic example. In the Umbria–Marche Basin OAE1b is composed of several major organic-rich horizons (Jacob, Kilian, Urbino, and Leenhardt Levels) intercalated with numerous thin black shale horizons (Huber et al., 2011). Although the short unradiogenic Os isotopic shifts have been reported around the Kilian Level, other black shale horizons lack unradiogenic Os isotopic shifts (Matsumoto et al., 2020). Besides, the upper part of the OAE1b is characterized by the temporal radiogenic Os isotopic excursions, which is a different feature from other mid-Cretaceous OAEs. Since OAE1b continued for several million years and contains different types of organic-rich sediments, I considered that OAE1b may be a mixture of volcanic- and monsoon-induced OAEs.

The mid-Cretaceous has often been regarded as a warm geological interval caused by high pCO_2, which was sustained by enhanced hydrothermal activity associated with oceanic crustal production (Larson, 1991). Considering the extremely high temperature and pCO_2 during major OAEs (OAE1a and OAE2) (O'Brien et al., 2017; Naafs et al., 2016; Bottini and Erba, 2018), this model seems correct over a short time scale. However, the model cannot explain the long-term temperature variations of the mid-Cretaceous. The $^{187}Os/^{188}Os$, $^{87}Sr/^{86}Sr$, and $\delta^{34}S$ records suggest an intensification of hydrothermal activity during the Aptian, corresponding to the relatively cool interval during the mid-Cretaceous (Bodin et al., 2015; O'Brien et al., 2017) (Fig. VI-3). Furthermore, the highest temperature during the mid-Cretaceous was recorded during the Cenomanian–Turonian.

However, no long-term hydrothermal activity associated with LIPs formation has been reported during the Cenomanian (Fig. VI-3).

This contradiction may be explained by the location and style of the volcanic activity. When a basaltic plateau was emplaced under submarine conditions, outgassing from submarine volcanism and the expansion of the volatile to shallower waters could have been suppressed by high hydrostatic pressure (Cas and Simmons, 2018), and, thus, they may not have contributed to the long-term increase in the pCO_2. Indeed, most of OJN was emplaced under submarine conditions during the Aptian and may not have caused a long-term increase in pCO_2. The temperature started to increase at the Aptian–Albian boundary and reached a maximum at the Cenomanian, which corresponded to the subaerial eruption of the Kerguelen Plateau (Fig. VI-3). As most of the Kerguelen Plateau was emplaced under subaerial conditions, a large amount of CO_2 could have been directly released into the atmosphere, and could have contributed to the increase in pCO_2 and temperature. During the Cenomanian, subaerial volcanic eruptions occurred at Kerguelen (Coffin et al., 2002; Duncan, 2002; Jiang et al., 2021) and the High Arctic Large Igneous Province (Naber et al., 2020), which could have caused the increase in temperature during the Cenomanian–Turonian interval. In addition, subaerial volcanic activity in the circum-Pacific region was active during the mid-Cretaceous. For example, the volcanic events associated with the formation of Japanese granitoids were most active during the Cenomanian to Turonian (95–80 Ma) (Fig. VI-3f) (Takagi et al., 2004), approximately corresponding to the mid-Cretaceous thermal maximum. At the Cenomanian–Turonian boundary, the massive submarine volcanic eruptions at the Caribbean Plateau could have further contributed to the intensification of global warming during the OAE2 (Robinson, S.A. et al., 2019). I conclude that massive and continuous subaerial volcanism could have contributed to the high pCO_2 and high temperature, whereas submarine volcanism had a minor effect on the long-term increase in temperature. The low pCO_2 interval during the late Aptian is associated with the substantial carbonate phytoplankton production called *Nannoconus truitti* acme (Erba et al., 2015). Therefore, the eruption style (e.g., submarine or subaerial) and its duration could have potentially influenced not only the temperature variations but also the diversity of calcareous planktons during the mid-Cretaceous.

At present, the compilation of circum-Pacific volcanic ages (especially North and South America) is not enough to correlate them to the mid-Cretaceous environmental perturbations. Besides, volcanic events forming kimberlites could have released a large amount of CO_2 into the atmosphere although the duration of the volcanic events has not been constrained so far. Therefore, determining the frequencies of these volcanic events will further confirm the relationship between subaerial volcanic events and long-term

Cretaceous environmental perturbations.

VI.6. Conclusion

I measured Os isotopic ratios ($^{187}Os/^{188}Os_i$) of lower Albian to lower Turonian sedimentary rock samples collected from the Poggio le Guaine (PLG) core and the Bottaccione section (Umbria–Marche Basin) and ODP Site 763 (Indian Ocean). Combining the new data with previously published information, I, for the first time, constructed a high-resolution mid-Cretaceous (~120 to 94 Ma) Os isotopic record covering all major OAEs in the interval. The $^{187}Os/^{188}Os_i$ values display the pronounced unradiogenic shifts during the early to mid-Aptian, late Albian, and end-Cenomanian, which may reflect massive hydrothermal activity associated with the formation of LIPs. In addition, temporal radiogenic $^{187}Os/^{188}Os_i$ shifts observed during the early Albian can be interpreted as due to an enhancement of continental weathering.

During the mid-Cretaceous, the OAEs are classified into: (1) volcanic-induced OAEs (e.g., OAE1a, Wezel Level, Fallot Level, and OAE2); and (2) non-volcanic-induced OAEs (OAE1c and OAE1d).

The warmest interval during the mid-Cretaceous corresponds to a phase of enhanced subaerial volcanic episodes with no evidence of long-term enhanced hydrothermal activity. Thus, I conclude that subaerial volcanic episodes and the subsequent outgassing were the main cause of the warm mid-Cretaceous climate.

Figures of Chapter VI

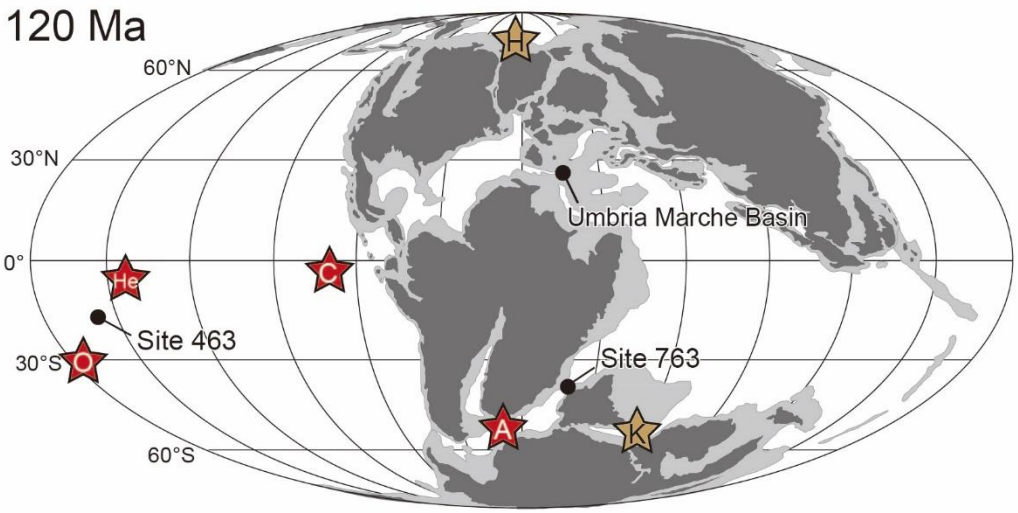

Figure VI-1. Paleogeographical reconstruction at 120 Ma and sampling sites modified from Matsumoto et al. (2020): A: Agulhas Plateau, C: Caribbean Plateau, K: Kerguelen Plateau, H: High Arctic Large Igneous Provinces, He: Hess Rise, O: Ontong Java Nui.

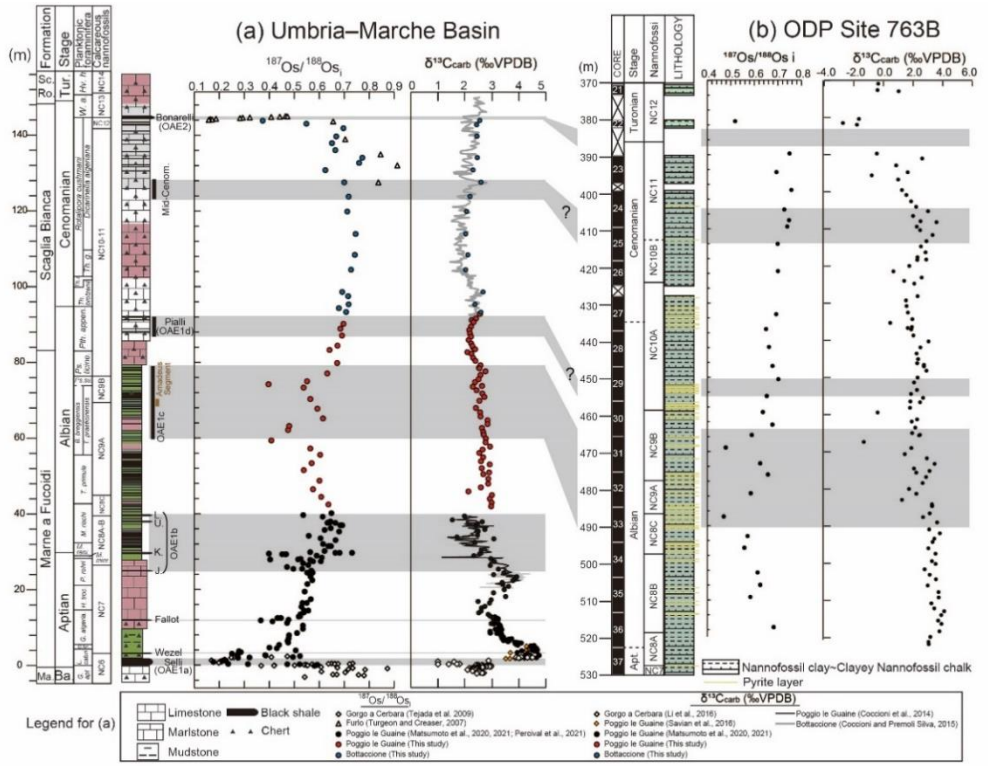

Figure VI-2. Osmium and carbon isotopic records of (a) the Umbria–Marche Basin and (b) ODP Site 763B: Umbria–Marche Basin: lithology is based on Coccioni et al. (2012, 2014), Coccioni and Premoli Silva (2015), and Coccioni (2020); biostratigraphy is from Coccioni et al. (2012, 2014), Coccioni (2020), and Matsumoto et al. (2020, 2021); $\delta^{13}C_{carb}$ is based on Coccioni et al. (2014), Coccioni and Premoli Silva (2015), Li et al. (2016), Savian et al. (2016), Matsumoto et al. (2020, 2021), and this study; $^{187}O/^{188}Os_i$ data are based on Turgeon and Creaser (2008) (Furlo section, during OAE2), Tejada et al. (2009) (Gorgo a Cerbara section, upper Barremian to end of OAE1a), Matsumoto et al. (2020, 2021a) (PLG record, lower Aptian to lower Albian), Percival et al. (2021) (PLG record, upper Barremian to end of OAE1a), and this study. ODP Site 763B litho- and biostratigraphy are based on Haq et al. (1990) and Bralower et al. (1997); $\delta^{13}C_{carb}$ and $^{187}O/^{188}Os_i$ data are based on this study. Ma.—Maiolica, Sc. Ro.—Scaglia Rossa, Ba.—Barremian, Tur.—Turonian, *G.—Globigerinelloides*, *apt—aptiensis*, *L.—Leupoldina*, *fer.—ferreolensis*, *algeria.—algerianus*, *H.—Hedbergella*, *troc.—trocoidea*, *M.—Microhedbergella*, *P.—Paraticinella*, *mini.—miniglobularis*, *reni.—renilaevis*, *T.—Ticinella*, *B.—Biticinella*, *Ps.—Pseudothalmanninella*, *su.—subticinensis*, *ticine.—ticinensis*, *Pth.—Parathalmanninella*, *appen.—appenninica*, *Th.—Thalmanninella*, *R.—Rotalipora*, *r.—reicheli*, *g.—globotruncanoides*, *W.—Whiteinella*, *a.—archaeocretacea*, *Hv.—Helvetoglobotruncana*, *h.—Helvetica*, J—Jacob Level, K—Kilian Level, U—Urbino Level, L—Leenhardt Level.

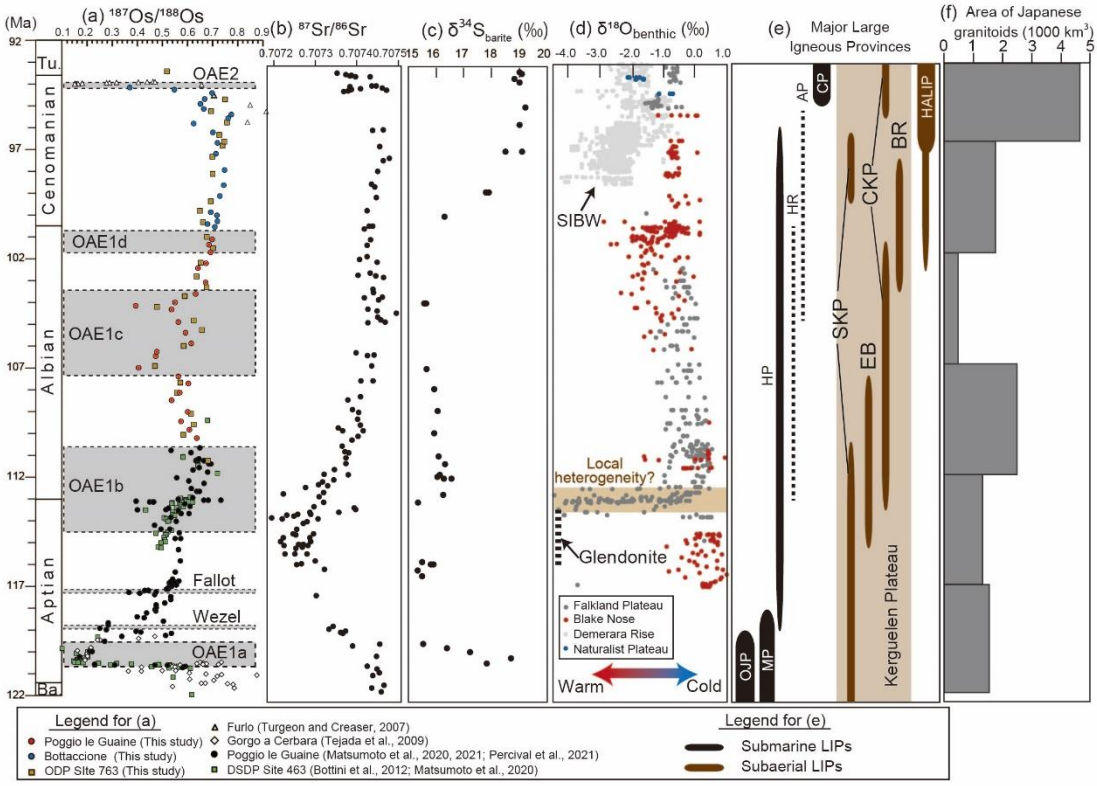

Figure VI-3. (a) $^{187}Os/^{188}Os_i$, (b) $^{87}Sr/^{86}Sr$, (c) $\delta^{34}S_{barite}$, (d) $\delta^{18}O_{carb}$ of benthic foraminifera, (e) ages of major large igneous provinces, and (f) ages of Japanese granitoid formation: The $^{187}Os/^{188}Os_i$ data are from Turgeon and Creaser (2008) (Furlo section, during OAE2), Tejada et al. (2009) (Gorgo a Cerbara section, upper Barremian to end of OAE1a), Bottini et al. (2012) (DSDP Site 463, upper Barremian to end of OAE1a), Matsumoto et al. (2020, 2021) (PLG record, lower Aptian to lower Albian), Percival et al. (2021) (PLG record, upper Barremian to end of OAE1a), and this study. The $^{87}Sr/^{86}Sr$ data are from Bralower et al. (1997); $\delta^{34}S_{barite}$ from Paytan et al. (2020); and $\delta^{18}O_{carb}$ of benthic foraminifera from Fassel and Bralower (1999), Huber et al. (2002, 2011, 2018), Gustafsson et al. (2003), Moriya et al. (2007), Petrizzo et al. (2008), and Friedrich et al. (2012). The $\delta^{18}O_{carb}$ values of benthic foraminifera from the Falkland Plateau are highly negative at the Aptian–Albian boundary, possibly reflecting local heterogeneity (Huber et al., 2018). In addition, $\delta^{18}O_{carb}$ data of benthic foraminifera from the Demerara Rise show highly negative values for the Cenomanian, which are interpreted as the values of warm, saline intermediate to bottom waters (SIBW). Age scale is based on Gale et al. (2020). Abbreviations in (e) are as follows: OJP—Ontong Java Plateau, MP—Manihiki Plateau, HP—Hikurangi Plateau, HR—Hess Rise, AP—Agulhas Plateau, CP—Caribbean Plateau, SKP—Southern Kerguelen Plateau, EB, Elan Bank, CKP—Central Kerguelen Plateau, BR—Broken Ridge, HALIP—High Arctic Large

Igneous Provinces. Age dates were obtained as follows: the Ontong Java Plateau from Mahoney et al. (1993) and Tejada et al. (2002); the Manihiki Plateau is from Ingle et al. (2007) and Timm et al. (2011), Hikurangi Plateau from Hoernle et al. (2010), the Hess Rise from Vallier et al. (1987); the Agulhas Plateau from Parsiegla et al. (2008); the Caribbean Plateau from Sinton et al. (1998); the Kerguelen Plateau from Coffin et al. (2002), Duncan et al. (2002), and Jiang et al. (2021); and the High Arctic Large Igneous Provinces from Naber et al. (2020). Solid lines in (e) represent radiometric ages; dashed lines represent the estimated age from plate-tectonic reconstructions. Ages of Japanese granitoids are from Takagi (2004).

Supplementary Tables of Chapter VI

Sample Name	$\delta^{13}C_{carb}$ (‰VPDB)	1SD	$\delta^{18}O_{carb}$ (‰VPDB)	1SD	Depth (mbsf)
PLG-C 0.25	2.55	0.05	-2.22	0.05	92.86
PLG-C 1.43	2.41	0.07	-1.99	0.08	91.68
PLG-C 1.85	2.25	0.05	-2.84	0.05	91.26
PLG-C 2.26	2.32	0.07	-2.16	0.08	90.85
PLG-C 2.39	2.32	0.05	-2.70	0.05	90.72
PLG-C 3.54	2.23	0.07	-2.14	0.08	89.57
PLG-C 4.50	2.16	0.05	-2.35	0.05	88.61
PLG-C 5.37	2.19	0.07	-2.12	0.08	87.74
PLG-C 6.21	2.22	0.07	-1.77	0.08	86.90
PLG-C 7.10	2.14	0.05	-1.75	0.05	86.01
PLG-C 8.02	2.23	0.05	-2.46	0.05	85.09
PLG-C 8.66	2.28	0.05	-2.15	0.05	84.45
PLG-C 9.16	2.30	0.07	-1.84	0.08	83.95
PLG-C 9.56	2.38	0.07	-1.82	0.08	83.55
PLG-C 10.31	2.09	0.05	-1.95	0.05	82.80
PLG-C 10.75	2.24	0.07	-1.90	0.08	82.36
PLG-C 11.81	2.30	0.05	-2.18	0.05	81.30
PLG-C 12.60	2.39	0.07	-1.44	0.08	80.51
PLG-C 13.76	2.58	0.05	-2.62	0.05	79.35
PLG-C 14.44	2.52	0.07	-2.64	0.08	78.67
PLG-C 14.58	2.54	0.05	-2.20	0.05	78.53
PLG-C 15.36	2.76	0.07	-2.05	0.08	77.75
PLG-C 16.32	2.58	0.05	-2.35	0.05	76.79
PLG-C 17.44	2.51	0.07	-1.50	0.08	75.67
PLG-C 18.22	2.37	0.05	-2.12	0.05	74.89
PLG-C 19.20	2.63	0.07	-2.17	0.08	73.91
PLG-C 19.42	2.29	0.05	-1.94	0.05	73.69
PLG-C 20.35	2.43	0.07	-1.82	0.08	72.76
PLG-C 21.20	2.64	0.05	-2.51	0.05	71.91
PLG-C 22.12	2.72	0.07	-2.17	0.08	70.99
PLG-C 23.13	2.54	0.05	-2.29	0.05	69.98
PLG-C 25.00	2.40	0.11	-2.00	0.08	68.11
PLG-C 26.18	2.56	0.05	-1.94	0.05	66.93
PLG-C 27.25	2.58	0.11	-1.69	0.08	65.86
PLG-C 28.27	2.83	0.05	-2.08	0.05	64.84
PLG-C 29.26	2.84	0.11	-2.10	0.08	63.85
PLG-C 30.30	2.63	0.05	-1.97	0.05	62.81
PLG-C 31.33	2.68	0.11	-2.04	0.08	61.78
PLG-C 32.08	2.69	0.05	-1.83	0.05	61.03
PLG-C 33.09	2.77	0.11	-2.23	0.08	60.02
PLG-C 34.09-34.10	2.77	0.05	-2.02	0.05	59.02
PLG-C 35.20	2.93	0.11	-2.26	0.08	57.91
PLG-C 36.00	2.65	0.05	-1.89	0.05	57.11
PLG-C 36.88	2.53	0.11	-2.13	0.08	56.23
PLG-C 38.02	2.67	0.05	-2.15	0.05	55.09
PLG-C 39.09	2.60	0.11	-2.37	0.08	54.02
PLG-C 39.93	2.92	0.05	-2.43	0.05	53.18
PLG-C 40.92	2.62	0.11	-2.35	0.08	52.19
PLG-C 42.01-42.05	2.90	0.05	-2.38	0.05	51.10
PLG-C 42.48-42.49	2.68	0.11	-2.41	0.08	50.63
PLG-C 43.70	2.86	0.05	-2.26	0.05	49.41
PLG-C 45.00-45.03	2.86	0.05	-2.23	0.05	48.11
PLG-C 45.98	2.59	0.11	-2.21	0.08	47.13
PLG-C 47.03	2.13	0.11	-2.41	0.08	46.08
PLG-C 48.01	3.00	0.05	-2.23	0.05	45.10
PLG-C 48.99	2.92	0.11	-2.08	0.08	44.12
PLG-C 50.00	2.99	0.05	-1.97	0.05	43.11
PLG-C 50.98-50.99	2.97	0.11	-2.19	0.08	42.13

Supplementary Table VI-S1. Carbon and oxygen isotopic ratios of carbonate from the Poggio le Guaine section.

Sample Name	δ^{13}Ccarb (‰VPDB)	1SD	δ^{18}Ocarb (‰VPDB)	1SD	Depth (mbsf)
BTT 561	2.55	0.11	-3.18	0.08	143.92
BTT 548	2.43	0.05	-3.56	0.05	142.79
BTT 521	2.44	0.11	-3.34	0.08	139.76
BTT 484	2.46	0.05	-3.16	0.05	134.13
BTT 463	2.30	0.11	-3.02	0.08	130.85
BTT 434	2.59	0.05	-3.22	0.05	127.63
BTT 404	2.19	0.05	-3.47	0.05	123.86
BTT 372	2.06	0.11	-3.04	0.08	119.91
BTT 318	2.03	0.11	-2.81	0.08	113.99
BTT 268	2.11	0.05	-2.86	0.05	108.46
BTT 225	2.03	0.11	-3.31	0.08	104.53
BTT160	2.67	0.05	-3.04	0.05	98.66
BTT131	2.37	0.11	-3.18	0.08	95.39
BTT 107	2.59	0.05	-2.90	0.05	93.35

Supplementary Table VI-S2. Carbon and oxygen isotopic ratios of carbonate from the Bottaccione section.

Sample Name	$\delta^{13}C_{carb}$	1SD	$\delta^{18}O_{carb}$	1SD	Depth
	(‰VPDB)		(‰VPDB)		(mbsf)
763B_36-7_14-17	3.05	0.07	-0.50	0.08	521.79
763B_36-6_100-103	3.04	0.05	-1.12	0.05	521.15
763B_36-5_117-120	3.16	0.07	-1.43	0.08	519.82
763B_36-4_81-84	3.77	0.05	-1.59	0.05	518.31
763B_36-3_30-33	3.91	0.07	-1.34	0.08	516.3
763B_36-2_93-96	3.68	0.05	-1.82	0.05	515.43
763B_36-1_94-97	3.90	0.07	-1.53	0.08	513.94
763B_35-CC_41-43	4.09	0.05	-1.80	0.05	512.91
763B_35-6_115-119	3.42	0.07	-1.95	0.08	512.15
763B_35-5_129-133	3.23	0.05	-2.22	0.05	510.79
763B_35-4_121-126	3.72	0.07	-1.36	0.08	509.21
763B_35-3_124-128	3.71	0.05	-1.91	0.05	507.74
763B_35-2_99-102	2.99	0.07	-1.11	0.08	505.99
763B_35-1_81-84	3.54	0.05	-1.90	0.05	504.31
763B_34-7_9-14	3.12	0.07	-2.57	0.08	503.09
763B_34-6_14-18	2.77	0.11	-2.39	0.08	501.64
763B_34-5_17-23	3.52	0.07	-1.82	0.08	500.17
763B_34-4_94-98	3.27	0.11	-1.82	0.08	499.44
763B_34-3_42-46	3.51	0.07	-1.51	0.08	497.42
763B_34-2_50-53	3.03	0.07	-1.98	0.07	496
763B_34-1_27-29	3.31	0.11	-1.79	0.08	494.27
763B_33-7_24-27	3.43	0.07	-1.91	0.08	493.39
763B_33-6_30-32	3.80	0.11	-1.49	0.08	491.95
763B_33-5_40-43	3.08	0.07	-1.83	0.08	490.9
763B_33-4_2-5	3.62	0.11	-2.09	0.08	489.02
763B_33-3_7-10	2.67	0.07	-2.06	0.08	487.57
763B_33-2_56-59	3.12	0.11	-2.36	0.08	486.56
763B_32-CC_15-19	3.28	0.11	-1.80	0.08	484.6
763B_33-1_5-8	3.26	0.07	-2.35	0.08	484.55
763B_32-7_14-17	3.27	0.07	-2.00	0.08	484.14
763B_32-6_45-51	1.24	0.11	-2.17	0.08	482.95
763B_32-5_29-33	2.22	0.07	-2.32	0.07	481.29
763B_32-4_49-52	1.72	0.07	-2.10	0.08	479.99
763B_32-3_43-48	2.64	0.11	-2.40	0.08	478.43
763B_32-2_30-32	2.87	0.07	-2.58	0.08	476.8
763B_32-1_60-63	2.20	0.11	-2.53	0.08	475.6
763B_31-CC_28-33	3.11	0.07	-2.47	0.08	475.155
763B_31-7_1-6	2.05	0.11	-2.14	0.08	474.51
763B_31-6_25-29	3.45	0.07	-2.16	0.08	473.25
763B_31-5_26-28	2.93	0.11	-1.87	0.08	471.76
763B_31-4_63-65	1.43	0.07	-1.96	0.08	470.63
763B_31-3_48-52	1.88	0.11	-1.96	0.08	468.98
763B_31-2_36-39	-1.33	0.07	-1.85	0.08	467.36
763B_31-1_9-12	2.40	0.11	-2.00	0.08	465.59
763B_30-CC_39-41	2.46	0.07	-1.83	0.08	465.44
763B_30-7_32-35	1.93	0.11	-2.36	0.08	464.97
763B_30-6_33-37	2.14	0.07	-1.72	0.08	463.48
763B_30-5_20-24	1.90	0.07	-1.82	0.07	461.85
763B_30-4_78-83	2.27	0.11	-2.10	0.08	461.28
763B_30-3_41-44	-0.40	0.07	-1.87	0.08	459.41
763B_30-2_64-68	1.79	0.07	-1.96	0.07	458.14
763B_29-CC_72-75	2.46	0.07	-2.03	0.08	456.67
763B_30-1_45-47	1.81	0.11	-2.35	0.08	456.45
763B_29-7_0-5	2.67	0.11	-2.31	0.08	455.5
763B_29-6_43-48	1.85	0.07	-2.11	0.08	454.43
763B_29-5_85-88	2.25	0.07	-2.12	0.07	453.35
763B_29-4_33-36	2.06	0.11	-2.13	0.08	451.33
763B_29-3_52-56	2.30	0.07	-2.14	0.08	450.02
763B_29-2_17-21	2.90	0.07	-2.37	0.07	448.17
763B_29-1_51-54	2.73	0.11	-2.62	0.08	447.01
763B_28-CC_16-21	2.73	0.07	-2.75	0.08	446.61
763B_28-7_16-19	2.27	0.11	-2.54	0.08	446.16
763B_28-6_55-59	2.33	0.07	-2.37	0.08	445.05
763B_28-5_54-57	2.23	0.07	-2.38	0.07	443.54
763B_28-4_40-44	2.49	0.11	-2.37	0.08	441.9
763B_28-3_30-34	3.04	0.07	-2.53	0.08	440.3
763B_28-2_20-23	2.02	0.07	-2.91	0.07	438.7
763B_28-1_7-11	1.87	0.11	-2.95	0.08	437.07
763B_27-CC_21-24	1.64	0.07	-2.50	0.08	436.685
763B_27-7_27-32	1.91	0.11	-2.48	0.08	436.42
763B_27-6_64-68	0.45	0.07	-2.79	0.08	435.29
763B_27-5_115-116	1.94	0.07	-2.96	0.07	434.3
763B_27-4_52-55	1.64	0.11	-2.51	0.08	432.52
763B_27-3_29-32	1.56	0.07	-3.32	0.08	430.79
763B_27-2_25-28	1.52	0.07	-2.59	0.07	429.25
763B_27-1_64-66	2.30	0.11	-2.64	0.08	428.14
763B_26-CC_29-32	2.08	0.07	-2.63	0.08	424.74
763B_26-5_6-9	1.39	0.07	-2.46	0.07	424
763B_26-4_60-63	2.57	0.11	-2.63	0.08	423.1
763B_26-3_44-47	0.67	0.07	-2.42	0.08	421.44
763B_26-2_48-51	1.74	0.07	-2.27	0.07	419.98
763B_25-CC_52-54	2.28	0.07	-2.55	0.08	418.345
763B_26-1_44-47	2.88	0.11	-2.29	0.08	418.265
763B_25-7_14-17	2.29	0.11	-2.43	0.08	417.64
763B_25-6_33-36	2.83	0.07	-2.18	0.08	416.33
763B_25-5_23-26	2.52	0.07	-2.54	0.07	414.73
763B_25-4_31-35	2.90	0.11	-2.90	0.08	413.31
763B_25-3_16-19	3.31	0.07	-2.36	0.08	411.66
763B_25-2_35-38	2.47	0.07	-2.43	0.07	410.35
763B_25-1_92-94	2.24	0.11	-2.34	0.08	409.42
763B_24-CC_10-12	3.57	0.07	-2.26	0.08	408.2
763B_24-7_27-30	2.50	0.11	-2.34	0.08	407.92
763B_24-6_36-38	1.99	0.07	-2.85	0.08	406.51
763B_24-5_25-28	3.00	0.07	-2.56	0.07	405.25
763B_24-4_57-60	2.20	0.11	-2.88	0.08	404.07
763B_24-3_60-63	1.86	0.07	-2.33	0.08	402.6
763B_24-2_39-40	1.54	0.07	-2.69	0.07	400.89
763B_24-1_56-58	1.24	0.11	-2.48	0.08	399.56
763B_23-CC_15-18	0.99	0.07	-2.43	0.08	396.725
763B_23-5_10-14	-0.79	0.11	-2.11	0.08	395.6
763B_23-4_76-80	1.63	0.07	-2.24	0.07	394.76
763B_23-3_43-46	0.85	0.07	-2.25	0.08	392.93
763B_23-2_6-9	2.61	0.07	-2.40	0.07	391.06
763B_23-1_24-27	-0.45	0.11	-1.87	0.08	389.74
763B_22-CC_28-30	-1.79	0.07	-1.80	0.07	381.98
763B_22-2_3-7	-2.74	0.07	-1.80	0.08	381.53
763B_22-1_42-43	-1.66	0.07	-1.94	0.07	380.42
763B_21-CC_16-19	1.02	0.07	-2.19	0.07	372.96
763B_21-2_66-69	-0.40	0.11	-1.54	0.08	372.66
763B_21-1_42-45	-0.35	0.07	-1.59	0.07	370.92

Supplementary Table VI-S3. Carbon and oxygen isotopic ratios of carbonate from the ODP Site 763B.

Sample Name	Lithology	Os	1sd	$^{187}Os/^{188}Os$	1sd	Re conc	1sd	$^{187}Re/^{188}Os$	1sd	$^{187}Os/^{188}Os_{initial}$	1sd	Depth	Age
		(pg g^{-1})				(pg g^{-1})						(m)	(Ma)
PGC2.26	Marlstone	25.13	0.17	0.716	0.010	52	3	10.7	0.6	0.698	0.010	90.23	101.1
PGC-3.54	Marlstone	20.7	0.4	0.686	0.020	1	8	0.4	1.9	0.69	0.02	88.95	101.4
PGC-5.37	Marlstone	15.09	0.14	0.701	0.011	16	3	5.4	1.0	0.692	0.011	87.12	101.7
PGC-8.02	Marlstone	35.65	0.18	0.677	0.009	15	3	2.1	0.4	0.674	0.009	84.47	102.2
PLGC-9.16	Marlstone	22.38	0.13	0.645	0.010	10	2	2.2	0.6	0.642	0.010	83.33	102.4
PGC-12.60	Marlstone	14.26	0.17	0.678	0.015	10	3	3.5	1.0	0.672	0.016	79.89	103.1
PGC-15.36	Marlstone	19.4	0.3	0.701	0.016	150	7	40.0	1.9	0.632	0.017	77.13	103.6
PGC-17.44	Marlstone	22.38	0.16	0.626	0.011	190	5	43.5	1.2	0.550	0.011	75.05	104.0
PLG-C 18.22	Marlstone	21.87	0.16	0.458	0.009	162	4	37.2	0.9	0.394	0.009	74.27	104.2
PGC-19.10	Marlstone	542	4	0.593	0.005	3449	19	32.5	0.3	0.536	0.005	73.39	104.3
PGC-22.12	Marlstone	40.6	0.3	0.577	0.008	60	12	7.6	1.5	0.563	0.009	70.37	104.9
PGC-24.68	Marlstone	138.0	0.9	0.798	0.009	3081	20	116.9	1.1	0.592	0.009	67.81	105.4
PGC-27.25	Marlstone	21.2	0.2	0.623	0.013	19	5	4.6	1.3	0.615	0.013	65.24	105.9
PGC-29.26	Marlstone	29.28	0.18	0.483	0.006	17	3	2.8	0.5	0.478	0.006	63.23	106.3
PGC-30.30	Marlstone	23.95	0.16	0.492	0.010	51	3	10.8	0.6	0.473	0.010	62.19	106.5
PGC-33.09	Marlstone	47.9	0.3	0.445	0.006	215	7	22.5	0.8	0.405	0.006	59.4	107.0
PGC-35.20	Marlstone	45.6	0.4	0.565	0.013	6	7	0.7	0.8	0.563	0.013	57.29	107.4
PGC-36.88	Marlstone	41.2	0.3	0.664	0.011	271	9	33.8	1.1	0.603	0.011	55.61	107.7
PGC-39.09	Shale	36.4	0.3	0.624	0.008	217	6	30.5	0.8	0.569	0.008	53.4	108.1
PLG-C40.92	Marlstone	34.1	0.2	0.613	0.008	282	7	42.4	1.1	0.537	0.008	51.57	108.5
PGC-43.70	Marlstone	48.8	0.3	0.618	0.008	90	4	9.4	0.4	0.601	0.008	48.79	109.0
PGC-45.98	Marlstone	29.4	0.3	0.682	0.013	335	16	59	3	0.574	0.014	46.51	109.5
PGC-48.01	Marlstone	34.3	0.2	0.629	0.009	79	3	11.8	0.5	0.608	0.009	44.49	109.8
PGC-50.00	Marlstone	16.44	0.13	0.651	0.013	25	3	7.8	1.0	0.637	0.013	42.49	110.2

Supplementary Table VI-S4. Re and Os abundance and Os isotopic ratios of the Poggio le Guaine core samples.

Sample Name	Lithology	Os (pg g-1)	1sd	$^{187}Os/^{188}Os$	1sd	Re (pg g-1)	1sd	$^{187}Re/^{188}Os$	1sd	$^{187}Os/^{188}Osi$	1sd	Depth (m)	Age (Ma)
BT107	Limestone	12.30	0.10	0.713	0.013	5.5	1.8	2.3	0.8	0.709	0.013	93.35	100.55
BTT120	Limestone	13.11	0.09	0.682	0.008	4	2	1.4	0.9	0.679	0.008	94.38	100.42
BTT131	Limestone	15.07	0.13	0.721	0.014	3	3	1.0	1.1	0.719	0.014	95.39	100.29
BTT151	Limestone	21.25	0.18	0.720	0.012	8	3	1.9	0.6	0.717	0.012	97.54	100.02
BT160	Limestone	12.73	0.12	0.700	0.015	10	3	4.2	1.3	0.693	0.015	98.66	99.88
BT225	Limestone	11.83	0.13	0.734	0.016	6.5	1.5	2.8	0.7	0.729	0.016	104.53	99.14
BT268	Limestone	9.98	0.11	0.748	0.014	4.1	1.8	2.1	0.9	0.744	0.014	108.46	98.64
BT318	Limestone	10.64	0.12	0.752	0.015	5.4	1.7	2.6	0.8	0.747	0.015	113.99	97.94
BT372	Limestone	10.77	0.12	0.714	0.013	1	2	0.6	1.1	0.713	0.013	119.91	97.20
BT404	Limestone	17.29	0.16	0.720	0.009	2	2	0.6	0.7	0.719	0.009	123.86	96.70
BT434	Limestone	10.42	0.16	0.703	0.017	2	3	1.1	1.4	0.701	0.017	127.63	96.22
BTT450*	Limestone	74.5	0.5	1.152	0.011	144	3	10.6	0.2	1.135	0.011	129.51	95.99
BT463	Limestone	14.60	0.17	0.627	0.013	4	2	1.4	0.8	0.625	0.013	130.85	95.82
BTT474	Limestone	12.15	0.12	0.763	0.014	2	3	0.9	1.2	0.761	0.014	132.76	95.58
BT484	Limestone	13.76	0.14	0.781	0.013	10	2	3.9	0.8	0.775	0.013	134.13	95.40
BTT496	Limestone	13.31	0.14	0.670	0.012	8	3	3.2	1.2	0.665	0.013	136.14	95.15
BTT508	Limestone	13.42	0.13	0.652	0.013	2	3	0.7	1.1	0.651	0.013	137.99	94.92
BT521	Limestone	16.56	0.13	0.672	0.011	6	3	2.0	0.8	0.669	0.011	139.76	94.69
BTT542	Limestone	15.63	0.15	0.699	0.010	2	2	0.6	0.8	0.698	0.010	141.93	94.42
BTT552	Limestone	15.57	0.10	0.549	0.007	3	2	0.9	0.8	0.547	0.007	143.13	94.27
BT561B	Limestone	29.06	0.13	0.375	0.005	19.4	1.9	3.3	0.3	0.370	0.005	143.92	94.17

* excluded from the discussion

Supplementary Table VI-S5. Re and Os abundance and Os isotopic ratios of the Bottaccione samples.

Supplementary Table 6: Re and Os abundance and Os isotopic ratios of ODP Site 763B

Sample Name	Lithology	Os	1sd	$^{187}Os/^{188}Os$	1sd	Re	1sd	$^{187}Re/^{188}Os$	1sd	$^{187}Os/^{188}Osi$	1sd	Depth	Age
		(pg g-1)				(pg g-1)						(m)	(Ma)
763B_36-3_138-141	Nannofossil claystone	38.0	0.3	0.704	0.008	85	2	11.6	0.2	0.682	0.008	517.38	111.25
763B_35-4_121-126	Nannofossil claystone	45.8	0.2	0.605	0.010	106	3	11.8	0.3	0.583	0.010	509.21	110.07
763B_35-2_99-102	Nannofossil claystone	47.1	0.5	0.633	0.010	37.9	1.1	4.1	0.13	0.625	0.010	505.99	109.60
763B_34-6_111-115	Calcareous claystone	40.1	0.2	0.640	0.007	113	3	14.5	0.4	0.614	0.007	502.61	109.10
763_34-2_50-53	Calcareous claystone	45.3	0.3	0.609	0.008	250	6	28.2	0.7	0.558	0.008	496	108.14
763B_33-6_115-118	Calcareous claystone	53.2	0.3	0.585	0.008	80	3	7.7	0.3	0.571	0.008	492.8	107.68
763B_33-3_7-10	Calcareous claystone	54.4	0.2	0.510	0.007	242	7	22.5	0.6	0.470	0.007	487.57	106.92
763_32-5_29-33	Calcareous claystone	44.8	0.3	0.609	0.008	119	4	13.6	0.4	0.585	0.008	481.29	106.00
763B_32-1_125-129	Calcareous claystone	33.94	0.16	0.682	0.007	93	2	14.2	0.3	0.658	0.007	476.25	105.27
763B_31-6_25-29	Calcareous claystone	51.6	0.2	0.669	0.005	251	3	25.1	0.4	0.625	0.005	473.25	104.83
763B_31-3_48-52	Calcareous claystone	40.49	0.17	0.512	0.007	156	4	19.5	0.5	0.478	0.007	468.98	104.21
763B_31-1_9-12	Calcareous claystone	25.5	0.2	0.711	0.011	348	4	70.7	1.1	0.589	0.011	465.59	103.72
763B_30-5_115-118	Nannofossil claystone	22.69	0.14	0.712	0.010	91	2	20.8	0.5	0.676	0.010	462.8	103.31
763_30-3_41-44	Nannofossil claystone	18.3	0.4	0.70	0.03	138	5	39.1	1.5	0.64	0.03	459.41	102.82
763B_29-6_110-113	Calcareous claystone	34.25	0.17	0.699	0.008	179	3	27.0	0.5	0.653	0.008	455.1	102.19
763B_29-3_104-109	Calcareous claystone	21.7	0.2	0.738	0.011	90	4	21.6	0.9	0.702	0.012	450.54	101.53
763B_29-1_51-54	Calcareous claystone	22.98	0.11	0.735	0.010	152	2	34.3	0.6	0.677	0.010	447.01	101.01
763B_28-4_40-44	Calcareous claystone	24.35	0.11	0.709	0.007	133	3	28.2	0.6	0.662	0.007	441.9	100.33
763_28-1_7-11	Calcareous claystone	20.3	0.2	0.71	0.02	152	5	38.9	1.5	0.65	0.02	437.07	99.81
763B_27-4_108-111	Nannofossil claystone	22.42	0.14	0.748	0.017	143	3	33.2	0.7	0.693	0.017	433.08	99.38
763_26-3_44-47	Nannofossil claystone	32.8	0.3	0.725	0.013	95	4	15.0	0.6	0.700	0.013	421.44	98.13
763B_25-4_111-115	Nannofossil claystone	36.2	0.3	0.737	0.018	164	4	23.6	0.6	0.699	0.018	414.11	97.34
763B_25-1_92-94	Nannofossil claystone	31.7	0.19	0.788	0.011	184	4	30.4	0.6	0.739	0.011	409.42	96.83
763B_24-7_6-9	Clayey Nannofossil chalk	32.51	0.17	0.805	0.010	223	4	36.0	0.6	0.747	0.010	407.71	96.65
763B_24-4_134-137	Clayey Nannofossil chalk	45.7	0.3	0.852	0.011	676	16	78	2	0.727	0.012	404.84	96.34
763B_24-1_56-58	Clayey Nannofossil chalk	33.95	0.11	0.785	0.008	115	2	17.7	0.3	0.757	0.008	399.56	95.77
763_23-4_76-78	Clayey Nannofossil chalk	39.3	0.2	0.716	0.008	104	5	13.8	0.6	0.694	0.008	394.76	95.25
763B_23-1_24-27	Clayey Nannofossil chalk	24.88	0.13	0.762	0.009	38	2	8.0	0.4	0.749	0.009	389.74	94.71
763B_22-1_104-106	Clayey Nannofossil chalk	34.4	0.2	0.542	0.011	104	2	15.4	0.4	0.518	0.011	381.04	93.43

Supplementary Table VI-S6. Re and Os abundance and Os isotopic ratios of the ODP Site 763.

CHAPTER VII

General summary

VII-1. Mid-Cretaceous Os isotopic record

VII-1.1. The intensive magmatic pulses during the mid-Cretaceous

In this dissertation, I reconstructed a continuous long-term mid-Cretaceous Os isotopic stratigraphy covering all mid-Cretaceous OAEs (Fig. VII-1) and tried to constrain the timing of massive volcanic events. As the result, the Os isotopic record showed less radiogenic shifts to the mantle values during the early to mid-Aptian, earliest Albian, late Albian, end-Cenomanian (Fig. VII-1). These less radiogenic shifts cannot be explained by the changes in the continental weathering rate and/or the oceanic crustal production at ridges (see Chapter VI and VII-3). By combining the other isotopic data ($^{87}Sr/^{86}Sr$ and $\delta^{34}S_{barite}$) and the radiometric ages of the large igneous provinces (LIPs), the most likely candidates for these unradiogenic Os isotopic shifts are the massive volcanic events associated with the formation of the large igneous provinces (LIPs) (Chapter VI). Since early to mid-Aptian and end-Cenomanian unradiogenic Os isotopic shifts correspond to the formation ages of the Ontong Java Nui and Caribbean Plateau (Chapters III), respectively, they could represent the massive input of unradiogenic Os through these volcanic events. However, since no well-dated large LIPs have been reported from the late Albian, further research is required to explore the unradiogenic Os source during the late Albian (Chapter VI). Considering such Os isotopic variation associated with the LIPs formation has not been reported from the Cenozoic (Fig. VII-1), repeated emplacement of LIPs are characteristic events in the Cretaceous. This conclusion is consistent with the compilation of the radiometric ages of LIPs (Fig. VII-1c) (Coffin and Eldholm, 2005; Bergman et al., 2021).

Most of the radiometric ages of mid-Cretaceous LIPs (e.g., Ontong Java, Manihiki, and Kerguelen Plateaus) have large variations and uncertainties on the scale of 10^6 to 10^7 years (e.g., Olierook et al., 2019; Jiang et al., 2021), which have hampered the understanding of the durations of LIPs volcanism. This study revealed that each unradiogenic Os isotopic pulse during the mid-Cretaceous was shorter than 10^6 years. This result suggests that each main volcanic pulses forming the mid-Cretaceous LIPs occurred within the short geological interval within ~1 myr.

VII-1.2. The triggering factors of the mid-Cretaceous OAEs

This study revealed that mid-Cretaceous OAEs can be classified into two types: (1) volcanic-induced OAEs accompanied by the unradiogenic Os isotopic shifts and (2) non-volcanic-induced OAEs not accompanied by the unradiogenic Os isotopic shifts (Chapter VI). The former OAEs are global events and caused by the increase in the primary productivity triggered by the massive LIPs volcanism. On the other hand, latter OAEs are

mainly reported from the Tethyan region and caused by the ocean stratification induced by the enhancement of monsoonal activity. Interestingly, most of the Cretaceous OAEs (OAE1a, Fallot and Wezel Levels, OAE1b, OAE 1c, OAE1d, and OAE2) (Fig. VII-2) are concentrated in the short geological interval from the earliest Aptian to the end-Cenomanian (~120–94 Ma). There are two possible reasons for this: (1) high frequency of the LIPs formations, and (2) changes in the Tethyan paleogeography.

VII-1.2.1. High frequency of the LIPs formation

As discussed in Chapter VI, I concluded that the mid-Cretaceous major organic-rich horizons (OAE1a, Fallot and Wezel Levels, and OAE2) are induced by the LIPs formation (volcanic-induced OAEs). Indeed, the compilation of radiometric ages of LIPs basalts suggests that especially many LIPs were formed during the mid-Cretaceous (Fig. VII-1c). On the other hand, the number of LIPs formation was limited after the mid-Cretaceous and there are no similar Os isotopic variations associated with the LIPs volcanism during Cenozoic (Fig. VII-1a,c). These pieces of evidence suggest that the high frequencies of LIPs volcanism could have been the cause of the concentration of volcanic-induced OAEs during the mid-Cretaceous.

VII-1.2.2. Changes in the Tethyan paleogeography

In Chapter VI, I defined monsoon-induced OAEs (Faraoni Event, OAE1b, OAE 1c, and OAE1d), which are characterized by the cyclic deposition of thin black shales without unradiogenic Os isotopic shifts. These OAEs could have been caused by the stratification of the Tethys Ocean triggered by the input of freshwater induced by the monsoonal activity (Chapter V: Matsumoto et al., 2021b). Indeed, during the Early Cretaceous, Tethyan regions were relatively closed oceanic settings compared to other Oceans (Fig. VII-2) and could have been susceptible to the freshwater input. In addition to these OAEs, numerous not-named cyclic black shales have been reported from the Tethyan sedimentary sequence during the Berriasian–earliest Aptian, earliest Albian to late Albian, and end-Cenomanian (Fig. VII-2). Considering these cyclic black shales are paced by the eccentricity (Mitchell et al., 2008; Lanci et al., 2010; Franceschi et al., 2011) and dominated by the terrestrial organic matter (Fig. VII-3), they are also considered as a kind of monsoon-induced OAEs. Combining these pieces of evidence, the monsoon-induced OAEs are not unique events during the mid-Cretaceous but more common in the Early to mid-Cretaceous Tethyan sedimentary record (Fig. VII-2).

Such kind of organic rich-sediments has never been reported from Tethyan sedimentary record after Turonian, which may be ascribed to the geographic changes.

Throughout the mid-Cretaceous, Tethys Ocean became larger and less restricted as Africa and Eurasia were pulled apart (Fig. VII-2). As a result, the freshwater input by the monsoonal activity to the Tethys Ocean could no longer cause the ocean stratification and following oxygen-depleted condition in the Tethys regions.

Besides, changes in the paleo-geography may have weakened monsoonal activity in the Late Cretaceous. As discussed in Chapter V, the landmass of the Cretaceous are more aggregated than the present Earth. The strong contrast of heat capacity between the continent and ocean could have made a strong monsoonal activity (Ikeda et al., 2017). However, as the break-up of the continents proceeded, the contrast of the heat capacity and the monsoonal activity may have become also weaker during the Late Cretaceous. As a result, the input of freshwater to the Tethys Ocean decreased and ocean stratification may have never occurred during the Late Cretaceous.

VII-1.3. Volcanism and temperature variations

Early Cretaceous (Beriassian to earliest Albian) and a part of Late Cretaceous (Campanian to Maastrichtian) were characterized by the cool climate (Bodin et al., 2015; Huber et al., 2018). On the other hand, the markedly hot climate during the mid-Cretaceous was restricted from Cenomanian to Turonian (Fig. I-3). This study reveals that the hot climate did not correspond to the intensive phases of hydrothermal activity, which suggests that the traditional mid-Cretaceous understanding of "*hot-house world supported by high pCO_2 associated with the enhanced oceanic crustal production*" (Larson, 1991) could not be precise. Since the hottest interval corresponds to the subaerial LIPs eruption (e.g., Kerguelen Plateau and High Arctic Large Igneous Provinces) and circum-Pacific volcanism, the hot climate during the Cenomanian–Turonian during the mid-Cretaceous could have been triggered by the subaerial volcanism and following outgassing.

The remarkably cool interval during the mid-Cretaceous is late Aptian (Aptian called snap), which is supported by the oxygen isotopic ratios, TEX_{86} index, and mineralogical evidence (see Chapter I-1-1). However, the exact cause of this cool climate has not been understood so far. One of the possible causes of the Aptian cold snap is a decrease in the pCO_2 caused by the enhanced burial of organic matter. However, no organic-rich interval has been reported in this geological interval and this possibility seems unlikely. Another possibility is the temporal decrease in volcanic outgassing associated with the plate production, circum-Pacific volcanism, and LIPs formations. Although this possibility potentially influenced the atmospheric pCO_2, the compilation of radiometric ages of volcanic rocks is not enough for further discussion of this effect. The last possibility is

the draw-down of CO_2 through the low-temperature hydrothermal alteration of basalt (e.g., Alt and Teagle, 1999). A large amount of fresh basalt was formed during the early to mid-Aptian (Ontong Java, Manihiki, Hikurangi, and a part of Kerguelen Plateaus) under submarine conditions. Previous studies suggest that low-temperature hydrothermal alteration of basaltic rocks (seafloor weathering) takes up CO_2 from seawater through the precipitation of $CaCO_3$ (Brady and Gíslason, 1996). Indeed, the basalt of the Ontong Java Plateau contains abundant calcite veins (Banerjee et al., 2004), which may have contributed to the drawdown of CO_2 from the atmosphere. Besides, since a part of the Ontong Java Plateau was formed under the subaerial condition (Thordarson, 2004), subaerial weathering of the basaltic plateau may have contributed to the decrease in the pCO_2. Although further geochemical analysis of basaltic samples is required to explore this possibility, the style of the volcanic events (as discussed in Chapter VI-5) and the low-temperature hydrothermal activity may have been other important factors that regulated the long-term mid-Cretaceous climate.

VII-1.4. LIPs volcanism and biotic crises

Mid-Cretaceous has experienced several significant biotic crises of the marine organism (planktonic foraminifera, calcareous nannofossils, radiolaria, and ammonite). Especially significant turnovers occurred from early to mid-Aptian, Aptian–Albian transition, Albian–Cenomanian transition, and end-Cenomanian (Fig. I-3). Since they roughly corresponded to the major Cretaceous OAEs, oceanic anoxia is one of the possible triggering factors of these extinction events. However, the magnitude of oceanic anoxia and biotic crises were inconsistent. For example, planktonic foraminifera experienced the largest biotic turnover around the latest Aptian which does not correspond to the major organic-rich horizons (Coccioni et al., 2014) (Chapter II). On the other hand, the planktonic foraminiferal extinctions across the OAE1a and OAE2, which were the largest mid-Cretaceous OAEs, were minor than that of the latest Aptian. These pieces of evidence cast doubt on the relationship between the oceanic anoxia and the mid-Cretaceous biotic crises.

In Chapter II, I concluded that massive subaerial eruption and following ocean acidification was the main trigger of the most significant extinction of the planktonic foraminifera during the latest Aptian. Indeed, this interval corresponds to the subaerial eruptions of the Kerguelen Plateau which could have directly injected a large amount of massive CO_2 into the atmosphere, which could have easily caused ocean acidification. On the other hand, OAE1a and OAE2, which experienced the less severe planktonic extinction than OAE1b, were triggered by submarine volcanic events. Since volcanic

events occurred in subaerial conditions, volcanic degassing may be suppressed and insignificant to cause large biotic crises. Indeed, the intensive extinction events during the Phanerozoic (e.g., Permian-Triassic boundary, Triassic-Jurassic boundary, and Toarcian extinction event) well corresponded to the subaerial volcanic events (e.g., Siberian Trap, Central Atlantic Magmatic Provinces, and Karoo-Ferrar LIP). Therefore, the style of the volcanic events may have been important for considering the changes in the ecosystems throughout the Phanerozoic era.

VII-2. Relationship between LIPs volcanism and Os isotopic variations

The linkages between emplacement of massive basaltic plateaus and marine Os isotopic variations have been discussed so far (e.g., Cohen and Coe, 2002, 2007; Cohen et al., 2004, Turgeon and Creaser, 2008; Tejada et al., 2009; Kuroda et al., 2010; Robinson, N. et al., 2009; Kemp et al., 2020; Tomimatsu et al., 2021; Martínez-Rodríguez et al., 2021; Matsumoto et al., 2021, 2022 and this dissertation). The patterns of the marine osmium isotopic variations during LIPs eruptions can be classified into the following three groups according to the location and styles of LIPs volcanism: (1) sharp unradiogenic Os isotopic shifts during the formation of submarine basaltic plateaus (e.g. Ontong Java, Caribbean Plateaus, Wrangellia, and so on), (2) gradual unradiogenic Os isotopic shifts during continental flood basalt emplacement at low latitude (Deccan Trap, Kerguelen Plateau, and Central Atlantic Magmatic Provinces: CAMP), and (3) radiogenic Os isotopic shifts during the volcanic events forming continental flood basalt emplaced at high latitude (e.g., Karoo-Ferrar, Kerguelen Plateau, and North Atlantic Igneous Provinces: NAIP) (Fig. VII-4). The first group shows the sharp less radiogenic shift of marine $^{187}Os/^{188}Os$ during the submarine LIPs eruption (Tejada et al., 2009, Botini et al., 2012, Turgeon and Creaser, 2008; Matsumoto et al., 2020; Tomimatsu et al., 2021; Martínez-Rodríguez et al., 2021; Matsumoto et al., 2021, 2022). These sharp declines have been interpreted that a huge amount of unradiogenic Os being supplied directly into the ocean through hydrothermal alteration (e.g., Tejada et al., 2009; and this dissertation). Similar unradiogenic shifts of $^{187}Os/^{188}Os$ can be seen in the group (2) (e.g., Robinson, N. et al., 2009; Cohen and Coe, 2002, 2007; Kuroda et al., 2010). In the case of continental flood basalts, mantle-derived Os was considered supplied into the ocean through the weathering of volcanic rocks. Therefore, those declines in $^{187}Os/^{188}Os$ likely reflect the increase in the mantle-derived Os input through the subaerial weathering of the basaltic plateaus (Cohen and Coe, 2002, 2007). In case of Deccan Trap, unradiogenic Os isotopic shift was small (from 0.6 to 0.4). This may be ascribed to relatively higher latitude (~30°S) of the Deccan Trap eruption (Sangode et al., 2021) and its relatively smaller

volume than other LIPs. Here, in the case of the CAMP volcanism, the timing of the unradiogenic Os isotopic shifts is inconsistent between the Tethyan and Pacific sections (Cohen and Coe, 2002, 2007; Kuroda et al., 2010), which may have been ascribed to the difficulties in the stratigraphic correlations of these sections or Os isotopic heterogeneity in the ocean (Dickson et al., 2021). Since Os isotopic data during the Triassic–Jurassic boundary is limited at present, further compilation of Os isotopic variation of well-dated sedimentary sequence will make it possible to estimate the influence of CAMP volcanism to the marine Os isotopic variations. On the other hand, in the group (3), $^{187}Os/^{188}Os$ showed rapid radiogenic shifts during the eruption of basaltic plateaus at high latitudes (Cohen and Coe, 2002, 2007; Cohen et al., 2004; Kemp et al., 2020 and this dissertation) that is the opposite Os isotopic trends during the submarine volcanism and subaerial volcanic events at the low latitude (Fig. VII-4). Recent studies on the U-Pb age dating of Karoo and Ferrar have revealed that Karoo LIP erupted just before the radiogenic Os isotopic shift and the Ferrar LIPs eruption could be the main cause for the Os isotopic perturbations (Al-Suwaidi et al., 2021). These differences in the Os isotopic variations during the subaerial volcanic events may be derived from the location and weatherability of basaltic plateaus. In most of the subaerial LIPs eruptions, the massive input of CO_2 or CH_4 were induced by the volcanism and related processes (e.g., Burgess et al., 2017; Capriolo et al., 2021) could have caused a surge in global temperature (e.g., Sun, Y. et al., 2012; Joachimski et al., 2020; Fernandez et al., 2021). Li and Ca isotopic studies have suggested that global warming rapidly accelerated continental weathering (e.g., Brazier et al., 2015; Sun, H. et al., 2018). If the continental flood basalt was located at the low latitudes where warm climate accelerates chemical weathering of basaltic rocks, a large amount of mantle-derived unradiogenic Os could be actively supplied into the ocean. In this case, marine $^{187}Os/^{188}Os$ could have declined gradually. However, if the basaltic rocks were located at the high latitudes, the increase in the weathering of continental crust at the low latitudes may have surpassed that of high latitudes basaltic rocks, which leads to the radiogenic shift of marine $^{187}Os/^{188}Os$ values. Therefore, marine $^{187}Os/^{188}Os$ could have acted differently according to the place of LIPs formation.

This hypothesis is further supported by the paleo-marine strontium isotopic variations ($^{87}Sr/^{86}Sr$). $^{87}Sr/^{86}Sr$ represents the balance of continental derived radiogenic Sr input, and mantle-derived unradiogenic Sr and, thus, act like osmium isotopic variations. $^{87}Sr/^{86}Sr$ variations show unradiogenic trends during the submarine volcanic events forming Wrangellia (~235 Ma), Ontong Java Plateau (~120 Ma), and Caribbean Plateau (~94 Ma) and subaerial LIPs eruptions at low latitude forming CAMP (~200 Ma). On the other hand, $^{87}Sr/^{86}Sr$ showed radiogenic shifts during the subaerial LIPs eruptions

at the high latitude forming Kerguelen Plateau (~113 Ma), and Karoo-Ferrar LIPs (~180 Ma) (McArthur et al., 2020). Considering Sr isotopic ratios acted similarly to Os, LIPs volcanism could have also influenced the global Sr cycle as well as Os cycle. In the case of the volcanism at the Decan Trap (~66 Ma), Sr isotopic values did not show an unradiogenic shift (Fig. VII-1). Considering the relatively small volume of the Deccan Trap and the long residence time of Sr, the input rate of unradiogenic Sr may not have been enough to alter the marine Sr isotopic record.

If this hypothesis is correct, marine $^{187}Os/^{188}Os$ may have shown radiogenic shifts during other high latitude LIPs eruptions, such as the Siberian Trap that erupted at the Permian–Triassic boundary (~252 Ma). Recently, some papers discussed the Os isotopic variations around the Permian–Triassic boundary (e.g., Georgiev et al., 2015; Liu et al., 2020, 2021). However, these Os isotopic variations are not in good agreement and sometimes take unrealistically high values ~1.7, which is possibly caused by the secondary alteration of sedimentary rock samples. Therefore, further compilations of Os isotopic records seem necessary to reveal Os isotopic variations during the volcanic events at the Siberian Trap.

Although available reliable Os isotopic data during the LIPs eruption are currently limited, a further compilation of reliable Os isotopic variations during the LIPs eruptions may validate this hypothesis. The understanding of the relationship between the style of LIPs eruption and marine Os isotopic variations may make it possible to explore the locations of the unknown past volcanic events from the sedimentary Os isotopic records.

VII-3. Limitations and future perspectives of Os isotopic studies

One of the useful and attractive applications of the sedimentary Os isotopic record is the quantitative estimation of hydrothermal activity and continental weathering rate throughout the earth's history. Based on the mid-Cretaceous Os isotopic records, I calculated changes in the mantle-derived unradiogenic Os flux using the simple box modeling (detailed explanations are described in Chapter II-4.4). In this box modeling, I changed the continental-derived radiogenic Os were calculated based on the temperature changes revealed in Steinig et al. (2020) and the Arrhenius relationship (White et al., 1999) (Fig. VII-5). Besides, the changes in the unradiogenic Os flux through hydrothermal activity at the mid-ocean ridges were calculated based on the oceanic crustal production rate reconstructed in Cogné and Humler (2006) (Fig. VII-5). Here, please note that the reconstructed oceanic crustal production and estimation of paleo-temperature have very large uncertainties as discussed in Chapter I-1 and further research is essential for the estimation of these factors.

The brown dashed line in Fig. VII-5 represents the calculated Os isotopic changes only caused by the changes in the continental weathering rate. This result has the potential to reproduce the unradiogenic Os isotopic shift from 0.7 in Barremian to 0.55 in the late Aptian and the following radiogenic shift to 0.8 during the Cenomanian (Fig. VII-5a). However, the variation takes more radiogenic values than actual Os isotopic variations throughout the mid-Cretaceous (Fig. VII-5a). Even if the changes in the oceanic crustal production rate are taken into account in addition to the changes in the continental weathering, the differences between the calculated and observed Os isotopic variations became larger (orange dashed line in Fig. VII-5). The blue shaded area in Fig. VII-5 is the area where excessive unradiogenic Os input is required, while the brownish parts represent the decrease in the unradiogenic Os input compared to the background state. Assuming that the Os concentrations and isotopic values in hydrothermal fluid and river water are constant, additional unradiogenic Os input through LIPs volcanic episodes are needed to explain the reconstructed Os isotopic variations. Based on the simple box model calculations, especially enhanced unradiogenic input were achieved during the early to mid-Aptian, late Alian, and end-Cenomanian, which is consistent with the conclusion of Chapter VI (Fig. VII-5).

However, in order to combine Os isotopic values with other isotopic records, such as $^{87}Sr/^{86}Sr$, $\delta^{34}S$, and $\delta^{13}C$, there are still many problems to overcome. For example, $^{87}Sr/^{86}Sr$ values in the ocean reflect the balance between radiogenic Sr from the continent and less radiogenic Sr from the mantle, which is a similar isotopic system with Os. Although these two isotopic records showed consistent variation patterns (Fig. VII-5d), the increase in the input rate of mantle-derived unradiogenic Sr is much smaller than that of Os. For example, unradiogenic Os isotopic shifts during the volcanic events at the OJN during the early to mid-Aptian require a 2.5–16-times increase in the mantle-derived unradiogenic Os (Fig. III-3). However, unradiogenic Sr isotopic shift requires at most ~30% increase in the mantle-derived Sr which is much smaller than Os (Fig. III-3). Considering that the present largest Oceanic Plateau occupies only 1% of the ocean, the 16 times increase in the hydrothermal activity is unrealistically large, implying the peculiar behavior of Os during the LIPs eruption. In order to quantitatively incorporate Os data with other isotopic proxies, there are many problems to be solved on Os system on the present earth, such as (1) the contamination of non-hydrogenous Os fraction in the sedimentary rocks, (2) the understanding of Os host phase in the sediments and process of Os removal from the seawater, (3) the comprehension of Os input process through hydrothermal activity, (4) the understanding of mantle-derived Os input process during the LIPs volcanism, (5) the changes in the riverine Os concentration and Os isotopic ratio

through geological ages, and (6) precise estimation of extraterrestrial Os flux. I'm going to discuss these topics in the following subsections.

VII-3.1. contamination of non-hydrogenous Os fraction in the sedimentary rocks

In this study, I mainly used inverse aqua regia in the digestion of sedimentary rock samples for Re-Os analysis. However, previous studies indicated that inverse aqua regia dissolves all silicate minerals and extracts not only Os from hydrogenous fraction but also Os in the silicate fractions (e.g., Selby and Creaser, 2003). In order to extract the pure hydrogenous information, several weak-leaching methods that do not attack silicate minerals have been proposed (e.g., CrO_3–H_2SO_4: Selby and Creaser, 2003, H_2O_2–HNO_3: Yin et al., 2017; 1M HCl: Dunlea et al., 2021). Although these papers insisted that they truly extract the Os in hydrogenous fraction, these methods still have problems with the contamination of Os derived from silicate fractions, partial dissolution of especially unradiogenic fractions from extraterrestrial materials (e.g., Dunlea et al., 2021). Besides, previous studies on the development of Re-Os extraction methods used only natural sedimentary rock samples whose hydrogenous Os isotopic values are unknown. Therefore, there is no way to confirm these digestion methods can successfully extract pure hydrogenous information. In order to explore the suitable digestion acid and condition to extract hydrogenous information, I suggest applying several digestion methods and conditions into pure endmembers of sedimentary rocks, such as clay minerals, organic matter, carbonate, and Fe-Mn oxides. If the average concentrations and dissolution rate of Re-Os in these components were determined, it would be possible to select the most suitable extraction method based on the mineral composition and elemental concentration (e.g., Al, Si, Fe, and Mn) of the sedimentary rock samples.

VII-3.2. Os host phase in the sediments and process of Os taken into sediments

The host phase and oxidation state of Os in the sediments have not been understood due to the very low concentration of Os in the sedimentary record. Several materials have been suggested as candidates for the host materials of Os in the sediments, such as Fe- and Mn- oxides, organic matter, and sulfide (e.g., Lu et al., 2017; Yamashita et al., 2007; Sekine et al., 2011). However, no consensus has been achieved because of low Os concentrations in the sedimentary rock. Therefore, in order to determine the host phases and oxidation state of Re-Os in the sediments, it is important to conduct X-ray Absorption Fine Structure (XAFS), Extended X-ray Absorption Fine Structure (EXAFS), and X-ray Absorption Near Edge Structure (XANES) using natural sedimentary rock samples with high Os concentrations such as Fe-Mn crust and black shales. Understating of host phases

of hydrogenous Re-Os is also important for the choice of Os extraction method discussed in Chapter VII-3.1.

VII-3.3. Os input through hydrothermal activity

Hydrothermal activity is one of the important sources of unradiogenic Os in seawater. In this study, I express all of the submarine mantle-derived unradiogenic Os flux as "hydrothermal activity". However, the precise process of Os emission during the hydrothermal activity has not been constrained so far. For example, previous studies revealed that Os concentration in the high-and low-temperature hydrothermal fluid is ~14±24 fg g^{-1} (Sharma et al., 2000, 2007), which is not so different from the Os concentration of the seawater (~10 fg g^{-1}) (Fig. VII-3a). Although the original hydrothermal fluid has an extremely high Os concentration (~250–500 fg g^{-1}), a large part of Os is retained in the sulfide minerals within the oceanic crust and cannot go out into the seawater (Syverson et al., 2021). Therefore, some previous studies concluded that hydrothermal activity is not a major unradiogenic Os source in the ocean (less than 5% of the riverine Os input) (Katchinoff et al., 2021).

However, the number of studies on Os concentration in the hydrothermal fluid is still limited, and some of the low- and high-temperature hydrothermal fluids have high Os concentrations (~100 fg g^{-1} and ~40 fg g^{-1}, respectively) (Fig. VII-3a) (Sharma et al., 2000, 2007). In addition, a recent paper proposed the possibility that Os concentration in the Cretaceous hydrothermal fluid was greater than today (Katchinoff et al., 2021). Since the estimated seawater SO_4^- concentration during the Cretraecous was much lower than today (Lowenstein et al., 2003), sulfide formation and associated Os adsorption during the hydrothermal alteration of basalt could have been minor than today. As the result, much more unradiogenic Os could have been released through the hydrothermal activity. Thus, the possibility that these hydrothermal activities played an important role in the unradiogenic Os source cannot be excluded.

Some previous studies examined the Os isotopic ratios and concentrations in altered basaltic rocks recovered from the oceanic drilling cores (Peucker-Ehrenbrink et al., 2003, 2012; Reisberg et al., 2008). These studies revealed the contamination of seawater Os in the oceanic crust and Os upward transportation within the oceanic crust during the hydrothermal activity (Fig. VII-3b). However, since a large part of the basaltic samples were hydrothermally altered and the reliable Os concentrations of the original fresh basalt samples were lacking, these studies could not conclude how much hydrothermal alteration released unradiogenic Os into the ocean.

In order to understand the Os behavior in the hydrothermal system during the mid-

Cretaceous, more precise measurements of Os isotope ratios and concentrations of fresh and altered basaltic samples are necessary. For example, many oceanic cores have been drilled on the Ontong Java Plateau, which contain both relatively fresh basalt samples and altered basaltic samples by low-temperature hydrothermal activity (e.g., Banerjee et al., 2004). By examining Os isotopic ratios and concentrations from fresh parts to the weathered parts continuously with a high resolution, it may be possible to estimate how Os behaves during the hydrothermal alteration. Besides, similar analysis at various depths of the many drilling sites may reveal the 100-meter scale vertical Os movement during the alteration, which will make it possible to estimate how much Os was released into the ocean during the LIPs volcanism through hydrothermal activity.

VII-3.4. Mantle-derived Os input process during the LIPs volcanism

The mechanism of massive-Os input during the submarine LIPs formation has not been fully elucidated. For example, during the volcanism forming large igneous provinces, a huge amount of mantle derived-Os into the ocean (5.1×10^6 t: Tejada et al., 2009), which is ~30–60% of the Ontong Java Plateau assuming most of the OJP is composed of the similar basaltic composition of the surface layer with Os concentration of 50–100 pg g^{-1}. This increase in the mantle-derived Os during the OJN volcanism corresponds to 16 times larger than the background steady-state mantle-derived Os supplied by hydrothermal activity along the mid-ocean ridge. However, such large input of mantle-derived Os into the ocean by the normal hydrothermal alteration is unrealistic. Indeed, based on Sr isotopic variations, the increase in the hydrothermal activity during OJN volcanism is only ~30%, which is much less than the estimated value based on Os isotopic ratio. These discrepancies sometimes led to the unrealistic estimation of weathering rate of the oceanic basalt during the major mid-Cretaceous OAEs (e.g., Pogge von Strandmann et al., 2013). Previous studies reported some of the peridotite xenoliths in OJP (low-T peridotite) have extremely low Os concentration (Ishikiawa et al., 2011), implying that a massive amount of Os could have been supplied into the ocean from the mantle. Since the osmium in the mantle is hosted by the sulfide minerals (Burton et al., 2000; Luguet et al., 2007), it is proposed that the intrusion of the sulfur-undersaturated mantle into the lower lithosphere had taken mantle-derived Os upwards during the Ontong Java volcanism (Ishikawa et al., 2011). However, the exact transport process of Os into the surface of the earth is not understood at all. The comprehension of the mechanism of Os supply during LIPs formation is important to understand the Os cycle and precise quantitative estimation of hydrothermal activity and continental weathering. However, we cannot access the deeper part of the Ontong Java Plateau which possesses

information of the initial volcanic phase of the Plateau. The sedimentary sequences around the OJP contain a large amount of volcanic materials (e.g., volcanic ash in DSDP Site 167 and 463) that record the very early stages of OJP volcanism. Therefore, geochemical analysis of these materials may provide the information of transition of volcanic process and Os transport process.

VII-3.5. Variations of riverine Os concentration and isotopic ratio through geological ages

The riverine Os information of today's earth has been relatively well-studied by several authors and compiled in Peucker-Ehrenbrink and Ravizza (2000). However, the Os concentrations and isotopic ratios of river water could have been changed through geological time due to the orogenic activity, vegetation covering, ophiolite formation, and changes in the weatherability caused by the climate variations and precipitation rate. These changes occur not only in long-timescale (~10^6 years) caused by tectonic changes (e.g., Peucker-Ehrenbrink et al., 1995) but also relatively short-time scale (~10^4 years) climate changes according to astronomical cycles (e.g., Oxburgh et al., 2007, Matsumoto et al., 2021b). Although these effects are very critical to estimate past riverine Os concentration and isotopic ratios, most of the previous studies have not incorporated these effects into the modeling calculations. In order to trace temporal variations of riverine Os, it is essential to reconstruct the paleo-geography, orogenic activity, ophiolite formation, and their Os information. Besides, reconstructions of Os isotopic record in muddy riverine/delta sediments and freshwater Fe-Mn oxides at various places and various ages may make it possible to reconstruct the changes in the riverine Os isotopic ratios and their fluxes.

VII-3.6. Precise estimation of extraterrestrial Os flux

In most previous studies including this study, the extraterrestrial Os input is set to constant because there has been no good method to estimate this flux. However, there is no valid reason to set the input rate of extraterrestrial materials through meteorite impact and cosmic dust constant. Some previous studies have tried to constrain this factor within ^{3}He concentration in the sedimentary record (e.g., Farley et al., 2012). The extraterrestrial materials are characterized by the extremely unradiogenic Os isotopic ratio (~0.12: Levasseur et al., 1999), high concentrations of platinum group elements (PGE: Ru, Rh, Pd, Os, Ir, Pt) (e.g., Robinson, N. et al., 2009; Paquay et al., 2014; Sato et al., 2016), PPGE enriched (Pd, Pt, and Rh) patterns, extremely high ^{3}He/^{4}He ratio (>100), and distinctive Cr isotopic record (Shukolyukov and Lugmair, 1998). Thus, by combining these proxies recorded in the sedimentary record, it may be possible to estimate the exact long-term input rate of the extraterrestrial materials.

In this study, I present the high-resolution continuous Os isotopic record which contains valuable information on hydrothermal, extraterrestrial and continental weathering and it is surely an important first step for the understanding of the cause and

consequences mid-Cretaceous environmental perturbations. However, for the quantitative estimation of hydrothermal activity and continental weathering rate from Os isotopic records, further understanding of the Os system through geologic time scale is required. By overcoming the problems discussed in this Chapter, Os isotopic record will truly provide a glimpse into the deep-geological past.

Figures of Chapter VII

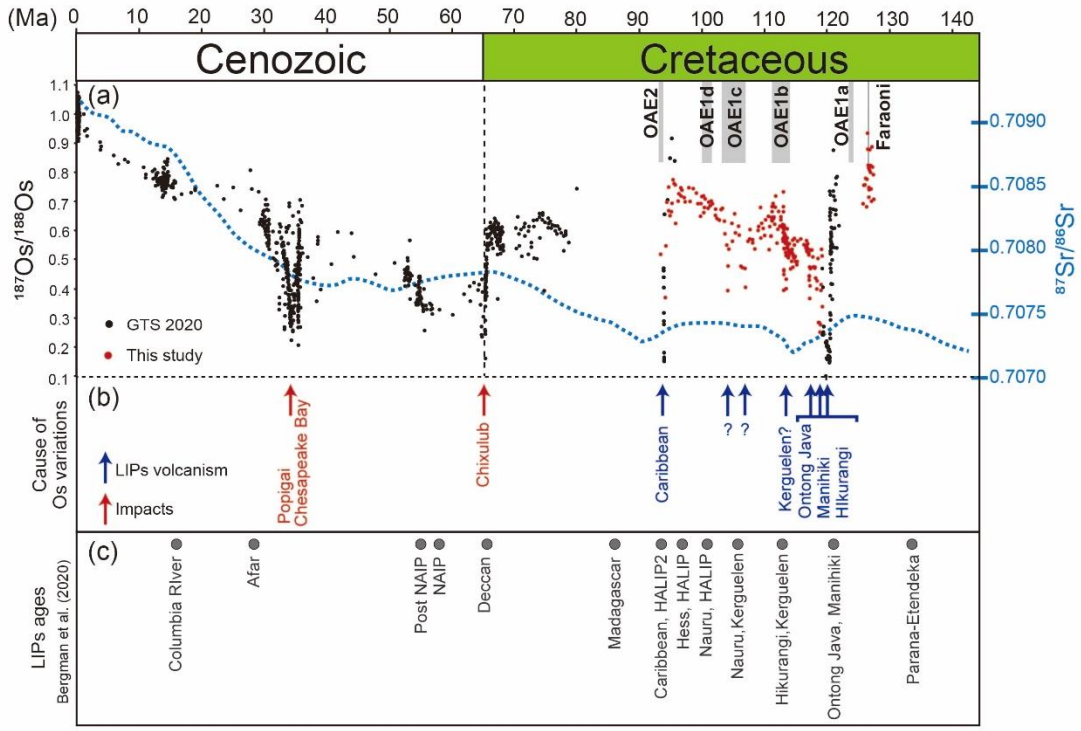

Figure VII-1. Os isotopic variations from the Cretaceous and Cenozoic: (a) Black points represent the Os isotopic data from Geologic Times Scale 2012 (Peucker-Ehrenbrink and Ravizza, 2012) and blue dashed lines represent the reconstructed marine Sr isotope ratios from the Geologic Time Scale 2020 (McArthur et al. 2020). Red circles represent the Os isotopic data revealed in this study. (b) Possible cause for the Os isotopic variations. (c) The compilation of LIPs ages after Bergman et al. (2021).

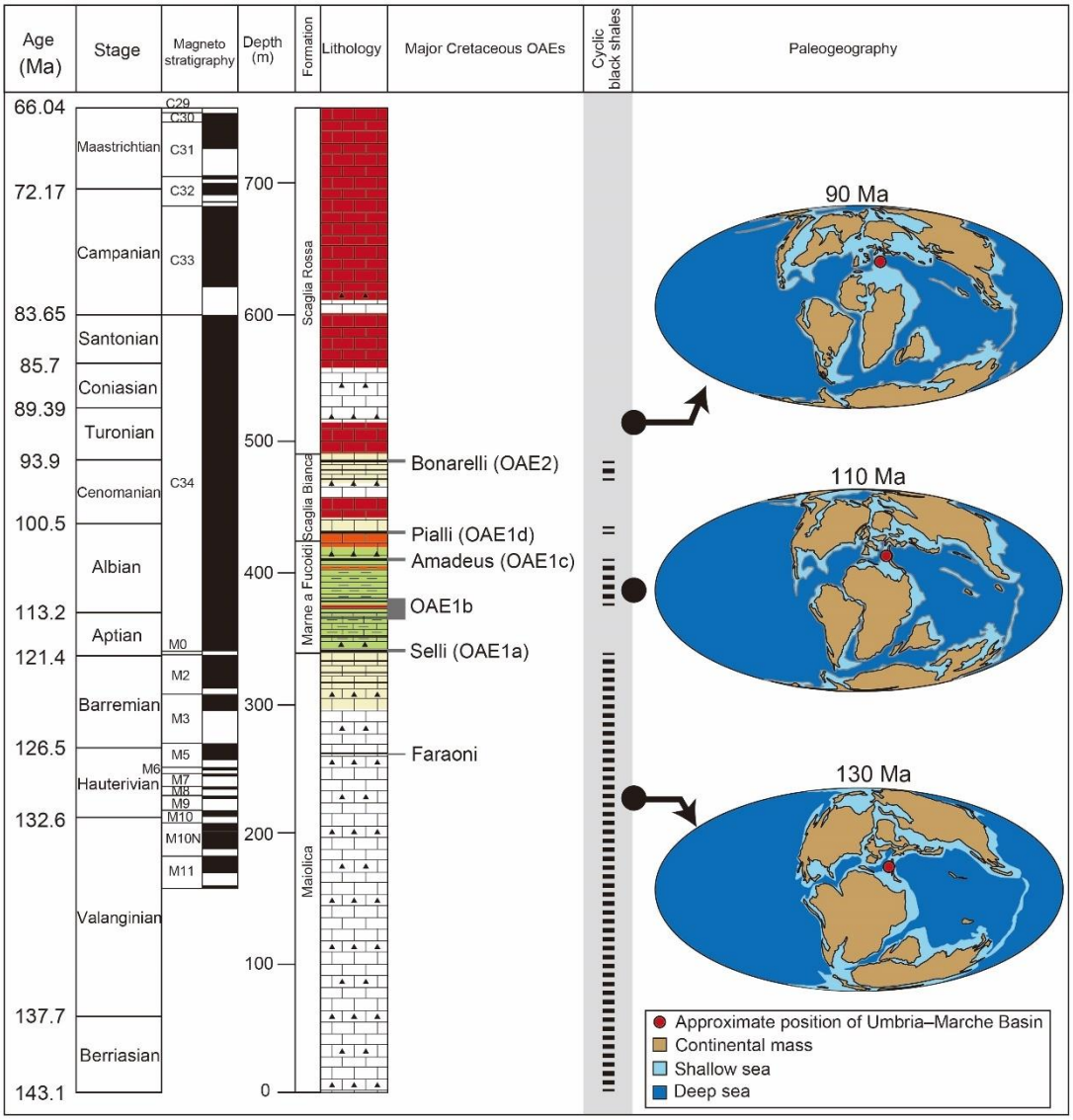

Figure VII-2. Cretaceous lithostratigraphy of the Umbria–Marche Basin: Lithostratigraphy is based on (Menichetti and Coccioni, 2015). The interval of cyclic black shale horizons are based on Bersezio et al., (2002) and Coccioni and Premoli Silva (2015).

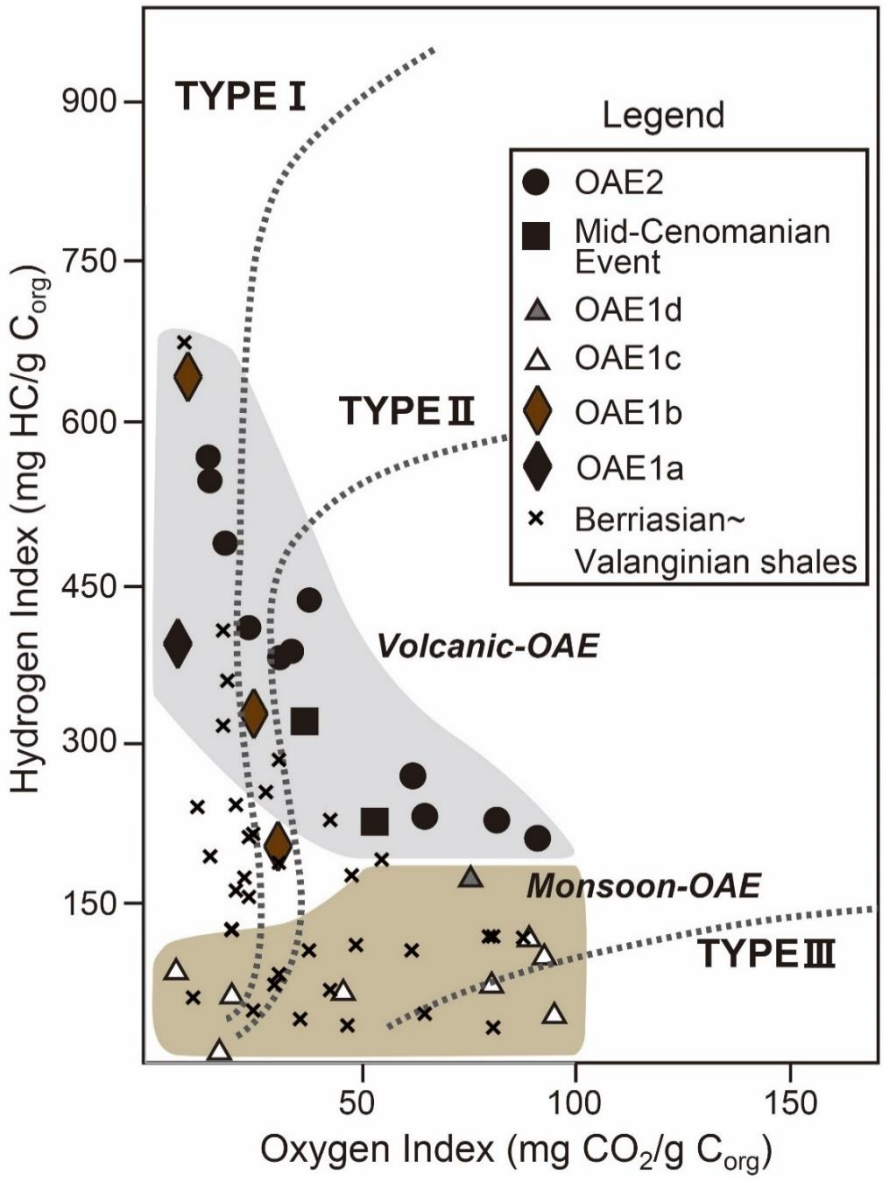

Figure VII-3. Hydrogen Index and Oxygen Index of Cretaceous organic-rich horizons. The data are based on Erbacher et al. (1996) and Bersezio et al., (2002).

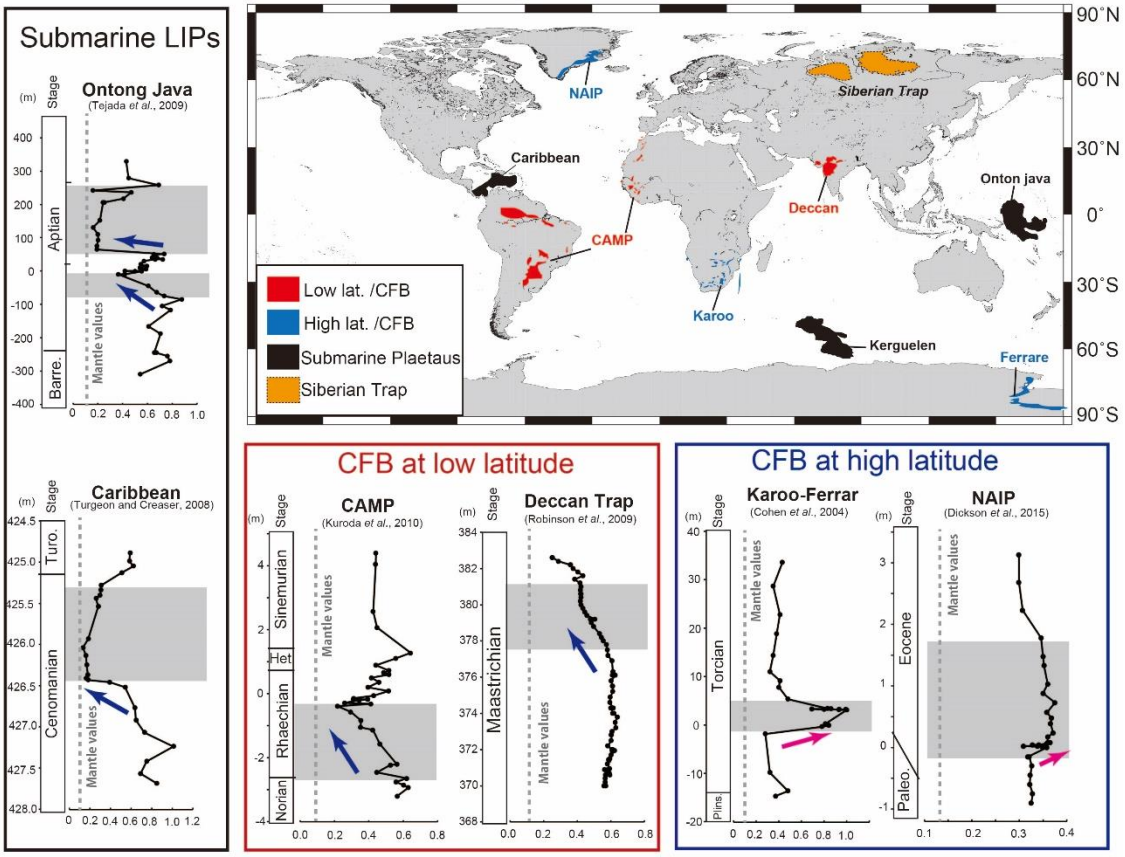

Figure VII-4. Os isotopic variation during the LIPs volcanism: Os isotopic data are from Cohen et al. (2004), Turgeon and Creaser (2008), Robinson, N. et al. (2009), Tejada et al. (2009), Kuroda et al. (2010), Dickson et al. (2015).

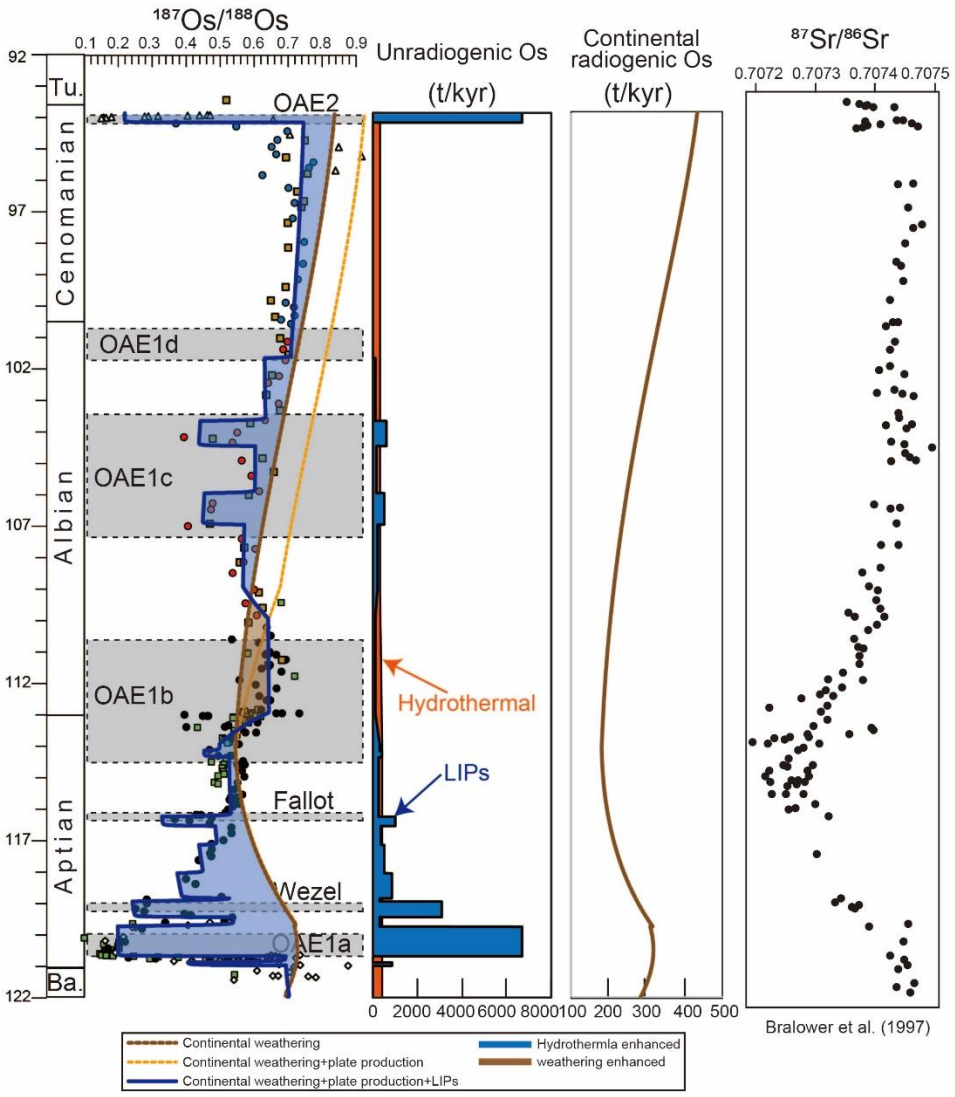

Figure VII-5. (a) Os isotopic compilation, (b) changes in the unradiogenic Os fluxes, (c) changes in the radiogenic Os fluxes from the continent, and (d) $^{87}Sr/^{86}Sr$ isotopic variations.

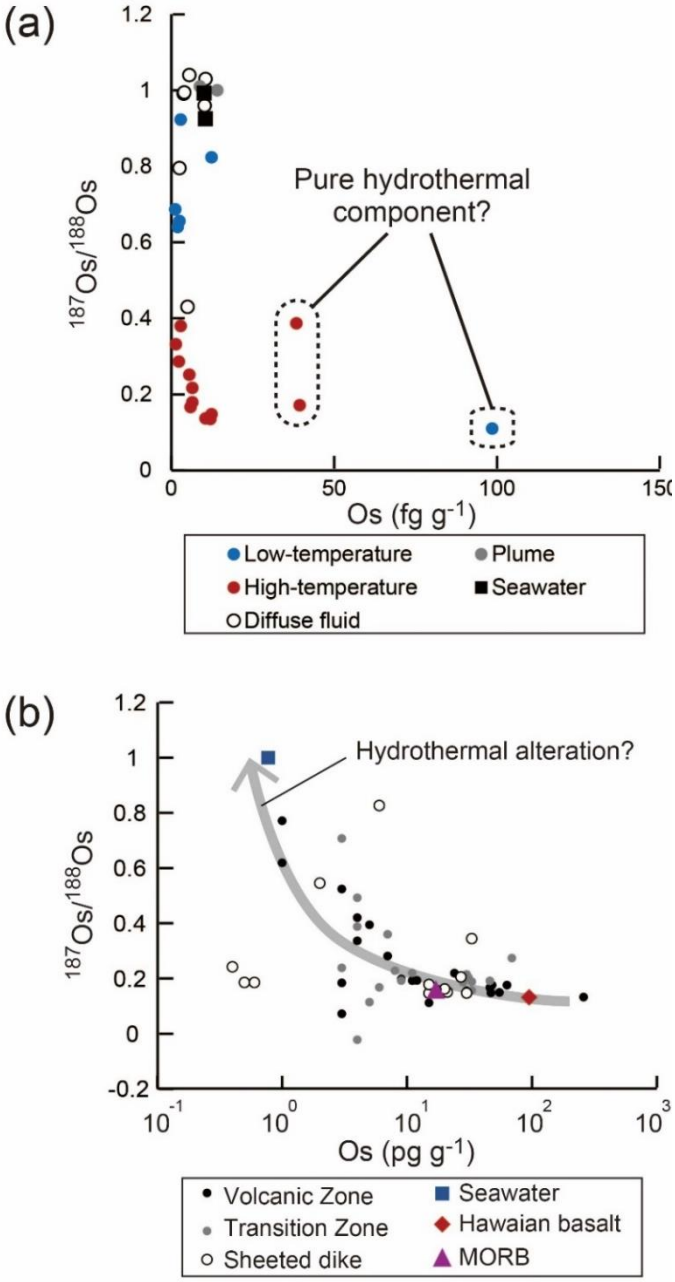

Figure VII-6. Os concentrations and isotopic ratios of hydrothermal fluid and altered basaltic rocks: (a) Os isotopic ratios and concentrations in the hydrothermal plume reported in Sharma et al. (2000, 2007). (b) Os isotopic ratios and concentrations in the altered basalt recovered from altered basaltic samples collected from DSDP Site 504B (Peucker-Ehrenbrink et al., 2003). Peucker-Ehrenbrink et al. (2003) conclude that the variations of the Os concentrations are derived from the original Os concentrations of basaltic samples. However, because of the lack of original Os concentrations, the possibility of a decrease in the Os concentration during hydrothermal alterations cannot be ruled out.

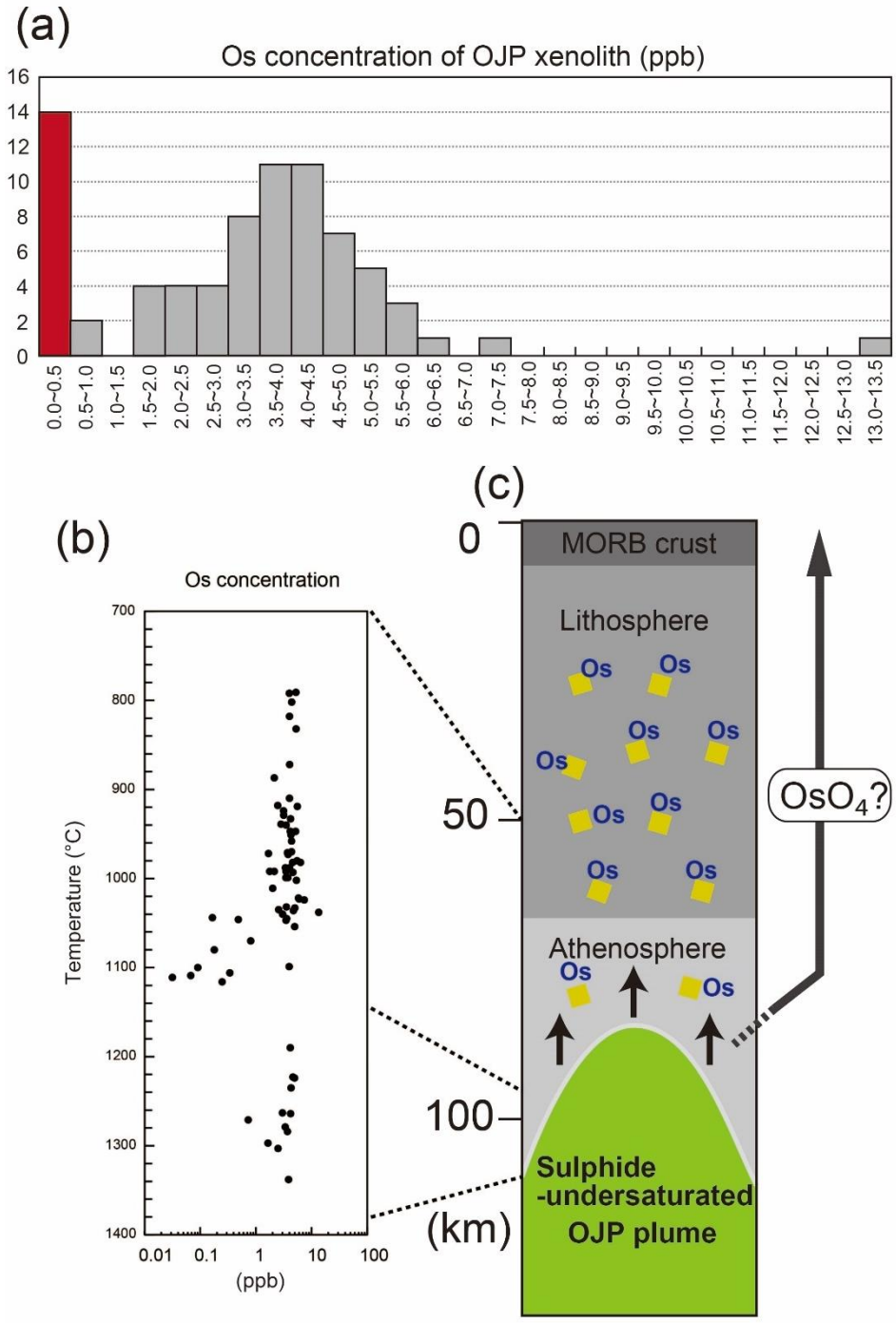

Figure VII-7. (a) The histogram of Os concentrations of xenolith and (b) its interpretations based on Ishikawa et al. (2011).

References

Algeo, T. J., & Li, C. (2020). Redox classification and calibration of redox thresholds in sedimentary systems. *Geochimica et Cosmochimica Acta*, *287*, 8–26, doi: 10.1016/j.gca.2020.01.055.

Allison, N., Austin, W., Paterson, D., & Austin, H. (2010). Culture studies of the benthic foraminifera *Elphidium williamsoni*: Evaluating pH, $\Delta[CO_3^{2-}]$ and inter-individual effects on test Mg/Ca. *Chemical Geology*, *274*(1–2), 87–93, doi: 10.1016/j.chemgeo.2010.03.019.

Al-Suwaidi, A. H., Ruhl, M., Jenkyns, H. C., Damborenea, S. E., Manceñido, M. O., Condon, D. J., ... & Hesselbo, S. (2021). New Chronostratigraphic Constraints on the Lower Jurassic Pliensbachian–Toarcian Boundary at Chacay Melehue (Neuquén Basin, Argentina).

Alt, J. C., & Teagle, D. A. (1999). The uptake of carbon during alteration of ocean crust. *Geochimica et Cosmochimica Acta*, *63*(10), 1527–1535, doi: 10.1016/S0016-7037(99)00123-4.

Abrajevitch, A., Hori, R. S., & Kodama, K. (2013). Rock magnetic record of the Triassic-Jurassic transition in pelagic bedded chert of the Inuyama section, Japan. *Geology*, *41*(7), 803–806, doi: 10.1130/G34343.1.

Adloff, M., Ridgwell, A., Monteiro, F. M., Parkinson, I. J., Dickson, A. J., Pogge von Strandmann, P. A., ... & Greene, S. E. (2021). Inclusion of a suite of weathering tracers in the cGENIE Earth system model-muffin release v. 0.9. 23. *Geoscientific Model Development*, *14*(7), 4187–4223, doi: 10.5194/gmd-14-4187-2021.

Allègre, C. J., & Luck, J. M. (1980). Osmium isotopes as petrogenetic and geological tracers. *Earth and Planetary Science Letters*, *48*(1), 148–154, doi: 10.1016/0012-821X(80)90177-6.

Aguado, R., de Gea, G. A., Castro, J. M., O'Dogherty, L., Quijano, M. L., Naafs, B. D. A., & Pancost, R. D. (2014). Late Barremian–early Aptian dark facies of the Subbetic (Betic Cordillera, southern Spain): Calcareous nannofossil quantitative analyses, chemostratigraphy and palaeoceanographic reconstructions. *Palaeogeography, Palaeoclimatology, Palaeoecology*, *395*, 198–221, doi: 10.1016/j.palaeo.2013.12.031.

Antonelli, M. A., Pester, N. J., Brown, S. T., & DePaolo, D. J. (2017). Effect of

paleoseawater composition on hydrothermal exchange in midocean ridges. *Proceedings of the National Academy of Sciences*, *114*(47), 12413–12418, doi: 10.1073/pnas.1709145114.

Armstrong, H.A., Wagner, T., Herringshaw, L.G., Farnsworth, A.J., Lunt, D.J., Harland, M., et al. (2016). Hadley circulation and precipitation changes controlling black shale deposition in the Late Jurassic Boreal Seaway. *Paleoceanography, 31*(8), 1041–1053. doi: 10.1002/2015PA002911

Arnaud, H. M., Flood, P. G., & Strasser, A. (1995). Resolution Guyot (Hole 866A, Mid-Pacific Mountains): facies evolution and sequence stratigraphy: Northwest Pacific atolls and guyots. In *Proceedings of the Ocean Drilling Program. Scientific results* (Vol. 142, pp. 133–159). College Station, Texas.

Arthur, M. A., Brumsack, H. J., Jenkyns, H. C., & Schlanger, S. O. (1990). Stratigraphy, geochemistry, and paleoceanography of organic carbon-rich Cretaceous sequences. In *Cretaceous resources, events and rhythms* (pp. 75–119). Springer, Dordrecht.

Baksi, A. K., Foulger, G. R., & Jurdy, D. M. (2007). A quantitative tool for detecting alteration in undisturbed rocks and minerals-I: water, chemical weathering, and atmospheric argon. *SPECIAL PAPERS-GEOLOGICAL SOCIETY OF AMERICA*, *430*, 285.

Banerjee, N. R., Honnorez, J., & Muehlenbachs, K. (2004). Low-temperature alteration of submarine basalts from the Ontong Java Plateau. *Geological Society, London, Special Publications*, *229*(1), 259–273, doi: 10.1144/GSL.SP.2004.229.01.15.

Barker, S., & Elderfield, H. (2002). Foraminiferal calcification response to glacial-interglacial changes in atmospheric CO_2. *Science*, *297*(5582), 833–836, doi: 10.1126/science.1072815.

Barnes, I., Irwin, W. P., & White, D. E. (1978). *Global distribution of carbon dioxide discharges, and major zones of seismicity* (Vol. 78, No. 39). US Geological Survey, Water Resources Division.

Baudin, F. (2005). A Late Hauterivian short-lived anoxic event in the Mediterranean Tethys: the ‘Faraoni Event’. *Comptes Rendus Geoscience, 337*(16), 1532–1540.

Baudin, F., & Riquier, L. (2014). The Late Hauterivian Faraoni ‘Oceanic Anoxic Event’: an update. *Bulletin de la Société Géologique de France*, *185*(6), 359–377, doi: 10.2113/gssgfbull.185.6.359.

Bauer, K. W., Bottini, C., Frei, R., Asael, D., Planavsky, N. J., Francois, R., ... & Crowe, S. A. (2021). Pulsed volcanism and rapid oceanic deoxygenation during Oceanic Anoxic Event 1a. *Geology*, *49*(12), 1452–1456, doi: 10.1130/G49065.1.

Beerling, D. J., Fox, A., Stevenson, D. S., & Valdes, P. J. (2011). Enhanced chemistry-climate feedbacks in past greenhouse worlds. *Proceedings of the National Academy of Sciences*, *108*(24), 9770–9775, doi: 10.1073/pnas.1102409108.

Bergman, N. M., Lenton, T. M., & Watson, A. J. (2004). COPSE: a new model of biogeochemical cycling over Phanerozoic time. *American Journal of Science*, *304*(5), 397–437, doi: 10.2475/ajs.304.5.397.

Bergman, S. C., Eldrett, J. S., & Minisini, D. (2021). Phanerozoic Large Igneous Province, Petroleum System, and Source Rock Links. *Large Igneous Provinces: A Driver of Global Environmental and Biotic Changes*, 191–228, doi: 10.1002/9781119507444.ch9.

Bersezio, R., Erba, E., Gorza, M., & Riva, A. (2002). Berriasian–Aptian black shales of the Maiolica formation (Lombardian Basin, Southern Alps, Northern Italy): local to global events. *Palaeogeography, Palaeoclimatology, Palaeoecology*, *180*(4), 253–275, doi: 10.1016/S0031-0182(01)00416-3.

Begg, G.C., Griffin, W.L., Natapov, L.M., O'Reilly, S.Y., Grand, S.P., O'Neill, C.J., et al. (2009). The lithospheric architecture of Africa: Seismic tomography, mantle petrology, and tectonic evolution. *Geosphere, 5*(1), 23–50. 10.1130/GES00179.1.

Berner, R. A. (2008). Addendum to "Inclusion of the Weathering of Volcanic Rocks in the GEOCARBSULF Model":(RA Berner, 2006, V. 306, p. 295–302). *American Journal of Science*, *308*(1), 100–103, doi: 10.2475/01.2008.04.

Birck, J.L., Barman, M.R., & Capmas, F. (1997). Re-Os isotopic measurements at the femtomole level in natural samples. *Geostandards newsletter, 21*(1), 19–27. 10.1111/j.1751-908X.1997.tb00528.x

Blättler, C. L., Jenkyns, H. C., Reynard, L. M., & Henderson, G. M. (2011). Significant increases in global weathering during Oceanic Anoxic Events 1a and 2 indicated by calcium isotopes. *Earth and Planetary Science Letters*, *309*(1–2), 77–88. doi: 10.1016/j.epsl.2011.06.029.

Bodin, S., Godet, A., Matera, V., Steinmann, P., Vermeulen, J., Gardin, S., et al. (2007). Enrichment of redox-sensitive trace metals (U, V, Mo, As) associated with the late

Hauterivian Faraoni oceanic anoxic event. *International Journal of Earth Sciences. 96*(2), 327–341, doi: 10.1007/s00531-006-0091-9.

Bodin, S., Meissner, P., Janssen, N. M., Steuber, T., & Mutterlose, J. (2015). Large igneous provinces and organic carbon burial: Controls on global temperature and continental weathering during the Early Cretaceous. *Global and Planetary Change*, *133*, 238–253, doi: 10.1016/j.gloplacha.2015.09.001.

Bolton, C. T., Hernández-Sánchez, M. T., Fuertes, M. A., González-Lemos, S., Abrevaya, L., Mendez-Vicente, A., ... & Stoll, H. M. (2016). Decrease in coccolithophore calcification and CO_2 since the middle Miocene. *Nature communications*, *7*(1), 1–13, doi: 10.1038/ncomms10284.

Bond, D. P., & Sun, Y. (2021). Global Warming and Mass Extinctions Associated With Large Igneous Province Volcanism. *Large Igneous Provinces: A Driver of Global Environmental and Biotic Changes*, 83–102, doi: 10.1002/9781119507444.ch3.

Bornemann, A., Pross, J., Reichelt, K., Herrle, J. O., Hemleben, C., & Mutterlose, J. (2005). Reconstruction of short-term palaeoceanographic changes during the formation of the Late Albian 'Niveau Breistroffer'black shales (Oceanic Anoxic Event 1d, SE France). *Journal of the Geological Society*, *162*(4), 623–639, doi: 10.1144/0016-764903-171.

Bottini, C., Erba, E., Tiraboschi, D., Jenkyns, H. C., Schouten, S., & Sinninghe Damsté, J. S. (2015). Climate variability and ocean fertility during the Aptian Stage. *Climate of the Past*, *11*(3), 383–402, doi: 10.5194/cp-11-383-2015.

Bottini, C., & Erba, E. (2018). Mid-Cretaceous paleoenvironmental changes in the western Tethys. *Climate of the Past*, *14*(8), 1147–1163, doi: 10.5194/cp-14-1147-2018.

Bottini, C., & Faucher, G. (2020). Biscutum constans coccolith size patterns across the mid Cretaceous in the western Tethys: Paleoecological implications. *Palaeogeography, Palaeoclimatology, Palaeoecology*, *555*, 109852, doi: 10.1016/j.palaeo.2020.109852.

Bottini, C., Cohen, A. S., Erba, E., Jenkyns, H. C., & Coe, A. L. (2012). Osmium-isotope evidence for volcanism, weathering, and ocean mixing during the early Aptian OAE 1a. *Geology*, *40*(7), 583–586, doi: 10.1130/G33140.1.

Brady, P. V., & Gíslason, S. R. (1997). Seafloor weathering controls on atmospheric CO_2

and global climate. *Geochimica et Cosmochimica Acta*, *61*(5), 965–973, doi: 10.1016/S0016-7037(96)00385-7.

Bralower, T. J., Fullagar, P. D., Paull, C. K., Dwyer, G. S., & Leckie, R. M. (1997). Mid-Cretaceous strontium-isotope stratigraphy of deep-sea sections. *Geological Society of America Bulletin*, *109*(11), 1421–1442, doi: 10.1130/0016-7606(1997)109<1421:MCSISO>2.3.CO;2.

Bralower, T. J., Silva, I. P., & Malone, M. J. (2002). New evidence for abrupt climate change in the Cretaceous and Paleogene: an Ocean Drilling Program expedition to Shatsky Rise, northwest Pacific. *Gsa Today*, *12*(11), 4–10.

Brazier, J. M., Suan, G., Tacail, T., Simon, L., Martin, J. E., Mattioli, E., & Balter, V. (2015). Calcium isotope evidence for dramatic increase of continental weathering during the Toarcian oceanic anoxic event (Early Jurassic). *Earth and Planetary Science Letters*, *411*, 164–176, doi: 10.1016/j.epsl.2014.11.028.

Broecker, W. S., and T.-H. Peng (1982), Tracers in the Sea, A publication of the Lamont-Doherty Geological Observatory, Columbia University, Palisades, New York.

Bryan, S. E., & Ernst, R. E. (2008). Revised definition of large igneous provinces (LIPs). *Earth-Science Reviews*, *86*(1–4), 175–202, doi: 10.1016/j.earscirev.2007.08.008.

Burgess, S. D., Muirhead, J. D., & Bowring, S. A. (2017). Initial pulse of Siberian Traps sills as the trigger of the end-Permian mass extinction. *Nature Communications*, *8*(1), 1–6, doi: 10.1038/s41467-017-00083-9.

Burton, K. W., Bourdon, B., Birck, J. L., Allègre, C. J., & Hein, J. R. (1999). Osmium isotope variations in the oceans recorded by Fe Mn crusts. *Earth and Planetary Science Letters*, *171*(1), 185–197, doi 10.1016/S0012-821X(99)00139-9.

Burton, K. W., Schiano, P., Birck, J. L., Allegre, C. J., Rehkämper, M., Halliday, A. N., & Dawson, J. B. (2000). The distribution and behaviour of rhenium and osmium amongst mantle minerals and the age of the lithospheric mantle beneath Tanzania. *Earth and Planetary Science Letters*, *183*(1–2), 93–106, doi: 10.1016/S0012-821X(00)00259-4.

Butler, R. W. H., Mazzoli, S., Corrado, S., De Donatis, M., Di Bucci, D., Gambini, R., ... & Zucconi, V. (2004). Applying thick-skinned tectonic models to the Apennine thrust belt of Italy—Limitations and implications.

Capriolo, M., Marzoli, A., Aradi, L. E., Ackerson, M. R., Bartoli, O., Callegaro, S., ... & Szabó, C. (2021). Massive methane fluxing from magma–sediment interaction in the end-Triassic Central Atlantic Magmatic Province. *Nature communications*, *12*(1), 1–9, doi: 10.1038/s41467-021-25510-w.

Cas, R. A., & Simmons, J. M. Why deep-water eruptions are so different from subaerial eruptions. *Front. Earth Sci.*, **6**, 198 (2018).

Cecca, F., Marini, A., Pallini, G., Baudin, F., & Begouen, V. (1994). A guide-level of the uppermost Hauterivian (Lower Cretaceous) in the pelagic succession of Umbria-Marche Apennines (Central Italy): the Faraoni Level. *Rivista italiana di Paleontologia e Stratigrafia, 99*, 551–568.

Chandler, M. T., Wessel, P., Taylor, B., Seton, M., Kim, S. S., & Hyeong, K. (2012). Reconstructing Ontong Java Nui: Implications for Pacific absolute plate motion, hotspot drift and true polar wander. *Earth and Planetary Science Letters*, *331*, 140–151, doi: 10.1016/j.epsl.2012.03.017.

Charbonnier, G., Duchamp-Alphonse, S., Adatte, T., Föllmi, K.B., Spangenberg, J.E., Gardin, S., et al. (2016). Eccentricity paced monsoon-like system along the northwestern Tethyan margin during the Valanginian (Early Cretaceous): new insights from detrital and nutrient fluxes into the Vocontian Basin (SE France). *Palaeogeography, Palaeoclimatology, Palaeoecology, 443*, 145–155. doi: 10.1016/j.palaeo.2015.11.027.

Charbonnier, G., Godet, A., Bodin, S., Adatte, T., & Föllmi, K.B. (2018). Mercury anomalies, volcanic pulses, and drowning episodes along the northern Tethyan margin during the latest Hauterivian-earliest Aptian. *Palaeogeography, Palaeoclimatology, Palaeoecology, 505*, 337–350, doi: 10.1016/j.palaeo.2018.06.013.

Clemens, S., Prell, W., Murray, D., Shimmield, G., & Weedon, G. (1991). Forcing mechanisms of the Indian Ocean monsoon. *Nature, 353*(6346), 720–725. doi: 10.1038/353720a0.

Coccioni, R. (2001) The “Pialli Level” from the latest Albian of the Umbria-Marche Apennines (Italy). *GeoItalia*, **3** Forum FIST, 192–193.

Coccioni, R. (2020). Revised upper Barremian–upper Aptian planktonic foraminiferal biostratigraphy of the Gorgo a Cerbara section (central Italy). *Newsletters on Stratigraphy*, 275–295.

Coccioni, R., & Galeotti, S. (1993). Orbitally induced cycles in benthonic foraminiferal morphogroups and trophic structure distribution patterns from the Late Albian "Amadeus Segment"(Central Italy). *Journal of Micropalaeontology*, *12*(2), 227–239, doi: 10.1144/jm.12.2.227.

Coccioni, R., & Galeotti, S. (2003). The mid-Cenomanian Event: prelude to OAE 2. *Palaeogeography, Palaeoclimatology, Palaeoecology*, *190*, 427–440, doi: 10.1016/S0031-0182(02)00617-X.

Coccioni, R., & Luciani, V. (2004). Planktonic foraminifera and environmental changes across the Bonarelli Event (OAE2, latest Cenomanian) in its type area: a high-resolution study from the Tethyan reference Bottaccione section (Gubbio, Central Italy). *The Journal of Foraminiferal Research*, *34*(2), 109–129, doi: 10.2113/0340109.

Coccioni, R., & Premoli Silva, I. (2015). Revised Upper Albian-Maastrichtian planktonic foraminiferal biostratigraphy and magnetostratigraphy of the classical Tethyan Gubbio section (Italy). *Newsletters on Stratigraphy*, *48*(1), 47–90.

Coccioni, R., Nesci, O., Tramontana, M., Wezel, F. C., & Moretti, E. (1987). Descrizione di un livello–guida "radiolaritico–bituminoso–ittiolitico" alla base delle Marne a Fucoidi nell'Appennino Umbro–Marchigiano. Bollettino della Società Geologica Italiana v. 106, p. 183–192.

Coccioni, R., Baudin, F., Cecca, F., Chiari, M., Galeotti, S., Gardin, S., & Salvini, G. (1998). Integrated stratigraphic, palaeontological, and geochemical analysis of the uppermost Hauterivian Faraoni Level in the Fiume Bosso section, Umbria-Marche Apennines, Italy. *Cretaceous Research, 19*(1), 1–23, doi: 10.1006/cres.1997.0093.

Coccioni, R., Jovane, L., Bancalà, G., Bucci, C., Fauth, G., Frontalini, F., ... & Ferreira da Trindade, R. I. (2012). Umbria-Marche Basin, Central Italy: A reference section for the Aptian-Albian interval at low latitudes. *Scientific Drilling*, *13*, 42–46, doi: 10.2204/iodp.sd.13.07.2011.

Coccioni, R., Sabatino, N., Frontalini, F., Gardin, S., Sideri, M., & Sprovieri, M. (2014). The neglected history of Oceanic Anoxic Event 1b: insights and new data from the Poggio le Guaine section (Umbria–Marche Basin). *Stratigraphy*, *11*(3–4), 245–282.

Coffin, M. F., & Eldholm, O. (2005). Large igneous provinces. *Encyclopedia of geology*,

315–323.

Coffin, M. F., Pringle, M. S., Duncan, R. A., Gladczenko, T. P., Storey, M., Müller, R. D., & Gahagan, L. A. (2002). Kerguelen hotspot magma output since 130 Ma. *Journal of petrology*, *43*(7), 1121–1137, doi: 10.1093/petrology/43.7.1121.

Cogné, J. P., & Humler, E. (2006). Trends and rhythms in global seafloor generation rate. *Geochemistry, Geophysics, Geosystems*, *7*(3), doi: 10.1029/2005GC001148.

Cohen, A. S., & Waters, F. G. (1996). Separation of osmium from geological materials by solvent extraction for analysis by thermal ionisation mass spectrometry. *Analytica Chimica Acta*, *332*(2–3), 269–275, doi: 10.1016/0003-2670(96)00226-7.

Cohen, A. S., & Coe, A. L. (2002). New geochemical evidence for the onset of volcanism in the Central Atlantic magmatic province and environmental change at the Triassic-Jurassic boundary. *Geology*, *30*(3), 267–270, doi: 10.1130/0091-7613(2002)030<0267:NGEFTO>2.0.CO;2.

Cohen, A. S., & Coe, A. L. (2007). The impact of the Central Atlantic Magmatic Province on climate and on the Sr-and Os-isotope evolution of seawater. *Palaeogeography, Palaeoclimatology, Palaeoecology*, *244*(1–4), 374–390, doi: 10.1016/j.palaeo.2006.06.036.

Cohen, A. S., Coe, A. L., Harding, S. M., & Schwark, L. (2004). Osmium isotope evidence for the regulation of atmospheric CO_2 by continental weathering. *Geology*, *32*(2), 157–160, doi: 10.1130/G20158.1.

Creaser, R. A., Sannigrahi, P., Chacko, T., & Selby, D. (2002). Further evaluation of the Re-Os geochronometer in organic-rich sedimentary rocks: A test of hydrocarbon maturation effects in the Exshaw Formation, Western Canada Sedimentary Basin. *Geochimica et Cosmochimica Acta*, *66*(19), 3441–3452, doi: 10.1016/S0016-7037(02)00939-0.

Cresta, S., Monechi, S. & Parisi, G. *Mesozoic–Cenozoic stratigraphy in the Umbria–Marche Area. Geological field trips in the Umbria–Marche Apennines (Italy), Mem. Descr. Carta Geol. Ital.* 39, 48–49 (1989).

Davis, C. V., Rivest, E. B., Hill, T. M., Gaylord, B., Russell, A. D., & Sanford, E. (2017). Ocean acidification compromises a planktic calcifier with implications for global carbon cycling. *Scientific reports*, *7*(1), 1–8. doi: 10.1038/s41598-017-01530-9.

De Gea, G. A., Castro, J. M., Aguado, R., Ruiz-Ortiz, P. A., & Company, M. (2003).

Lower Aptian carbon isotope stratigraphy from a distal carbonate shelf setting: the Cau section, Prebetic zone, SE Spain. *Palaeogeography, Palaeoclimatology, Palaeoecology*, *200*(1–4), 207–219, doi: 10.1016/S0031-0182(03)00451-6.

Demicco, R. V. (2004). Modeling seafloor-spreading rates through time. *Geology*, *32*(6), 485–488, doi: 10.1130/G20409.1.

De Vleeschouwer, D., Drury, A.J., Vahlenkamp, M., Rochholz, F., Liebrand, D., & Pälike, H. (2020). High-latitude biomes and rock weathering mediate climate–carbon cycle feedbacks on eccentricity timescales. *Nature communications, 11*(1), 1–10, doi: 10.1038/s41467-020-18733-w.

Dias, B. B., Hart, M. B., Smart, C. W., & Hall-Spencer, J. M. (2010). Modern seawater acidification: the response of foraminifera to high-CO2 conditions in the Mediterranean Sea. *Journal of the Geological Society*, *167*(5), 843–846, doi: 10.1144/0016-76492010-050.

Dickson, A. J., Cohen, A. S., Coe, A. L., Davies, M., Shcherbinina, E. A., & Gavrilov, Y. O. (2015). Evidence for weathering and volcanism during the PETM from Arctic Ocean and Peri-Tethys osmium isotope records. *Palaeogeography, Palaeoclimatology, Palaeoecology*, *438*, 300–307, doi: 10.1016/j.palaeo.2015.08.019.

Dickson, A. J., Cohen, A. S., & Davies, M. (2021). The Osmium Isotope Signature of Phanerozoic Large Igneous Provinces. *Large Igneous Provinces: A Driver of Global Environmental and Biotic Changes*, 229–246, doi: 10.1002/9781119507444.ch10.

Dubin, A., & Peucker-Ehrenbrink, B. (2015). The importance of organic-rich shales to the geochemical cycles of rhenium and osmium. *Chemical Geology*, *403*, 111–120, doi: 10.1016/j.chemgeo.2015.03.010.

Duncan, R. A. (2002). A time frame for construction of the Kerguelen Plateau and Broken Ridge. *Journal of Petrology*, *43*(7), 1109–1119, doi: 10.1093/petrology/43.7.1109.

Dunlea, A. G., Tegler, L. A., Peucker-Ehrenbrink, B., Anbar, A. D., Romaniello, S. J., & Horner, T. J. (2021). Pelagic clays as archives of marine iron isotope chemistry. *Chemical Geology*, *575*, 120201, doi: 10.1016/j.chemgeo.2021.120201.

Du Vivier, A. D., Selby, D., Sageman, B. B., Jarvis, I., Gröcke, D. R., & Voigt, S. (2014). Marine 187Os/188Os isotope stratigraphy reveals the interaction of volcanism and ocean circulation during Oceanic Anoxic Event 2. *Earth and Planetary Science*

Letters, *389*, 23–33, doi: 10.1016/j.epsl.2013.12.024.

Du Vivier, A. D. C., Selby, D., Condon, D. J., Takashima, R., & Nishi, H. (2015). Pacific $^{187}Os/^{188}Os$ isotope chemistry and U–Pb geochronology: Synchroneity of global Os isotope change across OAE2. *Earth and Planetary Science Letters*, *428*, 204–216, doi: 10.1016/j.epsl.2015.07.020.

Elderfield, H., Ferretti, P., Greaves, M., Crowhurst, S., McCave, I.N., Hodell, D., & Piotrowski, A.M. (2012). Evolution of ocean temperature and ice volume through the mid-Pleistocene climate transition. *Science, 337*(6095), 704–709, doi: 10.1126/science.1221294.

Eldholm, O., & Coffin, M. F. (2000). Large igneous provinces and plate tectonics. *Geophysical Monograph-American Geophysical Union*, *121*, 309–326.

Elkhazri, A., Abdallah, H., Razgallah, S., Moullade, M., & Kuhnt, W. (2013). Carbon-isotope and microfaunal stratigraphy bounding the Lower Aptian Oceanic Anoxic Event 1a in northeastern Tunisia. *Cretaceous Research*, *39*, 133–148, doi: 10.1016/j.cretres.2012.05.011.

Erba, E. (1994). Nannofossils and superplumes: the early Aptian “nannoconid crisis”. *Paleoceanography*, *9*(3), 483–501, doi: 10.1029/94PA00258.

Erba, E., Channell, J. E., Claps, M., Jones, C., Larson, R., Opdyke, B., Silva, I., P., Riva, A., Salvini, G., and Torricelli, S., (1999). Integrated stratigraphy of the Cismon Apticore (southern Alps, Italy); a" reference section" for the Barremian-Aptian interval at low latitudes. *The Journal of Foraminiferal Research*, *29*(4), 371–391.

Erba, E. (2004). Calcareous nannofossils and Mesozoic oceanic anoxic events. *Marine micropaleontology*, *52*(1–4), 85–106, doi: 10.1016/j.marmicro.2004.04.007.

Erba, E., Bottini, C., Weissert, H. J., & Keller, C. E. (2010). Calcareous nannoplankton response to surface-water acidification around Oceanic Anoxic Event 1a. *Science*, *329*(5990), 428–432, doi: 10.1126/science.1188886.

Erba, E., Duncan, R. A., Bottini, C., Tiraboschi, D., Weissert, H., Jenkyns, H. C., & Malinverno, A. (2015). Environmental consequences of Ontong Java Plateau and Kerguelen Plateau volcanism. *The origin, evolution, and environmental impact of oceanic large igneous provinces. Geological Society of America Special Paper*, *511*, 271–303.

Erbacher, J., Thurow, J., & Littke, R. (1996). Evolution patterns of radiolaria and organic

matter variations: A new approach to identify sea-level changes in mid-Cretaceous pelagic environments. *Geology*, *24*(6), 499–502, doi: 10.1130/0091-7613(1996)024<0499:EPORAO>2.3.CO;2.

Ernst, R. E., Bond, D. P., Zhang, S. H., Buchan, K. L., Grasby, S. E., Youbi, N., ... & Doucet, L. S. (2021). Large Igneous Province Record Through Time and Implications for Secular Environmental Changes and Geological Time-Scale Boundaries. *Large Igneous Provinces: A Driver of Global Environmental and Biotic Changes*, 1–26, doi: 10.1002/9781119507444.ch1.

Esser, B. K., & Turekian, K. K. (1993). The osmium isotopic composition of the continental crust. *Geochimica et Cosmochimica Acta*, *57*(13), 3093–3104, doi: 10.1016/0016-7037(93)90296-9.

Falzoni, F., Petrizzo, M. R., Clarke, L. J., MacLeod, K. G., & Jenkyns, H. C. (2016). Long-term Late Cretaceous oxygen-and carbon-isotope trends and planktonic foraminiferal turnover: A new record from the southern midlatitudes. *Bulletin*, *128*(11–12), 1725–1735, doi: 10.1130/B31399.1.

Farley, K. A., Montanari, A., & Coccioni, R. (2012). A record of the extraterrestrial ^{3}He flux through the Late Cretaceous. *Geochimica et Cosmochimica Acta*, *84*, 314–328, doi: 10.1016/j.gca.2012.01.015.

Fassell, M. L., & Bralower, T. J. (1999). Warm, equable mid-Cretaceous: Stable isotope evidence. *Special Paper of the Geological Society of America*, *332*, 121–142, doi: 10.1130/0-8137-2332-9.121.

Fernandez, A., Korte, C., Ullmann, C. V., Looser, N., Wohlwend, S., & Bernasconi, S. M. (2021). Reconstructing the magnitude of Early Toarcian (Jurassic) warming using the reordered clumped isotope compositions of belemnites. *Geochimica et Cosmochimica Acta*, *293*, 308–327, doi: 10.1016/j.gca.2020.10.005.

Ferraro, S., Coccioni, R., Sabatino, N., Del Core, M., & Sprovieri, M. (2020). Morphometric response of late Aptian planktonic foraminiferal communities to environmental changes: A case study of Paraticinella rohri at Poggio le Guaine (central Italy). *Palaeogeography, Palaeoclimatology, Palaeoecology*, *538*, 109384, doi: 10.1016/j.palaeo.2019.109384.

Fletcher, B. J., Brentnall, S. J., Anderson, C. W., Berner, R. A., & Beerling, D. J. (2008). Atmospheric carbon dioxide linked with Mesozoic and early Cenozoic climate change. *Nature Geoscience*, *1*(1), 43–48, doi: 10.1038/ngeo.2007.29.

Fitton, J. G., & Godard, M. (2004). Origin and evolution of magmas on the Ontong Java Plateau. *Geological Society, London, Special Publications*, *229*(1), 151–178.

Franceschi, M., Preto, N., Hinnov, L. A., Huang, C., & Rusciadelli, G. (2011). Terrestrial laser scanner imaging reveals astronomical forcing in the Early Cretaceous of the Tethys realm. *Earth and Planetary Science Letters*, *305*(3–4), 359–370, doi: 10.1016/j.epsl.2011.03.017.

Frey, F. A., Coffin, M. F., Wallace, P. J., & Weis, D. (2003). Leg 183 snthesis: Kerguelen Plateau-Broken Ridge-a large igneous province. In *Proceedings of the Ocean Drilling Program, scientific results* (Vol. 183, pp. 1–48).

Friedrich, O., Norris, R. D., & Erbacher, J. (2012). Evolution of middle to Late Cretaceous oceans—a 55 my record of Earth's temperature and carbon cycle. *Geology*, *40*(2), 107–110, doi: 10.1130/G32701.1.

Fujisaki, W., Sawaki, Y., Yamamoto, S., Sato, T., Nishizawa, M., Windley, B. F., & Maruyama, S. (2016). Tracking the redox history and nitrogen cycle in the pelagic Panthalassic deep ocean in the Middle Triassic to Early Jurassic: Insights from redox-sensitive elements and nitrogen isotopes. *Palaeogeography, Palaeoclimatology, Palaeoecology*, *449*, 397–420, doi: 10.1016/j.palaeo.2016.01.039.

Gaffin, S. (1987). Ridge volume dependence on seafloor generation rate and inversion using long term sealevel change. *American Journal of Science*, *287*(6), 596–611, doi: 10.2475/ajs.287.6.596.

Gale, A. S., Mutterlose, J., Batenburg, S., Gradstein, F. M., Agterberg, F. P., Ogg, J. G., & Petrizzo, M. R. (2020). The Cretaceous Period. In *Geologic Time Scale 2020* (pp. 1023–1086). Elsevier, doi: 10.1016/B978-0-12-824360-2.00027-9.

Gambacorta, G., Jenkyns, H. C., Russo, F., Tsikos, H., Wilson, P. A., Faucher, G., & Erba, E. (2015). Carbon-and oxygen-isotope records of mid-Cretaceous Tethyan pelagic sequences from the Umbria–Marche and Belluno Basins (Italy). *Newsletters on Stratigraphy*, *48*(3), 299–323.

Gustafsson, M., Holbourn, A., & Kuhnt, W. (2003). Changes in Northeast Atlantic temperature and carbon flux during the Cenomanian/Turonian paleoceanographic event: the Goban Spur stable isotope record. *Palaeogeography, Palaeoclimatology, Palaeoecology*, *201*(1–2), 51–66, doi: 10.1016/S0031-0182(03)00509-1.

Georgiev, S., Stein, H. J., Hannah, J. L., Weiss, H. M., Bingen, B., Xu, G., ... & Piasecki,

S. (2012). Chemical signals for oxidative weathering predict Re–Os isochroneity in black shales, East Greenland. *Chemical Geology*, *324*, 108–121, doi: 10.1016/j.chemgeo.2012.01.003.

Georgiev, S. V., Stein, H. J., Hannah, J. L., Henderson, C. M., & Algeo, T. J. (2015). Enhanced recycling of organic matter and Os-isotopic evidence for multiple magmatic or meteoritic inputs to the Late Permian Panthalassic Ocean, Opal Creek, Canada. *Geochimica et Cosmochimica Acta*, *150*, 192–210, doi: 10.1016/j.gca.2014.11.019.

Godet, A., Bodin, S., Föllmi, K.B., Vermeulen, J., Gardin, S., Fiet, N., et al. (2006). Evolution of the marine stable carbon-isotope record during the early Cretaceous: A focus on the late Hauterivian and Barremian in the Tethyan realm. *Earth and Planetary Science Letters, 242*(3–4), 254–271, doi: 10.1016/j.epsl.2005.12.011.

Guex, J., Pilet, S., Müntener, O., Bartolini, A., Spangenberg, J., Schoene, B., ... & Schaltegger, U. (2016). Thermal erosion of cratonic lithosphere as a potential trigger for mass-extinction. *Scientific reports*, *6*(1), 1–9, doi: 10.1038/srep23168.

Gutjahr, M., Ridgwell, A., Sexton, P. F., Anagnostou, E., Pearson, P. N., Pälike, H., ... & Foster, G. L. (2017). Very large release of mostly volcanic carbon during the Palaeocene–Eocene Thermal Maximum. *Nature*, *548*(7669), 573–577, doi: 10.1038/nature23646.

Haq, B.U. (2014). Cretaceous eustasy revisited. *Global and Planetary change, 113*, 44–58. doi: 10.1016/j.gloplacha.2013.12.007.

Haq, B. U., von Rad, U. & O'Connell, S. (1990). *Proceedings of the Ocean Drilling Program, v. 122* (College Station, Texas, Ocean Drilling Program, 1990).

Helsley, C. E., & Steiner, M. B. (1968). Evidence for long intervals of normal polarity during the Cretaceous period. *Earth and Planetary Science Letters*, *5*, 325–332, doi: 10.1016/S0012-821X(68)80060-3.

Heimhofer, U., Hochuli, P. A., Herrle, J. O., & Weissert, H. (2006). Contrasting origins of Early Cretaceous black shales in the Vocontian basin: Evidence from palynological and calcareous nannofossil records. *Palaeogeography, Palaeoclimatology, Palaeoecology*, *235*(1–3), 93–109, doi: 10.1016/j.palaeo.2005.09.025.

Henehan, M. J., Evans, D., Shankle, M., Burke, J. E., Foster, G. L., Anagnostou, E., ... & Hull, P. M. (2017). Size-dependent response of foraminiferal calcification to seawater

carbonate chemistry. *Biogeosciences*, *14*(13), 3287–3308, doi: 10.5194/bg-14-3287-2017.

Herman, A. B., Spicer, R. A., & Spicer, T. E. (2016). Environmental constraints on terrestrial vertebrate behaviour and reproduction in the high Arctic of the Late Cretaceous. Palaeogeography, Palaeoclimatology, Palaeoecology, 441, 317–338, doi: 10.1016/j.palaeo.2015.09.041.

Herrle, J. O., Kößler, P., Friedrich, O., Erlenkeuser, H., & Hemleben, C. (2004). High-resolution carbon isotope records of the Aptian to Lower Albian from SE France and the Mazagan Plateau (DSDP Site 545): a stratigraphic tool for paleoceanographic and paleobiologic reconstruction. *Earth and Planetary Science Letters*, *218*(1–2), 149–161, doi: 10.1016/S0012-821X(03)00646-0.

Herrle, J. O., Schröder-Adams, C. J., Davis, W., Pugh, A. T., Galloway, J. M., & Fath, J. (2015). Mid-Cretaceous High Arctic stratigraphy, climate, and oceanic anoxic events. *Geology*, *43*(5), 403–406, doi: 10.1130/G36439.1.

Hilgen, F.J. (1991). Astronomical calibration of Gauss to Matuyama sapropels in the Mediterranean and implication for the geomagnetic polarity time scale. *Earth and planetary science letters, 104*(2-4), 226–244, doi: 10.1016/0012-821X(91)90206-W.

Hodell, D. A., Mead, G. A., & Mueller, P. A. (1990). Variation in the strontium isotopic composition of seawater (8 Ma to present): Implications for chemical weathering rates and dissolved fluxes to the oceans. *Chemical Geology: Isotope Geoscience section*, *80*(4), 291–307, doi: 10.1016/0168-9622(90)90011-Z.

Hoernle, K., Hauff, F., Van den Bogaard, P., Werner, R., Mortimer, N., Geldmacher, J., ... & Davy, B. (2010). Age and geochemistry of volcanic rocks from the Hikurangi and Manihiki oceanic Plateaus. *Geochimica et Cosmochimica Acta*, *74*(24), 7196–7219, doi: 10.1016/j.gca.2010.09.030.

Hong, S. K., & Lee, Y. I. (2012). Evaluation of atmospheric carbon dioxide concentrations during the Cretaceous. *Earth and Planetary Science Letters*, *327*, 23–28, doi: 10.1016/j.epsl.2012.01.014.

Hu, X., Zhao, K., Yilmaz, I. O., & Li, Y. (2012). Stratigraphic transition and palaeoenvironmental changes from the Aptian oceanic anoxic event 1a (OAE1a) to the oceanic red bed 1 (ORB1) in the Yenicesihlar section, central Turkey. *Cretaceous Research*, *38*, 40–51, doi: 10.1016/j.cretres.2012.01.007.

Huang, C., Hinnov, L., Fischer, A. G., Grippo, A., & Herbert, T. (2010). Astronomical tuning of the Aptian Stage from Italian reference sections. *Geology*, *38*(10), 899–902, doi: 10.1130/G31177.1.

Huber, B. T., & Leckie, R. M. (2011). Planktic foraminiferal species turnover across deep-sea Aptian/Albian boundary sections. *The Journal of Foraminiferal Research*, *41*(1), 53–95, doi: 10.2113/gsjfr.41.1.53.

Huber, B. T., Norris, R. D., & MacLeod, K. G. (2002). Deep-sea paleotemperature record of extreme warmth during the Cretaceous. *Geology*, *30*(2), 123–126, doi: 10.1130/0091-7613(2002)030<0123:DSPROE>2.0.CO;2

Huber, B. T., MacLeod, K. G., Gröcke, D. R., & Kucera, M. (2011). Paleotemperature and paleosalinity inferences and chemostratigraphy across the Aptian/Albian boundary in the subtropical North Atlantic. *Paleoceanography*, *26*(4), doi: 10.1029/2011PA002178.

Huber, B. T., MacLeod, K. G., Watkins, D. K., & Coffin, M. F. (2018). The rise and fall of the Cretaceous Hot Greenhouse climate. *Global and Planetary Change*, *167*, 1–23, doi: 10.1016/j.gloplacha.2018.04.004.

Huh, Y., Birck, J.L., & Allègre, C.J. (2004). Osmium isotope geochemistry in the Mackenzie River basin. *Earth and Planetary Science Letters, 222*(1), 115–129, doi: 10.1016/j.epsl.2004.02.026.

Ihoriya, N., Hori, R.S., and Ikehara, M. (2009). Constraints upon anoxic water mass and variations in carbon isotopes during OAE 1a (Early Cretaceous) from deep-sea sedimentary rocks of the Pacific Ocean. *News of Osaka Micropalaeontologists*, *Special Volume 14*, 297–315.

Ikeda, M., Hori, R. S., Okada, Y., & Nakada, R. (2015). Volcanism and deep-ocean acidification across the end-Triassic extinction event. *Palaeogeography, Palaeoclimatology, Palaeoecology*, *440*, 725–733, doi: 10.1016/j.palaeo.2015.09.046.

Ikeda, M., Tada, R., & Ozaki, K. (2017). Astronomical pacing of the global silica cycle recorded in Mesozoic bedded cherts. *Nature communications, 8*(1), 1–9, doi: 10.1038/ncomms15532.

Ikeda, M., Ozaki, K., & Legrand, J. (2020). Impact of 10-Myr scale monsoon dynamics on Mesozoic climate and ecosystems. *Scientific reports, 10*(1), 1–10, doi:

10.1038/s41598-020-68542-w.

Ingle, S., Mahoney, J. J., Sato, H., Coffin, M. F., Kimura, J. I., Hirano, N., & Nakanishi, M. (2007). Depleted mantle wedge and sediment fingerprint in unusual basalts from the Manihiki Plateau, central Pacific Ocean. *Geology*, *35*(7), 595–598, doi: 10.1130/G23741A.1.

Ishikawa, A., Pearson, D. G., & Dale, C. W. (2011). Ancient Os isotope signatures from the Ontong Java Plateau lithosphere: Tracing lithospheric accretion history. *Earth and Planetary Science Letters*, *301*(1-2), 159–170, doi: 10.1016/j.epsl.2010.10.034.

Jaffe, L. A., Peucker-Ehrenbrink, B., & Petsch, S. T. (2002). Mobility of rhenium, platinum group elements and organic carbon during black shale weathering. *Earth and Planetary Science Letters*, *198*(3–4), 339–353, doi: 10.1016/S0012-821X(02)00526-5.

Jiang, Q., Jourdan, F., Olierook, H. K., Merle, R. E., & Whittaker, J. M. (2021). Longest continuously erupting large igneous province driven by plume-ridge interaction. *Geology*, *49*(2), 206–210, doi: 10.1130/G47850.1.

Joachimski, M. M., Alekseev, A. S., Grigoryan, A., & Gatovsky, Y. A. (2020). Siberian Trap volcanism, global warming and the Permian-Triassic mass extinction: New insights from Armenian Permian-Triassic sections. *GSA Bulletin*, *132*(1–2), 427–443, doi: 10.1130/B35108.1.

Jones, C. E., & Jenkyns, H. C. (2001). Seawater strontium isotopes, oceanic anoxic events, and seafloor hydrothermal activity in the Jurassic and Cretaceous. *American Journal of Science*, *301*(2), 112–149, doi: 10.2475/ajs.301.2.112.

Jones, M. M., Sageman, B. B., Selby, D., Jicha, B. R., Singer, B. S., & Titus, A. L. (2021). Regional chronostratigraphic synthesis of the Cenomanian-Turonian Oceanic Anoxic Event 2 (OAE2) interval, Western Interior Basin (USA): New Re-Os chemostratigraphy and 40Ar/39Ar geochronology. *Bulletin*, *133*(5–6), 1090–1104, doi: 10.1130/B35594.1.

Katchinoff, J. A., Syverson, D. D., Planavsky, N. J., Evans, E. S., & Rooney, A. D. (2021). Seawater chemistry and hydrothermal controls on the Cenozoic osmium cycle. *Geophysical Research Letters*, *48*(20), e2021GL095558, doi: 10.1029/2021GL095558.

Kawahata, H., Nomura, R., Matsumoto, K., & Nishi, H. (2015). Linkage of deep sea rapid

acidification process and extinction of benthic foraminifera in the deep sea at the Paleocene/Eocene transition. *Island Arc*, *24*(3), 301–316, doi: 10.1111/iar.12106.

Kemp, D. B., Selby, D., & Izumi, K. (2020). Direct coupling between carbon release and weathering during the Toarcian oceanic anoxic event. *Geology*, *48*(10), 976–980, doi: 10.1130/G47509.1.

Khanna, N., Godbold, J. A., Austin, W. E., & Paterson, D. M. (2013). The impact of ocean acidification on the functional morphology of foraminifera. *PLoS One*, *8*(12), e83118, doi: 10.1371/journal.pone.0083118.

Klages, J. P., Salzmann, U., Bickert, T., Hillenbrand, C. D., Gohl, K., Kuhn, G., ... & Dziadek, R. (2020). Temperate rainforests near the South Pole during peak Cretaceous warmth. *Nature*, *580*(7801), 81–86, doi: 10.1038/s41586-020-2148-5.

Kößler, P., Herrle, J. O., Appel, E., Erbacher, J., & Hemleben, C. (2001). Magnetic records of climatic cycles from mid-Cretaceous hemipelagic sediments of the Vocontian Basin, SE France. *Cretaceous Research*, *22*(3), 321–331, doi: 10.1006/cres.2001.0256.

Kodama, K., Taira, A., Okamura, M., and Saito, Y. (1983) Paleomagnetism of the Shimanto Belt in Shikoku, Southwest Japan, in Hashimoto, M., and Ueda, S., eds., Accretion Tectonics in the Circum-Pacifi c Regions, Tokyo, Terrapub, 231–241.

Kuroda, J., Ohkouchi, N., Ishii, T., Tokuyama, H., & Taira, A. (2005). Lamina-scale analysis of sedimentary components in Cretaceous black shales by chemical compositional mapping: Implications for paleoenvironmental changes during the Oceanic Anoxic Events. *Geochimica et Cosmochimica Acta*, *69*(6), 1479–1494, doi: 10.1016/j.gca.2004.06.039.

Kuroda, J., Ogawa, N. O., Tanimizu, M., Coffin, M. F., Tokuyama, H., Kitazato, H., & Ohkouchi, N. (2007). Contemporaneous massive subaerial volcanism and late cretaceous Oceanic Anoxic Event 2. *Earth and Planetary Science Letters*, *256*(1–2), 211–223, doi: 10.1016/j.epsl.2007.01.027.

Kuroda, J., Hori, R.S., Suzuki, K., Gröcke, D.R., & Ohkouchi, N. (2010). Marine osmium isotope record across the Triassic-Jurassic boundary from a Pacific pelagic site. *Geology, 38*(12), 1095–1098, doi: 10.1130/G31223.1.

Kuroda, J., Ihoriya, N., Hori, R. S., Ogawa, N. O., Ikehara, M., Tanimizu, M., & Ohkouchi, N. (2015). Geochemistry of Aptian bedded chert succession from the deep Pacific

basin: new insights into Cretaceous Oceanic Anoxic Event-1a, *in* Neal, C.R., Sager, W.W., Sano, T., and Erba, E., eds., The Origin, Evolution, and Environmental Impact of Oceanic Large Igneous Provinces: *The Geoogical Society of America Special Paper*, 511, 305–328, doi:10.1130/2015.2511(16).

Kuroyanagi, A., Kawahata, H., Ozaki, K., Suzuki, A., Nishi, H., & Takashima, R. (2020). What drove the evolutionary trend of planktic foraminifers during the Cretaceous: Oceanic Anoxic Events (OAEs) directly affected it?. Marine Micropaleontology, 161, 101924, doi: 10.1016/j.marmicro.2020.101924.

Kutzbach, J.E., & Gallimore, R.G. (1989). Pangaean climates: megamonsoons of the megacontinent. *Journal of Geophysical Research: Atmospheres, 94*(D3), 3341–3357.

Laakso, T. A., Waldeck, A., Macdonald, F. A., & Johnston, D. (2020). Volcanic controls on seawater sulfate over the past 120 million years. *Proceedings of the National Academy of Sciences*, *117*(35), 21118–21124, doi: 10.1073/pnas.1921308117.

Lanci, L., Muttoni, G., & Erba, E. (2010). Astronomical tuning of the Cenomanian Scaglia Bianca Formation at Furlo, Italy. *Earth and Planetary Science Letters*, *292*(1–2), 231–237, doi: 10.1016/j.epsl.2010.01.041.

Larson, R. L. (1991). Geological consequences of superplumes. *Geology*, *19*(10), 963–966, doi: 10.1130/0091-7613(1991)019<0963:GCOS>2.3.CO;2.

Larson, R. L., & Erba, E. (1999). Onset of the Mid-Cretaceous greenhouse in the Barremian-Aptian: Igneous events and the biological, sedimentary, and geochemical responses. *Paleoceanography*, *14*(6), 663–678, doi: 10.1029/1999PA900040.

Lassiter, J. C. (2003). Rhenium volatility in subaerial lavas: constraints from subaerial and submarine portions of the HSDP-2 Mauna Kea drillcore. *Earth and Planetary Science Letters*, *214*(1–2), 311–325, doi: 10.1016/S0012-821X(03)00385-6.

Lechler, M., von Strandmann, P. A. P., Jenkyns, H. C., Prosser, G., & Parente, M. (2015). Lithium-isotope evidence for enhanced silicate weathering during OAE 1a (Early Aptian Selli event). *Earth and Planetary Science Letters*, *432*, 210–222, doi: 10.1016/j.epsl.2015.09.052.

Leckie, R. M., Bralower, T. J., & Cashman, R. (2002). Oceanic anoxic events and plankton evolution: Biotic response to tectonic forcing during the mid-Cretaceous. *Paleoceanography*, *17*(3), 13–1–13–29, doi: 10.1029/2001PA000623.

Levasseur, S., Birck, J. L., & Allègre, C. J. (1998). Direct measurement of femtomoles of

osmium and the $^{187}Os/^{186}Os$ ratio in seawater. *Science*, *282*(5387), 272–274, doi: 10.1126/science.282.5387.272.

Levasseur, S., Birck, J. L., & Allegre, C. J. (1999). The osmium riverine flux and the oceanic mass balance of osmium. *Earth and Planetary Science Letters*, *174*(1–2), 7–23, doi: 10.1016/S0012-821X(99)00259-9.

Li, J., Hu, X., Zhao, K., Cai, Y., & Sun, T. (2016). Paleoceanographic evolution and chronostratigraphy of the Aptian Oceanic Anoxic Event 1a (OAE1a) to oceanic red bed 1 (ORB1) in the Gorgo a Cerbara section (central Italy). *Cretaceous Research*, *66*, 115–128, doi: 10.1016/j.cretres.2016.04.016.

Liu, Z., Selby, D., Zhang, H., & Shen, S. (2020). Evidence for volcanism and weathering during the Permian-Triassic mass extinction from Meishan (South China) osmium isotope record. *Palaeogeography, Palaeoclimatology, Palaeoecology*, *553*, 109790, doi: 10.1016/j.palaeo.2020.109790.

Liu, Z., & Selby, D. (2021). Deep-water osmium-isotope record of the Permian–Triassic interval from Niushan, China reveals potential delayed volcanic signal post the mass extinction. *Global and Planetary Change*, *200*, 103473, doi: 10.1016/j.gloplacha.2021.103473.

Lowenstein, T. K., Hardie, L. A., Timofeeff, M. N., & Demicco, R. V. (2003). Secular variation in seawater chemistry and the origin of calcium chloride basinal brines. *Geology*, *31*(10), 857–860, doi: 10.1130/G19728R.1.

Lu, X., Kendall, B., Stein, H. J., & Hannah, J. L. (2017). Temporal record of osmium concentrations and 187Os/188Os in organic-rich mudrocks: Implications for the osmium geochemical cycle and the use of osmium as a paleoceanographic tracer. *Geochimica et Cosmochimica Acta*, *216*, 221–241, doi: 10.1016/j.gca.2017.06.046.

Luciani, V., Cobianchi, M., & Jenkyns, H. C. (2001). Biotic and geochemical response to anoxic events: the Aptian pelagic succession of the Gargano Promontory (southern Italy). *Geological Magazine*, *138*(3), 277–298, doi: 10.1017/S0016756801005301.

Luguet, A., Shirey, S. B., Lorand, J. P., Horan, M. F., & Carlson, R. W. (2007). Residual platinum-group minerals from highly depleted harzburgites of the Lherz massif (France) and their role in HSE fractionation of the mantle. *Geochimica et Cosmochimica Acta*, *71*(12), 3082–3097, doi: 10.1016/j.gca.2007.04.011.

Lund, D.C., & Asimow, P.D. (2011). Does sea level influence mid-ocean ridge magmatism on Milankovitch timescales?. *Geochemistry, Geophysics, Geosystems, 12*(12), doi: 10.1029/2011GC003693.

Ma, W., Tian, J., Li, Q., & Wang, P. (2011). Simulation of long eccentricity (400-kyr) cycle in ocean carbon reservoir during Miocene Climate Optimum: Weathering and nutrient response to orbital change. *Geophysical Research Letters*, *38*(10), doi: 10.1029/2011GL047680.

Mahoney, J. J., Storey, M., Duncan, R. A., Spencer, K. J., & Pringle, M. (1993). Geochemistry and age of the Ontong Java Plateau. *In* Pringle, M.S., Sager, W. W., Sliter, W., and Stein, S., eds., The Mesozoic Pacific: Geology, Tectonics, and Volcanism, 77. Geophysical Monograph, AGU, Washington, DC, p. 233–261.

Malinverno, A., Hildebrandt, J., Tominaga, M., & Channell, J. E. (2012). M-sequence geomagnetic polarity time scale (MHTC12) that steadies global spreading rates and incorporates astrochronology constraints. *Journal of Geophysical Research: Solid Earth*, *117*(B6), doi: 10.1029/2012JB009260.

Martinez, M., Deconinck, J.F., Pellenard, P., Reboulet, S., & Riquier, L. (2013). Astrochronology of the Valanginian Stage from reference sections (Vocontian Basin, France) and palaeoenvironmental implications for the Weissert Event. *Palaeogeography, Palaeoclimatology, Palaeoecology, 376*, 91–102, doi: 10.1016/j.palaeo.2013.02.021.

Martinez, M., Deconinck, J.F., Pellenard, P., Riquier, L., Company, M., Reboulet, S., & Moiroud, M. (2015). Astrochronology of the Valanginian–Hauterivian stages (Early Cretaceous): Chronological relationships between the Paraná–Etendeka large igneous province and the Weissert and the Faraoni events. *Global and Planetary Change, 131*, 158–173, doi: 10.1016/j.gloplacha.2015.06.001.

Martinez, M., Aguado, R., Company, M., Sandoval, J., & O'Dogherty, L. (2020). Integrated astrochronology of the Barremian Stage (Early Cretaceous) and its biostratigraphic subdivisions. *Global and Planetary Change*, *195*, 103368, doi: 10.1016/j.gloplacha.2020.103368.

Martínez-Rodríguez, R., Selby, D., Castro, J. M., de Gea, G. A., Nieto, L. M., & Ruiz-Ortiz, P. A. (2021). Tracking magmatism and oceanic change through the early Aptian Anoxic Event (OAE 1a) to the late Aptian: Insights from osmium isotopes from the westernmost Tethys (SE Spain) Cau Core. *Global and Planetary Change*, 103652,

doi: 10.1016/j.gloplacha.2021.103652.

Matsumoto, H., Kuroda, J., Coccioni, R., Frontalini, F., Sakai, S., Ogawa, N. O., & Ohkouchi, N. (2020). Marine Os isotopic evidence for multiple volcanic episodes during Cretaceous Oceanic Anoxic Event 1b. *Scientific reports*, *10*(1), 1–10, doi: 10.1038/s41598-020-69505-x.

Matsumoto, H., Coccioni, R., Frontalini, F., Shirai, K., Jovane, L., Trindade, R., ... & Kuroda, J. (2021a). Long-term Aptian marine osmium isotopic record of Ontong Java Nui activity. *Geology*, 49(9) 1148–1152, doi: 10.1130/G48863.1.

Matsumoto, H., Coccioni, R., Frontalini, F., Shirai, K., & Kuroda, J. (2021b) Osmium isotopic evidence for eccentricity-paced increases in continental weathering during the latest Hauterivian, Early Cretaceous. *Geochemistry, Geophysics, Geosystems*, e2021GC009789, doi: 10.1029/2021GC009789.

Matsumoto, H., Coccioni, R., Frontalini, F., Shirai, K., Jovane, L., Trindade, R., ... & Kuroda, J. (2022). Mid-Cretaceous marine Os isotope evidence for heterogeneous cause of oceanic anoxic events. *Nature communications*, *13*(1), 1–9.

McAnena, A., Flögel, S., Hofmann, P., Herrle, J. O., Griesand, A., Pross, J., ... & Wagner, T. (2013). Atlantic cooling associated with a marine biotic crisis during the mid-Cretaceous period. *Nature Geoscience*, *6*(7), 558–561, doi: 10.1038/ngeo1850.

McClelland, H. L. O., Barbarin, N., Beaufort, L., Hermoso, M., Ferretti, P., Greaves, M., & Rickaby, R. E. M. (2016). Calcification response of a key phytoplankton family to millennial-scale environmental change. *Scientific reports*, *6*(1), 1–11, doi: 10.1038/srep34263 (2016).

McArthur, J. M., Howarth, R. J., Shields, G. A., & Zhou, Y. (2020). Strontium isotope stratigraphy. In *Geologic Time Scale 2020* (pp. 211-238). Elsevier.

Menegatti, A. P., Weissert, H., Brown, R. S., Tyson, R. V., Farrimond, P., Strasser, A., & Caron, M. (1998). High-resolution δ13C stratigraphy through the early Aptian "Livello Selli" of the Alpine Tethys. *Paleoceanography*, *13*(5), 530–545, doi: 10.1029/98PA01793.

Menichetti, M., & Coccioni. R., (2013) Umbria -Marche Apennines geological field trip. 2013, Livret-Guide des Excursions du Groupe Français du Crétacé. hal-01236473.

Mitchell, R. N., Bice, D. M., Montanari, A., Cleaveland, L. C., Christianson, K. T., Coccioni, R., & Hinnov, L. A. (2008). Oceanic anoxic cycles? Orbital prelude to the

Bonarelli Level (OAE 2). *Earth and Planetary Science Letters*, *267*(1–2), 1–16, doi: 10.1016/j.epsl.2007.11.026.

Mills, B. J., Scotese, C. R., Walding, N. G., Shields, G. A., & Lenton, T. M. (2017). Elevated CO_2 degassing rates prevented the return of Snowball Earth during the Phanerozoic. *Nature communications*, *8*(1), 1–7, doi: 10.1038/s41467-017-01456-w.

Moiroud, M., Martinez, M., Deconinck, J.F., Monna, F., Pellenard, P., Riquier, L., & Company, M. (2012). High-resolution clay mineralogy as a proxy for orbital tuning: Example of the Hauterivian–Barremian transition in the Betic Cordillera (SE Spain). *Sedimentary geology, 282*, 336–346, doi: 10.1016/j.sedgeo.2012.10.004.

Moriya, K., Wilson, P. A., Friedrich, O., Erbacher, J., & Kawahata, H. (2007). Testing for ice sheets during the mid-Cretaceous greenhouse using glassy foraminiferal calcite from the mid-Cenomanian tropics on Demerara Rise. *Geology*, *35*(7), 615–618, doi: 10.1130/G23589A.1.

Müller, R. D., Sdrolias, M., Gaina, C., Steinberger, B., & Heine, C. (2008). Long-term sea-level fluctuations driven by ocean basin dynamics. *science*, *319*(5868), 1357–1362, doi: 10.1126/science.1151540.

Müller, R. D., Seton, M., Zahirovic, S., Williams, S. E., Matthews, K. J., Wright, N. M., ... & Cannon, J. (2016). Ocean basin evolution and global-scale plate reorganization events since Pangea breakup. *Annual Review of Earth and Planetary Sciences*, *44*, 107–138.

Naafs, B. D. A., Castro, J. M., De Gea, G. A., Quijano, M. L., Schmidt, D. N., & Pancost, R. D. (2016). Gradual and sustained carbon dioxide release during Aptian Oceanic Anoxic Event 1a. *Nature Geoscience*, *9*(2), 135–139, doi: 10.1038/ngeo2627.

Naber, T. V., Grasby, S. E., Cuthbertson, J. P., Rayner, N., & Tegner, C. (2021). New constraints on the age, geochemistry, and environmental impact of High Arctic Large Igneous Province magmatism: Tracing the extension of the Alpha Ridge onto Ellesmere Island, Canada. *Bulletin*, *133*(7–8), 1695–1711, doi: 10.1130/B35792.1.

Nakada, R., Ogawa, K., Suzuki, N., Takahashi, S., & Takahashi, Y. (2014). Late Triassic compositional changes of aeolian dusts in the pelagic Panthalassa: response to the continental climatic change. *Palaeogeography, Palaeoclimatology, Palaeoecology*, *393*, 61–75, doi: 10.1016/j.palaeo.2013.10.014.

Nozaki, T., Suzuki, K., Ravizza, G., Kimura, J. I., & Chang, Q. (2012). A method for

rapid determination of Re and Os isotope compositions using ID-MC-ICP-MS combined with the sparging method. *Geostandards and Geoanalytical Research*, *36*(2), 131–148, doi: 10.1111/j.1751-908X.2011.00125.x.

Nozaki, T., Kato, Y., & Suzuki, K., (2014). Geochemistry using Re–Os isotope system: from the age-determination to paleoenvironmental interpretations. *Geochemistry*, *48*(4), 279–305, doi: 10.14934/chikyukagaku.48.279. translated from Japanese.

Nozaki, T., Nikaido, T., Onoue, T., Takaya, Y., Sato, K., Kimura, J. I., ... & Matsuoka, A. (2019). Triassic marine Os isotope record from a pelagic chert succession, Sakahogi section, Mino Belt, southwest Japan. *Journal of Asian Earth Sciences: X*, *1*, 100004, doi: 10.1016/j.jaesx.2018.100004.

O'Brien, C. L., Robinson, S. A., Pancost, R. D., Damsté, J. S. S., Schouten, S., Lunt, D. J., ... & Wrobel, N. E. (2017). Cretaceous sea-surface temperature evolution: Constraints from TEX_{86} and planktonic foraminiferal oxygen isotopes. *Earth-Science Reviews*, *172*, 224–247, doi: 10.1016/j.earscirev.2017.07.012.

O'Dogherty, L. (1994). *Biochronology and paleontology of mid-Cretaceous radiolarians from northern Apennines (Italy) and Betic Cordillera (Spain)* (Vol. 21, pp. 1–415). Section des sciences de la terre, Université de Lausanne.

Ogg, J. G., Hinnov, L. A., & Huang, C. (2012). Cretaceous. In *The geologic time scale* (pp. 793–853). Elsevier.

Ohkouchi, N., Nakajima, Y., Okada, H., Ogawa, N. O., Suga, H., Oguri, K., & Kitazato, H. (2005). Biogeochemical processes in the saline meromictic Lake Kaiike, Japan: implications from molecular isotopic evidences of photosynthetic pigments. *Environmental Microbiology*, *7*(7), 1009–1016, doi: 10.1111/j.1462-2920.2005.00772.x.

Okamura, M., Umemura, H., and Yasuda, H. (1991) Major facies and deforma- tion of the Shimanto Belt in the middle to western Shikoku Island, in Geo- logical Field Trip Guidebook: Geological Society of Japan 98th Meeting, p. 85–119 (in Japanese with English abstract)

Olierook, H. K., Jourdan, F., & Merle, R. E. (2019). Age of the Barremian–Aptian boundary and onset of the Cretaceous Normal Superchron. *Earth-Science Reviews*, *197*, 102906, doi: 10.1016/j.earscirev.2019.102906.

Owens, J. D., Gill, B. C., Jenkyns, H. C., Bates, S. M., Severmann, S., Kuypers, M. M., ... & Lyons, T. W. (2013). Sulfur isotopes track the global extent and dynamics of euxinia during Cretaceous Oceanic Anoxic Event 2. *Proceedings of the National Academy of Sciences*, *110*(46), 18407–18412, doi: 10.1073/pnas.1305304110.

Oxburgh, R. (2001). Residence time of osmium in the oceans. *Geochemistry, Geophysics, Geosystems*, *2*(6), doi: 10.1029/2000GC000104.

Oxburgh, R. (1998). Variations in the osmium isotope composition of sea water over the past 200,000 years. *Earth and Planetary Science Letters*, *159*(3-4), 183–191, doi: 10.1016/S0012-821X(98)00057-0.

Oxburgh, R., Pierson-Wickmann, A.C., Reisberg, L., & Hemming, S. (2007). Climate-correlated variations in seawater $^{187}Os/^{188}Os$ over the past 200,000 yr: Evidence from the Cariaco Basin, Venezuela. *Earth and Planetary Science Letters, 263*(3–4), 246–258, doi: 10.1016/j.epsl.2007.08.033.

Ozaki, K., Tajima, S., & Tajika, E. (2011). Conditions required for oceanic anoxia/euxinia: Constraints from a one-dimensional ocean biogeochemical cycle model. *Earth and Planetary Science Letters*, *304*(1–2), 270–279, doi: 10.1016/j.epsl.2011.02.011.

Ozaki, K., & Tajika, E. (2013). Biogeochemical effects of atmospheric oxygen concentration, phosphorus weathering, and sea-level stand on oceanic redox chemistry: Implications for greenhouse climates. *Earth and Planetary Science Letters*, *373*, 129–139, doi: 10.1016/j.epsl.2013.04.029.

Palmer, M. R., & Edmond, J. M. (1989). The strontium isotope budget of the modern ocean. *Earth and Planetary Science Letters*, *92*(1), 11–26, doi: 10.1016/0012-821X(89)90017-4.

Paquay, F. S., Ravizza, G., & Coccioni, R. (2014). The influence of extraterrestrial material on the late Eocene marine Os isotope record. *Geochimica et Cosmochimica Acta*, *144*, 238–257, doi: 10.1016/j.gca.2014.08.024.

Parsiegla, N., Gohl, K., & Uenzelmann-Neben, G. (2008). The Agulhas Plateau: Structure and evolution of a large igneous province. *Geophysical Journal International*, *174*(1), 336–350, doi: 10.1111/j.1365-246X.2008.03808.x.

Paytan, A., Yao, W., Faul, K. L. & Gray, E. T. Sulfur isotope stratigraphy. In *Geologic Time Scale 2020* , (eds Gradstein, F. M., Ogg, J. G., Schmitz, M. D., Ogg, G. M.)

259–278 (Elsevier, 2020).

Pearson, D. G., & Woodland, S. J. (2000). Solvent extraction/anion exchange separation and determination of PGEs (Os, Ir, Pt, Pd, Ru) and Re–Os isotopes in geological samples by isotope dilution ICP-MS. *Chemical Geology*, *165*(1–2), 87–107, doi: 10.1016/S0009-2541(99)00161-8.

Pearson, P. N., Ditchfield, P. W., Singano, J., Harcourt-Brown, K. G., Nicholas, C. J., Olsson, R. K., ... & Hall, M. A. (2001). Warm tropical sea surface temperatures in the Late Cretaceous and Eocene epochs. *Nature*, *413*(6855), 481–487, doi: 10.1038/35097000.

Percival, L.M., Cohen, A.S., Davies, M.K., Dickson, A.J., Hesselbo, S.P., Jenkyns, H.C. et al. (2016). Osmium isotope evidence for two pulses of increased continental weathering linked to Early Jurassic volcanism and climate change. *Geology, 44*(9), 759–762, doi: 10.1130/G37997.1.

Percival, L. M. E., Tedeschi, L. R., Creaser, R. A., Bottini, C., Erba, E., Giraud, F., ... & Jenkyns, H. C. (2021). Determining the style and provenance of magmatic activity during the Early Aptian Oceanic Anoxic Event (OAE 1a). *Global and Planetary Change*, *200*, 103461, doi: 10.1016/j.gloplacha.2021.103461.

Petrizzo, M. R., Huber, B. T., Wilson, P. A., & MacLeod, K. G. (2008). Late Albian paleoceanography of the western subtropical North Atlantic. *Paleoceanography*, *23*(1), doi: 10.1029/2007PA001517.

Petrizzo, M. R., Huber, B. T., Gale, A. S., Barchetta, A., & Jenkyns, H. C. (2012). Abrupt planktic foraminiferal turnover across the Niveau Kilian at Col de Pré-Guittard (Vocontian Basin, southeast France): new criteria for defining the Aptian/Albian boundary. *Newsletters on Stratigraphy*, *45*(1), 55.

Pettit, L. R., Smart, C. W., Hart, M. B., Milazzo, M., & Hall-Spencer, J. M. (2015). Seaweed fails to prevent ocean acidification impact on foraminifera along a shallow-water CO_2 gradient. *Ecology and Evolution*, *5*(9), 1784–1793, doi: 10.1002/ece3.1475.

Peucker-Ehrenbrink, B., & Blum, J. D. (1998). Re-Os isotope systematics and weathering of Precambrian crustal rocks: Implications for the marine osmium isotope record. *Geochimica et Cosmochimica Acta*, *62*(19–20), 3193–3203, doi: 10.1016/S0016-7037(98)00227-0.

Peucker-Ehrenbrink, B., & Hannigan, R. E. (2000). Effects of black shale weathering on the mobility of rhenium and platinum group elements. *Geology*, *28*(5), 475–478, doi: 10.1130/0091-7613(2000)28<475:EOBSWO>2.0.CO;2.

Peucker-Ehrenbrink, B., & Ravizza, G. (2000). The marine osmium isotope record. *Terra Nova*, *12*(5), 205–219, doi: 10.1046/j.1365-3121.2000.00295.x.

Peucker-Ehrenbrink, B., & Jahn, B. M. (2001). Rhenium-osmium isotope systematics and platinum group element concentrations: Loess and the upper continental crust. *Geochemistry, Geophysics, Geosystems*, *2*(10), doi: 10.1029/2001GC000172.

Peucker-Ehrenbrink, B., & Ravizza, G. E. (2012). Osmium isotope stratigraphy. In *Geologic Time Scale 2012* (pp. 145–166). Elsevier.

Peucker-Ehrenbrink, B., & Fiske, G. J. (2019). A continental perspective of the seawater 87Sr/86Sr record: a review. *Chemical Geology*, *510*, 140–165, doi: 10.1016/j.chemgeo.2019.01.017.

Peucker-Ehrenbrink, B., Ravizza, G., & Hofmann, A. W. (1995). The marine $^{187}Os/^{186}Os$ record of the past 80 million years. *Earth and Planetary Science Letters*, *130*(1–4), 155–167, doi: 10.1016/0012-821X(95)00003-U.

Peucker-Ehrenbrink, B., Bach, W., Hart, S. R., Blusztajn, J. S., & Abbruzzese, T. (2003). Rhenium-osmium isotope systematics and platinum group element concentrations in oceanic crust from DSDP/ODP Sites 504 and 417/418. *Geochemistry, Geophysics, Geosystems*, *4*(7), doi: 10.1029/2002GC000414.

Peucker-Ehrenbrink, B., Hanghoj, K., Atwood, T., & Kelemen, P. B. (2012). Rhenium-osmium isotope systematics and platinum group element concentrations in oceanic crust. *Geology*, *40*(3), 199–202, doi: 10.1130/G32431.1.

Pogge von Strandmann, P. A., Jenkyns, H. C., & Woodfine, R. G. (2013). Lithium isotope evidence for enhanced weathering during Oceanic Anoxic Event 2. *Nature Geoscience*, *6*(8), 668–672, doi: 10.1038/ngeo1875.

Price, G. D. (2003). New constraints upon isotope variation during the early Cretaceous (Barremian–Cenomanian) from the Pacific Ocean. *Geological Magazine*, *140*(5), 513–522, doi: 10.1017/S0016756803008100**.**

Quijano, M. L., Castro, J. M., Pancost, R. D., de Gea, G. A., Najarro, M., Aguado, R., ... & Martín-Chivelet, J. (2012). Organic geochemistry, stable isotopes, and facies analysis of the Early Aptian OAE—New records from Spain (Western

Tethys). *Palaeogeography, Palaeoclimatology, Palaeoecology*, *365*, 276–293, doi: 10.1016/j.palaeo.2012.09.033.

Ravizza, G., Turekian, K. K., & Hay, B. J. (1991). The geochemistry of rhenium and osmium in recent sediments from the Black Sea. *Geochimica et Cosmochimica Acta*, *55*(12), 3741–3752, doi: 10.1016/0016-7037(91)90072-D.

Ravizza, G., & McMurtry, G. M. (1993). Osmium isotopic variations in metalliferous sediments from the East Pacific Rise and the Bauer Basin. *Geochimica et cosmochimica acta*, *57*(17), 4301–4310, doi: 10.1016/0016-7037(93)90324-P.

Ravizza, G., & VonderHaar, D. (2012). A geochemical clock in earliest Paleogene pelagic carbonates based on the impact-induced Os isotope excursion at the Cretaceous-Paleogene boundary. *Paleoceanography*, *27*(3), doi: 10.1029/2012PA002301.

Reisberg, L., Zindler, A., Marcantonio, F., White, W., Wyman, D., & Weaver, B. (1993). Os isotope systematics in ocean island basalts. *Earth and Planetary Science Letters*, *120*(3–4), 149–167, doi: 10.1016/0012-821X(93)90236-3.

Reisberg, L., Rouxel, O., Ludden, J., Staudigel, H., & Zimmermann, C. (2008). Re–Os results from ODP Site 801: Evidence for extensive Re uptake during alteration of oceanic crust. *Chemical Geology*, *248*(3–4), 256–271, doi: 10.1016/j.chemgeo.2007.07.013.

Ries, J. B. (2010). Geological and experimental evidence for secular variation in seawater Mg/Ca (calcite-aragonite seas) and its effects on marine biological calcification. *Biogeosciences*, *7*(9), 2795–2849, doi: 10.5194/bg-7-2795-2010.

Robinson, N., Ravizza, G., Coccioni, R., Peucker-Ehrenbrink, B., & Norris, R. (2009). A high-resolution marine $^{187}Os/^{188}Os$ record for the late Maastrichtian: Distinguishing the chemical fingerprints of Deccan volcanism and the KP impact event. *Earth and Planetary Science Letters*, *281*(3–4), 159–168, doi: 10.1016/j.epsl.2009.02.019.

Robinson, S. A., Clarke, L. J., Nederbragt, A., & Wood, I. G. (2008). Mid-Cretaceous oceanic anoxic events in the Pacific Ocean revealed by carbon-isotope stratigraphy of the Calera Limestone, California, USA. *Geological Society of America Bulletin*, *120*(11–12), 1416–1426, doi: 10.1130/B26350.1.

Robinson, S. A., Dickson, A. J., Pain, A., Jenkyns, H. C., O'Brien, C. L., Farnsworth, A., & Lunt, D. J. (2019). Southern Hemisphere sea-surface temperatures during the Cenomanian–Turonian: implications for the termination of Oceanic Anoxic Event

2. *Geology*, *47*(2), 131–134, doi: 10.1130/G45842.1.

Rodríguez-López, J. P., Liesa, C. L., Pardo, G., Meléndez, N., Soria, A. R., & Skilling, I. (2016). Glacial dropstones in the western Tethys during the late Aptian–early Albian cold snap: Palaeoclimate and palaeogeographic implications for the mid-Cretaceous. *Palaeogeography, Palaeoclimatology, Palaeoecology*, *452*, 11–27. doi: 10.1016/j.palaeo.2016.04.004.

Rodríguez-Tovar, F. J., & Uchman, A. (2017). The Faraoni event (latest Hauterivian) in ichnological record: The Río Argos section of southern Spain. *Cretaceous Research*, *79*, 109–121, doi: 10.1016/j.cretres.2017.07.018.

Rowley, D. B. (2002). Rate of plate creation and destruction: 180 Ma to present. *Geological Society of America Bulletin*, *114*(8), 927–933, doi: 10.1130/0016-7606(2002)114<0927:ROPCAD>2.0.CO;2.

Sabatino, N., Ferraro, S., Coccioni, R., Bonsignore, M., Del Core, M., Tancredi, V., & Sprovieri, M. (2018). Mercury anomalies in upper Aptian-lower Albian sediments from the Tethys realm. *Palaeogeography, Palaeoclimatology, Palaeoecology*, *495*, 163–170, doi: 10.1016/j.palaeo.2018.01.008.

Sato, H., Shirai, N., Ebihara, M., Onoue, T., & Kiyokawa, S. (2016). Sedimentary PGE signatures in the Late Triassic ejecta deposits from Japan: Implications for the identification of impactor. *Palaeogeography, Palaeoclimatology, Palaeoecology*, *442*, 36–47, doi: 10.1016/j.palaeo.2015.11.015.

Sager W.W., Winterer E.L., Firth J.V., et al. (1993). Proceedings of the Ocean Drilling Program, Initial Reports 143. 724 pp. College Station, TX (Ocean Drilling Program). doi: 10.2973/ odp.proc.ir.143.1993.

Sangode, S., Dongre, A., Bhagat, A., & Meshram, D. (2021). Discovery of Deccan Inclination Anomaly and its possible geodynamic implications over the Indian Plate.

Savian, J., Trindade, R., Janikian, L., Jovane, L., de Almeida, R. P., Coccioni, R., Frontalini, F., Sideri, M., and Jenkyns, H. C. (2016). The Barremian-Aptian boundary in the Poggio le Guaine core (central Italy): Evidence for magnetic polarity Chron M0r and oceanic anoxic event 1a. *in* Menichetti, M., Coccioni, R., and Montanari, A., eds., The Stratigraphic Record of Gubbio: Integrated Stratigraphy of the Late Cretaceous–Paleogene Umbria-Marche Pelagic Basin: The Geological Society of America Special Paper, 524, p. 57–78, doi: 10.1130/2016.2524(05).

Schlanger, S. O., & Jenkyns, H. C. (1976). Cretaceous oceanic anoxic events: causes and consequences. *Netherlands Journal of Geosciences/Geologie en Mijnbouw*, (Classic Papers).

Schlanger, S.O., Jackson, E.D., Robert E.B., Cook, H.E., Jenkyns, H.C., Johnson, D.A., ... & Winterer, E.L. (1976). Initial reports of the Deep Sea Drilling Project, Volume 33: Washington, D.C., U.S. Government Printing Office, 973 p.

Scopelliti, G., Bellanca, A., Neri, R., Baudin, F., & Coccioni, R. (2006). Comparative high-resolution chemostratigraphy of the Bonarelli Level from the reference Bottaccione section (Umbria–Marche Apennines) and from an equivalent section in NW Sicily: Consistent and contrasting responses to the OAE2. *Chemical Geology*, *228*(4), 266–285, doi: 10.1016/j.chemgeo.2005.10.010.

Scotese, C. R., & Golonka, J. (1997). *Paleogeographic atlas* (pp. 1–5). Arlington: PALEOMAP Project, University of Texas at Arlington.

Seiter, K., Hensen, C., Schröter, J., & Zabel, M. (2004). Organic carbon content in surface sediments—defining regional provinces. *Deep Sea Research Part I: Oceanographic Research Papers*, *51*(12), 2001–2026.

Sekine, Y., Suzuki, K., Senda, R., Goto, K. T., Tajika, E., Tada, R., ... & Maruoka, T. (2011). Osmium evidence for synchronicity between a rise in atmospheric oxygen and Palaeoproterozoic deglaciation. *Nature communications*, *2*(1), 1–6, doi: 10.1038/ncomms1507.

Selby, D., & Creaser, R. A. (2003). Re–Os geochronology of organic rich sediments: an evaluation of organic matter analysis methods. *Chemical Geology*, *200*(3-4), 225–240, doi: 10.1016/S0009-2541(03)00199-2.

Seton, M., Gaina, C., Müller, R. D., & Heine, C. (2009). Mid-Cretaceous seafloor spreading pulse: Fact or fiction?. *Geology*, *37*(8), 687–690, doi: 10.1130/G25624A.1.

Sharma, M., Papanastassiou, D. A., & Wasserburg, G. J. (1997). The concentration and isotopic composition of osmium in the oceans. *Geochimica et Cosmochimica Acta*, *61*(16), 3287–3299, doi: 10.1016/S0016-7037(97)00210-X.

Sharma, M., Wasserburg, G. J., Hofmann, A. W., & Butterfield, D. A. (2000). Osmium isotopes in hydrothermalS fluids from the Juan de Fuca Ridge. *Earth and Planetary Science Letters*, *179*(1), 139–152, doi: 10.1016/S0012-821X(00)00099-6.

Sharma, M., Rosenberg, E. J., & Butterfield, D. A. (2007). Search for the proverbial mantle osmium sources to the oceans: Hydrothermal alteration of mid-ocean ridge basalt. *Geochimica et Cosmochimica Acta*, *71*(19), 4655–4667, doi: 10.1016/j.gca.2007.06.062.

Shipboard Scientific Party, (2001). Leg 192 summary. *in* Mahoney, J.J., Fitton, J.G., Wallace, P.J., et al., Proceedings of the Ocean Drilling Program, Initial Reports, v. 192, p. 1–75.

Shirai, K., Koyama, F., Murakami-Sugihara, N., Nanjo, K., Higuchi, T., Kohno, H., ... & Sano, M. (2018). Reconstruction of the salinity history associated with movements of mangrove fishes using otolith oxygen isotopic analysis. *Marine Ecology Progress Series*, *593*, 127–139, doi: 10.3354/meps12514.

Shirey, S.B., & Walker, R.J. (1995). Carius tube digestion for low-blank rhenium-osmium analysis. *Analytical Chemistry, 67*(13), 2136–2141.

Shukolyukov, A., & Lugmair, G. (1998). Isotopic evidence for the Cretaceous-Tertiary impactor and its type. *Science*, *282*(5390), 927–930, doi: 10.1126/science.282.5390.927.

Sierro, F.J., Ledesma, S., Flores, J.A., Torrescusa, S., & del Olmo, W.M. (2000). Sonic and gamma-ray astrochronology: Cycle to cycle calibration of Atlantic climatic records to Mediterranean sapropels and astronomical oscillations. *Geology, 28*(8), 695–698, doi: 10.1130/0091-7613(2000)28<695:SAGACT>2.0.CO;2.

Sinton, C. W., Duncan, R., Storey, M., Lewis, J., & Estrada, J. J. (1998). An oceanic flood basalt province within the Caribbean plate. Earth and Planetary Science Letters, 155(3–4), 221–235, doi: 10.1016/S0012-821X(97)00214-8.

Sliter, W. V. (1999). Cretaceous planktic foraminiferal biostratigraphy of the Calera Limestone, northern California, USA. *The Journal of Foraminiferal Research*, *29*(4), 318–339.

Smoliar, M. I., Walker, R. J., & Morgan, J. W. (1996). Re-Os ages of group IIA, IIIA, IVA, and IVB iron meteorites. *Science*, *271*(5252), 1099–1102, doi: 10.1126/science.271.5252.1099.

Spicer, R. A., & Herman, A. B. (2010). The Late Cretaceous environment of the Arctic: a quantitative reassessment based on plant fossils. *Palaeogeography, Palaeoclimatology, Palaeoecology*, *295*(3–4), 423–442, doi:

10.1016/j.palaeo.2010.02.025.

Sprovieri, M., Coccioni, R., Lirer, F., Pelosi, N., & Lozar, F. (2006). Orbital tuning of a lower Cretaceous composite record (Maiolica Formation, central Italy). *Paleoceanography*, *21*(4), doi: 10.1029/2005PA001224.

Steinig, S., Dummann, W., Park, W., Latif, M., Kusch, S., Hofmann, P., & Flögel, S. (2020). Evidence for a regional warm bias in the Early Cretaceous TEX_{86} record. *Earth and Planetary Science Letters*, *539*, 116184, doi: 10.1016/j.epsl.2020.116184.

Sullivan, D. L., Brandon, A. D., Eldrett, J., Bergman, S. C., Wright, S., & Minisini, D. (2020). High resolution osmium data record three distinct pulses of magmatic activity during cretaceous Oceanic Anoxic Event 2 (OAE-2). *Geochimica et Cosmochimica Acta*, *285*, 257–273, doi: 10.1016/j.gca.2020.04.002.

Sun, H., Xiao, Y., Gao, Y., Zhang, G., Casey, J. F., & Shen, Y. (2018). Rapid enhancement of chemical weathering recorded by extremely light seawater lithium isotopes at the Permian–Triassic boundary. *Proceedings of the National Academy of Sciences*, *115*(15), 3782–3787, doi: 10.1073/pnas.1711862115.

Sun, Y., Joachimski, M. M., Wignall, P. B., Yan, C., Chen, Y., Jiang, H., ... & Lai, X. (2012). Lethally hot temperatures during the Early Triassic greenhouse. *Science*, *338*(6105), 366–370, doi: 10.1126/science.1224126.

Syverson, D. D., Katchinoff, J. A., Yohe, L. R., Tutolo, B. M., Seyfried Jr, W. E., & Rooney, A. D. (2021). Experimental partitioning of osmium between pyrite and fluid: Constraints on the mid-ocean ridge hydrothermal flux of osmium to seawater. *Geochimica et Cosmochimica Acta*, *293*, 240–255, doi: 10.1016/j.gca.2020.10.029.

Tajika, E. (1999). Carbon cycle and climate change during the Cretaceous inferred from a biogeochemical carbon cycle model. *Island Arc*, *8*(2), 293–303, doi: 10.1046/j.1440-1738.1999.00238.x.

Takagi, T. (2004). Origin of magnetite-and ilmenite-series granitic rocks in the Japan arc. *American Journal of Science*, *304*(2), 169–202, doi: 10.2475/ajs.304.2.169.

Takashima, R., Sano, S. I., Iba, Y., & Nishi, H. (2007). The first Pacific record of the Late Aptian warming event. *Journal of the Geological Society*, *164*(2), 333–339, doi: 10.1144/0016-76492006-006.

Taylor, B. (2006). The single largest oceanic plateau: Ontong Java–Manihiki–Hikurangi. *Earth and Planetary Science Letters*, *241*(3–4), 372–380, doi: 10.1016/j.epsl.2005.11.049.

Tejada, M. L. G., Mahoney, J. J., Duncan, R. A., & Hawkins, M. P. (1996). Age and geochemistry of basement and alkalic rocks of Malaita and Santa Isabel, Solomon Islands, southern margin of Ontong Java Plateau. *Journal of Petrology*, *37*(2), 361–394, doi: 10.1093/petrology/37.2.361.

Tejada, M. L. G., Mahoney, J. J., Neal, C. R., Duncan, R. A., & Petterson, M. G. (2002). Basement geochemistry and geochronology of Central Malaita, Solomon Islands, with implications for the origin and evolution of the Ontong Java Plateau. *Journal of Petrology*, *43*(3), 449–484, doi: 10.1093/ petrology/43.3.449.

Tejada, M. L. G., Suzuki, K., Kuroda, J., Coccioni, R., Mahoney, J. J., Ohkouchi, N., ... & Tatsumi, Y. (2009). Ontong Java Plateau eruption as a trigger for the early Aptian oceanic anoxic event. *Geology*, *37*(9), 855–858, doi: 10.1130/G25763A.1.

Thiede, J., Vallier, T.L., Adelseck, C., Boersma, A., Dean, W.E., Fujii, N., …, & Windom, K.E. (1981). Western Mid-Pacific Mountains. *In* Thiede, J., et al., *Initial Reports of Deep Sea Drilling Project, vol. 62*: Washington (U.S. Government. Printing Office), 33–156, doi: 10.2973/dsdp.proc.62.102.1981.

Thordarson, T. (2004). Accretionary-lapilli-bearing pyroclastic rocks at ODP Leg 192 Site 1184: a record of subaerial phreatomagmatic eruptions on the Ontong Java Plateau. *Geological Society, London, Special Publications*, *229*(1), 275–306, doi: 10.1144/GSL.SP.2004.229.01.16.

Tierney, J. E. (2014). Biomarker-based inferences of past climate: the TEX_{86} paleotemperature proxy, p 379–393. *Treatise on geochemistry, 2nd ed. Elsevier, Oxford, United Kingdom*.

Timm, C., Hoernle, K., Werner, R., Hauff, F., van den Bogaard, P., Michael, P., ... & Koppers, A. (2011). Age and geochemistry of the oceanic Manihiki Plateau, SW Pacific: New evidence for a plume origin. *Earth and Planetary Science Letters*, *304*(1–2), 135–146, doi: 10.1016/j.epsl.2011.01.025.

Tomimatsu, Y., Nozaki, T., Sato, H., Takaya, Y., Kimura, J. I., Chang, Q., ... & Onoue, T. (2021). Marine osmium isotope record during the Carnian “pluvial episode”(Late Triassic) in the pelagic Panthalassa Ocean. *Global and Planetary Change*, *197*,

103387, doi: 10.1016/j.gloplacha.2020.103387.

Tornaghi, M. E., Silva, I. P., and Ripepe, Maurizio, (1989), Lithostratigraphy and planktonic foraminiferal biostratigraphy of the Aptian-Albian" Scisti a Fucoidi" in the Piobbico core, Marche, Italy: background for cyclostratigraphy: Rivista Italiana di Paleontologia e Stratigrafia, v. 95, p. 223–264.

Toucanne, S., Minto'o, C.M.A., Fontanier, C., Bassetti, M.A., Jorry, S.J., & Jouet, G. (2015). Tracking rainfall in the northern Mediterranean borderlands during sapropel deposition. *Quaternary Science Reviews, 129*, 178–195, doi: 10.1016/j.quascirev.2015.10.016.

Toyofuku, T., Suzuki, M., Suga, H., Sakai, S., Suzuki, A., Ishikawa, T., ... & Kitazato, H. (2011). Mg/Ca and $\delta^{18}O$ in the brackish shallow-water benthic foraminifer Ammonia 'beccarii'. *Marine Micropaleontology*, *78*(3–4), 113–120, doi: 10.1016/j.marmicro.2010.11.003.

Trabucho Alexandre, J. T., van Gilst, R. I., Rodoríguez-López, J. P., & De Boer, P. L. (2011). The sedimentary expression of oceanic anoxic event 1b in the North Atlantic. *Sedimentology*, *58*(5), 1217–1246, doi: 10.1111/j.1365-3091.2010.01202.x.

Tribovillard, N., Algeo, T. J., Lyons, T., & Riboulleau, A. (2006). Trace metals as paleoredox and paleoproductivity proxies: an update. *Chemical geology*, *232*(1–2), 12–32, doi: 10.1016/j.chemgeo.2006.02.012.

Turgeon, S. C., & Creaser, R. A. (2008). Cretaceous oceanic anoxic event 2 triggered by a massive magmatic episode. *Nature*, *454*(7202), 323–326, doi: 10.1038/nature07076.

Vail, P. R., Mitchum, R. M. & Thompson, S. (1977a). Seismic Stratigraphy and Global Changes of Sea Level, Part 3: Relative Changes of Sea Level from Coastal Onlap, American Association of Petroleum Geologists Memoir, 36, 63–81.

Vail, P. R., Mitchum, R. M. & Thompson, S. (1977b). Seismic stratigraphy and global changes of sea level, Part 3: Global Cycles of Relative Changes of Sea Level, American Association of Petroleum Geologists Memoir, 36, 83–97.

Vallier, T. L., Dean, W. E., Rea, D. K., & Thiede, J. (1983). Geologic evolution of Hess Rise, central North Pacific Ocean. *Geological Society of America Bulletin*, *94*(11), 1289–1307, doi: 10.1130/0016-7606(1983)94<1289:GEOHRC>2.0.CO;2.

Van Andel, T. H. (1975). Mesozoic/Cenozoic calcite compensation depth and the global

distribution of calcareous sediments. *Earth and Planetary Science Letters*, *26*(2), 187–194, doi: 10.1016/0012-821X(75)90086-2.

Vance, D., Teagle, D.A., & Foster, G.L. (2009). Variable Quaternary chemical weathering fluxes and imbalances in marine geochemical budgets. *Nature, 458*(7237), 493–496, doi: 10.1038/nature07828.

Vandermark, D., Tarduno, J. A., & Brinkman, D. B. (2007). A fossil champsosaur population from the high Arctic: implications for Late Cretaceous paleotemperatures. *Palaeogeography, Palaeoclimatology, Palaeoecology*, *248*(1–2), 49–59, doi: 10.1016/j.palaeo.2006.11.008.

Vickers, M. L., Price, G. D., Jerrett, R. M., Sutton, P., Watkinson, M. P., & FitzPatrick, M. (2019). The duration and magnitude of Cretaceous cool events: Evidence from the northern high latitudes. *Bulletin*, *131*(11–12), 1979–1994.

Wang, P. (2009). Global monsoon in a geological perspective. *Chinese Science Bulletin, 54*(7), 1113–1136.

Wang, P., Tian, J., & Lourens, L.J. (2010). Obscuring of long eccentricity cyclicity in Pleistocene oceanic carbon isotope records. *Earth and Planetary Science Letters, 290*(3–4), 319–330, doi: 10.1016/j.epsl.2009.12.028.

Wang, Y., Huang, C., Sun, B., Quan, C., Wu, J., & Lin, Z. (2014). Paleo-CO2 variation trends and the Cretaceous greenhouse climate. *Earth-Science Reviews*, *129*, 136–147, doi: 10.1016/j.earscirev.2013.11.001.

Wehausen, R., & Brumsack, H.J. (2002). Astronomical forcing of the East Asian monsoon mirrored by the composition of Pliocene South China Sea sediments. *Earth and Planetary Science Letters, 201*(3–4), 621–636, doi: 10.1016/S0012-821X(02)00746-X.

White, A. F., Blum, A. E., Bullen, T. D., Vivit, D. V., Schulz, M., & Fitzpatrick, J. (1999). The effect of temperature on experimental and natural chemical weathering rates of granitoid rocks. *Geochimica et Cosmochimica Acta*, *63*(19–20), 3277–3291, doi: 10.1016/S0016-7037(99)00250-1.

Winterer, E. L., Ewing, J. L., and others, (1973). Initial reports of the Deep Sea Drilling Project, Volume 17: Washington, D.C., U.S. Government Printing Office, p. 145–234.

Woodhouse, O. B., Ravizza, G., Falkner, K. K., Statham, P. J., & Peucker-Ehrenbrink, B. (1999). Osmium in seawater: vertical profiles of concentration and isotopic

composition in the eastern Pacific Ocean. *Earth and Planetary Science Letters*, *173*(3), 223–233, doi: 10.1016/S0012-821X(99)00233-2.

Yamashita, Y., Takahashi, Y., Haba, H., Enomoto, S., & Shimizu, H. (2007). Comparison of reductive accumulation of Re and Os in seawater–sediment systems. *Geochimica et Cosmochimica Acta*, *71*(14), 3458–3475, doi: 10.1016/j.gca.2007.05.003.

Yin, L., Li, J., Liu, J., Li, C., Sun, S., Liang, H., & Xu, J. (2017). Precise and accurate Re–Os isotope dating of organic-rich sedimentary rocks by thermal ionization mass spectrometry with an improved H_2O_2-HNO_3 digestion procedure. *International Journal of Mass Spectrometry*, *421*, 263–270, doi: 10.1016/j.ijms.2017.07.013.

Yang, H. J., Frey, F. A., Weis, D., Giret, A., Pyle, D., & Michon, G. (1998). Petrogenesis of the flood basalts forming the northern Kerguelen Archipelago: Implications for the Kerguelen plume. *Journal of Petrology*, *39*(4), 711–748, doi: 10.1093/petroj/39.4.711.

Yao, H., Chen, X., Yin, R., Grasby, S. E., Weissert, H., Gu, X., & Wang, C. (2021). Mercury evidence of intense volcanism preceded oceanic anoxic event 1d. *Geophysical Research Letters*, *48*(5), e2020GL091508, doi: 10.1029/2020GL091508.